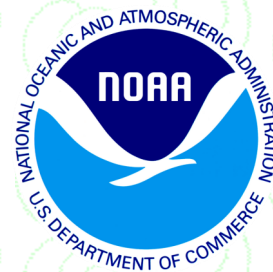Santa Barbara, CA

Climate Prediction S&T Digest

April 2019

NWS Science & Technology Infusion Climate Bulletin Supplement

Inside this issue:

1. Coupled atmosphere-ocean climate system

2. IDSS-impact decision support services

3. Improved understanding, prediction, and simulation of climate variability

4. Recent high impact weather and climate events

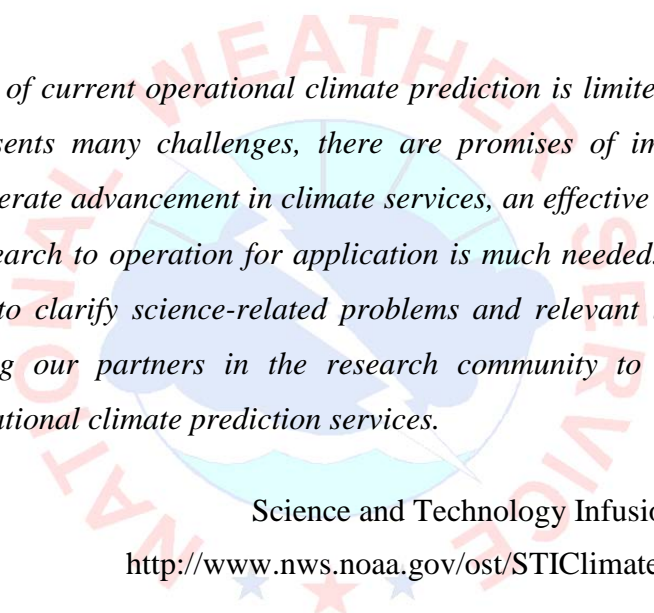5. Improving models, forecasts and observational data sets

Appendix
   Workshop Photo Gallery

Although the skill of current operational climate prediction is limited and the research on the topic presents many challenges, there are promises of improvement on the horizon. To accelerate advancement in climate services, an effective mechanism of S&T infusion from research to operation for application is much needed. This bulletin has been established to clarify science-related problems and relevant issues identified in operation, inviting our partners in the research community to work together on improvement of national climate prediction services.

Science and Technology Infusion Climate Bulletin
http://www.nws.noaa.gov/ost/STIClimateBulletin/index.htm

National Weather Service
National Oceanic and Atmospheric Administration
U.S. Department of Commerce

PREFACE

It is with great pleasure that the Climate Prediction Center (CPC) and the Office of Science and Technology Integration (STI) offer you this synthesis of the 42nd Climate Diagnostics and Prediction Workshop (CDPW). The CDPW remains a must attend workshop for the climate monitoring and prediction community. As is clearly evident in this digest, considerable progress is being made both in our ability to monitor and predict climate. The purpose of this digest is to ensure that climate research advances are shared with the broader community and also transitioned into operations. This is especially important as NOAA works to enhance climate services both across the agency and with external partners. We hope you find this digest to be useful and stimulating. And please drop me a note if you have suggestions to improve the digest.

I would like to thank Dr. Jiayu Zhou of the Office of Science and Technology Integration, for developing the digest concept and seeing it through to completion. This partnership between STI and CPC is an essential element of NOAA climate services.

David G. DeWitt

Director, Climate Prediction Center

National Centers for Environmental Prediction

NOAA's National Weather Service

CONTENTS

iv

APPENDIX

OVERVIEW

NOAA's 43rd Climate Diagnostics and Prediction Workshop was held in Santa Barbara, California on 23-25 October 2018. The workshop was hosted by the Earth Research Institute and Department of Geography at the University of California Santa Barbara and co-sponsored by the Climate Prediction Center (CPC) of the National Centers for Environmental Prediction (NCEP) and the Climate Services Branch (CSB) of the National Weather Service (NWS).

The workshop focused on five major themes, with an emphasis on climate prediction, monitoring, attribution, diagnostics, and service delivery related to:

1. Improved understanding of the coupled atmosphere-ocean climate system through dynamical and statistical models and methods, forecaster practices and protocols, reanalysis data and model improvement, and scientific concepts;

2. Prospects for improved understanding, prediction, and simulation of intra-seasonal, seasonal, and inter-annual climate variability, including the extratropical annular modes, stratosphere/troposphere coupling, tropical-extratropical interactions, land-surface forcing, atmospheric river events and drought/precipitation events etc.;

3. Climate variability and prediction in relation to the hydrologic cycle and in particular Western water resources.;

4. Observation, prediction and attribution of recent high impact weather and climate events, and implications for extreme precipitation and temperatures, heat/cold waves, droughts and wildfires;

5. Improving climate information delivery for impact-based decision support services through the application of new technologies, including GIS, statistical tools, and software development practices.

The workshop featured daytime oral presentations, invited speakers, and discussions with a poster session event in one evening.

This Digest is a collection of extended summaries of the presentations contributed by participants. The workshop is continuing to grow and expected to provide a stimulus for further improvements in climate monitoring, diagnostics, prediction, applications and services.

1. IMPROVED UNDERSTANDING OF THE COUPLED ATMOSPHERE-OCEAN CLIMATE SYSTEM

43rd NOAA Annual Climate Diagnostics and Prediction Workshop

Santa Barbara, California

23-25 October 2018

A Hybrid Dynamic-Statistical Approach to Link Predictive Understanding to Improve Seasonal Prediction of Rainfall Anomalies at the Regional Scale

Rong Fu[1], Amir Erfanian[1], Nelun Fernando[2], Sudip Chakraborty[1], and Bing Pu[3]

[1]Department of Atmospheric and Oceanic Sciences, University of California, Los Angeles
[2]Texas Water Development Board
[3]Department of Geography and Atmospheric Science, University of Kansas

1. Introduction

Seasonal prediction of summer rainfall anomalies over the United State (US) Great Plains (GP) is central for drought early warning and society preparedness. Yet, current dynamic models' predictions have failed to predict recent extreme droughts in 2011 and 2012 and shown virtually no skills for seasonal prediction of the summer rainfall anomalies (*e.g.* Quan *et al.* 2012; Hoerling *et al.* 2014). In addition, whether summer rainfall anomalies, especially droughts, are intrinsically predictable without oceanic forcing, if so, what are the underlying physical mechanisms, are still debatable. Namias (1982) have observed a persistent circulation anomaly from March to June for 1980 and 1988 summer droughts. He suggested that such persistence can provide reasonably good seasonal predictability. Fernando *et al.* (2016) have shown that 13 out of 18 severe-to-extreme summer droughts over the US southern GP since 1895 were linked to dry spring, only 3 summer droughts occurred after wet springs. There is a significant correlation between soil moisture anomalies and the 500 hPa geopotential height anomalies 2-4 weeks later that is stronger than the autocorrelation of the 500 hPa geopotential height anomalies. Thus, the observed drought persistence is likely due to land surface feedbacks, as suggested by previous studies (*e.g.* Carson and Sangster 1981; Dirmeyer 1994; Myoung and Nielsen-Gammon 2010; Oglesby and Erickson 1989). However, soil moisture feedbacks in the current dynamic models can only sustain drought memory for about a month. Why soil moisture memory in these models is so short lived compared to that appears in observation is not clear. In addition, the apparent drought memory can be a result of a sequence of random weather events induced by stationary Rossby waves (*e.g.* Hoerling *et al.* 2014, Schubert *et al.* 2011). Whether soil moisture memory plays a significant role in sustaining the dry anomalies between these random dry spells is not clear. Furthermore, soil moisture anomalies can lead to Rossby wave like large-scale circulation anomalies (*e.g.* van den Dool *et al.* 2003; Koster *et al.* 2014). Our research is motivated by these outstanding questions, focusing on the role of land-atmospheric coupling processes in determining the observed spring to summer drought persistence, its implication for seasonal predictability and potential causes of the inadequate representation of the spring to summer drought memory.

2. Data and model products

We have used the monthly precipitation of Precipitation Reconstruction over Land (Chen *et al.* 2002; hereafter PRECL) from National Oceanic and Atmospheric Admiration (NOAA) from 1948 to present at 1° by 1° resolution, the European Centre for Medium-Range Weather Forecasts (ECMWF) Interim Re-Analysis (ERA-Interim) (Dee *et al.* 2011) for the moisture budget analysis (Erfanian and Fu 2019) and the radiosonde profiles provided by the Department of Energy (DOE) Atmospheric Radiation Measurement (ARM) at its southern GP site. In addition, we have used the Climate Forecasting System Version 2 (CFSv2) real time forecasts and the CFS reanalysis (CFSR) products to train a Canonical Correlation Analysis (CCA) based statistical model provided by Climate Predictability Tool (CPT) of the International Research Institute for Climate and Society at Columbia University. The predictors of this model are the anomalous large-scale atmospheric circulation (500 hPa geopotential height), convective inhibition energy (CIN) and soil moisture anomalies in April. The predictant is the rainfall anomalies during May-July.

Correspondence to: Rong Fu, Department of Atmospheric and Oceanic Sciences, University of California, Los Angeles, CA; E-mail: rfu@atmos.ucla.edu

3. Highlight of the results

What process initiates the summer droughts over the US GP? Figure 1 suggests a connection between rainfall deficit over the southwestern (SW) US in spring (March-May) and rainfall deficit over the US GP in summer (June-August), through anomalous zonal advection of drier air. In particular, Fig. 1a shows a significant positive correlation between rainfall anomalies over SW US and the zonal moisture advection anomalies into the GP during March-May. The dry anomalies over the SW US in spring is often induced by La Niñas (*e.g.* Leathers *et al.* 1991)). Figure 1b shows a significant positive correlation between the zonal moisture advection anomalies into the GP in spring and the rainfall anomalies over the GP in summer. Figure 1c shows persistent dry zonal advection anomalies to the GP during 2012 in the lower troposphere (900 – 600 hPa) started in March, and intensified in May-June. This persistence is in contrast to the zonal moisture advection in the middle and upper troposphere, which changed between dry and wet anomalies, presumably influenced by random large-scale circulation anomalies associated with the Rossby waves. Thus, the persistent dry advection to the GP due to rainfall deficits over the SW US from late winter to early summer plays a significant role in initiating the summer rainfall deficit over the US GP, as illustrated schematically in Fig. 1d. This result has been reported as part of the publication (Erfanian and Fu 2019).

Fig. 1   a) and b) Single point correlation maps between the standardized time series (1979-2018) of the March-May zonal moisture advection at 700 mb averaged over the GP (shown by the black box) with the standardized anomalies of precipitation in (a) the March-May; (b) in June-August. The correlation coefficients greater than 0.3 and 0.4 are statistically significant at the 90% and 98% confidence level, respectively. c) The seasonal evolution of the standardized mean zonal moisture advection anomalies induced by the anomalous moisture gradient as a function of the pressure (hPa) for the 2012 GP drought. d) Schematic illustration of the mechanism that initiates the summer drought over the US GP.

What process intensify the summer droughts over the US GP? In particular, whether the dry anomalies are intensified by a bottom-up land-atmospheric interaction, or by a top-down Rossby wave induced atmospheric circulation anomalies? Figure 2 shows the evolution of the dry atmospheric layers associated with the intensification of the 2011 and 2012 droughts, compared to that of 2013, a non-drought year, based on the radiosonde profiles provided by the Department of Energy (DOE) Atmospheric Radiation Measurement (ARM) at its Southern GP site. As one can see, a drier relative humidity layer started in the atmospheric boundary layer and the lower troposphere (below 3 km in height) in April of 2011, and 2012 (Fig. 2a). The drier layer deepened and reached mid-troposphere (surface to 7 km height) in May (Fig. 2b), and then further deepened and reached to the upper troposphere (surface to 13 km height) in June (Fig. 2c) and July (Fig. 2d) of 2011 and 2012, respectively. Such a gradual deepening of the drier layer from the lower troposphere to the mid-troposphere and then to the upper troposphere suggest that a drier air advection from the US SW in spring reduces shallow convection and increasing land surface dryness, which reduces moisture transport to the mid-troposphere and suppresses convective congests and deep convection (*e.g.* Holloway and Neelin 2009; Zhang and Klein 2010). The latter reduces moisture in the middle and upper troposphere. Fig. 2 suggests that the intensification of the 2011 and 2012 GP droughts is primary contributed by a bottom-up positive land-atmospheric feedbacks.

Could the above discussed mechanisms enable us to improve seasonal prediction of the US GP summer rainfall anomalies? To answer this question, in Fig. 3 we compare the prediction skills of our CCA based statistical model (Figs. 3a-3c) with the skills of the North American Multi-model Ensemble (NMME) seasonal predictions (including all the ensemble members of the seven models, Figs. 3d-3f) for the southern GP, both are initialized in April. The statistical prediction shows overall higher prediction skills than those of the NMME ensemble predictions, as measured by the Spearman's correlation (Figs. 3a, 3d), the Receiving Operating Characteristic (ROC, Figs. 3b, 3e) and Two-Alternative Forced Choice (2AFC, Figs. 3c, 3f), especially over Texas, the central area of the southern GP. The statistical prediction shows less skills than the NMME predictions near the western margin of the domain though. In addition, this statistical model can be used to improve NMME extended seasonal prediction of rainfall anomalies during May-July through a hybrid dynamic-statistical approach. This hybrid system uses NMME ensemble predictions for April as the predictors of the statistical prediction for the rainfall anomalies in May-July. Using the NMME ensemble predictions initialized in January, February and March, respectively, this hybrid dynamic-statistical prediction system can provide extended seasonal prediction with lead-time up to 4-6 months, with the prediction skills higher than those of the NMME prediction of rainfall anomalies initialized in April (not shown here due to page space limit). This result further suggests the importance of the adequate representation of mechanisms that initiate and intensify the summer droughts over the US GP, as suggested by figures 1 and 2. The aforementioned statistical and the hybrid dynamic-statistical prediction systems have been used as an important climate indicator by the Texas Water Development Board (TWDB) in the drought briefing newsletter and at their Water For Texas website since 2015 to support water management decisions (http://waterdatafortexas.org/drought/drought-forecast).
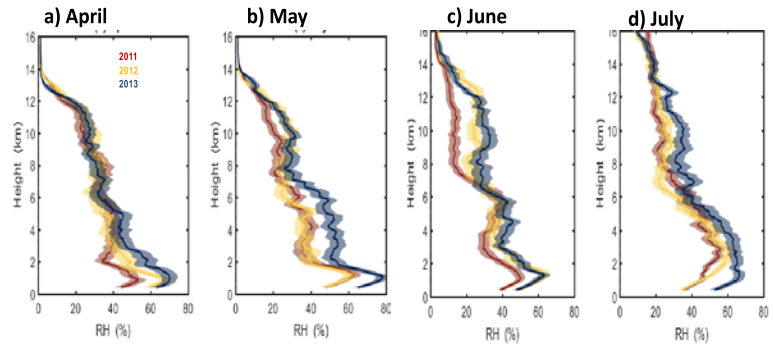
Fig. 2 Monthly mean relative humidity profiles derived from the radiosonde profiles provided by the DOE ARM program at its Southern GP site for a) April, b) May, c) June, and d) July for 2011 (brown curves), 2012 (orange curves) and 2013 (blue curves), respectively. The shades represent the standard error.
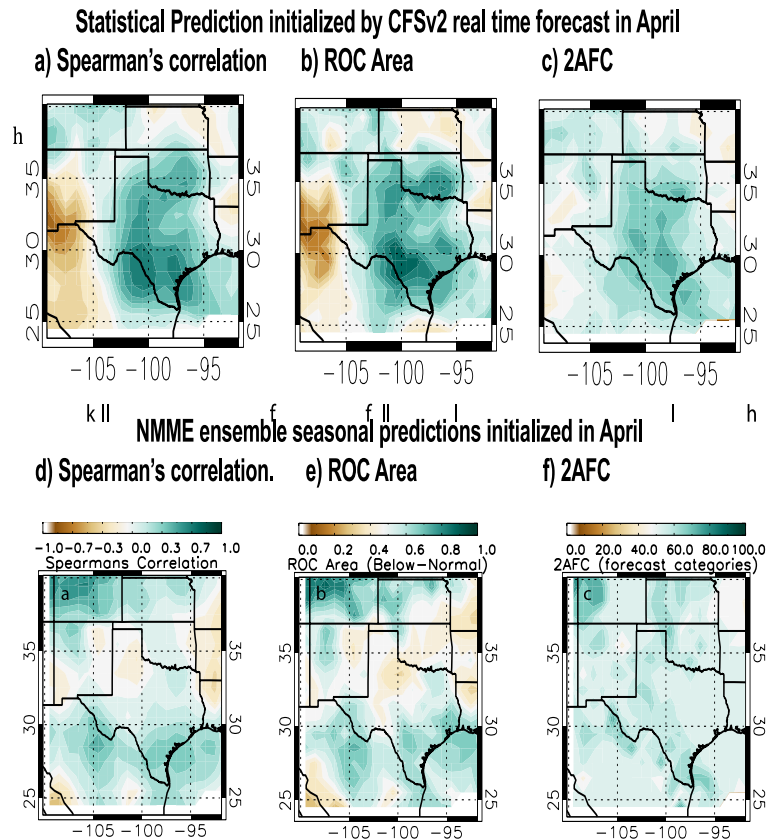
Fig. 3 Maps of the statistical seasonal prediction skills (a-c), compared to those of the NMME multi-model ensemble seasonal predictions for May-July rainfall anomalies initialized in April. The prediction skills are measured by the Spearman's correlation (a, d), ROC Area (b, e), and 2AFC (c, f), respectively. The period of evaluation is 1982-2010 using the 3-point cross-validation (Barnston *et al.*, 1992).

4. Conclusions and Discussion

Our observational analysis supported by the NOAA MAPP program has shown that the reduced westerly moisture transport in the lower troposphere, due to dryness over US SW and the positive feedbacks between surface dryness and large-scale circulation, especially through the coupling between land surface, shallow clouds, deep convection, play important roles in initiating and intensify summer droughts over the US GP. These mechanisms can be used to improve predictability of the summer rainfall anomalies over the US GP, as shown by improved prediction skills of a statistical prediction model based on these mechanisms, over those of the ensemble dynamic seasonal predictions by the NMME. Our hybrid dynamic-statistical seasonal prediction system has shown skills to improve summer rainfall predictions over the US GP using NMME seasonal predictions of the large-scale atmospheric circulation, CIN and soil moisture anomalies in April as predictors for the statistical prediction. Thus, this approach can provide a value-added product of NMME to support NOAA's mission of improving seasonal prediction of regional rainfall over the US to support societal drought preparedness.

References

Barnston, A. G., and C. F. Ropelewski, 1992: Prediction of ENSO episodes using canonical correlation analysis. *J. Climate*, **5**, 1316–1345, doi:10.1175/1520-0442(1992)005<1316:POEEUC>2.0.CO;2.

Carson, D. J., and A. J. Sangster, 1981: The influence of land-surface albedo and soil moisture on general circulation model simulations. *Research activities in atmospheric and oceanic modelling,* ID Rutherford, Ed., Numerical Experimentation Program Rep. 2, 5.14-5.21.

Chen, M., P. Xie, and J. E. Janowiak, 2002: Global land precipitation: A 50-yr monthly analysis based on gauge observations. *J. Hydrometeor.*, **3**, 249-266, doi:10.1175/1525-7541(2002)003<0249:GLPAYM>2.0.CO;2

Dee, D. P., and Coauthors, 2011: The ERA-Interim reanalysis: Configuration and performance of the data assimilation system. *Q. J. R. Meteorol. Soc.*, **137**, 553–597, doi:10.1002/qj.828.

Dirmeyer, P. A., 1994: Vegetation stress as a feedback mechanism in midlatitude drought. *J. Climate*, **7**, 1463–1483, doi:10.1175/1520-0442(1994)007<1463:VSAAFM>2.0.CO;2.

van den Dool, H., J. Huang, and Y. Fan, 2003: Performance and analysis of the constructed analogue method applied to U.S. soil moisture over 1981–2001. *J. Geophys. Res.: Atmos.*, **108**, 8617, doi:10.1029/2002JD003114.

Erfanian, A., and R. Fu, 2019: Drier spring over the US Southwest as an important precursor of summer droughts over the US Great Plains. *Atmos. Chem. Phys. Discuss.*, 1–29, doi:10.5194/acp-2019-154.

Fernando, D. N., and Coauthors, 2016: What caused the spring intensification and winter demise of the 2011 drought over Texas? *Clim. Dyn.*, **47**, 3077–3090, doi:10.1007/s00382-016-3014-x.

Hoerling, M., J. Eischeid, A. Kumar, R. Leung, A. Mariotti, K. Mo, and R. Seager, 2014: Causes and predictability of the 2012 Great Plains drought. *Bull. Amer. Meteor. Soc.*, **95**, 269–282, doi:10.1175/BAMS-D-13-00055.1.

Holloway, C. E., and J. D. Neelin, 2009: Moisture vertical structure, column water vapor, and tropical deep convection. *J. Atmos. Sci.*, **66**, 1665–1683, doi:10.1175/2008JAS2806.1.

Koster, R. D., Y. Chang, and S. D. Schubert, 2014: A mechanism for land-atmosphere feedback involving planetary wave structures. *J. Climate*, **27**, 9290–9301, doi:10.1175/JCLI-D-14-00315.1.

Leathers, D. J., B. Yarnal, M. A. Palecki, 1991: The Pacific/North American teleconnection pattern and United States climate. Part I: Regional temperature and precipitation associations. *J. Climate*, **4**, 517–528, doi:10.1175/1520-0442(1991)004<0517:TPATPA>2.0.CO;2.

Myoung, B., and J. W. Nielsen-Gammon, 2010: The convective instability pathway to warm season drought in Texas. Part II: Free-tropospheric modulation of convective inhibition. *J. Climate*, **23**, 4474–4488, doi:10.1175/2010JCLI2947.1.

Namias, J., 1982: Anatomy of Great Plains protracted heat waves (especially the 1980 U.S. summer drought). *Mon. Wea. Rev.*, **110**, 824–838, doi:10.1175/1520-0493(1982)110<0824:AOGPPH>2.0.CO;2.

Oglesby, R. J., and D. J. Erickson, 1989: Soil moisture and the persistence of North American drought. *J. Climate*, **2**, 1362–1380, doi:10.1175/1520-0442(1989)002<1362:SMATPO>2.0.CO;2.

Quan, X.-W., M. P. Hoerling, B. Lyon, A. Kumar, M. A. Bell, M. K. Tippett, and H. Wang, 2012: Prospects for dynamical prediction of meteorological drought. *J. Appl. Meteor. Climatol.*, **51**, 1238–1252, doi:10.1175/JAMC-D-11-0194.1.

Schubert, S., H. Wang, and M. Suarez, 2011: Warm season subseasonal variability and climate extremes in the Northern Hemisphere: The role of stationary Rossby waves. *J. Climate*, **24**, 4773–4792, doi:10.1175/JCLI-D-10-05035.1.

Zhang, Y., and S. A. Klein, 2010: Mechanisms affecting the transition from shallow to deep convection over land: Inferences from observations of the diurnal cycle collected at the ARM southern Great Plains site. *J. Atmos. Sci.*, **67**, 2943–2959, doi:10.1175/2010JAS3366.1

Mechanisms for the Formation of Super El Niños

Tim Li and Lin Chen

Department of Atmospheric Sciences, University of Hawaii at Manoa, HI

EXTENDED SUMMARY

Current operational models have difficulty in predicting the intensity of El Niños. To improve the El Niño forecast skill, it is critical to understand statistically significant precursory signals between regular and super El Niños. With the use of observed sea surface temperature (SST) and rainfall data and oceanic and atmospheric reanalysis datasets, El Niño events during 1958-2008 were separated into two groups, a super El Niño group (with Niño 3.4 index being greater than 2.5 standard deviation, hereafter S-group) and a regular El Niño group (with Niño 3.4 index being less than 2.0 standard deviation, hereafter R-group) (Chen *et al.* 2016). A composite analysis shows that during the El Niño onset phase (Apr-May) when the amplitude of the
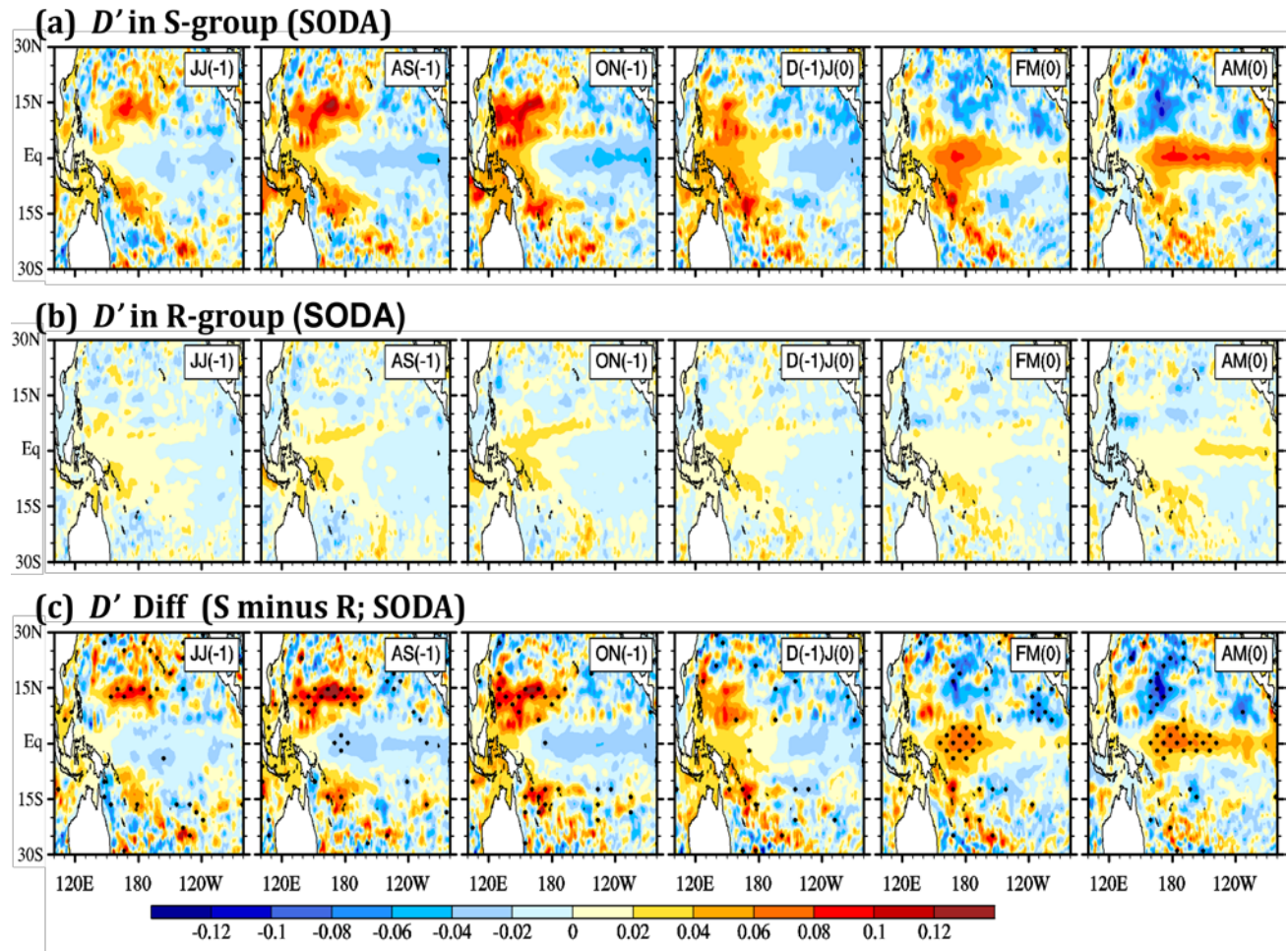
Fig. 1 Evolution of composite sea surface height anomaly (unit: m) for JJ[−1], AS[−1], ON[−1], D[−1]J[0], FM[0] and AM[0], derived from (a) S-group, (b) R-group and (c) the difference between S-group and R-group. The stippling in (c) indicates that the difference exceeds a 95% confidence level using a *t*-test. The ocean reanalysis dataset SODA was used. (From Chen *et al.* 2016)

_____

Correspondence to: Tim Li, Department of Atmospheric Sciences, University of Hawaii at Manoa, HI.
E-mail: timli@hawaii.edu

eastern Pacific SST anomaly (SSTA) is still small in both the groups, a significantly larger positive SSTA tendency appears in S-group than in R-group. A mixed-layer heat budget analysis was further conducted, and the result indicated that the SSTA tendency difference arises primarily from the difference in anomalous advection of mean temperature by zonal current anomaly. The major factor controlling the zonal current anomaly is geostrophic current associated with oceanic thermocline depth anomaly (D').

To understand the cause of the D' difference during the onset phase, we investigated the evolution of D' from the pre-onset stage to the onset phase. Figure 1 shows the evolution of D' from June-July of the preceding year (denoted as year [-1]) to April-May of El Niño developing year (denoted as year [0]) in the S-group and R-group, as well as their difference (S minus R). A similar buildup of positive D' (which represents the upper ocean heat content anomaly) appeared in the western equatorial Pacific in both the S- and R- group (Fig. 1a–b). However, the signal of D' was much stronger in the S-group. Most important difference lies in the off-equatorial region from JJ[-1] to ON[-1]. A significantly larger positive D' anomaly appeared over the off-equatorial (10°N-20°N and 10°S-20°S) western Pacific region in S-group than in R-group (Fig. 1c). As the significantly different D' signals propagated westward as Rossby waves and were reflected in the western boundary, they contributed to distinctive differences in the magnitude of D' at the equator in FM[0] and AM[0], with a much larger positive D' in S-group than in R-group. Thus, the accumulation of deepened thermocline depth anomaly in the off-equatorial western Pacific in preceding months (JJAM[−1]) holds a key for the subsequent differences in the thermocline depth, zonal current and vertical velocity anomalies in later months (*i.e.*, FM[0] and AM[0]). The difference in D' was further caused by the difference in anomalous wind stress curl patterns in JJAS[-1] in the western Pacific, which were regulated by anomalous SST and precipitation fields over the Maritime Continent and western Pacific.

While a clear positive D' signal was seen in western Pacific during the onset phase of super El Niños in 1982 and 1997, such a precursory signal was not presented in the 2015 El Niño case (Chen *et al.* 2017). Figure 2 compares the evolutions of the Niño3 SSTA for 2015 El Niño (hereafter 2015EN) and traditional super El Niño (defined as ensemble average of 1982 and 1997 events, hereafter TR-super EN). Two marked differences are worth noting. Firstly, in contrast to TR-super EN that started from a cold episode in the preceding year, 2015EN was preceded by a weak warming event peaked in November 2014. In the preceding winter (November to ensuing February, *i.e.*, the pre-onset phase), the TR-super EN shows a warming tendency but 2015EN shows a cooling tendency. Secondly, in 2015EN a marked turnabout of the SSTA tendency (from negative to positive) happened around February 2015.
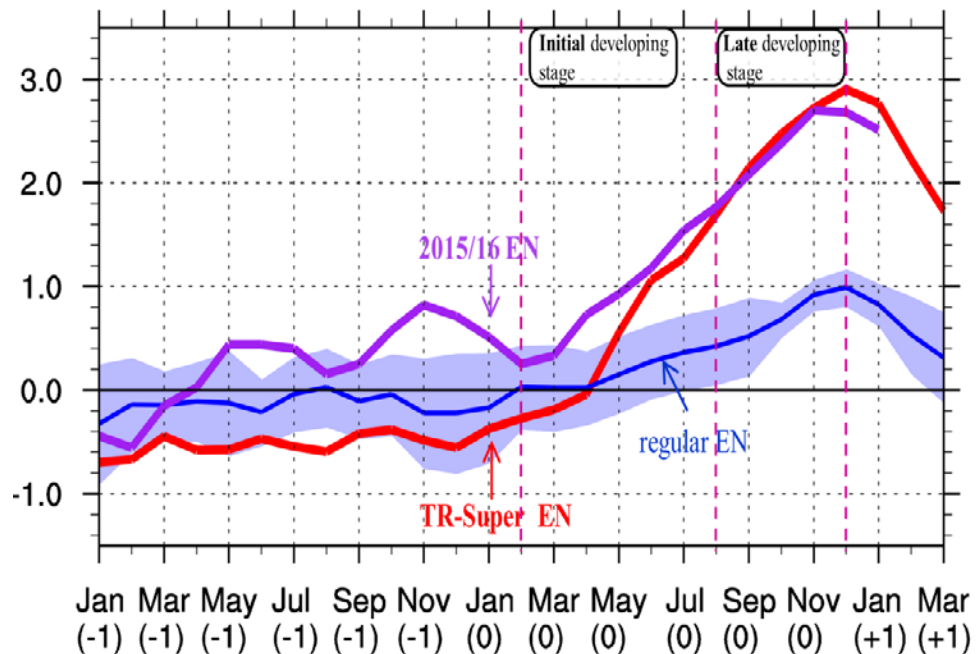
Fig. 2 Time evolution of Niño3 SSTA. Purple line indicates the 2015 El Niño, red line indicates the composite of traditional super El Niño events (*i.e.*, 1982 and 1997 events), and the blue line indicates the composite of regular El Niño events during 1980-2015 (including 1986/87, 1987/88, 1991/92, 1994/95, 2002/03, 2004/05, 2006/07 and 2009/10 El Niños). The light blue shading indicates the inter-case spread, estimated with the inter-case standard deviation of the regular El Niño events. (From Chen *et al.* 2017)

A mixed layer heat budget analysis indicated that the turnabout of the SSTA tendency in February 2015 was caused by the change of anomalous zonal advection associated with sudden built-up of positive D' over equatorial central Pacific. A further examination showed that the sudden increase of D' resulted from exceptionally strong westerly wind events (WWEs) in early 2015. An accumulated WWE index was introduced by Chen et al. (2017), and the result showed that this index attained the largest value in the past 37 years (*i.e.*, 1979-2015). Idealized ocean modeling experiments were further carried out to illustrate the important role of the WWEs in setting up the positive D' in early 2015.
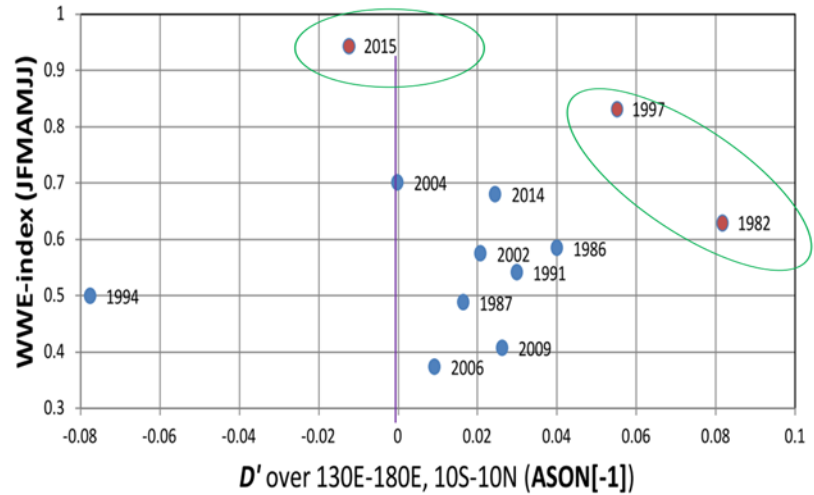
Fig. 3 Scatter diagram for each El Niño since 1979 as a function of precursory thermocline anomaly signal (horizontal axis) and an accumulated WWE index (vertical axis). Green circle indicates two distinctive regimes for super El Niño formation: exceptionally strong WWEs versus exceptional strong D' signal. (From Chen *et al.* 2017)

In summary, the occurrence of a series of exceptionally strong WWEs in early 2015 is the major driver to flare up a positive D' center over equatorial Pacific and cause the formation of the 2015 super El Niño. The unique developing characteristic breaks our traditional view of El Niño formation, which emphasized the off-equatorial thermocline recharging process. The result suggests that two routes may lead to super El Niño formation (Fig. 3). The first route is the occurrence of exceptionally strong positive precursory D' signal in off-equatorial western Pacific. The 1997 and 1982 events are such examples. The second route is the occurrence of exceptionally strong WWEs. The formation of 2015EN is such an example – while a precursory negative off-equatorial D' signal favored the occurrence of thermocline shoaling at the equator in subsequent months, such a discharging process was interrupted by the consecutive extremely strong WWEs. Thus the 2015 episode is a shining example showing how important WWEs are. They can turn around slow coupled dynamics and cause the generation of a super El Niño.

The works above have been published in referred journals (see references below).

Reference

Chen, L., T. Li, B. Wang, and L. Wang, 2017: Formation mechanism for 2015/16 super El Niño. *Scientific Reports*, **7**, doi:10.1038/s41598-017-02926-3.

Chen, L., T. Li, Swadhin K. Behera, and Takeshi Doi, 2016: Distinctive precursor air-sea signals between regular and super El Niños. *Adv. Atmos. Sci.*, **33**, 996-1004.

The Influence of the Atlantic Multidecadal Oscillation on the Eastern Andes Low-Level Jet and Precipitation in South America

Charles Jones and Leila M. V. Carvalho

Department of Geography, University of California, Santa Barbara, California

ABSTRACT

The South America low-level jet (SALLJ) on the eastern slopes of the Andes is a unique climatological feature in the continent. The SALLJ transports large amounts of moisture and controls the spatiotemporal variability of precipitation in southeast South America. This study shows a remarkable influence of the Atlantic Multidecadal Oscillation (AMO) on decadal-to-multidecadal variability of the SALLJ. The results show a consistent pattern in which active SALLJ days during negative AMO phases are associated with negative precipitation anomalies over northern Amazon and the Atlantic Intertropical Convergence Zone (ITCZ). Increased cross-equatorial flow over northwestern South America combined with the outflow associated with the atmospheric subsidence over the negative precipitation anomalies enhances northerly winds along the eastern slopes of the Andes and Amazon. This atmospheric circulation response, which is more prevalent in the austral winter, intensifies the SALLJ. In the exit region of the SALLJ over southern Brazil, Uruguay and northern Argentina, an anomalous low-level cyclonic circulation is associated with enhanced precipitation. The influence of the AMO on the SALLJ is consistent with paleo-proxy studies showing multidecadal changes in precipitation over the La Plata River drainage basin. The analysis shows that secular trends reinforce the SALLJ and precipitation patterns. Moreover, the study highlights the importance of natural variability (*i.e.*, decadal-multidecadal variations) occurring within long-term trends in the mean state, possibly associated with global warming, and significant changes in the SALLJ and precipitation over South America.
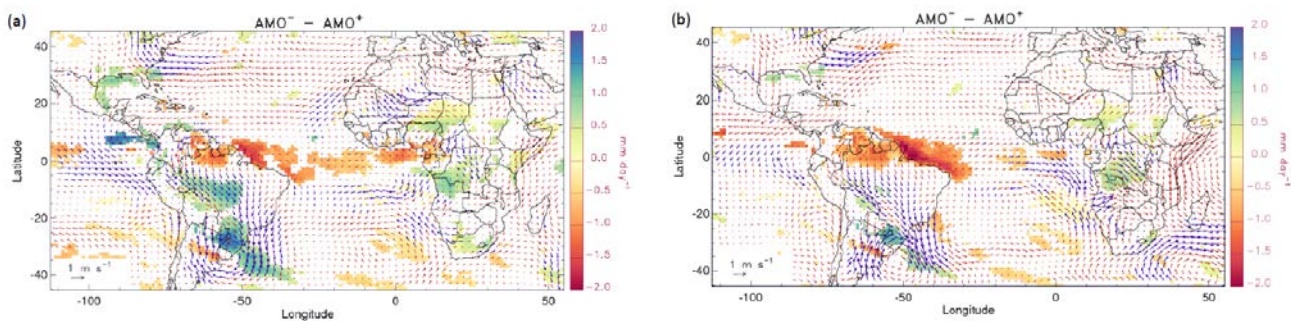
Fig. 1 a) Differences in mean winds (850-hPa) and precipitation during SALLJ days between negative (Nov 1965–Aug 1996) and positive (Sep1924–Oct 1965) AMO phases. Time series of winds and precipitation contain linear trends. b) As in (a), but linear trends in winds and precipitation have been removed before calculating the difference between negative and positive AMO phases. Vectors in blue colors are statistically significant at 5% confidence; vectors in red are not statistically significant. Vector scale is shown in the inset. Shading shows statistically significant (5% level) differences in mean precipitation.

This work has been published in *npj Climate and Atmospheric Science* in 2018.

Reference

Jones, C., and L. M. V. Carvalho, 2018: The influence of the Atlantic Multidecadal Oscillation on the eastern Andes low-level jet and precipitation in South America. *npj Climate and Atmospheric Science,* **1**, doi:10.1038/s41612-018-0050-8

_____

Correspondence to: Charles Jones, Department of Geography, University of California, Santa Barbara, California;
E-mail: cjones@eri.ucsb.edu

Enhanced Ocean Monitoring Products Using Ensemble Ocean Reanalyses: ENSO Precursors and NMME False Alarms

Y. Xue[1], C. Wen[1,2], A. Kumar[1], and E. Becker[1,2]

[1]Climate Prediction Center, NOAA/NWS/NCEP, College Park, MD

[2]Innovim, Greenbelt, Maryland

ABSTRACT

For those ocean reanalyses (ORA) produced by operational centers for initialization of climate models, *e.g.* the North American Multi-Model Ensemble (NMME), there is an opportunity to conduct ORA intercomparison in real-time, and to use the ensemble approach to quantify the signal (ensemble mean) and noise (ensemble spread) in our estimation of climate variability such as ENSO. In support of the Tropical Pacific Observing System (TPOS) 2020 Project (http://tpos2020.org), an ensemble of *nine* operational ORAs has been routinely collected at the Climate Prediction Center to monitor the consistency and discrepancy in the tropical Pacific temperature analysis in real time in support of ENSO monitoring and prediction.

Two ENSO precursors, referred to as Warm Water Volume (WWV) and Central Tropical Pacific (CTP) index respectively, have been derived with the ensemble ORAs. The two precursors have comparable skill in forecasting El Niño with a hit rate of 0.6-0.7, while the CTP is more skillful than the WWV in forecasting La Niña, with a hit rate of 0.85 from June initial conditions.

The two ENSO precursors provide independent information that is complementary to the NMME ensemble forecast. For example, for the La Niña years in 2000, 2008, and 2017, the NMME forecast warm conditions, while the CTP successfully forecasts La Niña conditions. For the neutral years in 2001 and 2012, the NMME models forecast false-alarm El Niño, while the CTP forecasts neutral-to-cold conditions. Therefore, the two ENSO precursors can not only be used to forecast the chances for El Niño/Neutral/La Niña conditions, but also to assess false alarms in the NMME forecast.

1. Introduction

Ocean reanalyses (ORAs) aim to provide an optimal estimation of the time-varying, 3-dimensional structures of the ocean by combining model dynamics with ocean observations via data assimilation methods. The accuracy of ORAs, however, varies spatially and temporally, depending on the biases of ocean models, the uncertainties of atmospheric fluxes, the amount of ocean observations, and the assumptions used in data assimilation methods. For the purpose of analyzing the tropical Pacific ENSO variability, the accuracy of ORAs depends critically on the Tropical Pacific Observing System (TPOS), which was initially populated by the Tropical Atmospheric Ocean (TAO) array in the early 1980s (McPhaden *et al.* 1998), and was later enhanced by the Triangle Trans-Ocean Buoy Network (TRITON) array in the western tropical Pacific (west of 160°E) after 2000 (Ando *et al.* 2005). There was a massive data loss of the TAO array in 2012-2013 due to resource constraints. Concurrently, there was an ongoing decline of the TRITON array. This degradation of the TAO/TRITON array raised serious concerns as to whether the quality of the operational ORAs has been (or will be) compromised due to the loss of observations. One of the recommendations from the TPOS 2020 workshop held at Scripps in 2014 (http://www.ioc-goos.org/tpos2020) was to monitor the consistency and discrepancy across the operational ORAs in real time in order to assess the impact of changes in the TAO/TRITON array on our ability to monitor and forecast ENSO (Fujii *et al.* 2015).

_____

Correspondence to: Yan Xue, Climate Prediction Center, NOAA/NWS/NCEP, 5830 University Research Court, College Park, MD 20740; E-mail: yan.xue@noaa.gov

Following the recommendation of the TPOS2020 workshop, the Climate Prediction Center (CPC) at the National Centers for Environmental Prediction (NCEP) initiated and led the Real-Time Ocean Reanalysis Intercomparison Project (Real-Time ORA-IP, Xue *et al.* 2017), which follows the framework of the ORA-IP that was organized by the CLIVAR Global Synthesis and Observations Panel (GSOP) a few years earlier (Balmaseda *et al.* 2015). With the goal of analyzing upper ocean heat content variability in support of seasonal forecast, the Real-Time ORA-IP focuses on the monthly temperature analysis in the upper 300m of the global ocean. A similar effort has been undertaken at the Australian Bureau of Meteorology, focusing on the monthly salinity analyses (http://poama.bom.gov.au/project/salinity/). CPC has collected an ensemble of seven ORAs that cover the period from 1979 to present, and a second ensemble of nine ORAs from 1993 to present. For the first ensemble, anomalies were calculated with the 1981-2010 climatology, and available plots show the anomalies of individual ORAs, the ensemble mean (signal), the ensemble spread (noise), and the signal-to-noise ratio for each month from January 1979 to present (http://www.cpc.ncep. noaa.gov/products/GODAS/multiora_body.html). For the second ensemble, anomalies were calculated with the 1993-2013 climatology, and the plots show the anomalies for each month from January 1993 to present (http://www. cpc.ncep.noaa.gov/products/GODAS/multiora93_body.html).

All of the nine ORAs included in the Real-Time ORA-IP have been used as ocean initial conditions for seasonal forecast models in operational centers around the world. Thus, monitoring the consistency and discrepancy among the operational ORAs provides an assessment of the uncertainties in ocean initial conditions for seasonal forecast models, which are particularly important for ENSO forecasting. The spread among the ensemble ORAs is also a good indicator of the adequacy of ocean observing systems in constraining the operational ORAs in real-time. Most importantly, the individual ORAs included in the Real-Time ORA-IP have been upgraded with time, in synchronization with those that have been continuously upgraded in each operational center around the world. For example, we have upgraded the Japan Meteorological Agency (JMA) product in 2017 and the European Centre for Medium-Range Weather Forecasts (ECMWF) product in early 2019.

The ensemble mean has been shown to be more accurate than individual ORA, suggesting the ensemble approach is an effective tool in reducing uncertainties in the temperature analysis for ENSO (Xue *et al.* 2017). In this paper, the ensemble ORAs have been used to obtain a best estimation of the upper ocean heat content variability critical for ENSO forecasting. In Section 2, we describe two ENSO precursors that are based on heat content analyses from six ORAs, and demonstrate that they are skillful in forecasting El Niño/Neutral/La Niña conditions. Furthermore, one of the ENSO precursors has excellent skill in forecasting La Niña conditions that is not well known by the ENSO forecasting community. In Section 3, we compare the forecast skill of the two ENSO precursors with that of the ensemble forecast of the NMME models. We find that the two ENSO precursors provide independent information complementary to the ensemble NMME forecast, and specifically that they can be used to assess false alarms in the NMME forecast. Section 4 includes summary and discussions.

2. Results

2.1 ENSO precursors based on ensemble ORAs

One important indicator of ENSO is the variability of the depth of the thermocline, often measured by the depth of the 20°C isotherm (D20). According to the "recharge oscillator" paradigm, the recharge (discharge) of the equatorial ocean heat content, measured by D20 anomalies, provides the necessary conditions for the onset of El Niño (La Niña) (Jin 1997). A measure of the equatorial ocean heat content is the volume of water warmer than 20°C, referred to as WWV. Meinen and McPhaden (2000) suggest that WWV is a good ENSO precursor as it leads the NINO3.4 SST index by 6–9 months.

The WWV is calculated as the average of the D20 anomaly in the equatorial Pacific in [120°E-80°W, 5°S-5°N]. The WWV indices calculated from six ORAs, the ensemble mean, and the ensemble spread of WWV indices in 1979-2019 are shown in Fig. 1. The ensemble spread of WWV indices is about 4m in early 1980s, and decreases to less than 2m in the early 1990s, after the TAO array was fully implemented. The ensemble mean provides the best estimation of ENSO variability, and is generally much larger than the ensemble spread. It is noted that the variability of WWV has much larger amplitude and a longer period before 2000 compared

to after 2000. The relationship between WWV and NINO3.4, the average SST anomaly in [5°N-5°S, 120°-170°W], also experienced a significant shift after 2000 (McPhaden 2012; Hu *et al.* 2013). The lower correlation and shorter lead-time between WWV and NINO3.4 after 2000 raises the question if the characteristics of the ocean heat content precursor for ENSO have changed after 2000.

The ocean heat content precursor signal for ENSO has been further analyzed by Wen *et al.* (2014). They found that WWV is a poor precursor for forecasting neutral and La Niña conditions after 2000 (Fig. 7 in Wen *et al.* 2014). This change of WWV as a good ENSO precursor was related to the decadal shift around 1999 that led to increased (decreased) ocean heat content in the western (eastern) Pacific after 2000 (England *et al.* 2014). This decadal shift led to a positive mean shift in WWV after 2000 (Fig. 1), which predisposes it to forecast El Niño conditions more frequently than La Niña conditions. Wen *et al.* (2014) found that the

Fig. 1 Time evolution of 5-month running mean of WWV (upper panel) and CTP (bottom panel) indices from six ORAs (color lines), the ensemble mean (shade) and ensemble spread of the indices (black line) starting from January 1979 to February 2019. The y-axis on the left is for the indices, while the y-axis on the right is the ensemble spread.

D20 anomaly averaged in the central tropical Pacific in [160°W-110°W, 10°S-10°N], referred to as the CTP index, is a better ENSO precursor than the WWV, and it has similar forecast skill for ENSO in the period before and after 2000, without the sudden reduction of skill around 2000 that is seen in the WWV index. The physical mechanism behind the CTP precursor is that it includes both equatorial and off-equatorial D20 anomalies, both of which contribute to the onset of ENSO. Since there are uncertainties in the off-equatorial D20 anomaly, it is not clear if the conclusion is sensitive to the choice of individual ocean reanalysis used in that study. In this paper, we calculate the CTP indices using six ORAs and the ensemble mean CTP index is used to further explore the forecast skill of the CTP index.

The uncertainties in the CTP indices are relatively high (10m) in the 1980s, and decrease to less than 2m in 1990s and 2000s, but increase again to greater than 2m after 2010 (Fig. 1). This highlights the needs to maintain stationarity in the quality of ORAs with time. Due to the ensemble approach, uncertainties in this index have been minimized. Compared to the WWV, the variability of the CTP index is largely stationary throughout the period and does not have an apparent decadal shift around 1999. In addition, the CTP is dominated by low frequency variability throughout the period, while the WWV is dominated by low frequency variability before 2000 and high frequency variability after 2000.

2.2 Forecast skill of ENSO precursors

The ensemble mean WWV and CTP indices are used to forecast El Niño and La Niña events. The criterion for selecting El Niño and La Niña events is set at a threshold of +/- 0.5°C for 3 month-running-mean of NINO3.4 when the threshold is met for a minimum of 5 consecutive overlapping seasons. With this criterion, in 1980-2018 (a total of 39 years), there are 13 El Niño years (82, 86, 87, 91, 94, 97, 02, 04, 06, 09, 14, 15, 18), 13 La Niña years (83, 84, 88, 95, 98, 99, 00, 07, 08, 10, 11, 16, 17) and 13 neutral years.

To forecast El Niño/Neutral/La Niña years with the ENSO precursors, a threshold of +/- 0.5 standard deviations (STD) of the WWV and CTP is used. In other words, when the index is above (below) +0.5 (-0.5) STD, an El Niño (a La Niña) year is forecast. Otherwise, a neutral year is forecast. The forecast is made from

each initial month from January to September. The forecast skill is measured by the hit rate and false alarm rate calculated for each initial month and for El Niño and La Niña events separately. If the number of observed events is O and the number of events forecast correctly is C, the hit rate is C/O. If the number of events forecast incorrectly is F and the number of events forecast correctly is C, the false alarm rate is F/(F+C). A forecast is considered more skillful if the hit rate is higher and the false alarm rate is lower.

The hit rate of WWV and CTP for forecasting El Niño events is comparable, which typically increases from 0.5 in February to 0.8 in September (not shown). For CTP, the false alarm rate decreases from 0.55 in February to 0.01 in September, suggesting CTP is a reliable indicator for El Niño when the forecast is made in late summer. However, for WWV, the false alarm rate decreases from 0.55 in February to 0.3 in September, indicating it is less reliable than the CTP. For forecasting La Niña events, CTP is generally superior to WWV. The hit rate of CTP

Fig. 2 Scatter plot between the WWV index in June and observed NINO3.4 in Nov-Dec-Jan (NDJ) in 1979-2018. The numbers indicate the El Nino (red), Neutral (black) and La Nina (blue) years. The correlation is 0.6, indicating there is a moderate skill in forecasting NINO3.4 in NDJ with the WWV index in June. The purple lines indicate +/- 0.5 standard deviation of WWV.

increases from 0.5 in March to 0.85 in June, indicating CTP is an excellent precursor for forecasting La Niña events when the forecast is made in June. In addition, the false alarm rate of CTP reduces to 0.08 in June.

To see how the WWV and CTP forecast all El Niño/Neutral/La Niña years since 1979, Fig. 2-3 show scatter plots between the WWV and CTP in June and observed NINO3.4 in Nov-Dec-Jan (NDJ). The correlation between the WWV (CTP) in June and observed NINO3.4 in NDJ is 0.6 (0.8) respectively. This indicates CTP in June is a better predictor for NINO3.4 in NDJ than WWV in June, when all years are considered. Considering the El Niño years only, the hit rate of WWV and CTP is 0.69 and 0.62 respectively, while the false alarm rate is 0.36 and 0.2. So the WWV and CTP have comparable skill in forecasting El Niño years. Considering the La Niña years only, CTP is more skillful than WWV. For example, the hit rate of CTP and WWV is 0.85 and 0.54 respectively, while the false alarm of CTP and WWV is 0.1 and 0.3. The CTP only missed two La Niña events in 1995 and 2017, and for 2017 the CTP in June almost met the threshold for forecasting a La Niña (Fig. 3). In addition, the CTP had only one false alarm in 2012, in which it called for La Niña instead of neutral conditions, as were observed. In contrast, WWV missed six La Niña events in 1999, 2000, 2007, 2008, 2011 and 2017 respectively. In fact, it called for El Niño conditions in 2000, 2011 and 2008, and neutral conditions in 1999, 2007 and 2017. The WWV had three false-alarm La Niña forecasts, in 1987, 1992 and 1993, while an El Niño year was observed in 1987 and neutral years in 1992 and 1993 (Fig. 2).

The fact that the forecast skill for La Niña events is higher than that for El Niño events as shown by the two ENSO precursors may be related to the asymmetry in ENSO. It is well known that about 50% of La Niña events last two years or longer, while El Niño events rarely last more than one year (Okumura and Deser 2010). Hu *et al.* (2014) suggest a strong 1st year La Niña is necessary for developing a 2nd year La Niña. Furthermore, DiNezio and Deser (2014) suggest that the nonlinearity in the *delayed thermocline feedback* is the sole process controlling the duration of La Niña events. Therefore, the precursory signal for La Niña events largely reside in the thermocline variations and the influences of atmospheric noises are relatively small in La Niña events compared to El Niño events.

The reason that CTP is more skillful than WWV in forecasting La Niña is because it includes D20 anomalies in the central tropical Pacific that includes both equatorial and off-equatorial regions. However, WWV includes D20 anomalies across the equatorial Pacific and therefore includes the positive D20 anomalies in the western
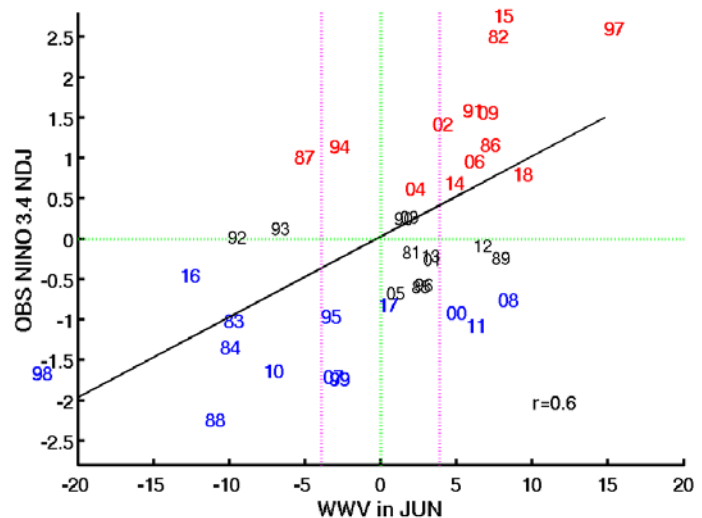
equatorial Pacific due to the decadal shift around 1999, which is not helpful for forecasting La Niñas. In fact, the WWV is positive in the 2nd year La Niña in 2008 and 2011, and in the 3rd year La Niña in 2000. In contrast, the CTP is negative in all those years, which favors a development of La Niña. So we hypothesize that D20 anomalies in the central tropical Pacific in off-equatorial regions (10°S-5°S, 5°N-10°N) play an important role in ENSO dynamics. A future study is needed to understand how temperature anomalies near the thermocline in off-equatorial regions are entrained into the equator, and upwelled to the mixed layer to influence ENSO development. Since the subtropical cell circulation is significantly enhanced after 2000 (Wen *et al.* 2014), off-equatorial D20 anomalies are expected to play a more important role in ENSO development after 2000 than before 2000.

Therefore, both WWV and CTP are useful for ENSO monitoring and prediction. CTP is a more reliable precursor than WWV in anticipating a La Niña. In addition, the two ENSO precursors

Fig. 3 Scatter plot between the CTP index in June and observed NINO3.4 in Nov-Dec-Jan (NDJ) in 1979-2018. The numbers indicate the El Nino (red), Neutral (black) and La Nina (blue) years. The correlation is 0.8, indicating there is a high skill in forecasting NINO3.4 in NDJ with the CTP index in June. The purple lines indicate +/- 0.5 standard deviation of CTP.

provide independent information that can be complementary to the ensemble forecast of NMME models, which will be discussed next.

2.3 The NMME ensemble forecast of ENSO

The North American Multi-Model Ensemble (NMME) is an experimental multi-model seasonal forecasting system consisting of coupled models from US modeling centers and Canadian Meteorological Center. The multi-model ensemble approach has proven to produce better prediction quality (on average) than any single model ensemble (Kirtman *et al.* 2014). It is currently delivering real-time seasonal predictions on the CPC operational schedule (https://www.cpc.ncep.noaa.gov/products/NMME).

The ensemble forecast is made of about 100 members from 7-8 models. The deterministic skill of ENSO predictions from NMME has been documented by Barnston *et al.* (2017). However, the forecast skill was not calculated for El Niño, Neutral and La Niña years separately. The recent paper by Timmermann *et al.* (2018) studied the forecast skill of El Niño and La Niña events in the NMME separately. They found that the forecast skill of El Niño is generally higher than that of La Niña, and correspondingly the spring predictability barrier is stronger in forecasting La Niña than in forecasting El Niño. They attribute this asymmetry in ENSO forecast skill to the asymmetry in the precursor signal of the western tropical Pacific heat content.

The results of Timmermann *et al.* (2018) appear at odds with our conclusion that the forecast skill of La Niña is higher than that of El Niño based on the two ocean heat content precursors. Since the NMME ensemble forecast contains about 100 members from 7-8 models, the systematic errors in each model and the influences of atmospheric noises in each member forecast should have been smoothed out and the ensemble mean forecast of NINO3.4 should have the best forecast skill.

To understand how well the ensemble mean forecast of NMME agrees with observation, Fig. 4 shows the scatter plot between the NMME forecast from July 1 initial conditions and observed NINO3.4 in NDJ for all years in 1982-2017. The correlation between the NMME forecast and observed NINO3.4 is 0.9, indicating a very high skill score. However, for the La Niña events, the NMME only captured 7 of 13 events (a hit rate of 0.53) while in contrast it captured 10 of 12 El Niño events (a hit rate of 0.83). This is consistent with the finding

of Timmermann *et al.* (2018) that the forecast skill of La Niña is lower than that of El Niño in the NMME forecast.

The NMME forecast had three false alarms of El Niño, in 2001, 2012 and 2017. In addition, the NMME forecast missed the La Niña events in 2000, 2008 and 2011, which were all very well forecast by the CTP (Fig. 3).The common feature among the false alarms and missed La Niña events in the NMME forecast is that they are either the 2nd year La Niña (2008, 2011, 2017), the 3rd year La Niña (2000), or the neutral year following the 3rd and 2nd La Niña years (2001, 2012). In all those cases, the CTP in June is negative or neutral, suggesting a high likelihood of La Niña or neutral. However, the NMME models had a tendency to forecast warm conditions in these cases, since subsurface temperature anomalies were positive in the western tropical Pacific and positive along the narrow belt of the equatorial Pacific. As an example, we will show how the warm biases in the NMME forecasts in 2011 and 2012 are related to subsurface temperature anomalies in initial conditions next.

Fig. 4 Scatter plot of NINO3.4 in Nov-Dec-Jan (NDJ) between the NMME forecast and observation for all the years in 1982-2017. The NMME forecast in NDJ is the ensemble mean forecast of about 100 members initialized from July 1 initial condition. The numbers indicate the El Nino (red), Neutral (black) and La Nina (blue) years. The correlation is 0.9, indicating there is a high consistency between the NMME forecast and observed NINO3.4 in NDJ.

The ensemble mean forecast from the NMME had a warm bias starting from spring/summer 2011 and 2012 (Fig. 5). In spring 2011, the positive D20 anomaly in the western tropical Pacific that was generated from the mature phase of the 2009/10 El Niño quickly discharged to the eastern Pacific, probably due to downwelling Kelvin waves. Due to the subsurface warming in initial conditions, the ensemble NMME forecast had a fast warming tendency in NINO3.4. When negative D20 anomalies emerged in the central equatorial Pacific in August, the NMME forecast reversed, indicating cold conditions in the winter.

The situation in spring 2012 was similar to that in spring 2011, except the SST in the far eastern Pacific had warmed to +1°C above-normal in spring, and NINO3.4 crossed +0.5°C threshold in summer 2012. The ensemble NMME forecast NINO3.4 to exceed +1°C in winter 2012/13, which was not realized in observations.

In both 2011 and 2012 cases, negative D20 anomalies averaged in 10°S-10°N had persisted in the central tropical Pacific in 160°W-110°W. This explains why the CTP is capable of avoiding El Niño forecast. Therefore, the CTP index provides independent information that can be used to assess false alarms in the NMME forecast.

3. Summary and discussions

In support of the Tropical Pacific Observing System (TPOS) 2020 Project (http://tpos2020.org), an ensemble of nine operational ocean reanalyses (ORAs) has been routinely collected at CPC to monitor the consistency and discrepancy in the tropical Pacific temperature analysis in real time in support of ENSO monitoring and prediction. All of the nine ORAs included in the real-time intercomparison have been used as ocean initial conditions for seasonal forecast models, *e.g.* the North American Multi-Model Ensemble (NMME). So monitoring the consistency and discrepancy among the operational ORAs provides an assessment of the uncertainties in ocean initial conditions for seasonal forecast models. The spread among the ensemble ORAs is also a good indicator of the adequacy of TPOS in constraining the operational ORAs for ENSO. Another advantage of the ensemble ORAs is that individual ORAs have been upgraded with time, in synchronization with those upgrades implemented by operational centers around the world.

CPC has collected an ensemble of seven ORAs that cover the period from 1979 to present, and a second ensemble of nine ORAs from 1993 to present. For the first ensemble, anomalies were calculated with the 1981-2010 climatology, and plots show anomalies of individual ORAs, the ensemble mean (signal), the ensemble spread (noise), and the signal-to-noise ratio for each month from January 1979 to present; see http://www.cpc.ncep. noaa.gov/products/GODAS/multiora _body.html. For the second ensemble, anomalies were calculated with the 1993-2013 climatology and plots show anomalies for each month from January 1993 to present; see http://www. cpc.ncep.noaa.gov/products/GODAS/ multiora93_body. html.

The ensemble mean has been shown to have better accuracy than individual ORA. Thus, the ensemble mean provides the best estimation of ENSO variability since 1979 (Xue *et al.* 2017). Two ENSO precursors were calculated with six ORAs that cover the period from 1979-present. The first ENSO precursor is Warm Water Volume (WWV), defined as the average of the depth of the 20°C (D20) anomaly in the equatorial Pacific in [120°E-80°W, 5°S-5°N] (Meinen and McPhaden 2000). The second ENSO precursor is the Central Tropical Pacific (CTP) index, defined as the average of the D20 anomaly in [160°W-110°W, 10°S-10°N] (Wen *et al.* 2014). Due to the ensemble approach, the signal-to-noise ratio is quite high in both the indices.

The ensemble mean of WWV and CTP indices based on six ORAs are used to forecast El Niño and La Niña events from each initial month in 1979-2019. For forecasting El Niño events, the hit rate of WWV and CTP is comparable, which typically increases from 0.5 in February to 0.8 in September. For forecasting La Niña events, CTP is generally superior to WWV. The hit rate of CTP increases from 0.5 in March to 0.85 in June, indicating CTP is an excellent precursor for forecasting La Niña events when a forecast is made from June.
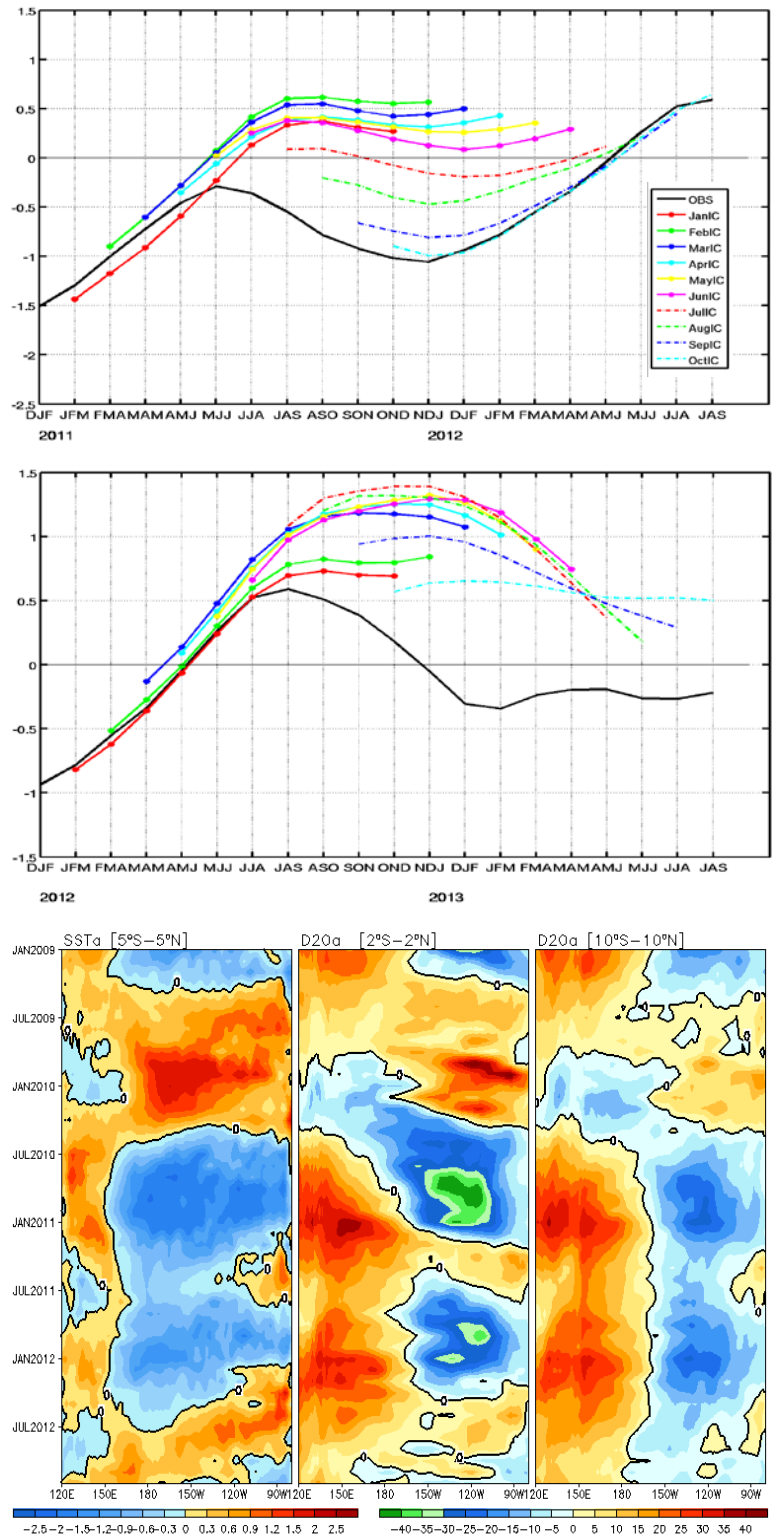
Fig. 5 The ensemble mean NMME forecast of NINO3.4 out to 9 months starting from January 1 to October 1 of 2011 (top panel) and 2012 (middle panel). SST anomaly average in 5°S-5°N (bottom left), D20 anomaly (m) average in 2°S-2°N (bottom middle) and in 10°S-10°N (bottom right) in 2009-2012 based on the ensemble mean of six ocean reanalyses.

In addition, the false alarm rate of CTP reduces to 0.08 in June.

From June initial conditions, CTP only missed two La Niña events in 1995 and 2017, and for 2017 the CTP in June almost met the threshold for forecasting a La Niña. In addition, CTP had only one false alarm in 2012, in which it called for La Niña instead of neutral as in observation. In contrast, WWV missed six La Niña events in 1999, 2000, 2007, 2008, 2011 and 2017 respectively. In fact, it called for El Niño conditions in 2000, 2011 and 2008, and neutral conditions in 1999, 2007 and 2017. WWV also had three false alarms of La Niña forecast in 1987, 1992 and 1993.

We compared the forecast skill of the two ENSO precursors from June with that of the NMME ensemble forecast from July 1 initial conditions. The correlation between the NMME forecast and observed NINO3.4 in Nov-Dec-Jan is 0.9, indicating a very high skill score. However, for the La Niña events, the NMME only captured 7 of 13 events (hit rate=0.53), while in contrast it captured 10 of 12 El Niño events (hit rate=0.83). This is consistent with the finding of Timmermann et al. (2018) that the forecast skill of La Niña is lower than that of El Niño in the NMME forecast.

From July 1 initial conditions, the NMME forecast had three false alarm predictions of El Niño in 2001, 2012 and 2017. In addition, the NMME forecast missed the La Niña events in 2000, 2008 and 2011, which were all very well forecast by the CTP. The common feature among the false alarms and missed La Niña events is that they are either the 2nd year La Niña (2008, 2011, 2017) or the 3rd year La Niña (2000) or the neutral year coming out of the 3rd and 2nd La Niña year (2001, 2012). In all those cases, the CTP in June is negative or neutral, suggesting a high likelihood of La Niña or neutral conditions.

The NMME models tended to forecast warm conditions, since subsurface temperature anomalies were positive in the western tropical Pacific and positive along the equatorial Pacific in those cases. However, for those cases, negative D20 anomalies averaged in 10°S-10°N had persisted in the central tropical Pacific in 160°W-110°W. Therefore, the CTP index provides independent information that can be used to assess false-alarm predictions of El Niño or warm biases in the NMME forecast.

The above study identified the warm biases in the ensemble NMME forecast in forecasting the 2nd and 3rd year La Niña events, as well as the neutral year following the 2nd and 3rd La Niña year. The warm biases are systematic biases in all the models, and are related to positive subsurface temperature anomalies near the equator in initial conditions. It is urgent to investigate why all the models had responded too strongly to positive subsurface temperature anomalies (overestimated the thermocline feedback) during those cases. Efforts should be devoted to understanding the nonlinearity in the delayed thermocline feedback during the long lasting La Niña cycle as suggested by DiNezio and Deser (2014). In observation, thermocline variations in off-equatorial regions in the central tropical Pacific appear play a critical role in the long lasting La Niña cycle. Therefore, a further study on the roles of off-equatorial D20 anomaly on the 2nd or 3rd year La Niña development is needed.

References

Ando, K., T. Matsumoto, T. Nagahama, I. Ueki, Y. Takatsuki, and Y. Kuroda, 2005: Drift characteristics of a moored conductive-temperaturedepth sensor and correction salinity data. *J. Atmos. Ocean. Technol.*, **22**, 282–291.

Balmaseda, M. A., and Co-authors, 2015: The Ocean Reanalyses Intercomparison Project (ORA-IP). *J Oper Oceanogr*, **8**, 80–97.

Barnston, A. G., M. K Tippett, M. Ranganathan, and M. L. L'Heureux, 2017: Deterministic skill of ENSO predictions from the North American Multimodel Ensemble. *Clim. Dyn.,* https://doi.org/10.1007/s00382-017-3603-3.

England, M. H., and Co-authors, 2014: Recent intensification of wind-driven circulation in the Pacific and the ongoing warming hiatus. *Nat. Clim. Chang*. 4, 222–227.

Fujii, Y., J. Cummings, Y. Xue, A. Schiller, T. Lee, M. A. Balmaseda, E. Remy, S. Masuda, G. Brassington, O. Alves, B. Cornuelle, M. Martin, P. Oke, G. Smith, and X. Yang, 2015: Evaluation of the tropical pacific

observing system from the ocean data assimilation perspective. *Q. J. R. Meteorol. Soc.*, **141**, 2481–2496. doi: 10.1002/qj.2579.

DiNezio, P. N., and C. Deser, 2014: Nonlinear controls on the persistence of La Niña. *J. Climate,* **27**, 7335–7355.

Hu, Z.-Z., A. Kumar, H.-L. Ren, H. Wang, M. L'Heureux, and F.-F. Jin, 2013: Weakened interannual variability in the tropical Pacific Ocean since 2000. *J. Climate*, **26**, 2601-2613.

Hu, Z.-Z., A. Kumar, Y. Xue, and B. Jha, 2014: Why were some La Niñas followed by another La Niña? *Clim. Dyn.,* **42**, 1029–1042.

Jin, F. F., 1997: An equatorial ocean recharge paradigm for ENSO. Part I: conceptual model. *J. Atmos. Sci.,* 54, 811–829.

Kirtman, B. P., and Co-authors, 2014: The North American Multi-Model Ensemble (NMME): Phase-1 seasonal to interannual prediction, Phase-2 toward developing intra-seasonal prediction. *Bull. Amer. Meteorol. Soc.*, **95**, 585–601.

McPhaden, M. J., and Co-authors, 1998: The tropical ocean–global atmosphere (TOGA) observing system: a decade of progress. *J. Geophys. Res.*, **103**,169–14,240.

McPhaden, M. J., 2012: A 21st century shift in the relationship between ENSO SST and warm water volume anomalies. *Geophys. Res. Lett.*, **39**, L09706, doi: 10.1029/2012GL051826.

Meinen, C. S., and M. J. McPhaden, 2000: Observations of warm water volume changes in the equatorial Pacific and their relationship to El Niño and La Niña. *J. Climate*, **13**, 3551–3559.

Okumura, Y. M., and C. Deser, 2010: Asymmetry in the duration of El Niño and La Niña. *J. Climate*, **23**, 5826–5843.

Timmermann, A., and Co-authors, 2018: El Niño–Southern Oscillation complexity. *Nature*, **559**, 535–545.

Wen, C., A. Kumar, Y. Xue, and M. McPhaden, 2014: Changes in tropical Pacific thermocline depth and their relationship to ENSO after 1999. *J. Climate,* **27**, 7230-7249.

Xue, Y., and Co-authors, 2017: A real-time ocean reanalyses intercomparison project in the context of tropical pacific observing system and ENSO monitoring. *Clim. Dyn.,* **49**, 3647–3672.

Untangling Seasonal Predictions over California During 2015/16 El Niño and the Parable of Blind Men and an Elephant: What Next?

Arun Kumar and Mingyue Chen

Climate Prediction Center, NOAA/NWS/NCEP

ABSTRACT

In the backdrop of an extended drought and growing concerns for water management related issues over Southern California (SCA), anticipation of a large amplitude El Niño during the winter of 2015/16 generated expectations for above normal rainfall, thus building hopes for a much needed drought relief. Expectations for above normal SCA rainfall were generated by the average rainfall response to El Niño sea surface temperature (SST) anomalies inferred based on the analysis of the observational data, supported further by model simulations. Indeed, seasonal forecasts based on North American Multi-Model Ensemble (NMME), and official predictions for December-January-February (DJF) 2015/16 indicated increased odds for the above normal seasonal mean rainfall anomaly. The observed DJF 2015/16 SCA rainfall anomalies, however, were below normal. The discrepancy between the expectations for above normal predicted rainfall versus below normal observed rainfall anomalies led to questions about the accuracy of seasonal predictions, and since then, has also led to a series of studies analyzing the atmospheric response during the winter of 2015/16. Despite vigorous attempts, a consensus on the question of the forecast performance during one of the biggest El Niño in the historical record has not emerged. This note proposes pathways to resolve some fundamental questions in the context of understanding atmospheric response to ENSO SSTs that are critical for the practice of seasonal predictions.

1. Background

In the backdrop of an extended drought and growing concerns for water management related issues over Southern California (SCA), anticipation of a large amplitude El Niño during the winter of 2015/16 generated expectations for above normal rainfall, thus building hopes for a much needed drought relief. The expectations for above normal SCA rainfall were supported by the rainfall composites during El Niño (inferred based on historical data), and also from dynamical model predictions using multi-model ensembles. Indeed, relying on such information, official seasonal forecast from Climate Prediction Center (CPC) indicated increased odds for above normal rainfall for December-January-February (DJF) 2015/16 seasonal mean. The observed seasonal mean rainfall anomalies over the SCA, however, were below normal (Fig. 1). An apparent discrepancy between various seasonal forecasts (for increased odds for above normal SCA rainfall) and observations led to the perception of a failed forecast during one of the strongest El Niño's in the historical record. This led to a series of studies that attempted to explain why the observed seasonal mean rainfall anomalies may have differed from the historical expectations as well as from model based predictions. Possibilities addressed included:

- Whether the uniqueness in the spatial structure of 2015/16 El Niño SST conditions altered the atmospheric response? In other words, while seasonal forecasts keyed more on the mean El Niño response, they failed to take into account the changes in atmospheric response to the "flavors of El Niño."

- Did a general warming of tropical SSTs (that has occurred in recent decades) have led to changes in atmospheric response to El Niño?

- Was drying over SCA due to extreme drought conditions modulated the canonical atmospheric response to El Niño?

_____

Correspondence to: Arun Kumar, Climate Prediction Center, NOAA/NWS/NCEP, 5830 University Research Court, College Park, MD 20740; E-mail: arun.kumar@noaa.gov
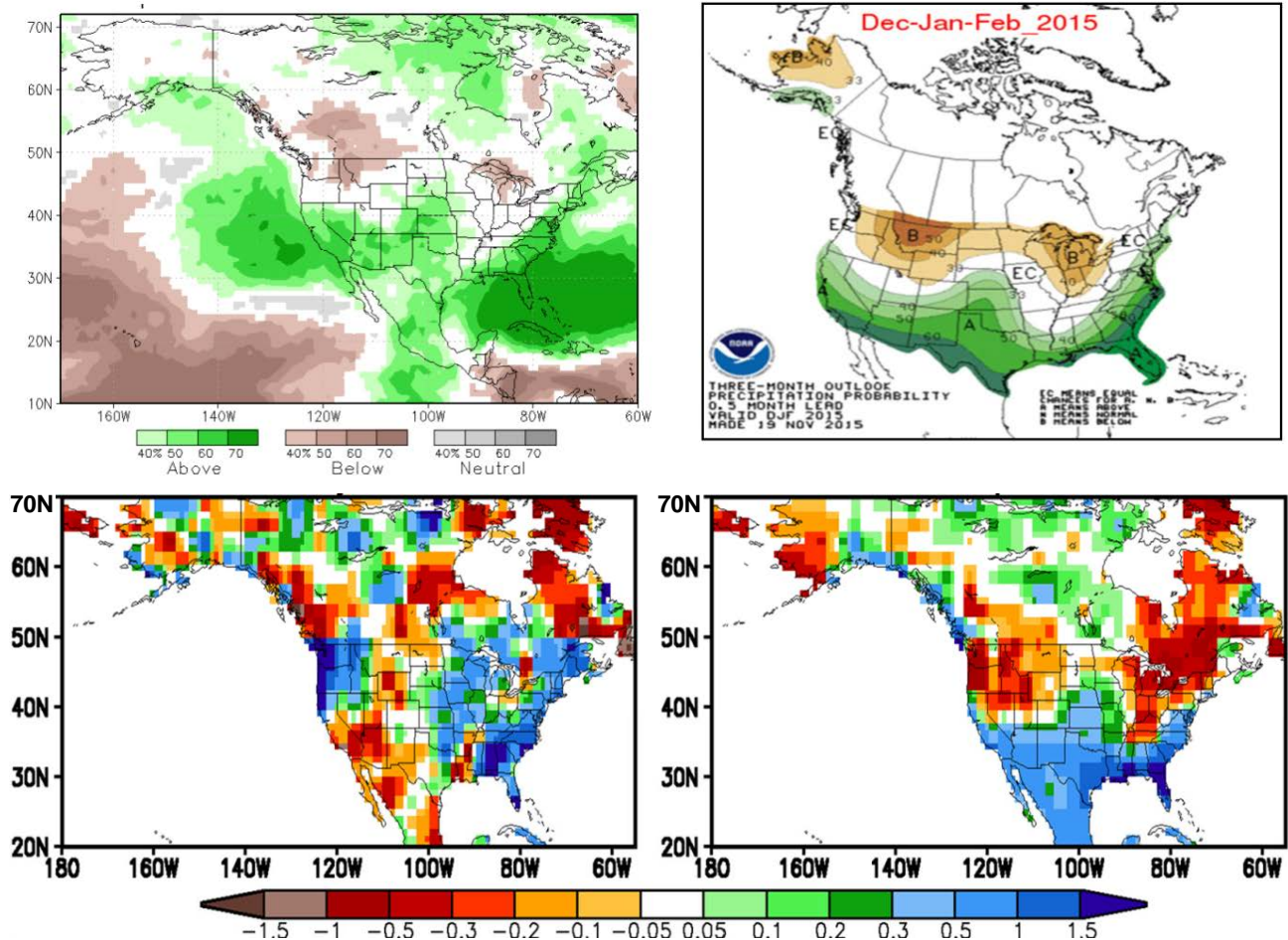
Fig. 1 (top left) NMME prediction of DJF 2015/16 rainfall anomaly; (top right) CPC's DJF 2015/16 forecast for rainfall. Forecast is in terms of probability for rainfall to be in the above normal (green) or below normal (yellow) category; (bottom left) observed DJF 2015/16 rainfall anomaly; and (bottom right) observed DJF composite rainfall anomaly during El Niño.

- Did recent decline in sea-ice may have played a role?

- Were the boundary conditions in the seasonal prediction systems themselves predicted well enough?

- How model biases may have influenced our inferences about the atmospheric response to El Niño?

- What was the role of atmospheric noise (or internal variability) in influencing observed seasonal mean rainfall anomalies? Under the influence of atmospheric internal variability, was discrepancy between the forecast and the observed outcome a consequence of incorrect forecast (*i.e.*, the response to El Niño) or just a consequence of internal variability having a large contribution to a single observed outcome?

Such questions present a baffling array of choices and the papers that have appeared in peer reviewed literature did not lead to a consensus viewpoint as to why forecast and observed anomalies may have differed, and if anything, likely added to further confusion. Given an already long history of research efforts spanning almost 40 years (using observational and model simulations) in quantifying atmospheric response to ENSO SSTs (Madden 1976; Horel and Wallace 1981; Kumar *et al.* 2007; Jha *et al.* 2017), and that we are still continually surprised by discrepancies between seasonal forecasts and observed outcomes, particularly during years with large amplitude anomalous boundary forcings, begs the question as what needs to be done to reach a consensus on some of the fundamental science questions that are of importance for the practice of seasonal predictions.

2. Thoughts on next steps

Some of the key science questions in the context of the practice of seasonal prediction are:

- What are the limits of ENSO related predictability for seasonal mean atmospheric variability?

- How linear is the atmospheric response to ENSO, for example, to the amplitude of the ENSO associated SST anomalies?

- How much flavors of ENSO should matter in constructing seasonal forecasts from one-year-to-another?

- How does the spread of the seasonal mean change under the influence of ENSO SSTs?

- To what extent model biases influence the realization of ENSO related predictability in the observed system?

- If the role of internal atmospheric variability in shaping observed seasonal means (particularly in extratropical latitudes) is large, and consequently the signal-to-noise (SNR) is small, how best the user expectations can be managed?

As mentioned earlier, despite a long history of research in understanding atmospheric response to ENSO, clear answers have not yet emerged or have been internalized by the seasonal forecasting community. Towards answering these questions, it is understood that the historical observational record is not long enough to provide enough samples of ENSO events for us to address above questions with any confidence. The answers, therefore, have to rely on model simulations where a large realization of atmospheric state under unique boundary focings can be generated. The model based approach, however, gets criticized because of model biases (on various spatial and temporal scales) could easily influence the inferences about atmospheric responses to ENSO. To place confidence in model based results, there is a critical need to establish metrics to assess if models are good enough to address the questions we are posing

Besides developing some metrics to assess "goodness" of the model to address a specific question (Kumar *et al.* 1996), the second pathway to establish "what factors in boundary conditions really matter in determining atmospheric response to ENSO" has to rely on community based multi-model approach. An example of such an approach was the effort under the US CLIVAR Drought Working Group (DWG) that attempted to establish which SST forcings may be important for modulating drought conditions over the US (Schubert *et al.* 2009). Building on that effort, the approach we propose would call for a (CMIP like) periodic and coordinated multi-model assessment under a varying degree of ENSO responses. It is possible that such an effort may still not lead to clear answers, however, an appropriate guidance to the practitioners of the seasonal forecasters can still be provided and could as well state that "at present no clear inference about the role of a particular aspect of ENSO SST forcing in modulating atmospheric response can be given."

In our attempts to establish what really matters in determining the atmospheric response to ENSO, it is also conceivable that not every detail in boundary condition matter, for such a scenario will make the practice of seasonal predictions an impossible endeavor. Further, scale analysis (or Taylor's expansion) is one of the basic tenets of making scientific advances, and is also likely to be true in quantifying ENSO response beyond what is inferred based on simple regression or composite based approaches (which quantify the first order influence of "average or canonical" ENSO SSTs on the atmospheric variability). The fact that establishing consensus beyond the first order response has proven to be such a difficult task may point to the fact that higher order influences of variations in ENSO on the atmospheric response are small (as they should be if the implicit meaning of *higher order response* does carries forward); however, such indications remain to be confirmed based on a periodic assessment of atmospheric responses to ENSO using multi-model approach.

References

Horel, J. D., and J. M. Wallace, 1981: Planetary-scale atmospheric phenomenon associated with the Southern Oscillation. *Mon. Wea. Rev.*, **109**, 2080-2092.

Jha, B., A. Kumar, Z.-Z., Hu, 2017: An update on the estimate of predictability of seasonal mean atmospheric variability using North American Multi-Model Ensemble. *Clim. Dyn.*, doi:10.1007/s00382-016-3217-1.

Kumar, A., M. P. Hoerling, M. Ji, A. Leetmaa and P. Sardeshmukh, 1996: Assessing a GCM's suitability for making seasonal predictions. *J. Climate*, **9**, 115-129.

—, B. Jha, Q. Zhang, L. Bounoua, 2007: A new methodology for estimating the unpredictable component of seasonal atmospheric variability. *J. Climate*, **20**, 3888-3901.

Madden, R. A., 1976: Estimates of the natural variability of time-averaged sea-level pressure. *Mon. Wea. Rev.*, **104**, 942–952.

Schubert, S., and Co-authors, 2009: A US CLIVAR project to assess and compare the responses of global climate models to drought-related SST forcing patterns: Overview and results. *J. Climate*, **22**, 5251-5272.

Water Vapor Budget in Atmospheric Rivers: A Multi-model Evaluation

Bin Guan[1,2], Duane E. Waliser[2], and F. Martin Ralph[3]

[1]*Joint Institute for Regional Earth System Science and Engineering,*
University of California, Los Angeles, California
[2]*Jet Propulsion Laboratory, California Institute of Technology, Pasadena, California*
[3]*Center for Western Weather and Water Extremes, Scripps Institution of Oceanography,*
University of California, San Diego, California

1. Introduction

Atmospheric rivers (ARs) are narrow, elongated, synoptic jets of water vapor that play important roles in the global water cycle and regional weather/hydrology. A recent study (Guan and Waliser 2017) revealed considerable challenges and inter-model differences in simulating the phenomenology of ARs (*e.g.*, geometry, frequency, intensity) with the state-of-the-art weather/climate models. The current work takes a step further to diagnose model errors at process levels, with a focus on quantifying the AR water vapor budget.

2. Data and methods

An AR detection algorithm (Guan and Waliser 2015; Guan *et al.* 2018) is applied to 20-year, 6-hourly simulations by 24 global weather/climate models from the GEWEX Atmosphere System Study - WCRP-WWRP/THORPEX Year of Tropical Convection (GASS-YoTC) Multi-model Experiment (Jiang *et al.*, 2015). Water vapor budget terms, including tendency of integrated water vapor (IWV), convergence of integrated water vapor transport (IVT), evaporation, and precipitation are calculated for four distinctive sectors (post-frontal, frontal, pre-frontal, and pre-AR) of ~6000 ARs in the northeastern Pacific during the winter months of 1991–2010, with the dominant terms identified in each sector. The simulated water vapor budget is evaluated against the ERA-Interim and MERRA-2 reanalyses, with the difference between the two reanalyses serving as a rough measure of observational uncertainty.

3. Key results

The results reveal the dominant water balance is different across the four AR sectors, with overall good agreement between ERA-Interim and MERRA-2. The largest observational uncertainty is associated with IVT convergence

Fig. 1 Water vapor budget terms in four AR sectors based on ~6000 ARs in the northeastern Pacific during the winter months of 1991–2010 identified in ERA-Interim and MERRA-2 reanalyses (cyan and magenta circles) and 24 global weather/climate models from the GASS-YoTC Multi-model Experiment (box-whiskers).

due to mass convergence in the frontal sector (difference between cyan and magenta circles in Fig. 1). Model spread is notable compared to observational uncertainty. The largest model spread occurs in post-frontal and frontal sectors in their respective dominant budget terms (box-whiskers in Fig. 1). Model performance in terms

of the correlation between each pair of the water vapor budget terms is also examined (not shown). The work contributes to the ongoing development of a suite of AR simulation diagnostics and model performance metrics and associated software packages, and can help guide dedicated observational efforts for better constraining AR processes in weather and climate models.

References

Guan, B., and D. E. Waliser, 2015: Detection of atmospheric rivers: Evaluation and application of an algorithm for global studies. *J. Geophys. Res. Atmos.*, **120**, 12514–12535, doi:10.1002/2015JD024257.

—, and —, 2017: Atmospheric rivers in 20 year weather and climate simulations: A multimodel, global evaluation. *J. Geophys. Res. Atmos.*, **122**, 5556–5581, doi:10.1002/2016JD026174.

—, —, and F. M. Ralph, 2018: An inter-comparison between reanalysis and dropsonde observations of the total water vapor transport in individual atmospheric rivers. *J. Hydrometeor.*, **19**, 321–337, doi:10.1175/JHM-D-17-0114.1.

Jiang, X., and Coauthors, 2015: Vertical structure and physical processes of the Madden-Julian oscillation: Exploring key model physics in climate simulations. *J. Geophys. Res. Atmos.*, **120**, 4718–4748, doi:10.1002/2014JD022375.

The Distinct Contributions of the Seasonal Footprinting and Charged-Discharged Mechanisms to ENSO Complexity

Jin-Yi Yu and Shih-Wei Fang

Department of Earth System Science, University of California, Irvine, California

ABSTRACT

Not all El Niño-Southern Oscillation (ENSO) events are the same. A significant component of ENSO complexity is manifested in the way one ENSO event transits to another. Some events are followed by events of the opposite phase (*i.e.*, El Niño to La Niña or La Niña to El Niño) to give rise to ENSO cycles, others are followed by neutral years to become episodic events, and still others are followed by events of the same phase to become multi-year El Niño or La Niña events. This study finds the seasonal footprinting (SF) mechanism to be a key source of ENSO complexity whereas the charged-discharged (CD) mechanism acts to reduce complexity. The CD mechanism forces El Niño and La Niña to follow each other resulting in a more cyclic and less complex ENSO evolution, while the SF mechanism involves subtropical forcing and results in an ENSO evolution that is more episodic and irregular (Fig. 1). The SF mechanism also contributes to El Niño-La Niña asymmetries by producing multi-year La Niña events but not multi-year El Niño events. It is found that the strength of CD mechanism has been steady over the past 60 years but SF mechanism has intensified during the past two decades making ENSO more complicated. For model simulations, most CMIP5 models overestimate the strength of the CD mechanism but underestimate the strength of the SF mechanism, causing their simulated ENSOs to be too regular and symmetric.
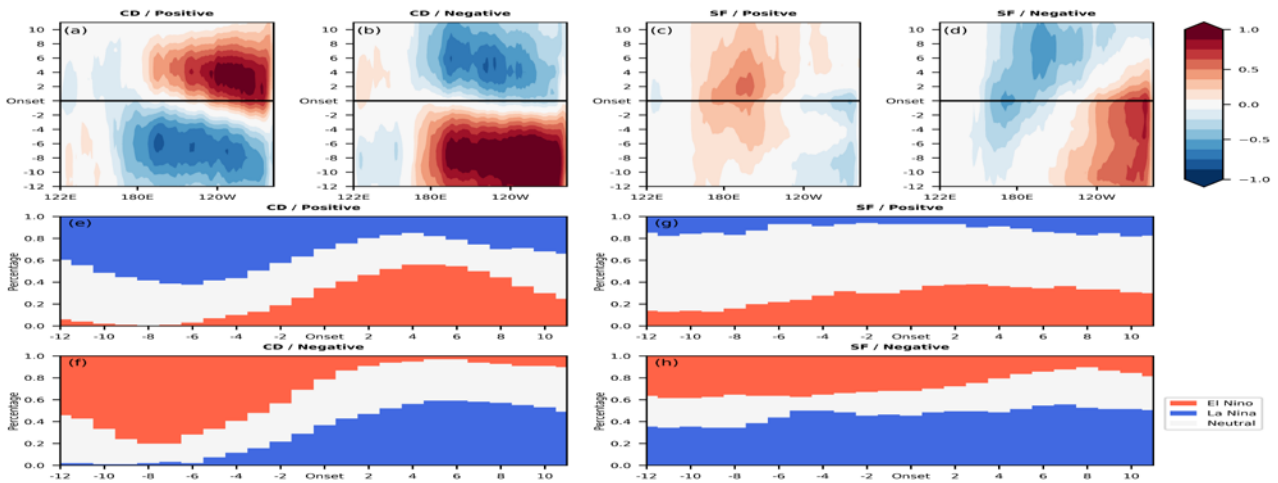
Fig. 1 (a)-(d) The evolution of equatorial Pacific (5°S-5°N) SST anomalies composited for (a) the positive CD mechanism, (b) the negative CD mechanism, (c) the positive SF mechanism, and (d) the negative SF mechanism. (e)-(h) The percentages of the composited months that are in an El Niño (red), La Niña (blue), or neutral (white) state during the period 12 months before to 12 months after the positive and negative phases of the CD mode (e and f) and the SF mode (g and h) reach their peak (at lag 0).

This work has been published in *Geophysical Research Letters* in 2018.

Reference

Yu, J.-Y., and S.-W. Fang, 2018: The distinct contributions of the seasonal footprinting and charged-discharged mechanisms to ENSO complexity. *Geophys. Res. Lett.*, **45**, 6611–6618. https://doi.org/10.1029/2018GL077664

_____

Correspondence to: Jin-Yi Yu, Department of Earth System Science, University of California, Irvine, California;
E-mail: jyyu@uci.edu

Responses of Global Atmospheric Circulation to Climate Indices Based on APCC Hindcast Data

Daeun Jeong and Yun-Young Lee

APEC Climate Center, Busan, South Korea

1. Introduction

From 14 centers in 10 countries, the Asia-Pacific Economic Cooperation (APEC) Climate Center (APCC) collects global climate prediction data every month and issues monthly-rolling Multi-Model Ensemble (MME) predictions for the upcoming six-month seasons, which are disseminated through the website (www.apcc21.org). In cooperation with KMA (Korea Meteorological Administration), the APCC also produces climate predictions of temperature and precipitation over South Korea every month. The climate indices e.g. Niño3.4 from reanalysis data have been taken into account for the predictions of the temperature and precipitation over South Korea even though the MME prediction data is also essential. The responses of atmospheric circulation to the climate indices and correlation between temperature and precipitation over South Korea and the indices are studied by using both reanalysis and hindcast data, which are finally provided as a guidance so that the APCC forecasters can produce more reliable predictions.

2. Data and methodology

APCC currently monitors 20 atmospheric and oceanic indices and predicts 9 indices out of them. The criteria for selecting indices for this study are as follows: 1) be predicted by APCC; 2) have high correlations with observed indices; and 3) have high correlations with temperature and rainfall over South Korea.

The data sets used in this study is described in Table 1. The station data of mean temperature and precipitation over South Korea are obtained from ASOS. With these data sets, four of global atmospheric variables of reanalysis and hindcast data are analyzed: geopotential height at 500 hPa, sea level pressure, temperature at 2m, and wind at 850 hPa.

The variables are regressed onto the selected climate indices for the months when the correlation between indices from reanalysis data and those from MME hindcast data is high. The regressed patterns of MME hindcast data are displayed as colored shadings, whereas those of individual model data spread are displayed as dots when standard deviations being less than average ones of regression coefficients of individual models.

Table 1 Descriptions of the data sets used in this study. The common data period of the above data is 1983-2005.

Data	Description	Variables
Automated Synoptic Observing system (ASOS; data.kma.go.kr)	61 stations over South Korea	- Mean temperature - Precipitation
CAMS OPI (Janowiak and Xie, 1999)		- Precipitation
NCEP-DOE Reanalysis (Kanamitsu et al., 2002)		- Geopotential height at 500 hPa - Sea level pressure - Temperature at 2m - Wind at 850 hPa
MME hindcast data of APCC	Simple Composite Method (SCM)	
Hindcast data of individual models	JMA NASA APCC NCEP CMCC PNU CWB POAMA MSC	

3. Results and conclusions

The Niño3.4 and AO (Arictic Oscillation) out of 20 indices are selected based on the correlations between indices from reanalysis and MME hindcast data (Fig. 1). The Niño3.4 shows high prediction skill all year round.

Correspondence to: Daeun Jeong, APEC Climate Center, Busan, South Korea; E-mail: downy@apcc21.org
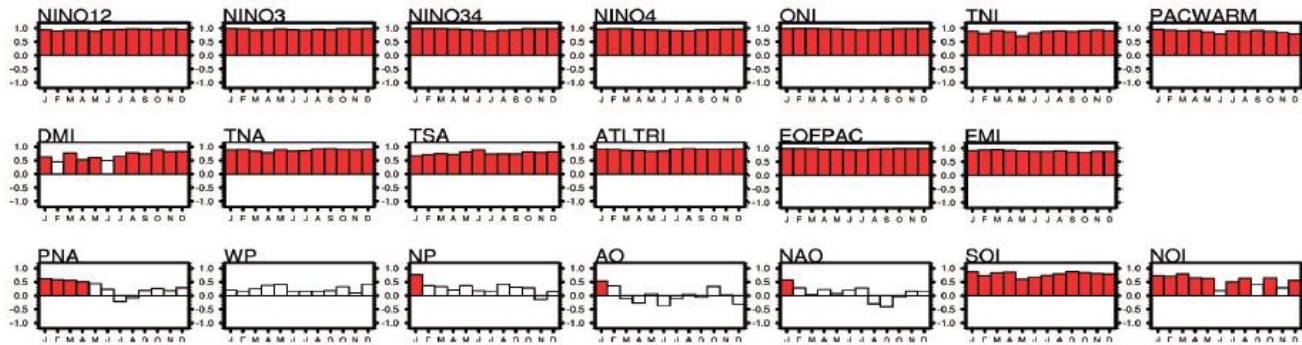
Fig. 1 Temporal correlations between observed and predicted indices. Red bars denote correlations which are significant at 95% level.
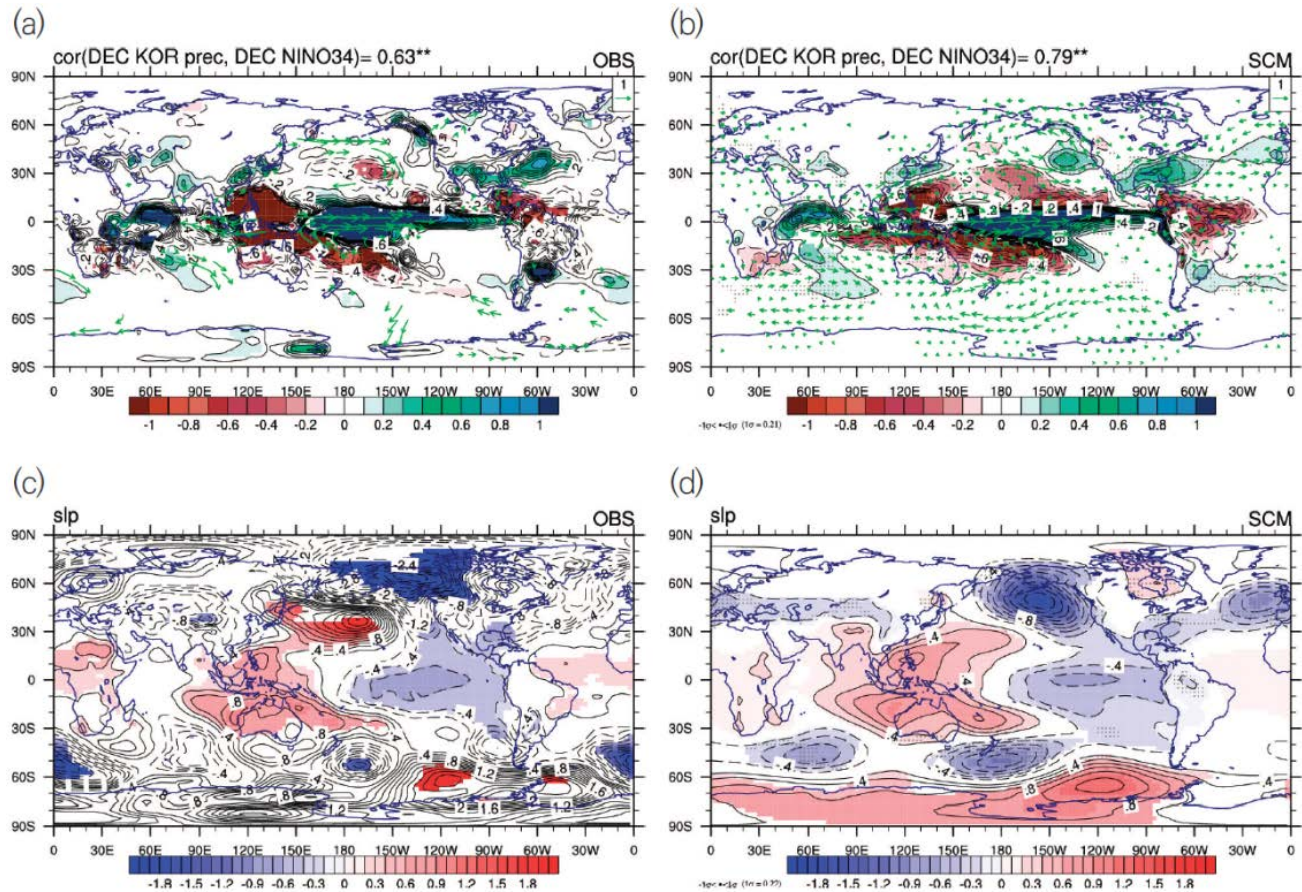
Fig. 2 Regressed precipitation (top) and sea level pressure (bottom) anomalies onto Niño 3.4 SST for December from reanalysis (left) and SCM hindcast (right) data.

The AO has significant prediction skill for January, which is taken into account for the prediction of winter temperature over South Korea.

The correlation coefficients between rainfall over South Korea and Niño3.4 for December are 0.63 in OBS and 0.79 in SCM, respectively (Fig. 2(a) and (b)). The wet condition and the southwesterly over South Korea are well simulated by SCM. The consistent responses of MME participating models on Niño3.4 are also shown. The anticyclonic circulation over the western Pacific and the cyclonic one over the eastern Pacific is predicted by SCM (Fig. 2(c) and (d)). Based on these results, not only the observed Niño3.4 but also the predicted one should be considered for the prediction of precipitation over South Korea for December.
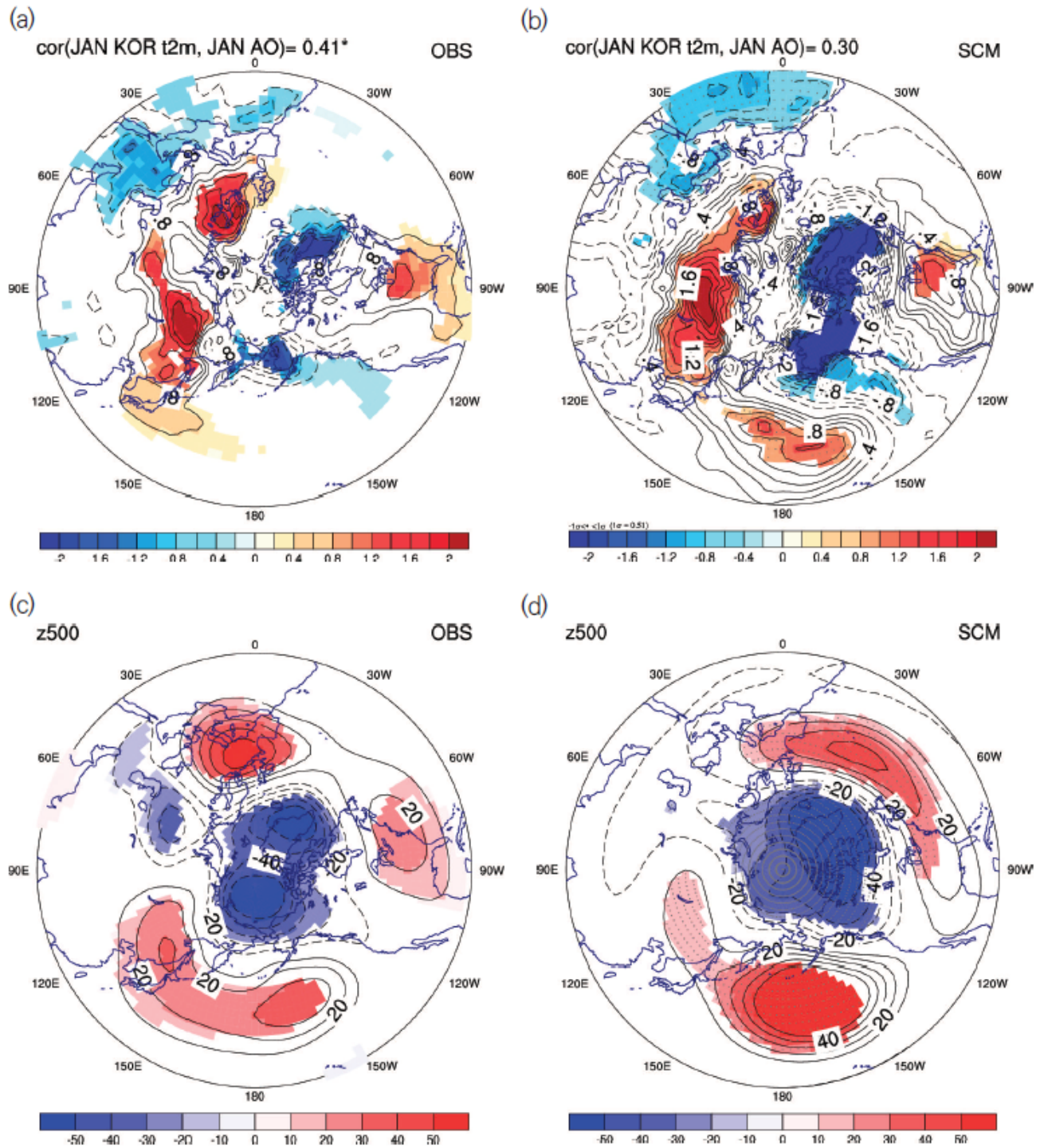
Fig. 3 Regressed temperature at 2m (top) and geopotential height at 500 hPa (bottom) anomalies onto AO index for January from reanalysis (left) and SCM hindcast (right) data.

On the other hand, no significant correlation between the temperature over South Korea and AO from SCM for January is shown. The regressed patterns of SCM are similar to that of OBS though (Fig. 3 (a) and (b)). The positive temperature anomalies over Northeast Asia, Siberia, and eastern USA and negative ones over Canada, Middle East, and North Africa from SCM are similar to the ones from OBS. The positive anomalies over South Korea in OBS don't cover it in SCM though. The AO-related pattern of geopotential height at 500 hPa - negative

anomalies over the Arctic and positive ones over the northern North Pacific and Atlantic is predicted by SCM and the consistency among the responses of the individual models is shown (Fig. 3 (c) and (d)).

This study covers the prediction skill of hindcast data. The predictability for the indices and related atmospheric circulation patterns with the real-time forecast data of APCC will be further studied.

References

Janowiak, J. E., and P. Xie, 1999: CAMS_OPI: a global satellite-raingauge merged product for real-time precipitation monitoring applications. *J. Climate*, **12**, 3335-3342.

Kanamitsu, M., W. Ebisuzaki, J. Woollen, S. K. Yang, J. Hnilo, M. Fiorino, and G. Potter, 2002: NCEP-DOE AMIP-II reanalysis (R-2). *Bull. Amer. Meteorol. Soc.*, **83**, 1631-1643.

Seamless Coupled Prediction System (SCoPS): Assessment of the APCC In-house Model Real-Time Seasonal Forecast

A-Young Lim, Young-Mi Min, and Suryun Ham

APEC Climate Center, Busan, South Korea

ABSTRACT

Asia-Pacific economic cooperation Climate Center (APCC) has made great efforts to develop and improve a seasonal forecast model to provide more reliable forecast information for the Asia-Pacific regions. Recently, as a result of the efforts, the APCC has launched a new dynamical seasonal forecast system, Seamless Coupled Prediction System (SCoPS). The newly developed SCoPS model is state-of-the-art global prediction system based on the fully-coupled atmosphere, land, ocean, and sea-ice model has been operationally implemented and participated in the APCC Multi Model Ensemble (MME) prediction since November 2017. This study focused on the skill assessment of SCoPS seasonal forecasts for sea surface temperature (SST), temperature, precipitation, and circulation fields on a monthly basis compared to that of Community Climate System Model version 3 (CCSM3) which is previous version of APCC in-house model in past years. Relative performances of SCoPS and participating models in the APCC MME prediction (*e.g.*, National Centers for Environmental Prediction (NCEP) Climate Forecast System, Predictive Ocean Atmosphere Model for Australia (POAMA), and Meteorological Service of Canada (MSC) Coupled Climate Model) are also discussed. Results indicate that SCoPS consistently better performance than CCSM3 in anomaly pattern correlation and temporal correlation skills for the spatial distribution of SST and Nino 3.4 index predictions (Fig.1). Similar results can also be found in temperature and precipitation that the real-time forecast skill of SCoPS generally outperforms that of CCSM3 for the whole period in both global and regional scales. Further, SCoPS is more skillful than CCSM3 in predicting the seasonal climate variability, including the ENSO, East Asian summer and winter monsoon.
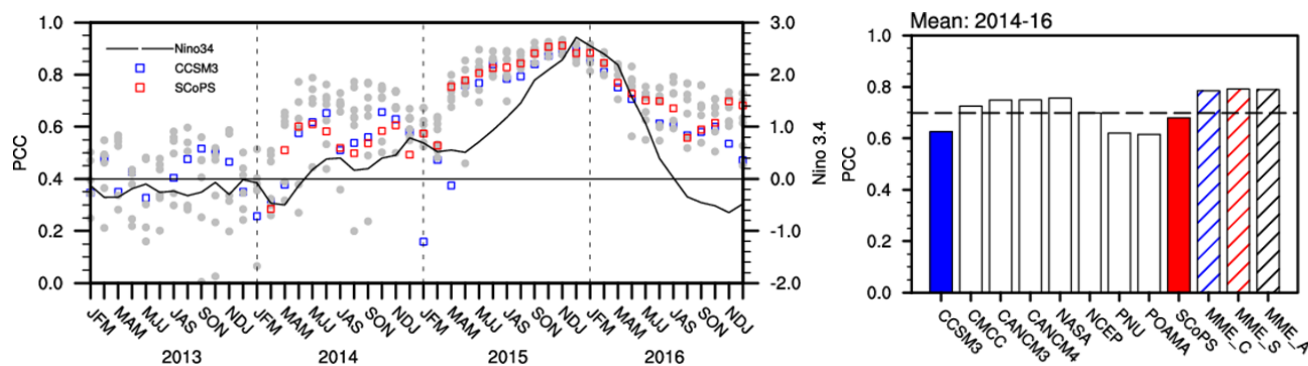
Fig. 1 Pattern correlation coefficient (PCC) of the SST anomalies between observation and APCC MME participant models over the tropical (20˚N-20˚S). Left panel shows the observed (black line) Nino3.4 index and PCC of SCoPS (red square) and CCSM3 (blue square) for strong El Nino events (2015-2016). Right panel shows PCC skill of participant models and MME

Reference

Ham, S., A-Y. Lim, S. Kang, H. Jeong, and Y. Jeong, 2018: A newly developed APCC SCoPS and its prediction of East Asia seasonal climate variability. *Clim. Dyn.*, doi:10.1007/s00382-018-4516-5

_____

Correspondence to: A-Young Lim, APEC Climate Center, Busan, South Korea; E-mail: limay@apcc21.org

Recent Slow Melt of Arctic Summer Sea Ice Due to
Tropical Pacific SST Changes

Ian Baxter[1], Qinghua Ding[1], Axel Schweiger[2], Michelle L'Heureux[3], Stephen Baxter[3], Tao Wang[4,5],
Qin Zhang[3], Kirstin Harnos[3], Bradley Markle[1], Daniel Topal[1,6], and Jian Lu[7]

[1]Department of Geography, and Earth Research Institute, University of California, Santa Barbara, CA
[2]Polar Science Center, Applied Physics Laboratory, University of Washington, Seattle, WA
[3]NOAA Climate Prediction Center, College Park, MD
[4]Earth System Science Interdisciplinary Center, University of Maryland, College Park, MD
[5]NASA Goddard Space Flight Center, Greenbelt, MD
[6]Department of Meteorology, Eötvös Loránd University, H-1117 Budapest, Hungary
[7]Atmospheric Sciences and Global Change Division, Pacific Northwest National Laboratory, Richland, WA

1. Introduction

In this study, we aim to understand the influence of tropical Pacific sea surface temperature (SST) changes on Arctic sea-ice decline in September. Arctic sea ice has shown accelerated melting from the early 2000's to the early 2010's and a slowing down thereafter (Swart *et al.* 2015). However, this slowdown is not expected with a steadily increasing rate of greenhouse gas emissions over this period. Our analysis of observational and model evidence shows that the recent slowdown of summer sea ice loss reflects a continuous anthropogenically forced melting enhanced and then masked by interdecadal variability of Arctic atmospheric circulation. This variation is driven by teleconnections originating from SST changes in the eastern-central tropical Pacific via a Rossby wave train propagating into the Arctic. This teleconnection, which we refer to as the "PARC", or Pacific-Arctic teleconnection, has contributed to abrupt warming and Arctic sea ice loss from 2007 to 2012, followed by a much slower decline in recent years, resulting in the slowdown appearance. Given the importance of this process in driving the Arctic climate on low–frequency time scales, accurate representation and prediction of the PARC mode in climate models is critical for future projections of the Arctic climate.
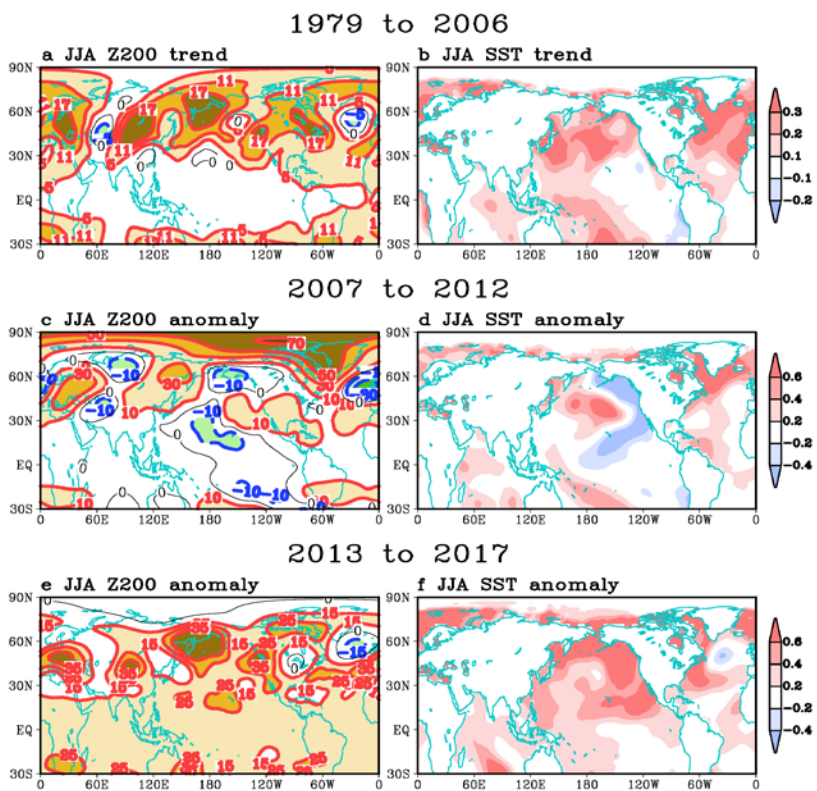
Fig. 1 1979-2006 linear trend in (a) ERA-Interim JJA 200hPa geopotential height and (b) ERSSTv4 JJA sea surface temperatures. (c) and (d) are the same as (a) and (b) but for 2007-2012 anomaly from 1979-2017 mean. (e) and (f) are the same as (c) and (d) but for 2013 to 2017 anomaly.

Correspondence to: Ian Baxter, Department of Geography, Earth Research Institute, University of California, Santa Barbara, CA 93106; E-mail: itbaxter@ucsb.edu

2. The observed Pacific-Arctic teleconnection

We first examined all linear trends longer than 10 years in the total September Arctic sea ice index and found two prominent trends: a period of the fastest melting from 2001 to 2012 and the only near-zero trend from 2007 to 2017. These two periods overlap from 2007 to 2012. Thus, to focus on this period and its role in the slowdown, we divided our analysis into three epochs: the linear trend from 1979 to 2006 and the anomalies from 2007 to 2012 and 2013 to 2017 (Fig. 1). The linear trend from 1979 to 2006 does not show a strong change in the eastern Pacific or in the Arctic. However, from 2007 to 2012 there is cooling in the eastern tropical Pacific that generates high pressure in the Arctic troposphere through Rossby wave propagation. The barotropic high pressure structure then leads to adiabatic descent of air, that warms and moistens the lower Arctic troposphere, increasing emission of longwave radiation and contributing to enhanced sea ice melt (Ding *et al.* 2014, 2017). Between 2012 and 2013, eastern-central Pacific SST switched to a warm phase, leading to a cooling effect in the Arctic and masking of CO_2-driven melting.

The PARC is the leading internal mode obtained through Maximum Covariance Analysis (also called Singular Value Decomposition) using a covariance matrix between detrended June-July-August (JJA) SST from 30°S to 30°N and 200 hPa geopotential height from 60°N to 90°N. The PARC links changes in eastern tropical Pacific SST to abrupt changes in geopotential height, temperature, and sea ice in the Arctic through a poleward propagating Rossby wave train. The PARC shows a peak between 2007 and 2012, coinciding with the most rapid period of September sea ice decline.

3. Model experiment

We utilize a pacemaker experiment to test the ability of tropical Pacific sea surface temperatures to drive Rossby wave propagation from the eastern-central Pacific to the Arctic during the enhanced melting period from 2007 to 2012. For this, we use the ECHAM4.6 general circulation model (GCM) coupled with a simple thermodynamic sea ice-ocean model. Since our model uses only a simple thermodynamic model, we focus primarily on the influence of tropical Pacific SST on Arctic circulation. The sensitivity simulation was driven by the observed SSTs in the eastern central Pacific (30°S to 30°N) averaged from 2007 to 2012 and run for 40 years with the first 10 years considered spin up. With this method, each year can be considered an individual realization and the 30-year average as an ensemble mean. The control simulation was driven by observed climatological SSTs (12-month annual cycle) everywhere and run for 40 years. The difference between the 30-year average of the sensitivity and control runs shows SST changes in the eastern-central Pacific can generate Rossby wave propagation to the Arctic from 2007 to 2012 with a high pressure center near Greenland similar to that seen in observations (Fig. 2).
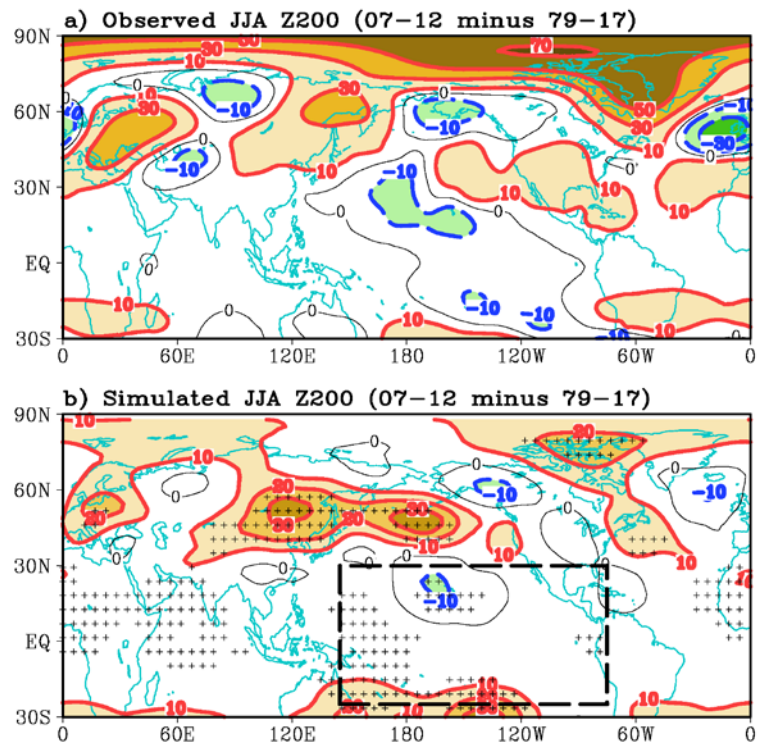
Fig. 2 a) Observed JJA 200hPa geopotential height anomaly (unit: m) for 2007-2012 against the 1979-2017 mean. (b) Same as (a) but for the model response from the sensitivity experiment described in the text. The dashed, black box (145°E-285°E, 25°S-30°N) indicates the region where observed SSTs were prescribed to force the model. Stippling in (b) indicates statistically significant differences at the 95% confidence level by the two-sample *t*-test.

4. Conclusions

Our observational analysis in combination with the results from the pacemaker experiment suggest an eastern-central Pacific-Arctic teleconnection (PARC) is partially responsible for the recent slowdown appearance in the decline of September Arctic sea ice. Through changes in Arctic circulation, the PARC is able to strengthen or mask the effects of CO_2-driven atmospheric warming in the Arctic. This is most clearly seen from 2007 to 2012 as cooling in the eastern-central Pacific led to Rossby wave propagation to high latitudes, high pressure near Greenland and in the Arctic and decreased September sea ice cover. A shift from the strengthening phase (2007-2012) to a masking phase (2013-2017) gives the appearance of a slowdown in September Arctic sea-ice decline.

References

Ding, Q., J. M. Wallace, D. S. Battisti, E. J. Steig, A. J. Gallant, H. J. Kim, and L. Geng, 2014: Tropical forcing of the recent rapid Arctic warming in northeastern Canada and Greenland. *Nature*, **509**, 209-212.

Ding, Q., and Coauthors, 2017: Influence of high-latitude atmospheric circulation changes on summertime Arctic sea ice. *Nat. Climate Change*, **7**, 289-295.

Swart, N. C., J. C. Fyfe, E. Hawkins, J. E. Kay, and A. Jahn, 2015: Influence of internal variability on Arctic sea-ice trends. *Nat. Climate Change*, **5**, 86-89.

Developing an Experimental Week 2
Severe Weather Outlook for the United States

Hui Wang[1], Alima Diawara[1,2], Arun Kumar[1], and David DeWitt[1]

[1]Climate Prediction Center, NOAA/NWS/NCEP, College Park, MD

[2]Innovim LLC, Greenbelt, MD

1. Introduction

Developing week 2 to 4 severe weather outlooks is one of the CPC projects under the Office of Science and Technology Policy initiative. The goals of this project are (1) to expand development and perform evaluation of week-2 severe weather model guidance, and (2) to explore the potential and develop experimental forecast tools for week 3 and 4 severe weather. The results presented at the workshop focus on week-2 severe weather forecast.

A study by Carbin *et al.* (2016) uses the Supercell Composite Parameter (SCP) derived from the CFSv2 45-day forecasts to provide extended-range severe weather environment guidance. When SCP is greater than 1, the chance for severe weather to occur is high. Here we take one more step to explicitly forecast severe weather based on the empirical relationship between model-predicted SCP and actual severe weather activity in historical records.

2. Data and methods

The data used in this study include both observational dada and model forecasts. For observations, the NCEP Climate Forecast System Reanalysis (CFSR) and NWS local storm reports (LSRs) are employed. The LSR consists of hail, tornado, and damaging wind reports, as well as their location, time and intensity. The sum of the LSRs for hail, tornado and damaging wind are referred to as

Fig. 1 Observed seasonal climatology of SCP (left) and LSR3 (right) for the four seasons.

LSR3 hereafter. They are re-gridded to a 0.5°×0.5° grid. We use the NCEP GEFS 16-day hindcasts to develop the forecast model for week-2 severe weather. The hindcast period is from 1996 to 2012. The hindcasts were

Correspondence to: Hui Wang, Climate Prediction Center, NOAA/NWS/NCEP, 5830 University Research Court, College Park, MD 20740; E-mail: hui.wang@noaa.gov

made every 4 days with 5 members and 0.5°×0.5° resolution. The analysis presented was performed using the 5-member ensemble mean forecasts.

Following Carbin *et al.* (2016), the SCP is defined as

$$SCP = (CAPE/1000 \text{ J kg}^{-1}) \times (SRH/50 \text{ m}^{-2} \text{ s}^{-2}) \times (BWD/20 \text{ m s}^{-1}),$$

where CAPE is convective available potential energy, SRH storm-relative helicity, and BWD bulk wind difference. The three constants are used to normalize SCP so that when SCP is greater than 1, severe weather likely occurs.

The forecast model developed in this study is a hybrid dynamical-statistical model (*e.g.*, Wang *et al.* 2009). It uses the dynamical model (GEFS) predicted SCP as a predictor, and then forecast severe weather (LSR3) based on the statistical relationship between model SCP and actual LSR3 in historical records. The forecast skill is cross-validated over the GEFS hindcast period (1996–2012).

3. Results

The observed seasonality of SCP is examined first. Figure 1 (left) shows the climatological seasonal mean daily SCP over the U.S. for the four seasons (DJF, MAM, JJA, and SON), respectively, derived from CFSR. The seasonal variation of SCP is characterized by relatively large values of SCP appearing in the Gulf States during winter.   Then SCP intensifies and peaks in spring. The region of the maximums moves northward from the Southern Plain in spring to the Northern Plain in summer. From summer to fall, the SCP value decreases and the center of the maximums movers back to the south.   The SCP displays strong seasonality over the central U.S.   Over the same region, the LSR3 also shows similar seasonality with strong severe weather activity in spring and summer (Fig. 1, right). During these two seasons, however, there are also strong activities in the eastern U.S. where SCP value is small. Therefore, in terms of the seasonal cycle, there is a good correspondence between SCP and LSR3 in the central U.S.

Fig. 2 Maps of one-point correlation for weekly SCP (top) and LSR3 (bottom) with anomalies at the 0.5° × 0.5° grid (left) and those area-averaged over the 5° × 5° box (right), respectively.
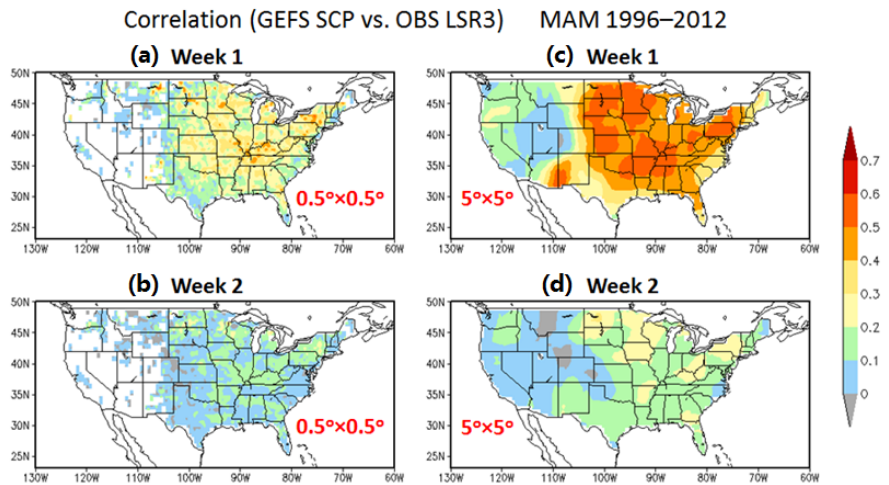
Fig. 3 Correlation between the GEFS predicted SCP and observed LSR3 for week 1 (top) and week2 (bottom) with anomalies at the 0.5° × 0.5° grid (left) and those area-averaged over the 5° × 5° box (right), respectively.

The SCP from the GEFS forecasts captures the observed seasonality of SCP for both week 1 and week 2 (not shown).

The difficulty in forecasting severe weather is mainly due to its short lifetime and a small spatial scale. Figure 2a–b shows the one-point correlation map for weekly CFSR SCP and LSR3, respectively, at the $0.5^o \times 0.5^o$ grid. It is the correlation map between weekly anomaly at one grid point (here 95.5^oW, 37.5^oN) and that at every grid point over the U.S. For SCP (Fig. 2a), there are high correlations between the selected grid point and the surrounding grid points, indicating that SCP has a large-scale feature. For LSR3 (Fig. 2b), in contrast, the correlations are small, except for the correlation with itself, consistent with the small spatial scale of severe weather. However, when averaging LSR3 over a $5^o \times 5^o$ box and then re-calculating the one-point correlation, the result (Fig. 2d) shows much higher spatial coherence for LSR3 and is comparable to that of SCP (Fig. 2c). It is thus reasonable to expect that forecasting weekly severe weather over a larger domain may have a better skill.

To develop a hybrid forecast model, we first establish some statistical relationship between GEFS predicted SCP and observed LSR3. Given the strong seasonality of both SCP and SLR3 (Fig. 1), a 3-month moving window is used in the analysis. Figure 3a-b shows the correlations between observed LSR3 and GEFS week-1 and week-2 forecasts of SCP at the $0.5^o \times 0.5^o$ grid, respectively, for MAM, the peak severe weather season. The correlation with the week-2 forecast is less than the

Fig. 4 Maps of homogeneous correlation for the first three SVD modes between weekly CFSR SCP and observed LSR3 during the MAM of 1996–2012. The percentage of the variance explained by each SVD mode is also provided at the bottom right of each panel.
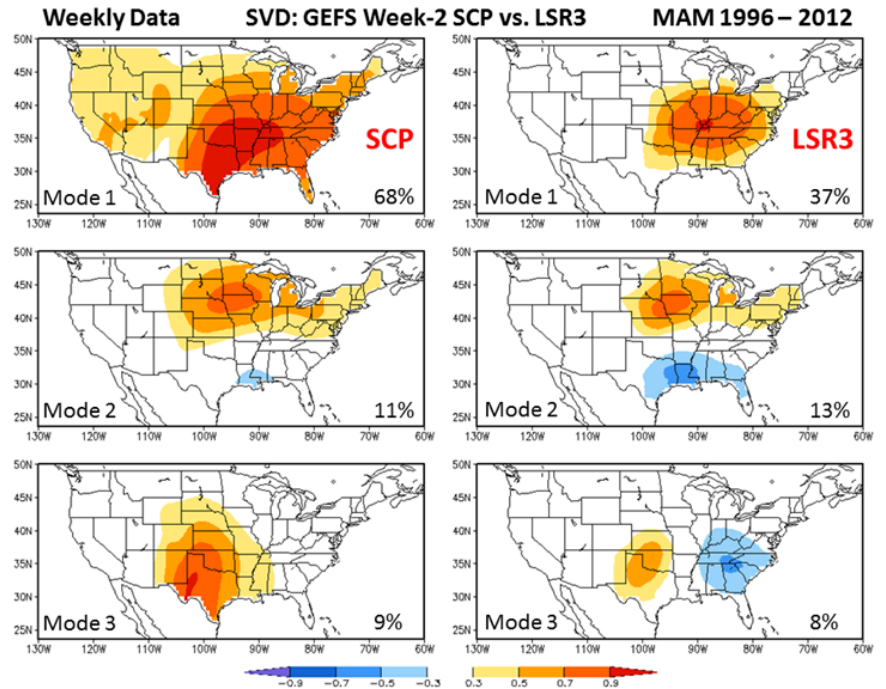
Fig. 5 Same as Fig. 4, but for the three leading SVD modes between the GEFS week-2 SCP and observed LSR3.

week-1 forecast, indicating a weak relationship between GEFS SCP and LSR3 for week 2. However, when using the $5^o \times 5^o$ area-averaged anomalies to reestablish the relationship between model SCP and observed LSR3, their correlations (Fig. 3c-d) are much higher than those at the $0.5^o \times 0.5^o$ grid (Fig. 3a-b) for both week 1 and
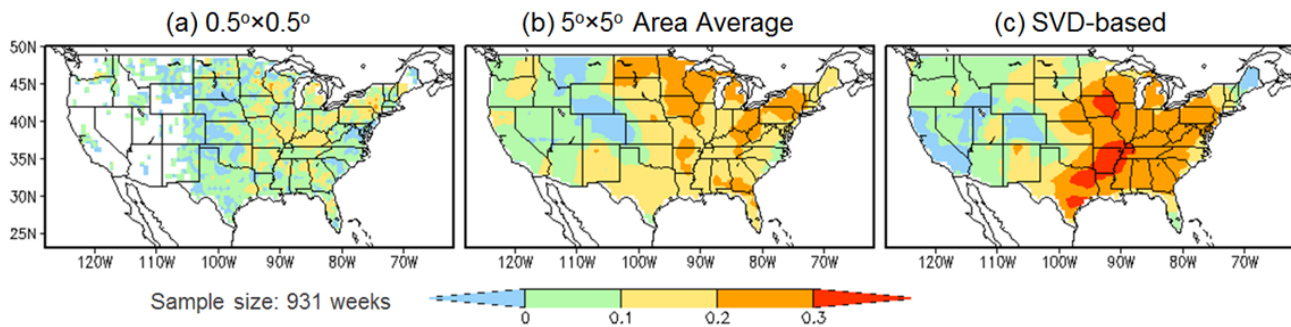
Fig. 6 Forecast skills for week-2 severe weather cross-validated over MAM 1996–2012 with (a) simple linear regression model at the 0.5º × 0.5º grid, (b) 5º × 5º area-averaged anomalies, and (c) the SVD-based hybrid model.

week 2. The result indicates a stronger relationship between the model SCP and LSR3 when considering averaging severe weather activity over a larger domain.

In addition to the relationship between the GEFS SCP and LSR3 at each grid point, their statistical relationship can also be established by the singular value decomposition (SVD) technique (Bretherton *et al.* 1992). This method can objectively identify pairs of modes (spatial patterns) of SCP and LSR3, both of which vary with a maximum temporal covariance between each other. Figure 4 shows the spatial patterns of the three leading SVD modes for weekly SCP (left) and LSR3 (right), respectively, using the observational data. Each SVD mode displays a distinctive pattern with consistent distributions between SCP and LSR3. The three modes account for 62% of weekly LSR3 variance. A similar SVD analysis using the GEFS week-2 SCP (Fig. 5) can reproduce the observed relationship between SCP and LSR3 well (Fig. 4).

A hybrid model is developed to forecast the number of severe weather (LSR3) using the GEFS predicted week-2 SCP as a predictor and based on their relationships depicted in either Fig. 3 or Fig. 5. The former applies a linear regression model to forecast LSR3 at each grid point, whereas the latter projects the week-2 GEFS SCP onto the SCP SVD modes and then predicts LSR3 based on the SCP-LSR3 relationship depicted by the SVD analysis (Fig 5).

The forecast skill for week-2 severe weather is cross-validated over the GEFS hindcast period (1996–2012). The anomaly correlation skill at the 0.5º × 0.5º grid is relatively low (Fig. 6a), and is very similar to the corresponding correlation between GEFS SCP and LSR3 (Fig. 3b). The forecast skill of the hybrid model is improved (Fig. 6b) by using the 5º×5º area-averaged anomalies, consistent with the stronger relationship between model SCP and LSR3 (Fig. 3d). The forecast skill is significantly improved (Fig. 6c) when using the SVD-based relationship. This may be due to the inclusion of the covariation of both SCP and LSR3 with their surrounding regions.

4. Conclusions

Following Carbin's work, the Supercell Composite Parameter (SCP) was selected as a variable to represent the large-scale environment and link the model forecast to actual severe weather. The hybrid model forecasts suggest a low skill for week-2 severe weather. However, the forecast can be improved by using the 5º×5º area-averaged anomalies and the SVD-based statistical relationship. Based on the analysis and results presented at the workshop, an experimental week-2 severe weather outlook has been implemented in real time.

For future work, we plan to extend the analysis for weeks 3 and 4 using the CFSv2 45-day hindcasts and forecasts. Because the forecast skill for week 3 and 4 SCP is expected to be low, we may consider forecasting week 3 and 4 severe weather over a larger domain, such as Midwest and Southeast US.

References

Bretherton, C. S., C. Smith, and J. M. Wallace, 1992: An intercomparison of methods for finding coupled patterns in climate data. *J. Climate*, **5,** 541–560.

Carbin, G. W., M. K. Tippett, S. P. Lillo, and H. E. Brooks, 2016: Visualizing long-range severe thunderstorm environment guidance from CFSv2. *Bull. Amer. Meteor. Soc.*, **97,** 1021–1032.

Wang H., J.-K. E. Schemm, A. Kumar, W. Wang, L. Long, M. Chellian, G. D. Bell, and P. Peng, 2009: A statistical forecast model for Atlantic seasonal hurricane activity based on the NCEP dynamical seasonal forecast. *J. Climate*, **22,** 4481–4500.

2. IDSS-IMPACT DECISION SUPPORT SERVICES

43rd NOAA Annual Climate Diagnostics
and Prediction Workshop

Santa Barbara, California

23-25 October 2018

Towards Increased Utilization of Weather Forecast Products in Agriculture

Aston Chipanshi[1], Mark Berry[1], Marilee Pregitzer[1], and Hai Lin[2]

[1]*Agroclimate, Geomatics and Earth Observation, Science & Technology Branch,*
Agriculture and Agri-Food Canada
[2]*Canadian Meteorological Centre, Environment Canada and Climate Change*

1. Introduction

For climate sensitive sectors such as agriculture, weather forecasts are an essential component of early warning, which contribute to reducing costs of replacing agricultural infrastructure, inputs and the planning of scheduling on-farm management activities. The costs associated with extreme devastation of infrastructure and crop loss in Canada, for example, can attain billions of dollars in a particular year.

Weather forecasts are provided at different scales both in time and space. Ideally, skillful weather forecasts at a finer scale and longer temporal resolution are needed for the majority of agricultural operations, however such forecasts are difficult to find as the science of weather forecasting has not developed to the level of making point specific forecasts and at longer time scales with a high degree of accuracy (Cai *et al.* 2011). In spite of this difficulty, significant efforts have been made or are under way to test a range of predictions from short range to sub-seasonal scales using ensemble forecasts from a variety of prediction models (Merryfield *et al.* 2013; Vitart 2004). As these products become increasingly available, there is a need to demonstrate their usability in climate sensitive sectors. Our goal in this study was to demonstrate how short (weeks) to medium range (up to a month) forecasts can be tailored to answering questions in the agricultural sector. Some typical questions which agricultural users ask include: Will there be enough precipitation in the next few weeks to end a dry spell? Will there be enough heat for the crop to mature? Is the crop on schedule or running behind in its development?

2. Methods

To make the most out of weather and climate forecasts in agriculture, we calculated agro-meteorological indices from the primary weather forecasts as multi-index products for direct use in management decisions for specific crops and operations. Forecast data sets were obtained from the Canadian Meteorological Centre's (CMC) Global Ensemble Prediction System (GEPS) and consisted of 16-day and 32-day integrations every Thursday at the 39km resolution, and each run had 21-ensemble members. The GEPS outputs were found skillful from a previous study (1995 to 2012 data) with correlation skill levels between predictions and observations of (R=0.4 to 0.8) for temperature and (R=0.3 to 0.6) for precipitation (Lin *et al.* 2016). The indices were calculated for three crop types: 1) cool season such as barley and oats, 2) warm season such as peas and soybean, and 3) over-winter crops such as forages and woody fruit trees. Agrometeorological indices included the water demand (the difference between precipitation and evapotranspiration), accumulation of precipitation at harvest time, effective growing degree days, heat stress and the drying index at harvest.

3. Results

A comparative analysis of selected agrometeorological indices in forecast mode was made with actual observations during the latter part of 2018 growing season (September) across southern Canada. Greatest daily precipitation amounts ranging from 16 to 30mm for weeks 1 and 2 (August 31 to September 6 and September 7 to 13, 2018 respectively) were forecasted for southern Ontario and Quebec as well as the east central areas of Saskatchewan and Manitoba (Fig. 1). While the observed precipitation accumulation totals were not exactly of the same order of magnitude as the predictions (the observed totals were higher than predictions), there was a spatial agreement about areas with the highest amounts. Traditionally, September is the month when the

_____
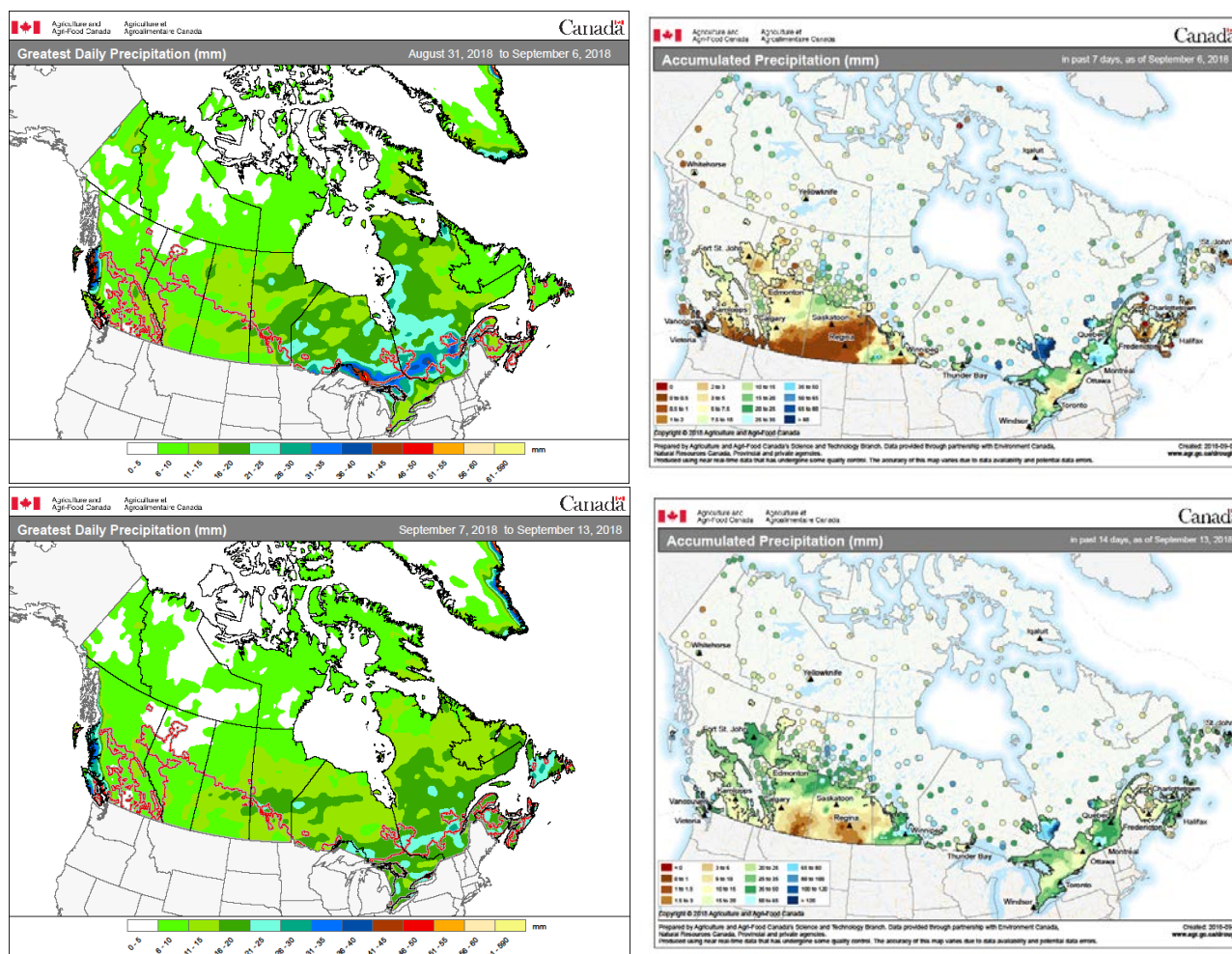
Fig. 1 Precipitation forecast and actual observations across southern Canada during weeks 1 (top) and 2 (bottom) in September of 2018. The left panel shows forecasts while the right panel shows observations.

majority of crop harvesting takes place, and while high precipitation accumulation can occur at any time, September is not usually associated with heavy precipitation accumulation (see Bonsal *et al*. 1999). Due to the wide-spread wetter conditions across the agricultural zone, the majority of the crop reporting districts reported less than the optimum progression of harvesting, which in the case of the Canadian Prairies was at around 40 to 70% completion (Saskatchewan Crop report: http://publications.gov.sk.ca/details.cfm?p=91572). Wetter conditions were accompanied by less than the optimum heat units required to dry the crop in readiness for harvesting as shown in Fig. 2. By the end of the season (see the right panel of Fig. 2), the accumulated heat units were less than what would be expected for cool and warm season crops, that are 1482 and 1376 respectively (Brown and Bootsma 1993; Stewart *et al*. 1998). Because of the relative wetter and low heat accumulation harvest period in September, there were fears that a potentially good grain harvest would be compromised by frost in early autumn. In order to avoid a total loss, the forecast products if used diligently would be used to carry out alternative actions. Where a harvest for grain is not possible, the crop could be put into animal feeds as silage and under very dire conditions, it could be ploughed under as a land management strategy. Large machinery such as combine harvesters are moved around at harvest. The movement of large machinery will be guided by the presence of good weather. This will in turn help with fuel usage and reduce the emission of GHGs at the farm level as machinery will be moved when the window for successful harvesting exists.
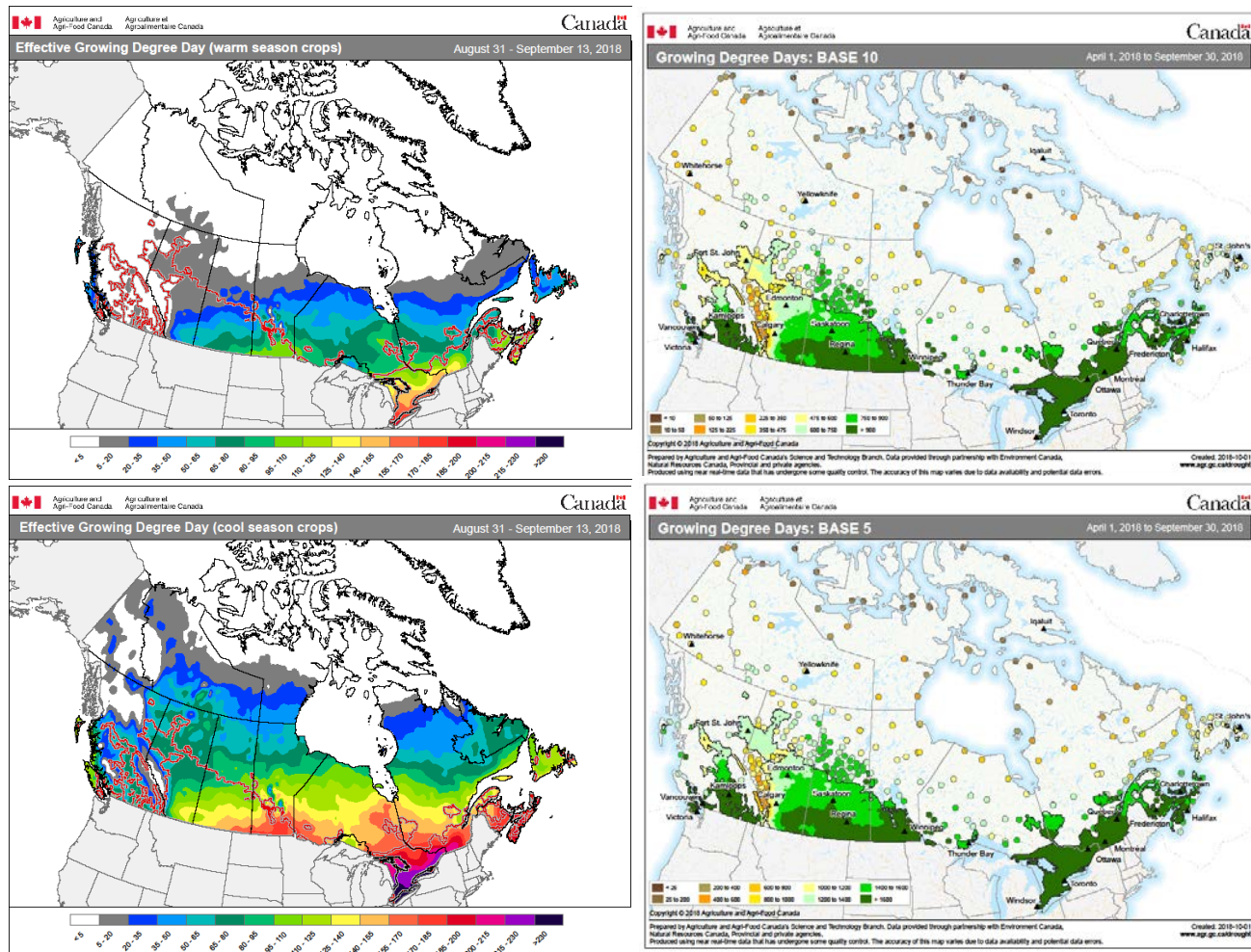
Fig. 2 Forecast Effective Growing Degree Days (EGDDs) during weeks 1 and 2 in September of 2018 (left) and actual GDD observations by end of the season (right) across southern Canada for warm (upper) and cool (lower) season crops.

4. Summary

Greatest precipitation and heat units were forecasted during the first and second week in September (harvest time) in 2018 across the agricultural landscape of Canada. The predicted conditions were not ideal for harvesting and as a result, there were delays in taking the crop off the fields. Armed with forecast information designed for specific crops (warm and cool season in this study), this information is useful for selecting alternative farm management actions which will prevent total loss as a result of climatic risks.

References

Bonsal, B. R., X. Zhang, and T. Hogg, 1999: Canadian Prairie growing season precipitation variability and associated atmospheric circulation. *Clim. Res.*, **11**, 191–208.

Brown, D. M. and A. Bootsma, 1993: Crop heat units for corn and other warm-season crops in Ontario. Ontario Ministry of Agriculture and Food, Fact sheet No. 93-119, Agdex 111/31, 10/93. 4p, http://www.omafra.gov.on.ca/english/crops/facts/93-119.htm.

Cai, X., M. Hejazi, and D. Wang, 2011: Value of probabilistic weather forecasts: Assessment by real-time optimization of irrigation scheduling. *Journal of Water Resources Planning and Management*, **137**, 391–403, doi:10.1061/(ASCE)WR.1943-5452.0000126.

Lin, H., N. Gagnon, S. Beauregard, R. Muncaster, M. Markovic, B. Denis, and M. Charron, 2016: GEPS-based monthly prediction at the Canadian Meteorological Centre. *Mon. Wea. Rev.*, **144**, 4867–4883, doi.org/10.1175/MWR-D-16-0138.1.

Merryfield, W. J., and Coauthors, 2013: The Canadian Seasonal to Interannual Prediction System. Part I: Models and initialization. *Mon. Wea. Rev.*, **141**, 2910–2945, doi:https://doi.org/10.1175/MWR-D-12-00216.1.

Stewart, D. W., and Coauthors, 1998: Phenological temperature response of maize. *Agronomy J.*, **90**, 73-79.

Vitart, F., 2004: Monthly forecasting at ECMWF. *Mon. Wea. Rev.*, **132**, 2761–2779, doi:https://doi.org/10.1175/MWR2826.1

Development of an Hourly Analysis of
Surface Air Temperature over the Global Land

Yutong Pan[1,2] and Pingping Xie[1]

[1]Climate Prediction Center, NOAA/NWS/NCEP, College Park, MD
[2]Innovim, LLC, Greenbelt, MD

1. Background

This work is to construct an hourly analysis of surface air temperature (T_{2m}) over the global land. A conceptual model is developed by adjusting the hourly T_{2m} generated by the NCEP operational global models against the observation-based CPC daily maximum (T_{max}) and minimum (T_{min}) surface air temperature.

2. Data and methodology

2.1 Data

Global elevation data used are the Climatic Research Unit (CRU, 0.16° lat/lon) and Digital Elevation Model (DEM, 0.01° lat/lon) data sets. The observed surface air temperatures are the Global Telecommunication System (GTS)-based CPC global analysis of daily T_{max} and T_{min} (2011−present, 0.16° lat/lon), and the Integrated Surface Database (ISD) station observations of
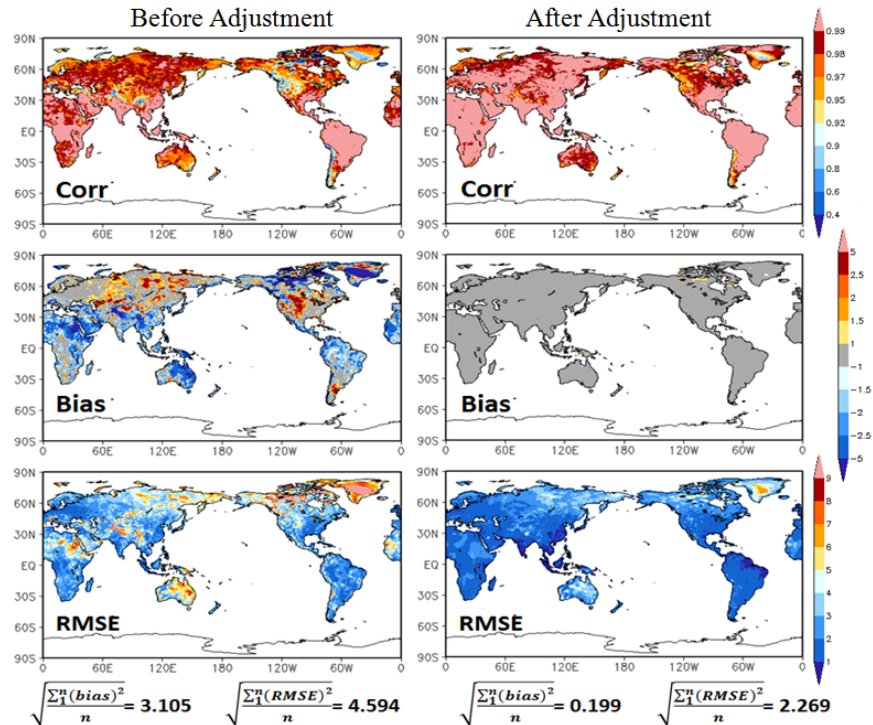
Fig.1. Correlation coefficient, bias, and RMSE between the CPC T_{min} and CFSR T_{min} for 2012.
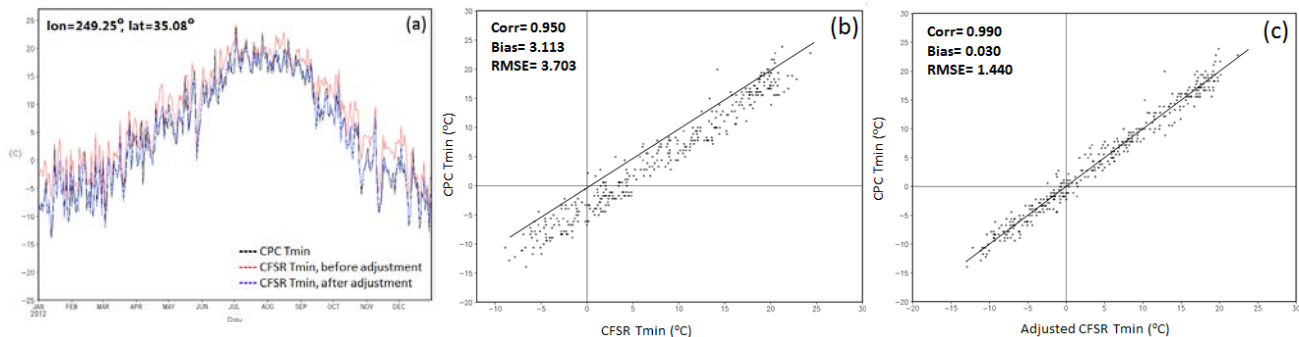
Fig. 2. (a) Time series of the CPC T_{min} and CFSR T_{min} at a selected location (lon=249.25°, lat=35.08°) in the US for 2012 and scatter plots between the CPC T_{min} and CFSR T_{min} (b) before adjustment and (c) after adjustment.

_____

Correspondence to: Yutong Pan, Climate Prediction Center, NOAA/NWS/NCEP, 5830 University Research Court, College Park, MD 20740, and Innovim, LLC, Greenbelt, MD; E-mail: yutong.pan@noaa.gov

hourly air temperature. Surface air temperatures from the NCEP CFS Reanalysis (CFSR, 2011−present, 0.2045° lat/lon) and the GFS 6-12 hour forecasts (March, 2018−present, 0.117° lat/lon) are used to define the global hourly T_{2m} for the retrospective production and real-time updates, respectively.

2.2 Methodology

The three-step adjustments include elevation correction, synoptic scale bias correction, and diurnal range adjustment. The CFSR hourly T_{2m} is adjusted on a monthly basis at target analysis grid of 0.16° lat/lon, and the GFS hourly T_{2m} is real-time adjusted 6-hourly at target analysis grid of 0.05° lat/lon.

First, the model T_{2m} data are down-scaled from their native Gaussian grids to the target analysis grids, through the local empirical relationship between T_{2m} and elevation. Elevation correction is applied based on the difference between the model elevation and real topography. For the synoptic scale bias correction, daily T_{max} and T_{min} are derived from the model hourly outputs. Then daily means for both the CPC GTS analysis and the model T_{2m} are calculated as the arithmetic mean of T_{max} and T_{min}. Synoptic scale bias is thus removed from the raw model hourly T_{2m} as the difference between the 5-day running means from the CPC analysis and the model values. The third step is implemented to further adjust the magnitude of the diurnal cycle in the model hourly T_{2m} after the removal of the synoptic scale bias. The magnitude of a diurnal cycle, defined as the difference between the daily T_{max} and T_{min}, is determined for each day for both the observations and the model T_{2m}. Ratio between the observation and model based diurnal amplitudes are calculated

Fig.3. Same as Fig. 1, but for CPC T_{min} and GFS T_{min} from March 26 to June 06, 2018.
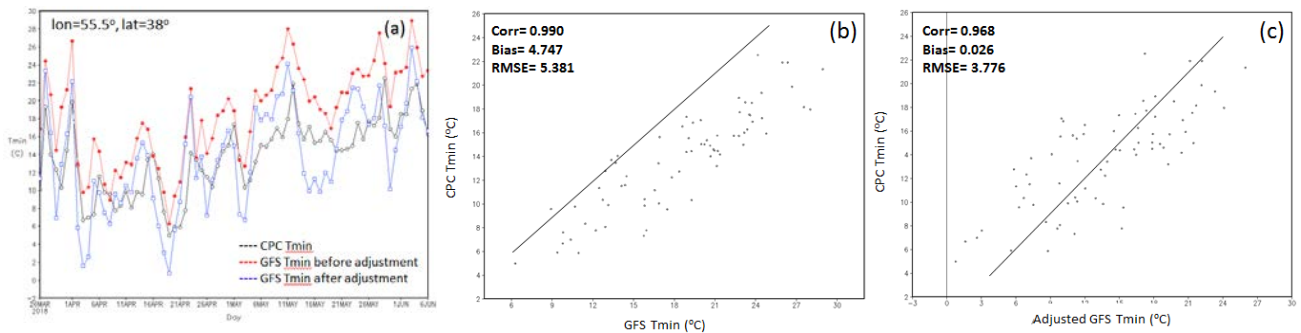
Fig. 4. Same as Fig. 2, but for (a) time series of CPC T_{min} and GFS T_{min} at a selected location (lon=55.5°, lat=38°) in Iran from March 26 to June 06, 2018 and scatter plots between the CPC T_{min} and GFS T_{min} (b) before adjustment and (c) after adjustment.

using data over the 5-day window and applied to correct the diurnal range of the model hourly T_{2m} for the target date.

3. Results

Figure 1 displays the correlation coefficient, bias, and root mean square error (RMSE) between the CPC T_{min} and CFSR T_{min} for 2012. Results indicate significant improvements of the adjusted CFSR T_{2m} globally. Figure 2 shows the time series of the CPC T_{min} and CFSR T_{min} at a selected location (lon=249.25º, lat=35.08º) in the US for 2012 and scatter plots between the CPC T_{min} and CFSR T_{min} before adjustment and after adjustment, respectively. Both the bias and the RMSE are reduced after adjustment. Similar results are obtained for T_{max} (not shown).

Figure 3 is another example of the correlation coefficient, bias, and RMSE, but between the CPC T_{min} and GFS T_{min} from March 26 to June 06, 2018. There are improvements of the GFS T_{2m} after adjustment, particularly for the mean bias. The ti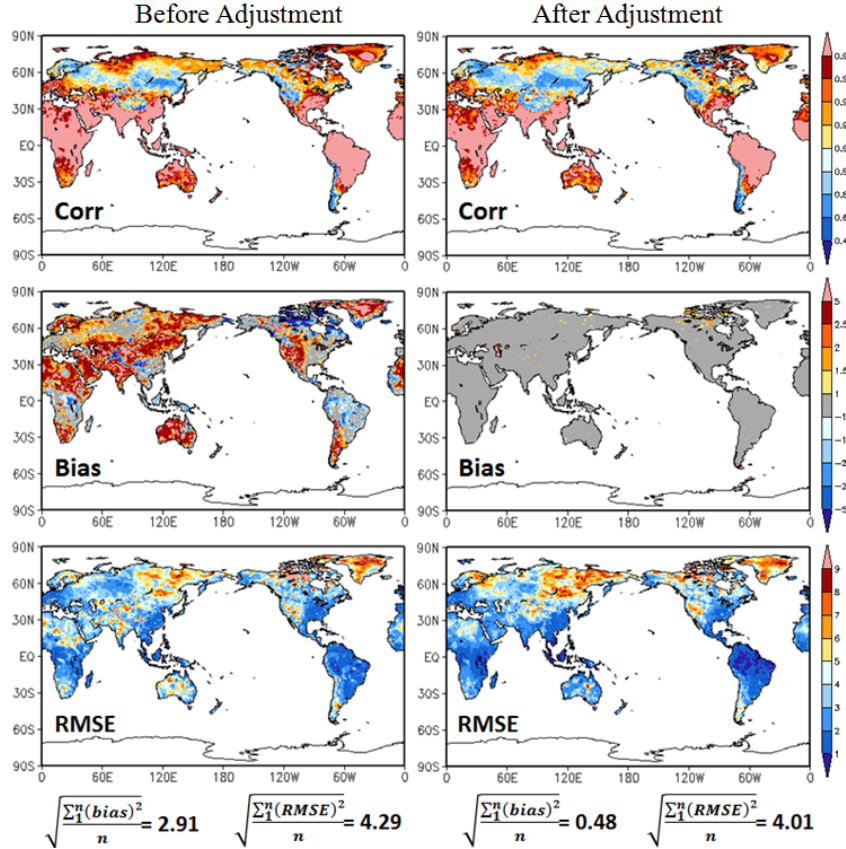me series of both the CPC T_{min} and GFS T_{min} at a selected location (lon=55.5º, lat=38º) in Iran from March 26 to June 06, 2018 are shown in Figure 4, together with the scatter plots between the CPC T_{min} and GFS T_{min} before adjustment and after adjustment, respectively. Both the bias and RMSE are reduced after adjustment. Results are similar for T_{max} (not shown).

Figure 5 presents the time series of the ISD and CFSR hourly T_{2m} at a selected location (lon=288.92º, lat=48.25º) in Canada from March 23 to June 06, 2018. The scatter plots between the ISD and CFSR T_{2m} before and after the adjustment are also displayed, respectively. Figure 6 is same as Figure 5, but for the ISD and GFS hourly T_{2m} at a location (lon=357.62º, lat=53.37º) in UK. Compared to the unadjusted data, both the bias and RMSE are reduced after the adjustment.

4. Conclusion

Evaluation of the adjusted hourly T_{2m} against independent observations of hourly surface air temperature (ISD station data) indicates improved quality of the adjusted CFSR/GFS T_{2m} compared to the unadjusted fields.
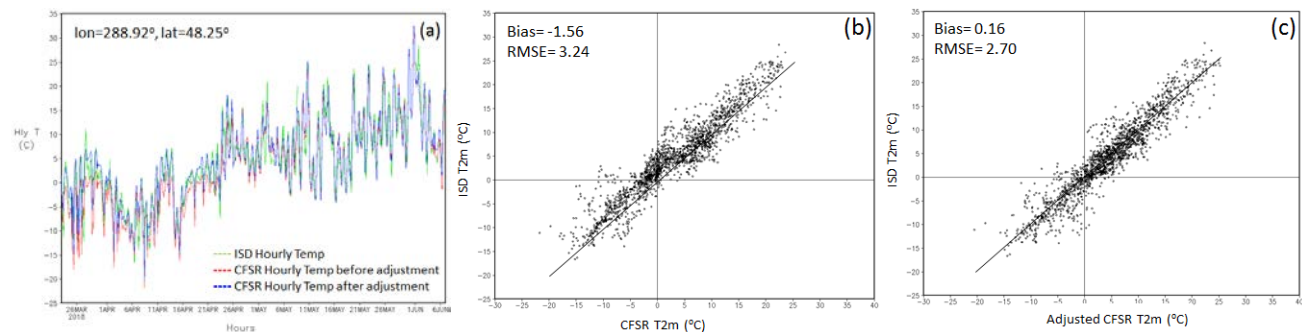
Fig. 5. (a) Time series of the ISD and CFSR hourly T_{2m} at a selected location (lon=288.92º, lat=48.25º) in Canada, from March 23 to June 06, 2018 and scatter plots between the ISD and CFSR T_{2m} **(b)** before adjustment and **(c)** after adjustment.
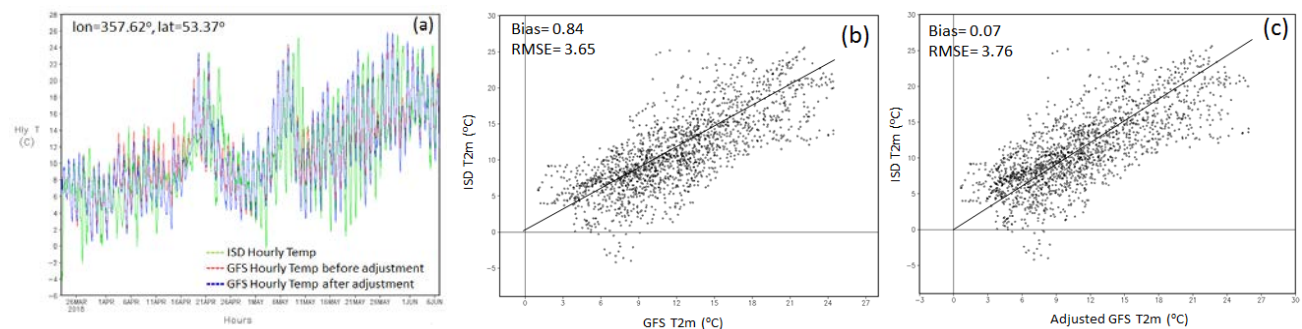
Fig. 6. Same as Fig. 5, but for the ISD and GFS hourly T_{2m} at a location (lon=357.62º, lat=53.37º) in UK.

In general, the improvements in the CFSR hourly T_{2m} are relatively larger than the GFS. Possible reasons may be related to larger forecast error in the GFS model (e.g., phase shift between model and observations) and approximations made in calculating daily mean values for the GFS adjustment. The global hourly T_{2m} analysis has been done for an 8-year period starting from 2011 and an automatic system has been established on a CPC server to real-time update the analysis.

Evaluation Week3/4 Forecast for Canadian GEPS

Qin Zhang, Liwei Jia, Adam Allgood, Dan Collins, and Jon Gottschalck

Climate Prediction Center, NOAA/NWS/NCEP, College Park, MD

1. Introduction

This study supports the current experimental Climate Prediction Center (CPC) week 3-4 temperature and precipitation outlooks, which are released once per week and focus on mean climate conditions anticipated for a two week forecast period. CPC is preparing to add realtime forecasts of the Global Ensemble Prediction System (GEPS) from the Environment Canada (EC) to its set of week3-4 forecast tools. Evaluation of the realtime forecast of GEPS is for development of model tools to improve CPC week3-4 outlooks.

2. Model and data procedure

The GEPS reforecast was implemented at the Canadian Meteorological Center (CMC) of Environment Canada for operations in December 2013 (see Gagnon *et al.* 2015). The main goal of the reforecast procedure is to generate a historical dataset that is representative of the current operational GEPS forecast. GEPS forecasts are an integral part of the collaboration with the United States National Centers for Environmental Prediction (NCEP) in the North American Ensemble Forecast System (NAEFS) project.

The reforecast dataset used in this study is the extension reforecast initialized once per week on Thursdays (2016 calendar) out to 32-days. There are 4 members (1 control run with 3 perturbation runs) at 1x1 spatial resolution. We evaluate the variables of 2m temperature, surface precipitation, 500hPa and 200hPa heights. We estimate model mean bias as well as derive skill information from the ensemble mean over the reforecast period (1995-2014). For comparing with observations, the verification data used are the CPC's unified temperature, CPC land only gauge-satellite merged precipitation data, and CDAS reanalysis for 500hPa and 200hPa heights.

3. Results

In order to assess model forecast ability, mean biases for the week 3-4 forecast period were removed from model climatology (1995-2014) of the ensemble mean (4 member averaged) for each IC to against the observed climatology. For convenience of discussion and easy display seasonal model biases of 4 variables were averaged for DJF, MAM, JJA and SON. Anomaly correlations were calculated to represent the ensemble mean forecast skill for DJF, MAM, JJA and SON of 2m temperature and precipitation from GEPS. The anomalies are uncalibrated but remove the model systematic errors by the reforecast from 1982-2014. The forecast skill of week3-4 temperature is relatively low on average over the U.S. The forecast skill of precipitation is even lower (see Fig. 1) than that of temperature, which is similar to the assessment results of ECMWF and JMA models.

4. Summary

In order to improve realtime week3/4 forecast for U.S. temperature and precipitation, a new week3/4 dynamic model forecast tool derived from Global Ensemble prediction system (GEPS) of Environment Canada is implemented in CPC. The realtime forecasts include the ensemble mean anomalies and probability prediction for temperature and precipitation over U.S., as well as 500hPa height over the Northern Hemisphere. This study examined the prospects of GEFS extension productions for week 3/4. Temperature anomaly correlations show some useful prediction skills of week3/4 in both temporal and spatial scores, which are calculated from the ensemble mean anomalies after the model bias being removed. We also evaluated forecasts by applying the ensemble regression to calibration from reforecast, which is initialized once a week with 4 members for period

---
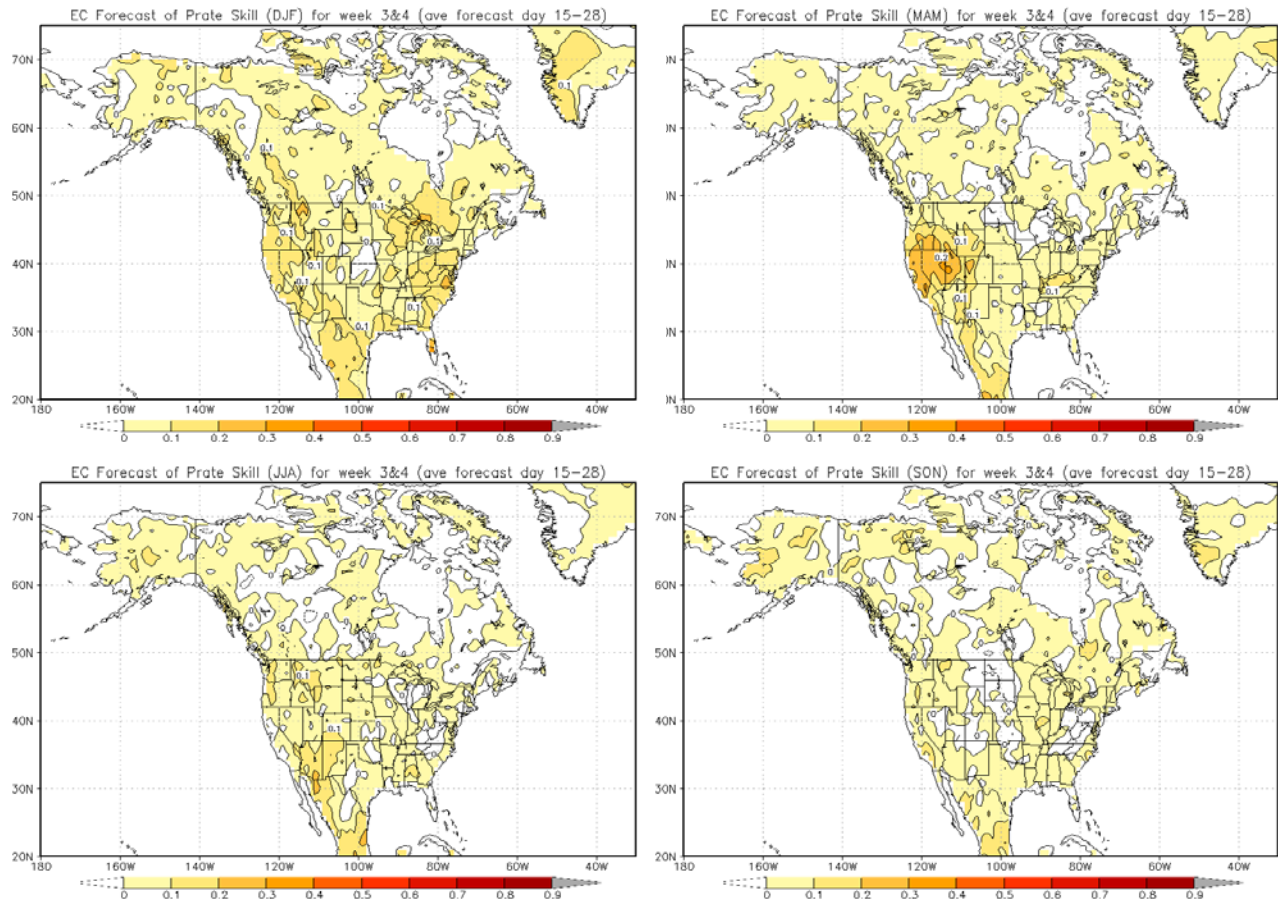
Fig. 1 Week 3-4 forecast skill of precipitation for DJF, MAM, JJA and SON seasons.

1995-2014. The skills measured by Brier Skill Score and Heidke Skill Score indicate moderate improvement for temperature forecasts. The skills of precipitation forecast for week3/4 are relatively low on average over U.S. and similar to that of ECMWF and JMA models. However, forecast opportunities exist in some regions and seasons.

References

Gagnon, N., and Co-authors, 2015: Improvement to the Global Ensemble Prediction System (GEPS) reforecast system from version 3.1.0 to version 4.0.0. Canadian Meteorological Centre Technical Note.

Subseasonal Tropical Cyclone Prediction at CPC:
A New Forecasting Tool for Weeks 1-4

Lindsey N. Long

Climate Prediction Center, NOAA/NWS/NCEP, College Park, MD
and
Innovim, LLC, Greenbelt, MD

1. Introduction

The Climate Prediction Center (CPC) currently produces a product called the Global Tropics Hazards and Benefits Outlook which highlights areas of tropical cyclone (TC) formation and above- and below-average rainfall for the upcoming Week 1-2 forecast period. The product is issued each Tuesday with an update on Friday during the peak of the Northern Hemisphere (NH) TC season (June 1st – November 30th). It consists of a graphic highlighting Moderate and High Confidence of TC development and rainfall in the upper and lower third tercile, a live briefing, and a detailed discussion summarizing the forecaster's reasoning. CPC is working to shift this product to weeks 2 and 3 (with an eye on week 4) and make it a probabilistic forecast. The goal of this study is to provide tools to support these TC forecasts at weeks 2-4. Work is also being performed on precipitation at these leads, but is beyond the scope of this presentation.

2. Data and methods

The CPC has access to three models in real-time that extend out to the week 4 time period. NCEP's Climate Forecast System Version 2 (CFSv2), the European Centre for Medium-Range Weather Forecasts's (ECMWF) Integrated Forecasting System, and the Canadian Meteorological Centre's (CMC) Environment Canada are examined to identify skill at the week 1 to 4 leads. Verification is performed using the Best Track datasets from NOAA and the Joint Typhoon Warning Center (JTWC).

In order to track TCs in the models, a detection algorithm based on Carmargo & Zebiak (2002) is utilized. This method uses seven criteria to designate a grid point as a TC. These criteria guarantee that the TC is a warm-core system, has a local minimum in sea level pressure, and a local
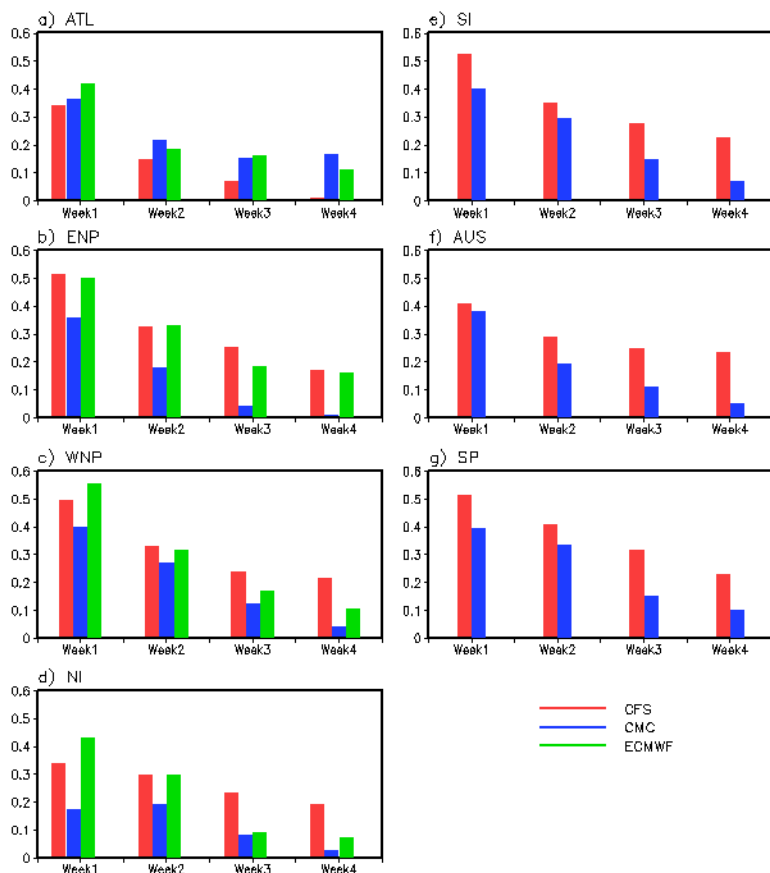
Fig. 1 Anomaly correlations of TC counts averaged over 1999-2012 with lead times from week 1 to week 4 for the a) Atlantic, b) Eastern North Pacific, c) Western North Pacific, d) North Indian, e) South Indian, f) Australian, and g) South Pacific basins for the CFSv2 (red), the CMC (blue), and the ECMWF (green). Note data from ECMWF does not yet extend into the full SH season.

_____

Correspondence to: Lindsey N. Long, Climate Prediction Center, NOAA/NWS/NCEP, 5830 University Research Court, College Park, MD 20740, and Innovim, LLC, Greenbelt, MD; E-mail: lindsey.long@noaa.gov

maximum in wind speed. The TC point is then tracked forward and backward in time following the vorticity maxima. For analysis, the globe in broken up into seven ocean basins: Atlantic (ATL), Eastern North Pacific (ENP), Western North Pacific (WNP), North Indian (NI), South Indian (SI), Australian (AUS), and South Pacific (SP).

The models produce a high number of False Alarms (FAs), which are storms that do not occur in observations but are produced by the model. Because of this, a filtering technique is employed on the tracks. Storm tracks are converted into a grid format to create storm track density distributions. Using this grid format, the number of FA storms are calculated and used to filter the tracks. A track is filtered by subtracting out the model climatology and the weekly FA climatology. Any point remaining above zero is considered a TC. This method increases skill when trying to predict TC track locations.

3. Results

Skill scores for both TC count and storm track are calculated using the model hindcasts to examine the viability of using these forecasts. Because the hindcasts are over different periods, only the overlapping years of 1999-2012 are used to compare results. Also note that ECMWF has only been available for this study since May, so values for November through April are not yet available, which includes the southern hemisphere (SH) season.

Fig. 2 Heidke skill scores for filtered storm tracks for Week 1 (red) and Week 2 (blue) for the a) Atlantic, b) Eastern North Pacific, c) Western North Pacific, d) North Indian, e) South Indian, f) Australian, and g) South Pacific basins averaged from 1999-2012. The CFSv2 is in solid lines, the CMC in dashed lines, and the ECMWF in dotted lines. The black dashed line at 0.2 is included as a reference point. Note the x-axis change from May-December for NH basins (a-c) to March-February for NI (d) and to July-June for SH basins (e-g).

For the TC count, the number of storms occurring in each week are averaged by ensemble member and compared to observations using an anomaly correlation (AC) which removes the skill from the seasonal cycle. The AC is calculated for each year during the basin's active season and averaged over the 14-year period to create the correlations seen in Figure 1. Because data for the ECMWF were not yet available during the SH season, results for this model are only included for the NH basins. As expected, correlations drop with increased lead, but there is some skill retained in later weeks. CFSv2 and ECMWF tend to outperform CMC with ECMWF having the highest correlations in week 1 and CFSv2 leading in weeks 2-4. The ATL tends to be the exception with low correlations from the CFSv2. Overall, the SI and three Pacific basins (ENP, WNP, and SP) show the highest level of predictability.

In order to quantify the skill in the storm track forecast, the Heidke Skill Score (HSS) is used as a verification tool. The HSS is based on a 2x2 contingency matrix of hits, misses, FAs, and correct null forecasts. A hit is defined as having a forecasted storm within three grid points (or 3°) of an observed storm. This score only gives credit for correct forecasts when a storm is observed, meaning no skill is given for correctly

predicting a lack of activity if a storm is never present. Therefore, months with no activity will have a zero score. Figure 2 shows HSSs for weeks 1 and 2, and Figure 3 shows the scores for weeks 3 and 4. During the earlier leads in weeks 1 and 2, ECMWF outperforms CFSv2 and CMC with scores surpassing 0.4 during the peak in the seasons. Skill is highest for the two NH Pacific basins (ENP and WNP) which is consistent with storm count ACs. The two SH Pacific basins do not show as much skill in TC track location as they do with storm count. The CMC does show some skill in week 1 for the Australian basin which is also consistent with the count correlations. In the longer leads of weeks 3 and 4, the ECMWF levels out with the rest of the models, rarely breaking the 0.2 mark. The WNP and ENP remain the most skillful basins for the ECMWF and CFSv2 with HSSs staying between 0.1 and 0.2.

4. Concluding remarks

The results presented here show that there is skill in predicting TC frequency and track at week 2 and somewhat in week 3. ECMWF shows the most skill in week 1, but by week 2 through 4, both the

Fig. 3 Same as Figure 2 but for Week 3 (orange) and Week 4 (green).

ECMWF and CFSv2 show similar skill. They both tend to outperform the CMC model. Basins with the most predictability in both storm count and track are the ENP and WNP.

These methods will soon be utilized to create a probabilistic forecast that will serve as a first guess for CPC forecasters. Work is ongoing to incorporate both a dynamical-statistical model and forecasts of equatorial waves and other modes into the information provided by the dynamical models. These additional tools will assist in forecasting the longer leads of weeks 3 and 4.

References

Camargo, S. J. and S. E. Zebiak, 2002: Improving the detection and tracking of tropical cyclones in atmospheric general circulation models. *Wea. Forecasting*, **17**, 1152-1162.

3. PROSPECTS FOR IMPROVED UNDERSTANDING, PREDICTION, AND SIMULATION OF CLIMATE VARIABILITY

43rd NOAA Annual Climate Diagnostics and Prediction Workshop

Santa Barbara, California

23-25 October 2018

The Influence of Tropical Forecast Errors on Higher Latitude Predictions

Juliana Dias[1,2] and George N. Kiladis[2]

[1]CIRES, University of Colorado, Boulder, Colorado

[2]NOAA Earth System Research Laboratory, Boulder, Colorado

ABSTRACT

The atmospheric response to variations in tropical latent heating is known to extend well beyond its source region, and therefore it is thought that a reduction of tropical forecast errors in numerical prediction models should also benefit forecasts over the extratropics. This study is based on the hypothesis that a positive correlation between short range tropical forecast skill and later lead times extratropical forecast skill implies that when the tropics is well predicted, subsequent extratropical skill is gained due to a better handling of connections between the two. This relationship between tropical and extratropical predictive skill is evaluated using a conditional skill analysis applied to subseasonal reforecasts from the National Centers for Environmental Prediction Coupled Forecast System (NCEP CFSv2) and the European Centre for Medium-Range Weather Forecasts Integrated Forecast System (ECMWF IFS). These two prediction systems are chosen to contrast the link between tropical and extratropical skill in a model that is known to perform relatively well in the tropics (IFS) to a model with lower tropical skill (CFSv2). It is shown that in both systems there is enhanced or attenuated skill in Northern Hemisphere Week 2-4 forecasts when tropical short range precipitation forecasts are ``good'' or ``poor'', respectively (Fig. 1). This conditional skill is further modulated by both El Nino Southern Oscillation (ENSO) and the Madden and Julian Oscillation (MJO), particularly in the IFS. The results presented here indicate that while midlatitude Week 2-4 predictive skill in both systems would benefit from improvements in Week 1 tropical performance, this improvement would be particularly advantageous for the NCEP system.

The paper has been submitted to *Geophysical Research Letters (GRL)* for publication.

Fig. 1 Solid (dashed) lines show the fractional increase (decrease) in N.H. z500 anomaly pattern correlation (APC) when Day-2 tropical precipitation model forecasts are "good" ("poor") relative to the mean APC. The x-axis correspond to the lead and averaging window used to calculate the APC (Zhu and Wheeler 2014), *e.g.* 1w1w is the APC of the average Week 2 prediction. CFSv2 (ECMWF) fractional APCs are shown in blue (red). CFSv2 (ECMWF) APCs are averaged from October through March from 1999-2010 (1999-2016), using reforecasts from the S2S database.

(Figure 3b from the manuscript submitted to GRL)

Reference

Zhu, H. and M. C. Wheeler, 2014: Seamless precipitation prediction skill in the tropics and extratropics from a global model. *Mon. Wea. Rev.*, **142**, 1556-1569, https://doi.org/10.1175/MWR-D-13-00222.1

_____

Correspondence to: Juliana Dias, CIRES, University of Colorado, and NOAA Earth System Research Laboratory, Boulder, Colorado; E-mail: juliana.dias@noaa.gov

Improve CFS Week 3-4 Precipitation and 2 Meter Air Temperature Forecasts with Neural Network Techniques

Yun Fan[1], Chung-Yu Wu[1], Jon Gottschalck[1], and Vladimir Krasnopolsky[2]
[1]Climate Prediction Center, NOAA/NWS/NCEP
[2]Environmental Modeling Center, NOAA/NWS/NCEP

1. Introduction

The public demand for sub-seasonal forecasts have been steadily increasing in recent years, primarily driven by many industries, such as water management, agriculture, transportation, commerce and insurance etc., to prepare for and reduce risk from damaging meteorological events well in advance. Numerical forecasts on the Week 3-4 time scale are relatively new and to be one of the most challenging and difficult forecast time scales. Past forecast efforts have been focused on the short term weather forecasts out to 7-10 days and operational short term climate outlooks from month to several seasons. There is a clear forecast gap between the Week 3 and 4.

In 2016, the National Oceanic and Atmospheric Administration (NOAA) initiated the efforts to improve its capability for the Weeks 3 and 4 extended range forecasts. Covering this extended-range Week 3~4 forecasts will enable NOAA to provide seamless S2S forecasts to the public for protecting life and property. So far, the Week 3 ~4 forecast skills from direct dynamical forecast models are much lower than the short range forecasts, such as 1~7 days and the Week 1~2 forecasts. In this study, the deep machine learning (*i.e.* Neural Network – NN) techniques are proposed to explore, test, evaluate, and eventually implement a reliable statistical post processing method utilizing model derived fields to improve the original NOAA CFS Week 3-4 time range model precipitation (P) and 2 meter air temperature (T2m) forecasts.

2. Methodology and data

Usually statistical post processing of model outputs is based on a reasonable assumption that there is a relationship between target variables (predictands) (e.g. observed weather and climate elements) and input variables (predictors) (e.g. the NWP model forecast variables). In a very generic symbolic way, this relationship can be written as:

$$Z = M(X); \quad X \in \Re^n, \ Z \in \Re^m \tag{1}$$

where *X* is a input vector composed of model forecast variables or predictors, *Z* is a output vector composed of observed meteorological elements or predictands, *n* is the dimensionality of the vector *X* (or input space), and *m* is the dimensionality of the vector *Z* (or output space). *M* denotes the mapping (relationship between the two vectors) that relates vectors *X* and *Z*.

Since both model forecast variables (predictors) and observations (predictands) contain errors in their data representations, a statistical approximation of the mapping Eq.(1) can be written as,

$$Y = M_s(X) \tag{2}$$

here vector *Y* can be considered as a vector of corrected model variables *X* and M_s isa statistical approximation for the mapping *M* in Eq (1).

The NN techniques are very flexible and convenient mathematical/statistical tools that can allow users to approximate different complicated nonlinear input/output relationships/mappings, by using statistical deep machine learning algorithms (Krasnopolsky 2013). The simplest NN approximations use a family of analytical functions like:

Correspondence to: Yun Fan, Climate Prediction Center, NOAA/NWS/NCEP, 5830 University Research Court, College Park, MD 20740; E-mail: yun.fan@noaa.gov

$$y_q = NN(X, \boldsymbol{a}, \boldsymbol{b}) = a_{q0} + \sum_{j=1}^{k} a_{qj} \cdot t_j; \qquad q = 1, 2, \dots, m \tag{3}$$

where

$$t_j = F(b_{j0} + \sum_{i=1}^{n} b_{ji} \cdot x_i) = \tanh(b_{j0} + \sum_{i=1}^{n} b_{ji} \cdot x_i); \tag{4}$$

here x_i and y_q are components of the input and output vectors X and Y, respectively, $\boldsymbol{a}$ and $\boldsymbol{b}$ are NN weights, n and m are the numbers of inputs and outputs respectively, and k is the number of the nonlinear basis activation function t_j (or hidden neurons). Here the hyperbolic tangent is used as an activation function. Eq. (3) is a mapping, which can approximate any continuous or almost continuous (with final discontinuities) mapping (Krasnopolsky 2013). A pictographic representation of the entire NN was shown in Fig.1 and the connections (arrows) correspond to the NN weights.

To find coefficients a_{qj} and b_{ji} in NN Eq. (3, 4), an error function, E, is created,

$$E = \frac{1}{N} \sum_{i=1}^{N} [Z_i - NN(X_i)]^2 \tag{5}$$

Fig.1 The simplest NN with one hidden layer and linear neurons in the output layer.

where vector Z_i is composed of observed weather elements, and N is the total number of paired records included in the training data set. Then, the error function (5) is minimized to obtain an optimal set of all coefficients a_{qj} and b_{ji} via a simplified version of the procedure known as the back propagation training algorithm. The back propagation algorithm searches for minimum of error (or cost) function in weight space through the steepest (gradient) descent method. It partitions the final total cost to each of the single neuron in the network and repeatedly adjusts the weights of neurons whose cost is high, and back propagate the error through the entire network from output to its inputs.

The data set used for predictors here is the bias corrected Week 3~4 forecast total precipitation (P) and mean 2 meter (T2m) temperature etc., and from the NOAA Climate Forecast System (CFS) (Saha *et al.* 2006, 2014) for period Jan. 01, 1999 to Dec. 31, 2018. The data domain used in this study covers the Conterminous US (CONUS) only, has 1x1 degree spatial resolution and on daily temporal resolution initialized at 4 different times (00Z, 06Z, 12Z and 18Z) per day.

The data set used for correspondent target variables (predictands) are the observed P from the gauge based daily CPC Unified Precipitation Analysis and the observed T2m from the Global Telecommunications System (GTS) based daily maximum and minimum 2 meter temperature analysis (Chen *et al.* 2008, Shi personal communication, Fan *et al.* 2008). Both the above observed P and T2m are converted to two weekly total and two weekly mean, and re-gridded to the same spatial-temporal resolutions as the above predictors.

3. Results

It is well known that the forecasts for the Week 3-4 time scale is one of toughest forecast areas and the skills are very low in general. In this study, an open question wanted to be addressed is if the deep machine learning techniques used here can add additional values to improve the targeted forecasts in the Week 3-4 time scale, when compared with the benchmark multiple linear regression (MLR) tools and also the bias corrected CFS the Week 3~4 forecasts as the inputs (or predictors).

Several tests have been conducted and the results indicate that using ensemble mean from 4 initial time (00Z, 06Z, 12Z and 18Z) the resultant Week 3~4 NN P and T2m forecasts in general are better than the results from using the CFS P and T2m forecasts on the individual initial time. In the following part of this paper, the main focus will be all on a more beneficial NN configuration that the entire NN training and testing at all locations will be done simultaneously in just one same training cycle.
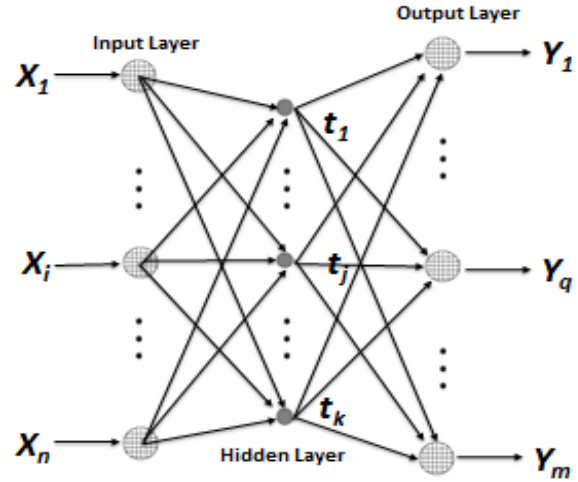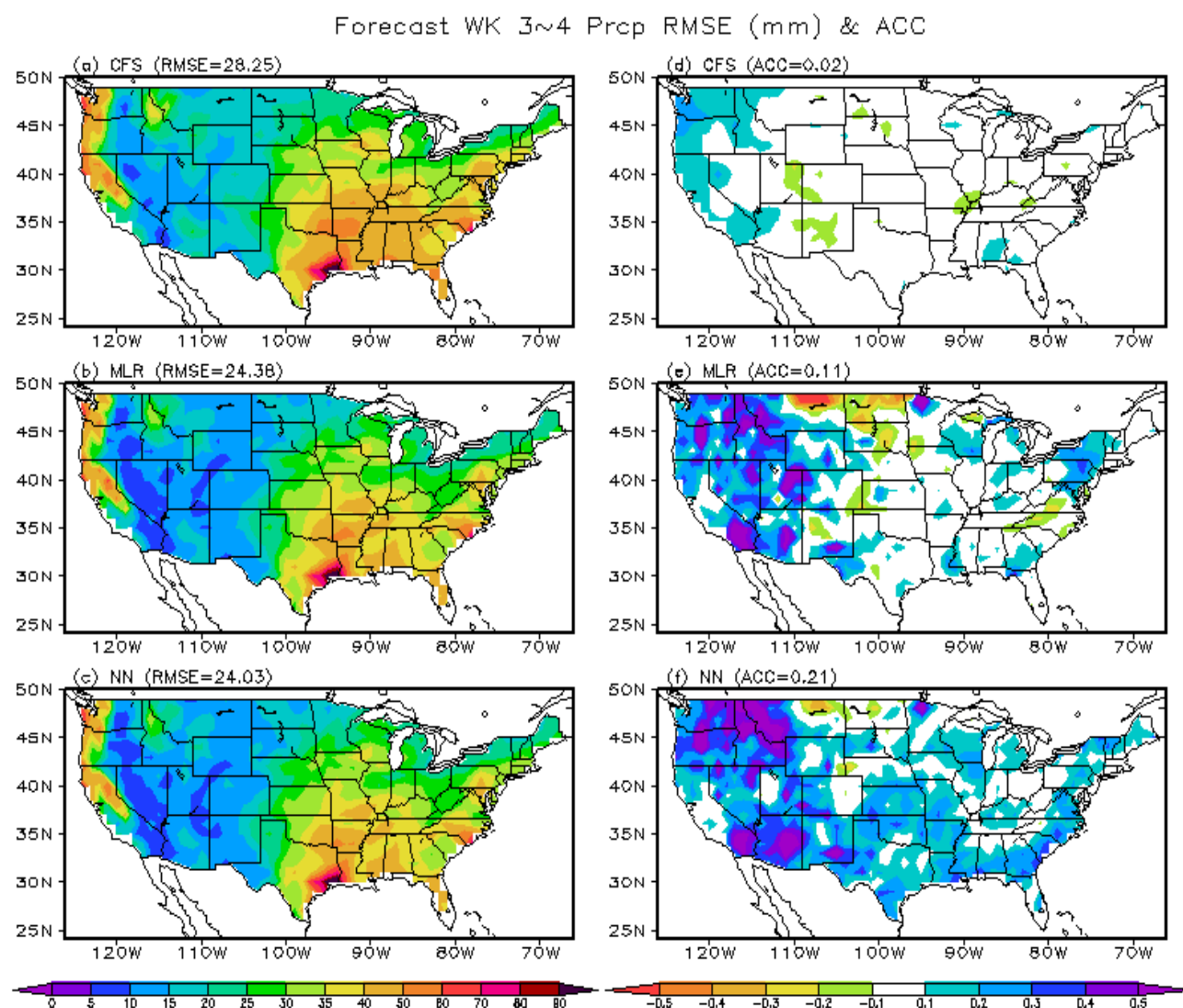
Fig.2 The RMSE and ACC of daily Week 3~4 total P by (a, d) Bias corrected CFS ensemble mean forecasts, (b, e) MLR forecasts, (c, f) NN forecasts, against correspondent observation for period of Jan.1 2017 to Oct. 31, 2018.

Figure 2 shows that overall the root mean square errors (RMSE) and anomaly correlation coefficients (ACC) of the bias corrected ensemble mean CFS P forecasts improved by the NN are better than that of the forecast results obtained from the benchmark multiple linear regression method for most locations. Here the NN training period is from 01/01/1991 to 12/31/2016 (6575 day records). The period of 01/01/2017 to 10/31/2018 (~670 day records) is used as independent verification period. The above results indicate both the NN and the MLR methods improved the bias corrected CFS Week 3~4 P forecasts, especially the forecast skills in quite parts of the western CONUS are encouraging (ACC over 0.4 or 0.5). The NN forecasts show clearly better forecast skills than the MLR forecasts over most locations in term of the RMSE and ACC. It may also indicate that the NN corrections which take into account of the non-linearity, pattern relationship and co-variability impacts are important for improving P forecasts.

Same as precipitation, Figure 3 shows that the root mean square errors (RMSE) and anomaly correlation coefficients (ACC) of the bias corrected ensemble mean CFS T2m forecasts by the NN are better than that of the forecast results obtained from both CFS and the benchmark MLR method for most locations. The above results indicate both the NN and the MLR methods improved the bias corrected CFS Week 3~4 T2m forecasts, especially the forecast skills in large parts of the southwestern CONUS and the eastern half of the CONUS are quite encouraging (ACC over 0.4 or 0.5). The NN forecasts show clearly better forecast skills than the MLR
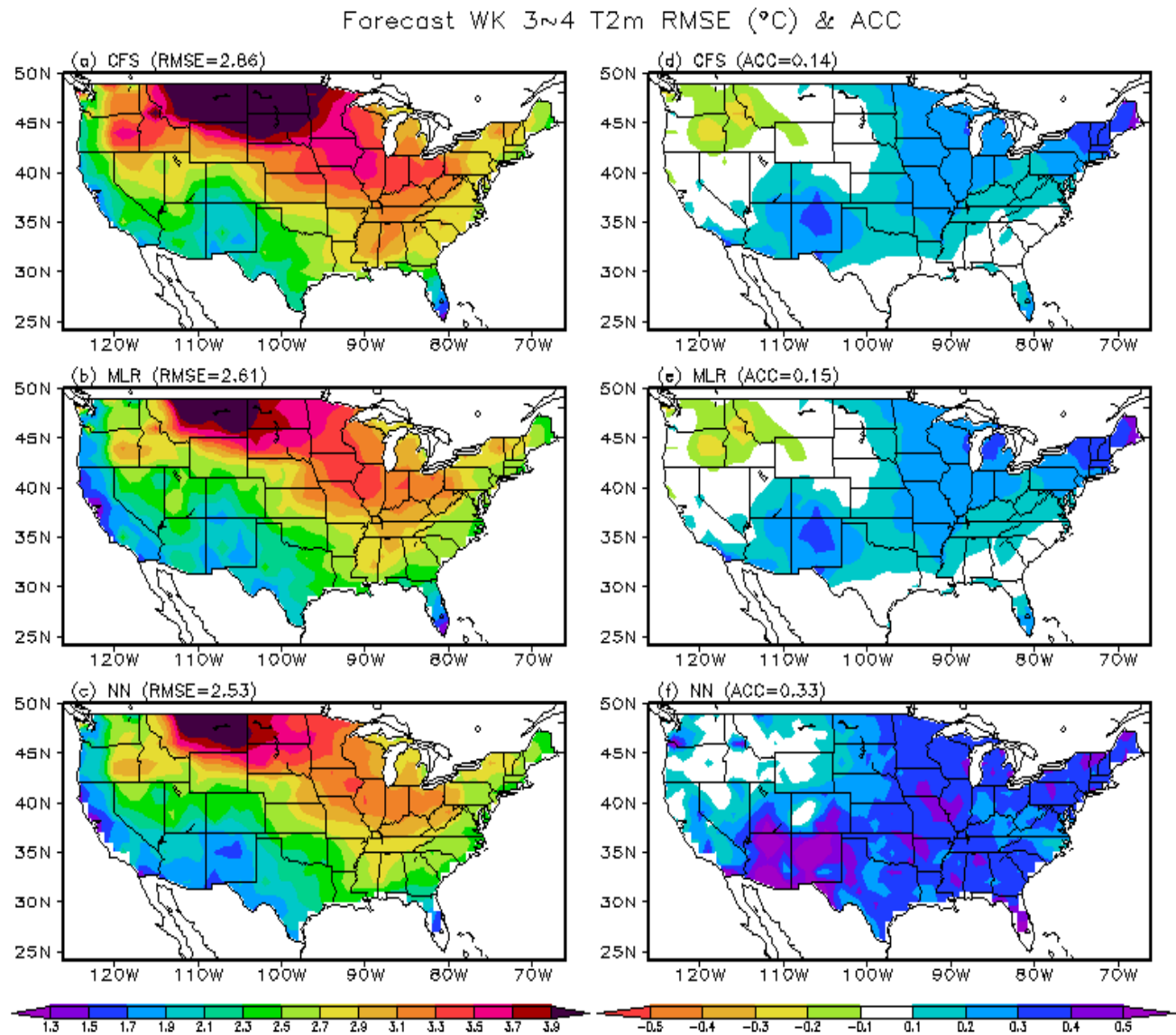
Fig. 3 The RMSE and ACC of daily Week 3~4 T2m by (a, d) Bias corrected CFS ensemble mean forecasts, (b,e) MLR forecasts, (c,f) NN-A forecasts, against daily observation for period of Jan.1 2017 to Oct. 31, 2018.

forecasts over most locations in term of the RMSE and ACC. It may also represent that the impacts of the non-linearity, pattern relationship and co-variability are also very important for the T2m correction.

Checking the overall forecast performance of three (CFS, MLR and NN) forecasts over the 2017-2018 two years verification period, both the MLR and the NN constantly beat the CFS. But the NN forecasts did much better job than the MLR forecasts in many aspects. Figure 4 depicts that the examples of the observed P and T2m anomalies, together with the correspondent Week 3-4 CFS, MLR and NN forecast anomalies. In both cases, the NN techniques show very impressive ability to reverse the wrong P and T2m forecast patterns.

4. Conclusion

In this study, the artificial neural network (deep machine learning) techniques are used to improve the NCEP CFS Week 3~4 P and T2m forecasts. Benefiting from the great advance in machine learning in recent years, the NN techniques show some advantages over traditional statistical methods (*e.g.* multiple linear regressions): such as flexible algorithm that can account for complicated linear and non-linear relationships, spatial dependency and co-variability *etc.*, at the same time is able to handle big data easily. Those learned statistical

patterns and relationships from the NN training processes then are used by the NN to make the corrected forecasts.

Better data representation is very important for the NN training. The EOF analysis indicates that the CFS is very good at predicting large-scale patterns and low frequency variations in observed precipitation, rather than at capturing those highly parameterized and unresolved processes in precipitation. Better data representation may be archived by using ensemble means to increase the explained percentage of the total variance and to reduce noise in the data.

Although the improvement on the Week 3~4 precipitation and T2m is very encouraging, the overall forecast skill (in terms of RMSE and ACC) for the Week 3~4 precipitation and 2m air temperature predictions is still not great. Further studies are definitely needed.

Fig. 4 The observed (Obs), CFS, MLR and NN forecast P (top 4 plots) and T2m (bottom 4 plots) week 3-4 forecast anomalies.

References

Chen, M., W. Shi, P. Xie, V. B. S. Silva, V E. Kousky, R. Wayne Higgins, and J. E. Janowiak, 2008: Assessing objective techniques for gauge-based analyses of global daily precipitation, *J. Geophys. Res.*, **113**, D04110, doi:10.1029/2007JD009132.

Fan, Y. and H. van den Dool, 2008: A global monthly land surface air temperature analysis for 1948–present, *J. Geophys. Res.*, **113**, D01103, doi:10.1029/2007JD008470.

Krasnopolsky, V., 2013: *The application of neural networks in the Earth system sciences. Neural network emulations for complex multidimensional mappings*. Springer, 200 pp.

Saha, S., and Coauthors, 2006: The NCEP Climate Forecast System. *J. Climate*, **19**, 3483-3517, doi:10.1175/JCLI3812.1.

Saha, S., and Coauthors, 2014: The NCEP Climate Forecast System Version 2. *J. Climate*, **27**, 2185–2208. doi:10.1175/JCLI-D-12-00823.1.

Dynamical and Thermodynamical Influences of the Maritime Continent on ENSO Evolution

Tuantuan Zhang[1], Bohua Huang[2*], Song Yang[1, 3, 4*], Junwen Chen[1] and Xingwen Jiang[5]

[1]School of Atmospheric Sciences, Sun Yat-sen University, Guangzhou, China

[2]Department of Atmospheric, Oceanic, and Earth Sciences and Center for Ocean-Land-Atmosphere Studies, George Mason University, Fairfax, Virginia, USA

[3]Guangdong Province Key Laboratory for Climate Change and Natural Disaster Studies, Sun Yat-sen University, Guangzhou, China

[4]Institute of Earth Climate and Environment System, Sun Yat-sen University, Guangzhou, China

[5]Institute of Plateau Meteorology, China Meteorological Administration, Chengdu, China

ABSTRACT

El Niño-Southern Oscillation (ENSO) exerts tremendous influences on the global climate. Through dynamic lifting and thermal forcing, the Maritime Continent (MC) plays an important role in affecting global atmospheric circulation. In spite of the extensive studies on ENSO mechanisms, the influence of MC on the characteristics of ENSO life cycle remains unclear. Our coupled model experiments reveal that the absence of the MC land contributes to a strong ENSO asymmetry and a weakened nonlinear atmospheric response to the combined seasonal and interannual SST variations (*i.e.* the combination mode) that prolongs the warm events, resulting in a reduction of ENSO frequency (see Figs. 1d and 1h). On the other hand, our experiments suggest that the global climate model applied (NCAR CESM) overestimates the MC topographic uplifting effect on ENSO simulation. Overall, this study provides a new physical insight into the nature of the MC influence on ENSO evolution.
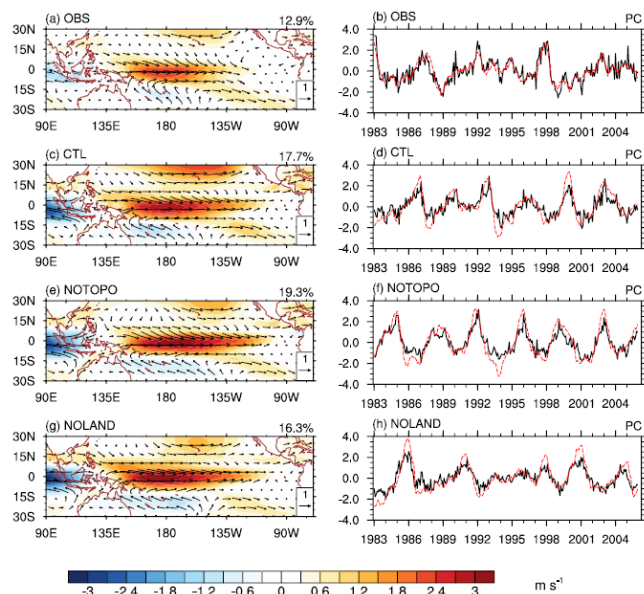
Fig. 1 First combined EOF modes of 925-hPa wind, representing the ENSO mode. Spatial pattern (left) and corresponding principal component (PC) (right) for (a-b) NCEP CFSR, (c-d) CTL experiment, (e-f) NOTOPO experiment (the elevation is reduced to zero over the MC to highlight the topographic effect which is dominated by dynamical lifting), and (g-h) NOLAND experiment (the land surface over the MC is replaced by a layer of seawater of 10-meter depth to show the combined effect of MC topography and thermal forcing), respectively. Shadings in the left panels represent the pattern of zonal wind. In the right panels, solid black lines denote the corresponding PC1s, and dashed red lines denote Niño-3.4 indices.

This work has been published in *Scientific Reports* in 2018.

Reference

Zhang, T., B. Huang, S. Yang, J. Chen, and X. Jiang, 2018: Dynamical and thermodynamical influences of the Maritime Continent on ENSO evolution. *Sci. Rep.*, **8**, 15352, doi:10.1038/s41598-018-33436-5

_____

Correspondence to: Tuantuan Zhang, School of Atmospheric Sciences, Sun Yat-sen University, Guangzhou, China;
E-mail: zhtuant@mail2.sysu.edu.cn

Recent Developments and Ongoing Challenges in Operational Seasonal Prediction at CPC

Stephen Baxter

Climate Prediction Center, NOAA/NWS/NCEP, College Park, MD

1. Introduction

The current seasonal forecast process at NOAA's Climate Prediction Center (CPC) dates back to 1995, and involves issuing temperature and precipitation forecasts for the upcoming 13 three-month overlapping seasons. Statistical and dynamical models are both used to inform the forecast process, with an objective consolidation introduced in 2006 (O'Lenic *et al.*, 2008). Beginning in 2011, forecasts from the National Multi-Model Ensemble (NMME) have been available to forecasters and used heavily in constructing official outlooks. A looming issue for seasonal forecasts, especially temperature, is the role of long-term trends – much of the skill of seasonal temperature forecasts can be attributed to the fact that above-normal temperatures are observed more in real time than over the reference climatology (currently 1981-2010).The first section will detail some recent developments in seasonal forecasting using empirical forecast techniques, as well as post-processing of dynamical guidance and subsequent consolidation across suites of forecast guidance. The second section will discuss research results related to a project that explores how to better handle long-term trends in seasonal forecasts.

2. Developments in the seasonal forecast process

Beginning in 2016 there have been multiple efforts to update the legacy empirical tools suite that forms the basis of the seasonal forecasts. Post-processing and calibration of dynamical model data from the NMME has been prioritized, and most recently a new consolidation of the statistical and dynamical forecast tools has been developed and made available to forecasters in real time.

Since 2017, three new empirical forecast tools have been derived and used in the forecast process:

- ENSO-OCN: This empirical model uses the official CPC Niño 3.4 consolidation forecast as a predictor in a linear regression model. The 15-year optimal climate normal (OCN; running 15-year mean anomaly relative to reference climatology) is removed prior to regression and then added back in the end. The process uses a leave-one-year-out cross validation to generate skill metrics and calibrate the forecast anomalies using linear regression. Probabilistic temperature and precipitation (precipitation data are subject to a square root correction)
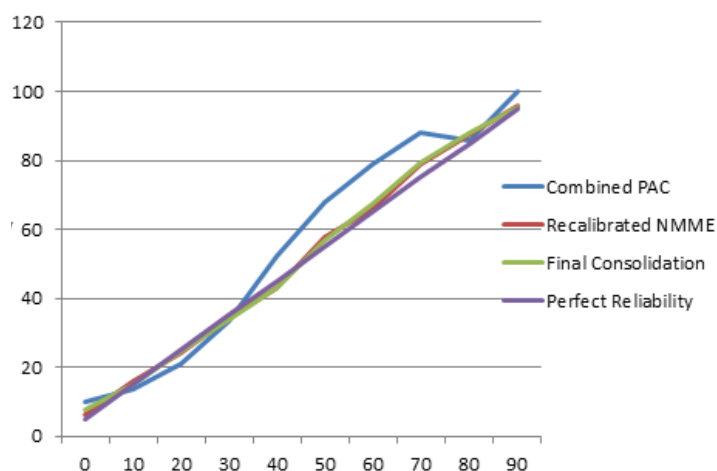
Fig. 1 Reliability diagram of lead-1 temperature forecasts valid for DJF from the NMME and final consolidation forecast over North America from 1981-2018. The blue line shows the reliability of the mean of individually PAC-calibrated NMME models, while the red line shows the reliability after the second pass PAC calibration. The final consolidation and perfect reliability are in green and purple, respectively.

Correspondence to: Stephen Baxter, Climate Prediction Center, NOAA/NWS/NCEP, 5830 University Research Court, College Park, MD 20740; E-mail: Stephen.Baxter@noaa.gov

forecasts are created by using the model's residual error to fit a single Gaussian distribution around the forecast anomaly.

- CCA: The current operational canonical correlation analysis (CCA) used for Niño 3.4 prediction is extended to temperature and precipitation by changing the predictands. This forecast system currently uses sea surface temperature (SST) and sea level pressure anomalies as predictors. A forward-moving hindcast from 1995 onward is used to calculate skill and calibrate using regression. Probability forecasts are likewise calculated by using the unexplained variance from the regression calibration process.

- SST Constructed Analog: A long-time favorite of CPC forecasters, this product has been reinvigorated by using its cross-validated hindcast to generate probabilistic forecasts.

The NMME dynamical model suite is currently calibrated using probability anomaly correlation (PAC; van den Dool *et al.* 2017). In real time this process works by calibrating each model and then averaging across models using equal weights; this can lead to under-confident forecasts (Fig. 1). This issue can be understood

Fig. 2 Loading patterns for the non-stationary trend (PC2, top panel) and AMV (PC6, middle panel) shown as correlations between the PCs and SST anomalies from 1900-2017. The bottom panel shows the PC times series over the 1900-2017 period.

intuitively by considering two models – one that is skillful and one that is not skillful. The probabilities from the model with no skill are damped to climatology in the PAC calibration process; however, some portion of the probability anomalies from the skillful model is retained. In this case the forecaster would not want to consider the skill-less model, however it has the effect of further damping the skillful model when included in the final, averaged product. To address this as part of the new consolidation process, the NMME constituent model forecasts are combined by weighting according to their PAC coefficients as a function of grid point. This combination is then subject to a second pass PAC calibration, thus eliminating the under-confidence. The statistical models are likewise combined into a statistical model constituent. The NMME and statistical combinations are then consolidated by weighting based on PAC coefficient and calibrating over the entire hindcast – this yields the final consolidation that can serve as a first guess for the official forecast. This process continues to update in real time, so model biases and the PAC coefficients are based on the maximum amount of available data.

3. Ongoing challenges – Long-term trends

An ongoing challenge in seasonal climate forecasting is how to optimally handle long-term trends. We know, for instance, that CPC's seasonal temperature forecast skill is largely due to observed long-term warming trends (*e.g.* Peng *et al.*, 2012). At first glance this might seem to indicate that beyond the linear trend there is little seasonal forecast skill. However, the apparent skill in predicting interannual and even decadal variability can be muted by the dominance of long-term trends in forecasts and observations. Therefore separating secular warming from decadal and interannual climate variability is potentially important for short-term climate
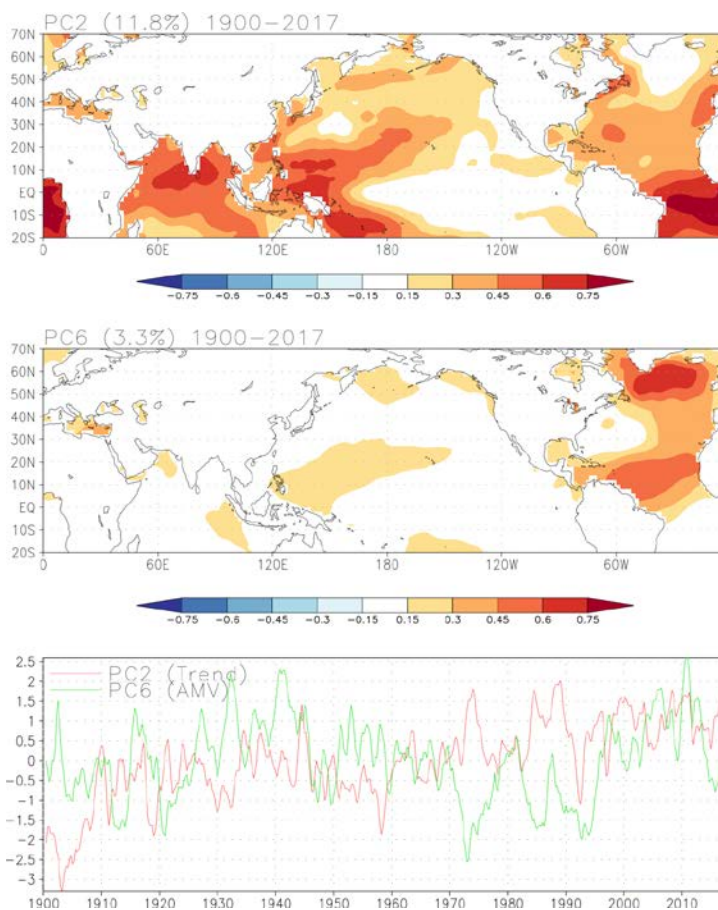
prediction. Furthermore, distinguishing between climate variability as a function of time scale can provide an on-the-fly attribution of forecast and observed seasonal climate anomalies.

Historically CPC has incorporated trends through the OCN tool, which takes advantage of the fact that the fixed 30-year WMO climatology is not likely the ideal 'first guess' for seasonal temperature and precipitation. One can test for the ideal number of preceding years, which will varying seasonally and spatially, but a fixed 15-year OCN is a simple and reasonable method currently used.

An ongoing research project has attempted to deal with the issue of trends by decomposing seasonal SST data following Guan and Nigam (2008). A rotated, extended EOF analysis of 20th century SST anomalies yields principal components (PCs) that correspond

Fig. 3   Anomaly correlation between the temperature hindcast and observations where anomalies are with respect to a trailing 15-year climatology. Left (right) column is for lead-3 DJF (MAM) forecasts. From top to bottom rows: forecast using trend PC as predictor, forecast using AMV PC as predictor, forecast using the leading 10 PCs as predictors.

to variability ranging from ENSO to the secular trend. Preliminary results showed that using the trend PC or a linear trend line was better than the OCN-15 at reconstructing seasonal temperature anomalies. Adding a PC corresponding to Atlantic multidecadal variability (AMV) closed the gap between the linear trend line and the SST PC comprising the secular trend. The overarching idea is that it would be desirable to have a small subset of physically-grounded time series (*e.g.* derived from SST) through which one might attribute climate anomalies to variability on decadal time scales or longer.

These preliminary results, however, were data dependent reconstructions, and so an experiment was devised that would test these PCs in a predictive capacity. Starting in 1980, the extended, rotated EOF analysis is computed for 1900-1980 using ERSSTv5, and various PCs are used as predictors. Temperature and precipitation data (GHCN+CAMS and CPC's gauge-based reconstruction, respectively) from 1950-1980 is used in a linear regression model to generate a forecast for seasons in 1981, using no future data. This process is repeated for each year from 1981 to 2017 resulting in a forward moving hindcast. Figure 2 shows the loading patterns associated with the long-term trend and AMV and their PC time series. Hindcast skill is calculated using anomaly correlation coefficients, and results are compared to the skill of an OCN-15 forecast. This process is repeated using a fixed climatology (anomalies relative to fixed mean and zeroed out in correlation calculation), a trailing 30-year WMO climatology (*i.e.* using 1951-1980 climatology from 1981-1990), and a trailing 15-year climatology (zeroing out OCN).

To emphasize the empirical model skill relative to OCN, Figures 3 and 4 show the skill of three reconstructions (trend alone, AMV along, and the leading 10 PCs) relative to a trailing 15-year climatology, for each of the four meteorological seasons. The AMV component seems to yield skillful temperature forecasts relative to OCN over the Plains during JJA and over much of southern Canada during SON. The Trend PC provides little value relative to OCN in this framework with marginal and mixed temperature results. The role
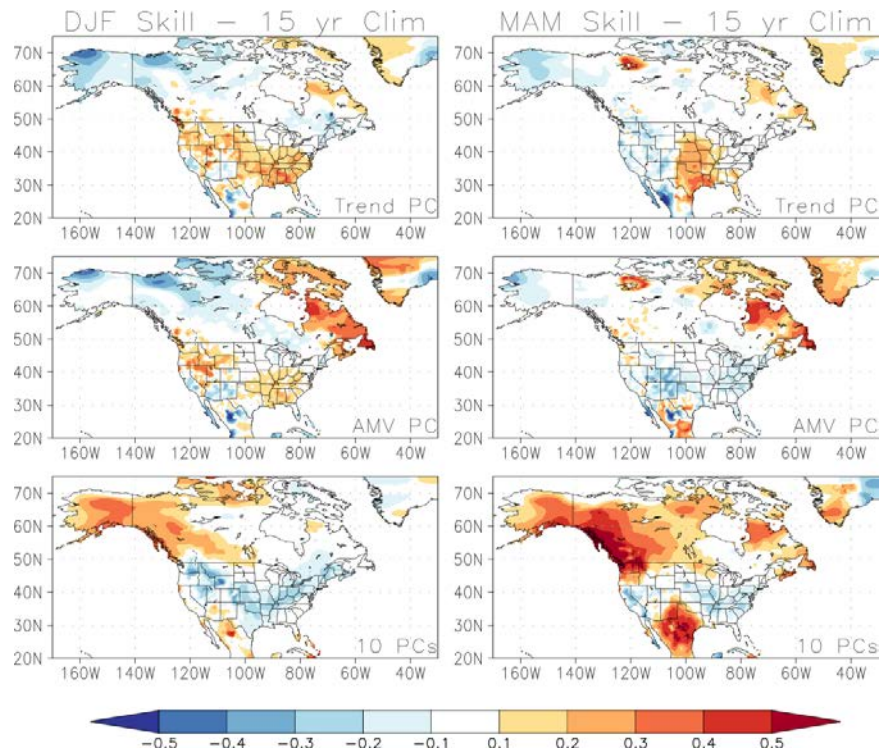
of ENSO can be seen in the skill of temperature forecasts using the 10 leading PCs (ENSO variability is contained in three to four of the leading patterns), especially during the transition seasons. The results with respect to precipitation are difficult to interpret (not shown). The skill with respect to a trailing 15-year climatology is surprisingly high, but this might point to the relative futility of OCN-based precipitation forecasts, at least as compared to temperature forecasts. Precipitation climatologies are more stationary than temperature, and these results may suggest that longer climate base periods are more appropriate for precipitation forecasts.

Overall the results of the forward-moving hindcast experiment are mixed – OCN proves difficult to beat on

Fig. 4 Same as Fig. 3, except for JJA (left column) and SON (right column).

independent data for temperature forecasts, but OCN may be ill-advised for precipitation forecasts. Some ideas for future directions include using a Hadley-OI blended dataset from 1900-present, which would be more akin to the Guan and Nigam (2008) method. Because ERSST uses recent data in its reconstruction of past data, it may not be as well suited to analyses targeting variability on decadal or longer time scales. The forward-moving approach is intentionally restrictive, but even outside of a prediction framework this analysis can be useful for monitoring and attribution of SST anomalies and associated climate impacts.

References

van den Dool, H., E. Becker, L. C. Chen, Q. Zhang: 2017. The probability anomaly correlation and calibration of probabilistic forecasts. *Wea. Forecasting*, **32**, 199-206.

Guan, B., and S. Nigam: 2008. Pacific sea surface temperatures in the Twentieth Century: an evolution-centric analysis of variability and trend. *J. Climate*, **21**, 2790-2809.

Peng, P., A. Kumar, M. Halpert, and A. Barnston: 2012. An analysis of CPC's operational 0.5-month lead seasonal outlooks. *Wea. Forecasting*, **27**, 898-917.

O'Lenic, E., D. Unger, M. Halpert, K. Pelman: 2008. Developments in operational long-range climate prediction at CPC. *Wea. Forecasting*, **23**, 496-51; 1024.

Uncertainties in the El Niño Response of Precipitation over the US West Coast

Mingyue Chen and Arun Kumar

Climate Prediction Center, NCEP/NWS/NOAA

1. Introduction

In this study, the possible reasons why the seasonal mean precipitation prediction skill over the US west coast during December-January-February (DJF) is low in the National Centers for Environmental Prediction (NCEP)'s Climate Forecast Systems version 2 (CFSv2) are explored. The analysis is based on the hindcasts and real-time forecasts from the North American Multi-Model Ensemble (NMME, Kirtman et al. 2014). We first examine how well basic features of the DJF precipitation in terms of its climatological mean, total interannual variability, and the mean response to ENSO SST are predicted across each of seven models in the NMME. We also assess the anomaly correlation skill and the signal-to-noise ratio (SNR) to validate whether the prediction skill of DJF precipitation over the west coast is low in general across the models. Then, we analyze the west coast precipitation response in individual models to anomalous ENSO SSTs during individual El Niño events to investigate to what extent the response during individual events differ from the composite response. Specially, it can be approached in two ways: 1) by analyzing the consistency of precipitation responses across El Niño events in a single model, and thereby, examine the influence of ENSO SST flavor and possible non-linearity in the response; and 2) by analyzing the consistency of precipitation responses across seven models for a specific El Niño event to examine if the consistency improves as the amplitude of El Niño events gets larger. In the final analysis, we also analyze the DJF precipitation for the regions of US southeast coast with the same ensemble forecasts from the same set of models. Over the southeast coast the precipitation prediction skill is higher, and therefore, provides a contrasting case study to the analysis over the west coast of the US.

2. Results

The results show that the simulated north-south variations in DJF precipitation climatology and its interannual variability, together with the linear response to ENSO is similar in generally to that in observations, but there are differences in details, particularly in the amplitude (Fig. 1). However, the prediction skill across all the models is unanimously low and is in close proximity of the skill for the CFSv2 (Fig. 2). It is noted that there does not seem to be a correspondence between the linear ENSO response and skill that be possibly due to non-linearity in the precipitation response to ENSO, sampling issues, or the model biases. Further, the SNR is low for all models, and there is a lack of correspondence between SNR
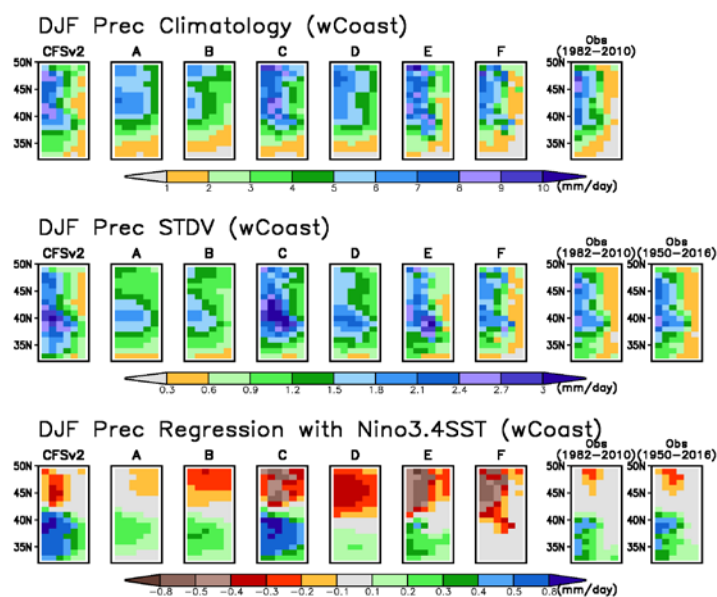
Fig. 1 The DJF Precipitation climatology (top row), standard deviation (middle row), and linear regression to Nino 3.4 SST (bottom row) for seven models (CFSv2, and models A, B, …and F) in the NMME (Kirtman et al. 2004) and observations (Chen et al. 2002) over the US west coast (wCoast). The US west coast area is aligned to an 8x21 degree longitude/latitude rectangle. The unit is mm/day for the climatology and standard deviation and is mm/day of unit standard deviation of Niño 3.4 SST index for the regression.

Correspondence to: Mingyue Chen, Climate Prediction Center, NCEP/NWS/NOAA, 5830 University Research Court, College Park, MD 20740; E-mail: Mingyue.Chen@noaa.gov

and skill due to the biases in the model, small ensemble size, and the influence of sampling over short verification time period (Fig. 2).

The analysis comparing individual El Niño events and in individual models (Fig. 3) highlights the basic features: 1) the observed seasonal mean, which is a combination of both the response and the contribution from the unpredictable internal variability, clearly indicates that the event-to-event variability is much larger than the model ensemble mean response; 2) the consistency is better for stronger El Niño events, particularly over Southern California (SCA) where all models have above normal precipitation (except for the model A in 1982); 3) for some models the response is very consistent across different El Niño events. In contrast, the response for some other models shows much stronger non-linearity; 4) comparing precipitation response across models for the same El Niño events does not lead to definitive conclusions; 5) the spatial pattern of the El Niño composite, in general, has a good resemblance with the linear regression pattern indicating that non-linaerity in the response may not be a dominant factor; 6) for the strongest El Niño event of DJF2015/16, the precipitation response in the NMME ensemble mean has a good consistency with positive anomalies over the SCA, where the observed anomalies were negative.

In contrasting to the case over the west coast, the precipitation ENSO response over the US southeast coast (seCoast) shows lower variability and similar amplitude of response indicating larger SNRs, consequently, the higher skills for the precipitation prediction. Further, the same models that had difficulties in replicating interannual precipitation variability along wCoast have a better performance in seCoast. The possible dynamical basis for differences in SNR for the precipitation variability along the wCoast and the seCoast is that precipitation variations over swCoast (seCoast) is less (more)
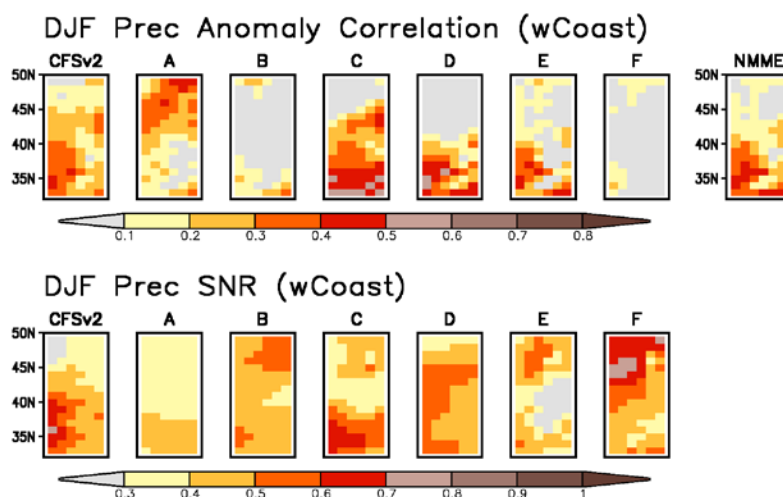
Fig. 2 The DJF precipitation correlation skill and SNR for the seven models over the wCoast. Correlations (SNR) below 0.1 (0.3) are not shown. The area average AC for each model and NMME (going from left to right) is 0.24, 0.22, 0.00, 0.26, 0.14, 0.16, -0.02, and, 0.20 and the area average SNR is 0.46, 0.38, 0.46, 0.47, 0.48, 0.38, and 0.52.
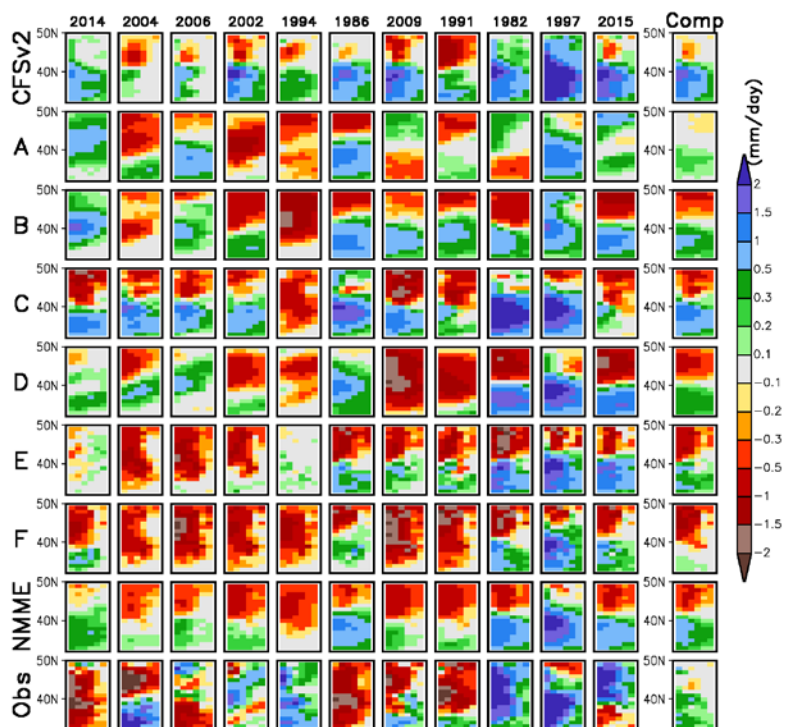
Fig. 3 The DJF precipitation ensemble means during each of 11 El Niño events arranged from the weak to strong event (from the left to right columns) for each models, multi-model average (labeled as NMME), and observation over the US west coast. Unit is mm/day.

constrained by ENSO SSTs and is influenced more (less) by internal variability resulting in lower (higher) SNR. A lower (higher) SNR, in turn, will result in smaller (larger) skill in seasonal prediction.

3. Concluding remarks

In summary, various analysis approaches based on the extensive dataset in the NMME from seven seasonal forecast models show that low skill in predicting seasonal mean precipitation along the US west coast is due to inherent predictability associated with a low signal-to-noise (SNR) regime. In contrast, for the same dataset, analysis over the US southeast presents a different paradigm of a higher SNR regime having a higher prediction skill. Another side of the analysis is that it did not provide answers to the questions like the sensitivity to different SST flavors in the ENSO response (non-linearity) for the precipitation over the US west coast, even though the analysis was based on a large multi-model dataset such as NMME. Such difficulty in itself may indicate it is in a low SNR regime, and a higher level of effort is required for extracting the signal above the noise and drawing robust inferences gets harder, for example, requiring larger ensemble sizes.

References

Kirtman, B. P., and Coauthors, 2014: The North American Multimodel Ensemble: Phase-1 seasonal to interannual prediction; phase-2 toward developing intraseasonal prediction. *Bull. Amer. Meteor. Soc* ., **95**, 85-601, doi: 10.1175/BAMS-D-12-00050.1.

Chen, M., P. Xie, J. E. Janowiak, and P. A. Arkin, 2002: Global land precipitation: A 50-yr monthly analysis based on gauge observations. *J. Hydrometeor*, **3**, 249-266.

How Well Do Climate Models Simulate the Internal Variability in Arctic Air-Sea Ice Trend?

Pengfei Zhang[1, 2] and Qinghua Ding[2]

1University of California, Los Angeles, California
2University of California, Santa Barbara, California

1. Introduction

It has been found with high confidence that human-induced climate warming drove the Arctic sea ice decline over recent several decades (IPCC 2013). It is very likely that the summer Arctic will be nearly sea ice free around 2040 based on model projections (Overland and Wang 2013). However, climate models are significantly underestimate the observed sea ice melting rate (*Stroeve et al.* 2012). This underestimation largely limits the confidence of the future projection of the sea ice change in climate models.
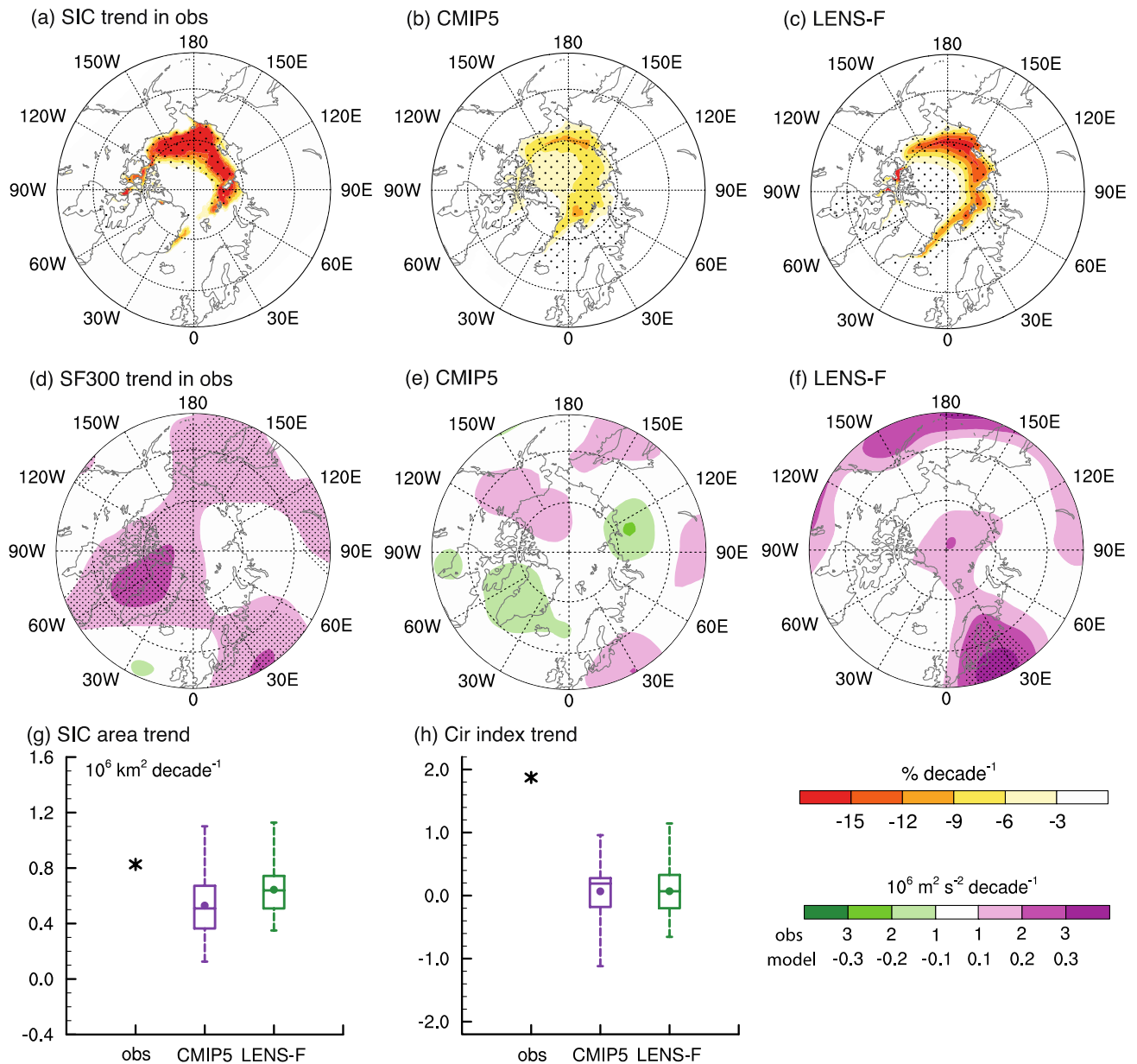
Recent studies revealed that both natural variability and anthropogenic warming modulate Arctic sea ice decline (Kay *et al.* 2011; Day *et al.* 2012; Swart *et al.* 2015). Especially, the significant contribution of atmospheric internal variability has been emphasized (Ogi and Wallace 2012; Ding *et al.* 2017). It found that the variability of minimum Arctic sea ice in September is highly related to JJA surface anticyclonic circulation anomalies (Ogi and Wallace 2012), which have vertical coherent structure from the surface to the upper troposphere (Ding *et al.* 2017). This atmospheric internal variability, in consort with warming directly induced by the external anthropogenic radiation forcing, contributes to the sea ice decline in recent decades (Ding *et al*. 2014). However, it is still unclear that if this internal air-sea ice linkage can be well represented in climate models.

2. Evaluation of model simulation

In this study we evaluated the role of internal air-sea ice linkage in the simulation of sea ice trend in the forced run of 27 Coupled Model Intercomparison Project 5 (CMIP5) models and Large Ensemble (LENS) project output using the CAM5-BGC/CESM model (The Community Earth System Model with Community Atmosphere Model 5.0 as its atmospheric component uses active biogeochemistry). The results show that the observed tropospheric circulation pattern centered over northern Greenland is biased shifted to Chukchi Sea and the neighboring Arctic Ocean in climate models, which impact the sea ice export out of Arctic Ocean via kinematic effect. Second, the air-sea ice linkage induced by the internal variability can be simulated by CAM5-BGC/CESM. This internal variability significantly contributes to the large spread of sea ice melting rates in forced climate model simulations. Stream function reasonably presents the internal circulation changes in the context of anthropogenic warming. Third, the underestimation of sea ice decline in the ensemble mean of model simulation is due to the atmospheric internal variability induced sea ice decline is mostly averaged out in the mean (see Fig. 1). The model simulations with an observation-like anticyclonic trend and anthropogenic forcing could reproduce a realistic sea ice decline.

3. Concluding remarks

Our results suggest that the model performance in Arctic atmospheric circulation needs improvement to advance the simulation of the internal air-sea ice linkage. The contribution of internal variability to sea ice melting cannot be neglected when we estimate the future amount of Arctic sea ice loss. A model with a well-represented internal variability, such as CESM-CAM5-BGC, is the precondition to get a reasonable projection of Arctic sea ice change.

_____

Correspondence to: Pengfei Zhang, University of California, Los Angeles, CA 90095, and University of California, Santa Barbara, CA 93106; E-mail: zpengfei@ucsb.edu

Fig. 1 (a-c) Arctic September sea ice trend (% per decade) in 1979-2016 in observation (a), CMIP5 (b) and LENS-F (c). (d-f) Same as the (a-c) but for the 300hPa stream function (units: 10^6 m^2 s^{-2} per decade. It is noted that the interval for observation is the ten times of that in model ensembles). (g) box plot of the trend of sea ice area (million km^2 per decade) in observation (black star), CMIP5 27 models (purple box) and LENS-F 40 runs (green box). The box values from bottom to top are the minimum, first quartile, median, third quartile and maximum of the CMIP5 27 model runs and LENS-F 40 runs, respectively. The dots denote the ensemble mean of CMIP5 and LENS-F, respectively. (h) Same as (g) but for the 300hPa stream function. The values in (g) were reversed to emphasize the sea ice loss.

References

Day, J. J., and Coauthors, 2012: Sources of multi-decadal variability in Arctic sea ice extent. *Environ. Res. Lett.*, **7**, 0340111, doi:10.1088/1748-9326/7/3/034011

Ding, Q., and Coauthors, 2014: Tropical forcing of the recent rapid Arctic warming in northeastern Canada and Greenland, *Nature*, **509**, 209-212, doi:10.1038/nature13260.

Ding, Q., and Coauthors, 2017: Influence of high-latitude atmospheric circulation changes on summertime Arctic sea ice. *Nat. Clim. Change*, **7**, 289–295, doi:10.1038/nclimate3241.

IPCC, 2013: *Climate Change 2013: The Physical Science Basis.* Cambridge University Press, 1535 pp.

Kay, J. E., and Coauthors, 2011: Inter-annual to multi-decadal Arctic sea ice extent trends in a warming world. *Geophys. Res. Lett.*, **38**, L15708, doi:10.1029/2011GL048008.

Ogi, M., and J. M. Wallace, 2012: The role of summer surface wind anomalies in the summer Arctic sea ice extent in 2010 and 2011. *Geophys. Res. Lett.*, **39**, L09704, doi:10.1029/2012GL051330.

Overland, J. E., and M. Wang, 2013: When will the summer Arctic be nearly sea ice free? *Geophys. Res. Lett.*, **40**, 2097-2101, doi:10.1002/grl.50316.

Stroeve, J. C., and Coauthors, 2012: Trends in Arctic sea ice extent from CMIP5, CMIP3 and observations, *Geophys. Res. Lett.*, **39**, L16502, doi:10.1029/2012GL052676

Swart, N. C., and Coauthors, 2015: Influence of internal variability on Arctic sea-ice trends, *Nat. Clim. Change*, 5, 86–89, doi:10.1038/nclimate2483.

Investigations on Moisture Transports, Budgets and Sources Responsible for the Decadal Variability of Precipitation in Southern China

Hu Yamin[1], Si Dong[2], and Liu Yanju[2]

[1]*Guangdong Climate Center, Guangdong Province, Guangzhou, China*
[2]*National Climate Center, Beijing, China*

1. Introduction

Hydrological cycle plays an important role in the interaction processes among elements of climate systems. It also acts as a major source for energy and precipitation in the global climate system, so the hydrological cycle can exert great influences on climate system variabilities (Webster 1994). Hence, the hydrological cycle is the major concern in various international projects, such as the World Climate Research Program (WCRP), the Global Energy and Water Cycle Exchange Project (GEWEX) and the Climate Variability and Predictability (CLIVAR).

Moisture transports influencing China mainly include the following routes: southwesterly transport originating from the Somali Jet via the Arabian Sea-Indian Ocean-Bay of Bangle (BOB); southeasterly advection from the southern flange of the western Pacific subtropical high; cross-equatorial flow around 105°E via the South China Sea (SCS) and regions around; water vapor transport from mid-high latitudes. These moisture transports can be traced back to the western Pacific, South China Sea, Arabian Sea, and Indian Ocean (Ding 1994; Li 1999). Droughts and/or floods tend to occur in tandem with anomalous moisture transports and resultant moisture budgets from diverse sources (Xie *et al.* 2001; Sun and Ding 2002; Zhou *et al.* 2005; Liu *et al.* 2009). Under global warming, obvious decadal shifts of summertime precipitation in southern China have been reported. Accordingly, some studies investigated the precipitation variabilities in the Yangtze River Valley (YRV) (Xie *et al.* 2002; Zhuo *et al.* 2006) and South China (Lü *et al.* 1998; Shi and Ding 2000; Chang *et al.* 2006) from the perspective of moisture transport qualitatively via the Eulerian scheme. Additionally, many recent studies quantitatively analyzed the water source of precipitation in Europe and North America via the Lagrangian scheme (Stohl and James 2004; Brimelow and Reuter 2005; Roberge *et al.* 2009; Brubaker *et al.* 2001; Stohl *et al.* 2008). Such Lagrangian scheme were also employed in the investigations on heavy rainfall in southern Anhui (Su *et al.* 2010), enhanced precipitation in North China (Ma *et al.* 2008), extreme precipitation in eastern China during 2007 (Chen *et al.* 2011), and rainstorms occurring in the Huai-River (Jiang *et al.* 2011) during 2007. Similar studies paid particular attention to specific cases or precipitation processes of short duration. In a comprehensive way, Jiang *et al.*'s study (2013) traced enormous air particles to
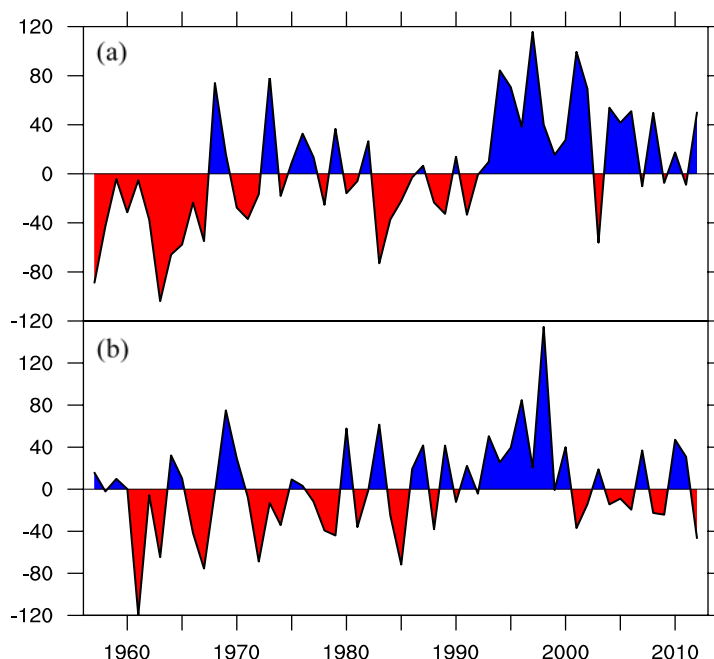
**Fig. 1** Summer moisture budget anomalies (10^6kg/s) during 1957-2012 in South China (a) and the Yangtze River Valley (b).

Correspondence to: Hu Yamin, Guangdong Climate Center, Guangdong Province, Guangzhou 510080, China;
E-mail: huym@grmc.gov.cn

provide climatological features of moisture transport from various sources to the mid-low reaches of the Yangtze River during Mei-Yu period in the past three decades. Pertinent results render a quantitative comparison between the water source of the Mei-Yu period in the YRV and precipitation periods in the northern part of the Huai-River (Yang *et al.* 2014).

2. Variability of atmospheric hydrological cycle in Asian monsoonal region

Changes in precipitation are closely associated with the variability of atmospheric hydrological cycle, in which the moisture budget change is one of the most direct contributors. Figure 1 displays the moisture budget variation derived by the NCEP/NCAR reanalysis in South China (a) and the YRV (b). Figure 1 shows generally in-phase evolution features between the moisture budget and precipitation in both regions, with respective correlation coefficients of 0.59 and 0.66 at the 0.01 significance level. On decadal-interdecdal scales, moisture budgets in South China experienced a phase transition from positive phase to negative phase in the mid-1970s, and a reverse process in the early 1990s. As indicated in Figure 1b, the moisture balance in the YRV is under positive phase during 1980s-1990s, followed by a negative phase after 2000. Such variations in moisture budget are in good agreement with the precipitation changes temporally, with the positive balance corresponding to above-normal precipitation and the negative value corresponding to below-normal precipitation. So, anomalies in precipitation of southern China may be related with the moisture balance shifts.

To evaluate the relative contributions of water supply from each side to moisture budget changes, Figure 2 presents the temporal evolution of meridional and zonal moisture budgets in both regions. Clearly, no matter for South China and the YRV, an anti-phase relationship exists between zonal and meridional moisture budgets, *i.e.* positive moisture residual from zonal sides accompanied by deficient moisture on meridional sides, and vice versa. In Fig. 2, variations of meridional moisture budgets in both regions match reasonably well with the total moisture budgets. Of particular note is that the meridional moisture budget turned into a regime with significantly positive balance in the early 1990s (Fig. 2b) and the meridional component for the YRV stepped into a deficient period (Fig. 2d). These transitions are explicitly consistent with the total moisture budget in both regions, indicating that the total moisture budgets in these regions are largely controlled by the meridional components.
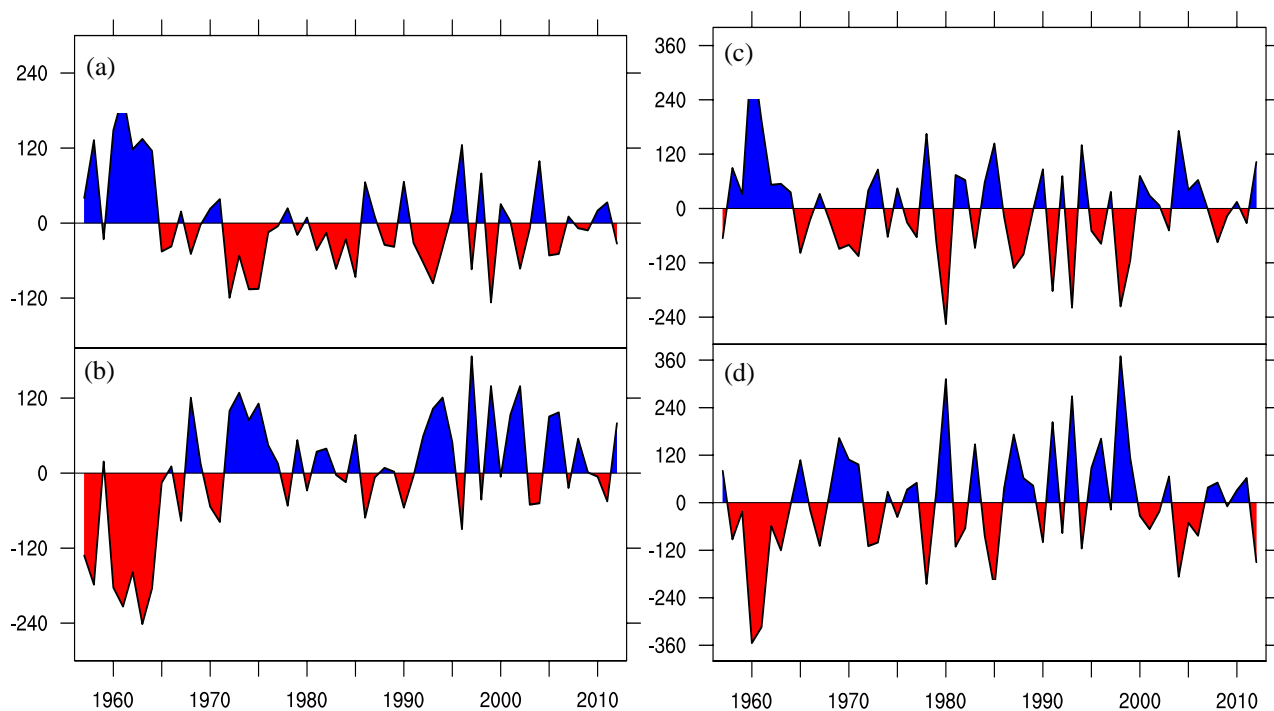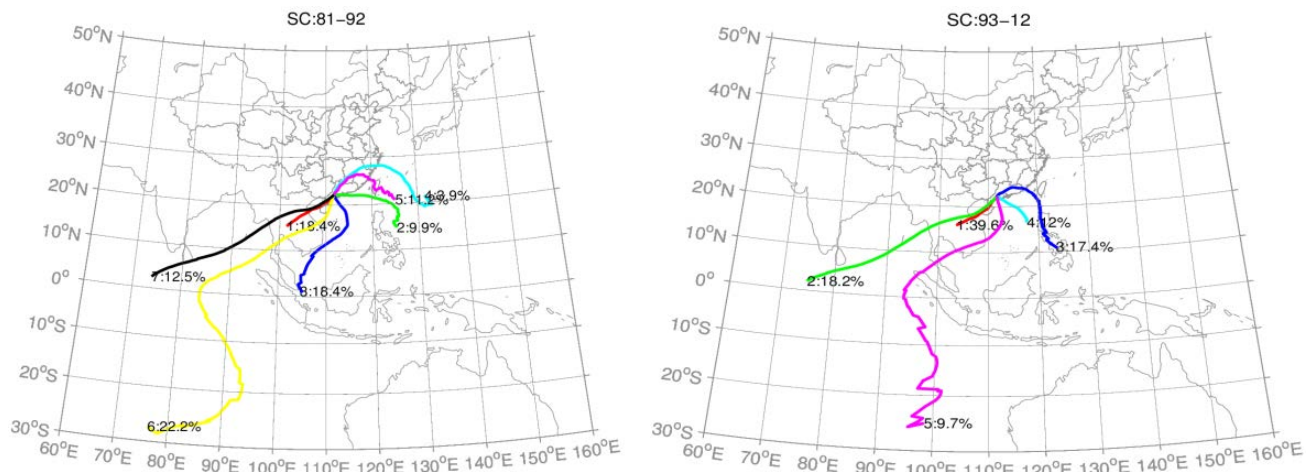

Fig. 2 Anomalies of zonal (a) and meridional (b) moisture budgets (10^6kg/s) in South China during 1957-2012. (c) and (d) same as (a) and (b), but for the Yangtze River Valley.
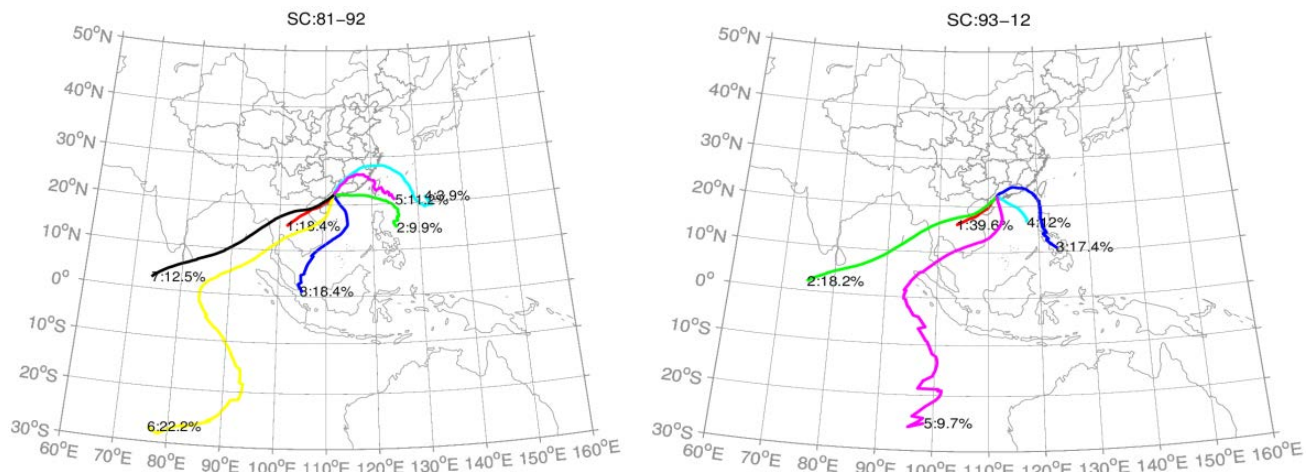
In this study, particular attention is paid to moisture budget variations from four sides in both two regions during the latest precipitation transition. As shown in Fig. 3a, after 1990s (difference between 1993-2012 and 1981-1992), moisture inflows increased by 77.1 * 10^{6}kg/s and 21.3 * 10^{6}kg/s via southern side and western side respectively. While, losses of moisture increased by 38.9 * 10^{6}kg/s and 6.5 * 10^{6}kg/s via the northern side and the eastern side respectively. Consequently, the positive moisture balance in South China after 1990 was mainly contributed by the increased meridional inflow from the southern side, and secondly contributed by the increased zonal inflow from the western side. For the YRV after 2000s (Fig. 3b, difference between 2000-2012 and 1981-1999), the moisture inflow via southern side decreased by 62.4 * 10^{6}kg/s, while the moisture inflow increased by 3.7 * 10^{6}kg/s from the western side. The loss of moisture via northern side increased by 11.1 * 10^{6}kg/s, while the outflow via the eastern side decreased by 49.1 * 10^{6}kg/s. Accordingly, the moisture deficiency in the YRV after 2000 mainly resulted from sharply decreased inflow via southern side.

Fig. 3 Moisture budget changes from four sides for South China around 1992/1993 (top) and the Yangtze River Valley around 1999/2000 (bottom). Directions of the arrows indicate the inflow and outflow; blue (red) denote moisture increase (decrease).

Increased outflow via northern side provide the secondary contribution to the dry condition.

3. Quantitative evaluations of relative moisture contributions from different sources

As displayed in Fig. 4a, during the regime with deficient precipitation in South China (1981-1992), seven routes can be detected. If clustered by above-mentioned five sources, two routes are associated with the channel from the Arabian Sea-Indian Peninsula-BOB, and their combined contribution reaches 34.7%; another two routes are linked with the channel from Indo-China Peninsula-SCS and around, and they contribute 36.8% to total moisture transport; three routes originate from the western Pacific with their joint contribution about 28.5%. During the regime with abundant precipitation in South China (1993-2012), 5 routes can be identified (Fig. 4b).


Fig. 4 Moisture transport paths during deficiency regime (left, 1981-1992) and abundance regime (right, 1993-2012) in South China and their contributions labeled on them.

Two belong to the channel from the Arabian Sea-Indian Peninsula-BOB, and their total contribution is 27.9; another two come across Indo-China towards the SCS and around with their joint contribution about 51.6%; the other one originate from the western Pacific, and it provides about 17.4% of total moisture.
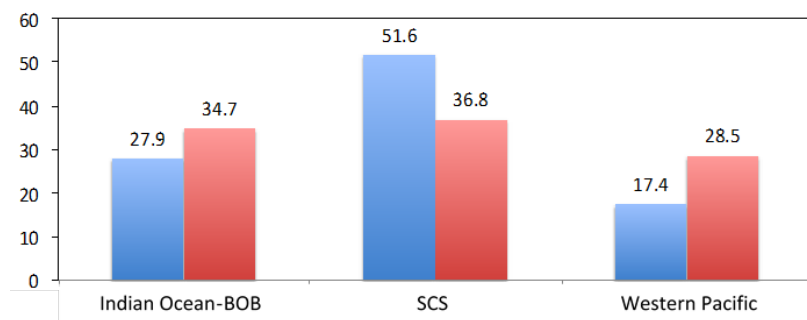
Fig. 5 Moisture contributions from diverse sources during different precipitation regimes in South China.

From Fig. 5, the moisture transport from Indo-China Peninsula to the SCS and around contribute most to precipitation in South China. The second largest contribution comes from the source of Arabian Sea-Indian Peninsula-BOB, followed by the contribution from source in western Pacific.

By comparing relative contributions from diverse sources during different regimes, it can be found that climatologically, moisture transport from the Indo-China Peninsula to the SCS and around, western Pacific, and Arabian Sea-Indian Peninsula-BOB contribute larger to precipitation anomaly in South China. After the transition from deficiency (red) to abundance (blue) condition after early 1990s, contribution of moisture steered from the Indo-China Peninsula to the SCS and around increased by 14.8%, while the contributions from the western Pacific and Arabian Sea- Indian Peninsula-BOB decreased by 11.1% and 6.8% respectively.

As displayed in Figure 6a, during abundant precipitation regime in the YRV (1981-1999), seven routes can also be detected. Based on the above classification, one route is associated with the channel from the Arabian Sea-Indian Peninsula-BOB with its contribution of 26.5%; two routes linked with the channel from Indo-China Peninsula-SCS contribute 32.3% to total moisture transport; three routes originated from western Pacific jointly contribute about 27.6%; the contribution from local moisture is 13.6%. During the regime with deficient precipitation in the YRV (2000-2012), 7 routes can be identified (Figure 6b). Three originate from Indian Ocean-BOB, and their total contribution is 39.6%; another comes across Indo-China towards the SCS and around with its contribution about 29.2%; two originate from the western Pacific, and they provides about 22.2% of total moisture; the moisture transport from north route account for 7.9%.

Based on total contributions from diverse sources during different regimes as revealed in Fig. 3, it can be concluded that climatologically the largest contribution to precipitation in the YRV is yielded via the transport from the Arabian Sea-Indian Peninsula-BOB. The contribution of moisture transport from the SCS and around
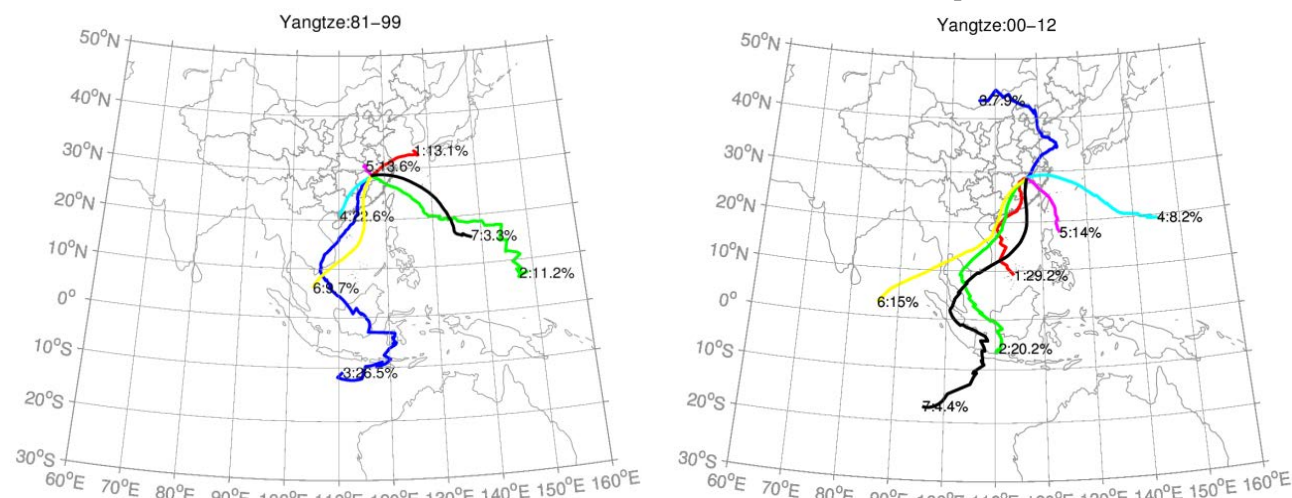
Fig. 6 Moisture transport paths during deficiency regime (left, 1981-1999) and abundance regime (right, 2000-2012) in the Yangtze River Valley and their contributions labeled on them.

ranks second, followed by source in western Pacific. The moisture from the north contributes least to precipitation in the YRV.

Figure 7 shows relative contributions from diverse sources during deficiency and abundance regimes. Larger contributions during abundant precipitation regime are mainly provided by sources in the Arabian Sea-Indian Peninsula-BOB, local source, and moisture from SCS and western Pacific. During the period with deficient precipitation in the YRV after 1990s, the contributions of moisture transport from local sources, western Pacific and sources from Indo-China to the SCS and around decreased by 13.6%, 5.4%, and 3.1% respectively. Increased contributions of 13.1% and 7.9% arise from the moisture transport from the Indian Ocean-BOB and northern China respectively.

After early 1990s, the anomalous westerly inhibited the eastward moisture transport, while the anomalous anticyclone over western Pacific-SCS promoted moisture from the SCS and around to advance towards South China. After late 1990s, the westerly moisture transport is conductive to moisture advection towards the YRV, while the anomalous cyclonic moisture transport is adverse to the moisture conveyed by cross-equatorial flow and from the SCS towards the YRV.

4. Conclusions

Based on daily rain gauge observations and NECP/NCAR reanalysis, changes in large-scale moisture transport and moisture budget in Asian monsoonal region under global warming are investigated. The influences of these changes on summer precipitation in southern China are further discussed, followed by quantitative estimation of contributions from diverse moisture sources to summer precipitation in southern China during different stages. Main conclusions are summarized as follows:
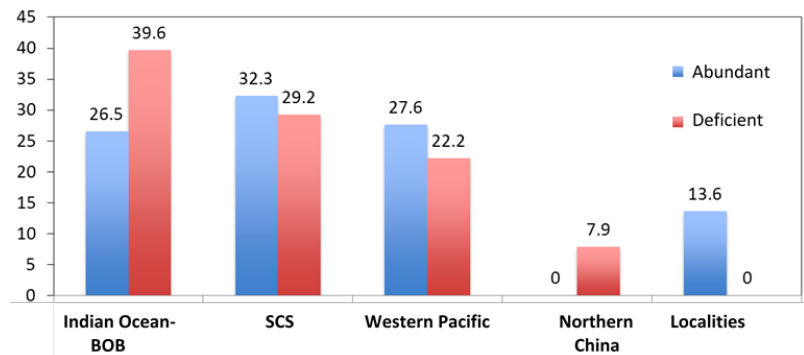

Fig. 7 Moisture contributions from diverse sources during different precipitation regimes in the Yangtze River.

(1) The northward moisture transport anomaly from lower-latitudes in Asian monsoonal region is responsible for variations of meridional and total moisture budget in South China and the YRV. For South China, before and after the regime shift around early 1990s, the anomalous moisture flux circulation in the SCS-western Pacific and the BOB remains consistent; while for the YRV, the anomalous moisture transport circulation behaves converse patterns after regime shift around late 1990s.

(2) By analyzing the model outputs of backward trajectory analyses, it can be found climatologically, the largest moisture contrition to precipitation in South China comes from the SCS and around, followed by the contribution from the sources in the Arabian Sea-Indian Peninsula-BOB and western Pacific consecutively. The largest moisture contribution to precipitation in the YRV is provided by the moisture source in the Indian Peninsula-BOB. The secondary and the third large contributions are from the SCS and western Pacific. The moisture from the north contributes least to precipitation in the YRV.

(3) Compared with deficiency period, the moisture contribution from the SCS and around increased by 14.8% during abundant regimes of precipitation in South China after early 1990s; respective contributions from the western Pacific and Indian Ocean-BOB decreased by 11.1% and 6.8%. After late 1990s, the YRV stepped into a deficiency regime. Moisture contributions from local source, western Pacific and the SCS to precipitation in the YRV decreased by 13.6%, 5.4%, and 3.1%; while increased contributions of 13.1% and 7.9% are detected in the sources of Indian Ocean-BOB and northern sources.

References

Brimelow, C. J., and W. G. Reuter, 2005: Transport of atmospheric moisture during three extreme rainfall events over the Mackenzie River Basin. *J. Hydrometeor*, **6**, 423-440.

Brubaker, K. L., P. A. Dirmeyer, A. Sudradjat, and Coauthors, 2001: A 36-yr climatological description of the evaporative sources of warm-season precipitation in the Mississippi river basin. *J hydrometeor*, **2**, 537-557.

Chang, Y., J.-H. He, Y.-Y. Liu, and Coauthors, 2006: Features of moisture transport of in Pre-summer flood season of drought and flood years over South China. *Plateau Meteorology*, **25**, 1064-1070.

Chen, B., X.-D. Xu, X.-H. Shi, 2011: Estimating the water vapor transport pathways and associated sources of water vapor for the extreme rainfall event over east of China in July 2007 using the Lagrangian method. *Acta Meteorologica Sinica*, **69**, 810-818.

Ding, Y.-H., 1994: Moisture budget in monsoonal region. *Asian monsoon*, Meteorological Press, Beijing, China, 105-113.

Jiang, Z.-H., Z.-R. Liang, Z.-Y. Liu, and Coauthors, 2011: A diagnostic study of water vapor transport and budget during heavy precipitation over the Huaihe River Basin in 2007. *Chinese Journal of Atmospheric Sciences*, **35**, 361-371.

Jiang Z.-H., W. Ren, Z.-Y. Liu, and Coauthors, 2013: Analysis of water vapor transport characteristics during the Meiyu over the Yangtze-Huaihe River Valley using the Lagrangian method. *Acta Meteorologica Sinica*, **71**, 295-304.

Li, W. P., 1999: Moisture flux and water balance over the South China Sea during late boreal spring and summer. *Theor Appl Climatol.*, **64**, 179-187.

Liu, Y. J., Y.-H. Ding, Y.-F. Song, and Coauthors, 2009: Climatological characteristics of the moisture budget and their anomalies over the joining area of Asia and the Indian-Pacific Ocean. *Adv. Atmos. Sci.*, **26**, 642-655.

Lü, M., X.-X. Cheng, Z.-Y. Chen, 1998: The character of summer monsoon and its transport to moisture in the range of South China heavy rain of 1994. *Journal of Tropical Meteorology*, **14**, 73-80.

Ma, J.-J., Bo Y., X.-Q. Gao, 2008: Change of large scale circulation and its impact on the water vapor over South China. *Plateau Meteorology*, **27**, 517-523.

Roberge, A., J. R, Gyakum, 2009: Analysis of intense poleward water vapor transports into high latitudes of western North America. *Weather and Forecasting*, **24**, 1732-1747.

Shi, X.-L., and Y.-H. Ding, 2000: A study on extensive heavy rain process in South China and the summer monsoon activity in 1994. *Acta Meteorologica Sinica*, **58**, 666-678

Stohl, A., C. Forster, and H. Sodemann, 2008: Remote sources of water vapor forming precipitation on the Norwegian west coast at 60°N-a tale of hurricanes and an atmospheric river. *J. Geophys. Res.*, **113**, 1-13.

Stohl, A., and R. James, 2004: A Lagrangian analysis of the atmospheric branch of the global water cycle. Part 1: Method description validation and demonstration for the August 2002 flooding in central Europe. *J. Hydrometeor*, **5**, 656-678.

Su, J.-F., T. Zhou, B. Zhou, and Coauthors, 2010: Diagnostic analysis on Meiyu rainstorm and its simulation based on backward trajectory analysis method during June 2009 in the south of Anhui Province. *Climatic and Environmental Research,* **26**, 34-38.

Sun, Y., and Y.-H. Ding, 2002: Role of summer monsoon in anomalous precipitation pattern during 1997 flooding season. *Journal of Applied Meteorological Science*, **13**, 227-287.

Webster P. J., 1994: The role of hydrological process in ocean-atmosphere interactions. *Rev. Geophys.*, **32**, 427-476.

Xie, A., D.-Y. Song, J.-Y. Mao, and Coauthors, 2001: Climatological characteristics of moisture transport during summer monsoon over South China Sea. *Climatic and Environmental Research*, **6**, 425-433.

Xie, A., J.-Y. Mao, D.-Y. Song, and Coauthors, 2002: Climatological characteristics of moisture transport over Yangtze River Valley. *Journal of Applied Meteorological Science*, **13**, 68-77.

Yang H., Z.-H. Jiang, Z.-Y. Liu, and Coauthors, 2014: Analysis of climatic characteristics of water vapor transport based on the Lagrangian method: a comparison between Meiyu in the Yangtze-Huaihe River region and the Huaibei rainy season. *Chinese Journal of Atmospheric Sciences*, **38**, 965-973.

Zhou C.-Y., J.-H. He, W. Li, and Coauthors, 2005: Climatological characteristics of water vapor transfer over East Asia in summer. *Journal of Nanjing Institute of Meteorology*, **28**, 18-27.

Zhou D.-Q., Y.-Q. Zheng, W. Li, and Coauthors, 2006: The distribution of atmospheric water vapor transports and income and expenses in the typical drought and flood summer in the Jiang-Huai Valley. *Scientia Meteorologica Sinica*, **26**, 245-251.

The Skills of the Probabilistic Forecast for
Meteorological Drought over the United States

Li Xu and Kingtse C. Mo

Climate Prediction Center, NOAA/NWS/NCEP, College Park, MD
and
Innovim, LLC, Greenbelt, MD

ABSTRACT

In this study, we evaluated the skills of probabilistic forecast for meteorological drought based on the precipitation forecast from Northern American Multi-model Ensemble (NMME). The total sixty ensemble members are selected from six NMME participated forecast models for the meteorological drought forecast. The NMME forecasts are downscaled to the 0.5 degree CONUS grid and bias corrected with BCSD method. The meteorological drought forecast, based on the standardized precipitation index SPI6 (six months accumulation), is computed and converted to the corresponding drought categories. The grand mean (GM) index summarize the mean state of drought from the all NMME ensemble members. The probabilistic information for each drought category, which is measured by the concurrence at each ensemble member, is computed to quantify the uncertainties of the drought forecast. The total 29 years hindcasts, during 1982-2010, are evaluated against observed drought categories. The assessments show that the meteorological drought forecasts based on the NMME display robust skills, both in grand mean and probabilistic forecast. More than half areas of USCONS are still skillful for lead four month forecast. The skills of probabilistic forecast over climatological forecast are obviously and decreasing with leading time. However, they only indicate very slight skills over the short-leading random ESP forecast that initial drought information dominated. With increasing the lead time, the values of climate forecast begin emerging.

1. Objectives

Drought occurred in the US had the major societal, economical, and environmental impacts. The current objective drought forecasts based on dynamical model, such as the forecasts from the NMME (Kirtman *et al.* 2014) *etc.*, however, exist large differences in the drought forecast, in particular to classify the drought into the drought categroies Dx (x=0-4) (Mo 2008). And also, current forecast has no estimation of the uncertainty and doesn't give risk manager or decision maker the best or worse scenarios. Since the chaotic nature of climate system, the demand for probabilistic information of drought forecast is undeniable.

2. Data and procedures

As prescribed by Xu and Mo (2018), we selected six representative models in NMME forecast set, i.e. CanCM3 model, CanCM4 model, GFDL_FLOR model, NASA GEOS5 model, NOAA CFSv2 model and NCAR CCSM4 model.. Each model was selected only 10 ensemble members which are closest to the common forecast initial time (the day 01 at each month). The hindcasts come back for every month from 1982 to 2010 (total 29 years), obtained from the NMME historical archives. The real-time forecast start from 2011 up to recently, issued the precipitation and temperature at the first of each month.

The precipitation (P) forecast for lead 1-6 months from NMME are firstly downscaled to 0.5 degree CONUS grid, by bilateral interpolation. The downscaled P forecasts are then bias corrected by the bias correction and spatial downscaling (BCSD) method (Yoon *et al*. 2012) with leave-one-out cross-validation, which guarantee the target year is removed from the training pool to avoid the overfitting problem. This step is critical for the drought forecast since any forecast bias will cause SPI error in the next computation with

_____

Correspondence to: Li Xu, Climate Prediction Center, NOAA/NWS/NCEP, 5830 University Research Court, College Park, MD 20740, and Innovim, LLC, Greenbelt, MD; E-mail: Li.Xu@noaa.gov

observed P data. The corrected P forecast, combined with the CPC unified P observations back to 50 years historical record, are utilized to calculate six month accumulated standardized precipitation index (SPI6), as the predictant for meteorological drought. The SPI6 could well capture the short-term drought signal and also balance the persisted long-term drought. The SPI6 forecasts from 60 ensemble members in the leading time 1-6 months, are then transferred to the uniform distribution (percentile) from the original normal distribution.

The sixty ensemble member for drought forecasts in percentile (uniform distribution) are mathematically averaged to the grand mean (GM) for the drought category Dx forecast. This percentile-mean method will reduce the "ensemble mean error" due to uneven distribution of SPI at "the long tail of normal distribution", in particular for the extreme events such as droughts. However, due to the offset effect (cancel out) of the arithmetic mean, the GM index will serious underestimated the drought intensity (Mo and Lettenmaier 2014). We remapped the grand mean index again to the uniform distribution based on the 29 year historical values. The probabilistic information for each drought category Dx, *i.e.* D0-D4, is measured by counting the concurrence of all sixty ensemble member in each drought category.

This objective probabilistic forecast is computed at the 10th day of each month, after collect all the six NMME forecasts initialized at the beginning of that month. The objective forecast could be delivered to drought forecasters, before the drought briefing, the seasonal drought overlook at the middle of the month and monthly drought overlook at the end of the month. Figure 1 shows an example of the probabilistic drought forecast for January 2019 based on the NMME forecast initialized at Dec 1, 2018. The top panel is the Grand Mean (GM) drought index that gives the mean state of drought by averaging all sixty ensemble member. The bottom four panel display the detail of probabilistic information for the Dx category or worse drought event (Dx and above). For instance, the "D0 and above" show the probabilistic for the "abnormally dry" or worse drought event (percentile < 30%). Similarly, the "D3 and D4" indicate the "extreme drought" (percentile <5%) and "exceptional drought" (percentile <2%). This objective forecast will help the forecaster to prepare the first guess map of the monthly drought overlook. Similarly, Fig. 2 shows the probabilistic drought forecast
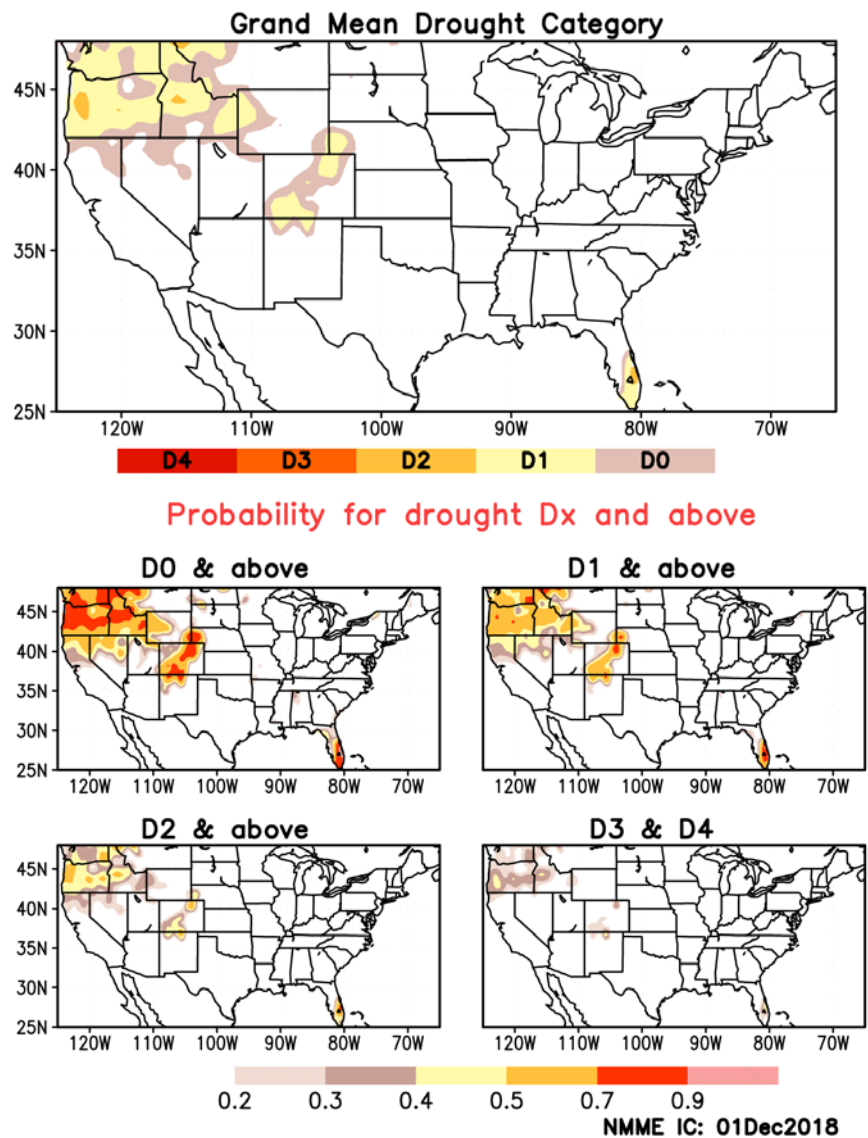
Fig. 1 The probabilistic drought forecast for January 2019 based on the NMME forecast initialized at Dec 01 2018.

for March 2018 based on the NMME forecast initialized at Dec 1, 2018. This map could help the operational seasonal drought overlook issued at the middle of each month.

3. Evaluations

Observed drought events are defined by the same SPI6 indices based on the observed rainfall analysis from CPC unified precipitation data. The rank correlation (Spearman Rho) is used to assess the GM index and Rank Probability Skill Score (RPSS) is used for the probabilistic forecast.

For skill assessment, the reference forecasts are defined to isolate the forecast skill origin from initial condition or climate forecast information. The persistent forecast is defined as the forecast map that prescribes the last month precipitation anomalous for the next six months. The climatological forecast are defined based on the drought categories definition, the 30% probability for "D0 and above" droughts, the 20% probability for "D1 and above" droughts, the 10% probability for "D2 and above" droughts, the 5% probability for "D3 and above" droughts and then 2% probability for D4 droughts. The random forecast, similar to the hydrological "ESP" type forecast, are calculated according to the random retrieved historical precipitation observation time series to computer the SPI forecast.
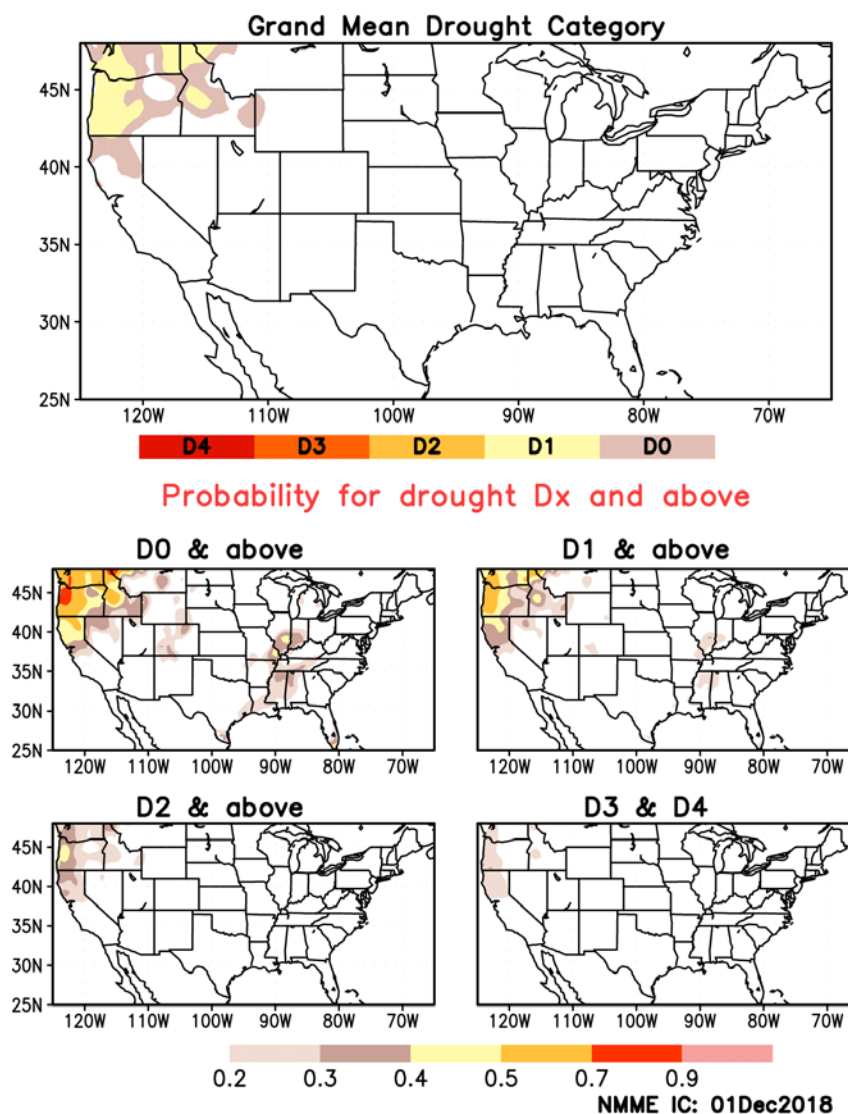
Fig. 2 The same as Fig. 1, but for March 2019.

3.1 Grand mean forecast

The grand mean forecast are the summary the mean drought state over the total 60 ensemble member. The rank correlation (Spearman Rho) is used to evaluate the GM forecast against the observed SPI indices based on the CPC unified precipitation. Figure 3 shows the Spearman Rho for January 01, April 01, July 01 and October 01 initialized forecast (from top to bottom), during 1982-2010 hindcast period.

As Fig. 3 shows, in the lead one month forecast (left column), the rank correlations are very high over the most area of USCONS. Except limited area in the Great Plain at April initialized forecast and some southwest area at July and October initialized forecast, Spearman Rho over the most area of USCONS are over 0.8. This indicates the GM forecast could well catch the drought situation at a short leading time, due to the strong persistence in the nature of the drought. For the lead-3 month forecast, the spearman Rho decrease with the lead
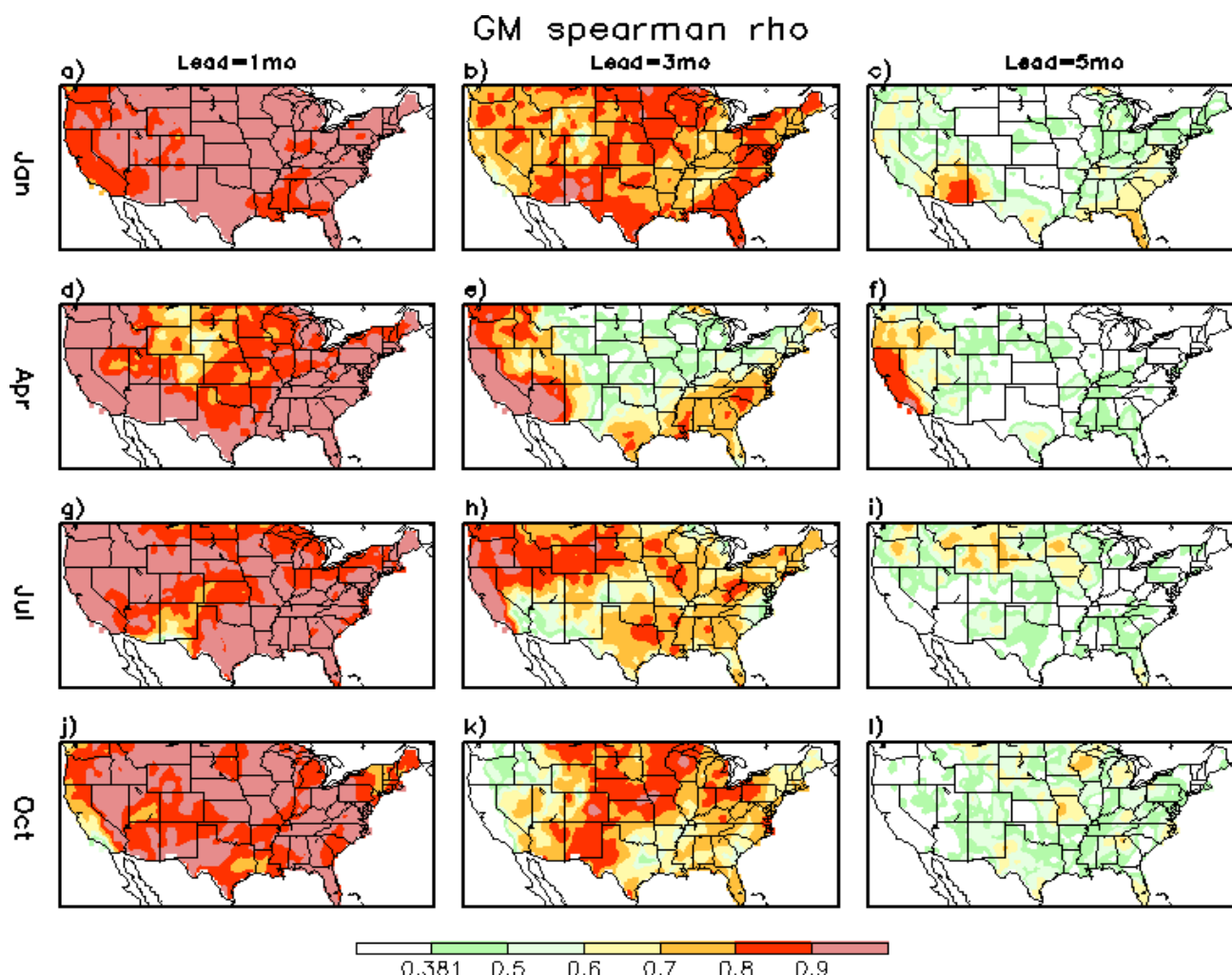
Fig. 3 The Spearman rank correlation (rho) for the Grand mean (GM) forecast with observed indices, for the January 01, April 01, July 01 and October 01 initialized forecast (from top to bottom) during 1982-2010. The left, central and right columns are the lead one, three and five months forecast respectively. Only the area where the correlation is 95% significance for student-t testing during 1982-2010 is colored.

time. But, more than half area of USCONS, the Rhos are still over 0.5 implying the useful of forecast. Except some scatter regions in the central plain for April initialized forecast, and part of southwest region for July and October initialized forecast, most area of Rho are still significant at 95% in student t testing. However, for the lead-5 month forecast, the forecast signals are serious weakened at most area (the Rho less than 0.5) and the area with significant correlation has greatly decreased.

Figure 4 shows the ratio of grid-points where are 95% significance in the Spearman rank correlation (rho) for January 01, April 01, July 01 and October
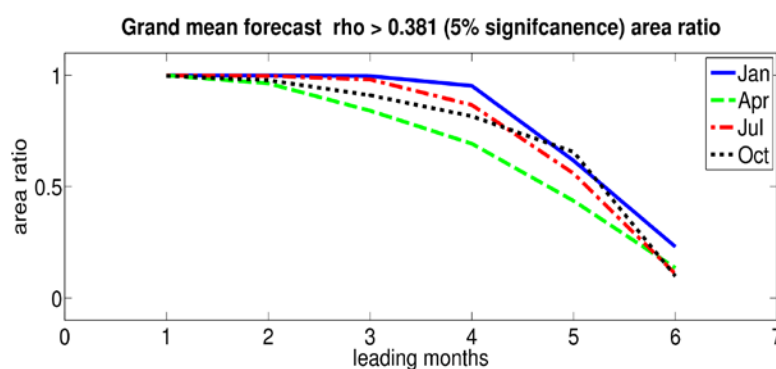
Fig. 4 The area ratio of the grid-points over USCONS with 95% significance in the Spearman rank correlation (rho) during 1982-2010 (larger than 0.381), for the GM forecast initialized at January 01, April 01, July 01 and October 01.
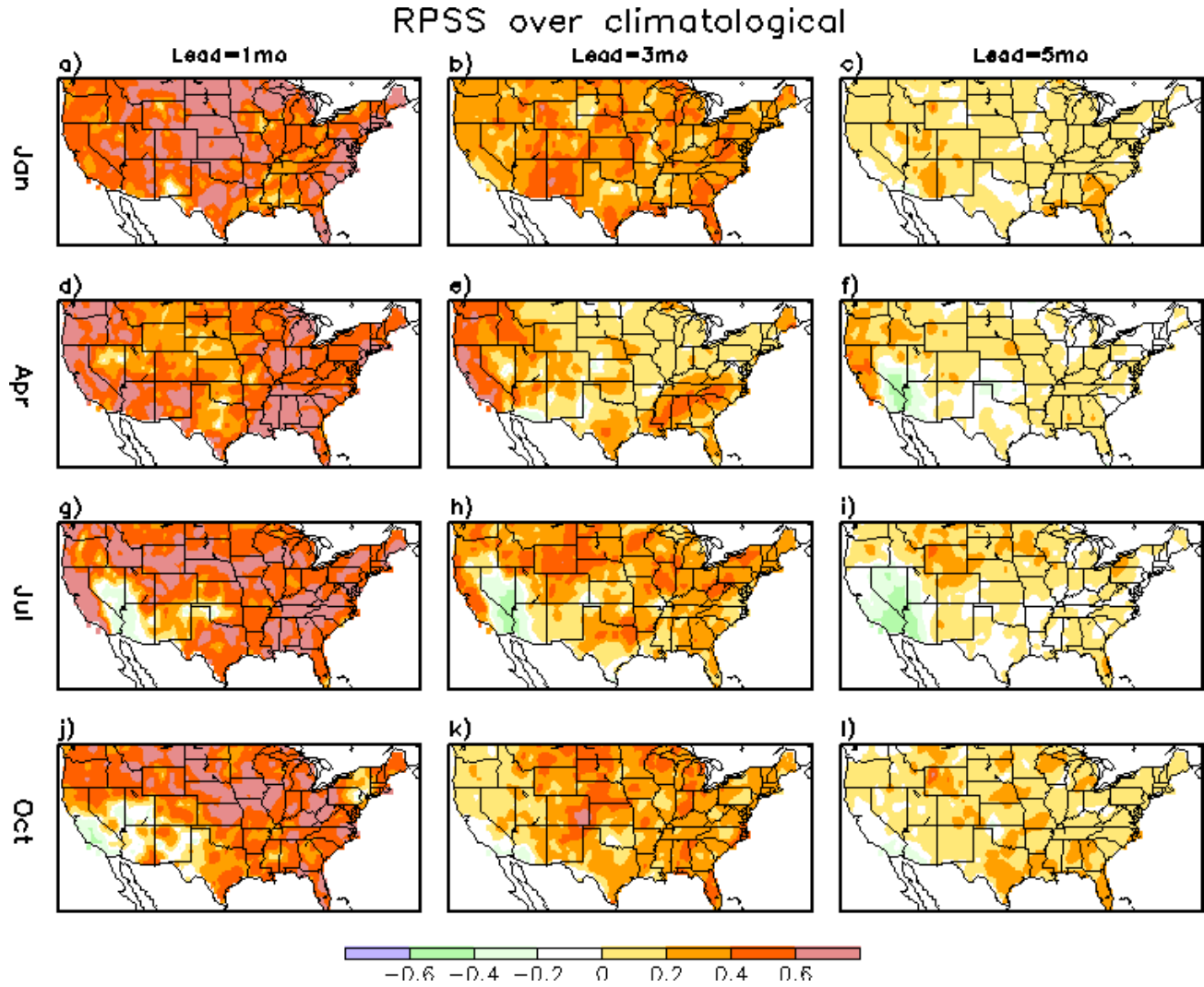
Fig. 5 The same as Fig. 3 but for the RPSS over the climatological forecast.

01 initialized forecast, based on the 29 years hindcast during 1982-2010. This ratio indicates the area with useful forecast. The forecasts initialized at the January are the best. More than half of areas are still useful at lead-5 month forecast. The forecasts initialized in the April are the worst; the forecast signal will reduce less than the half of USCONS in the lead-4 month. The forecasts initialized at the July and October are in the middle, still more than half area are useful at the lead-5 month forecast.

3.2 Probabilistic forecast

For Rank Probability Score (RPS) evaluation, the probabilistic forecast are equally divided by 10% probability as a bin, such as 90%, 80%, 70%....20%, 10%, where total bin n=10,

$$RPS = \sum_{m=1}^{n}(Y_m - O_m)^2, \quad Y_m = \sum_{j=1}^{m} y_j, \quad O_m = \sum_{j=1}^{m} o_j.$$

The RPS is the sum of the square of probabilistic differences at the each bin between forecast (Y_m) and observed (O_m) drought events. The skill score of RPS (RPSS) is the forecast skill with respect to the refference climatological forecast or random "ESP" type forecast.

$$RPSS = 1 - \frac{<RPS>}{<RPS_{Cl}>}$$

Figure 5 shows the RPSS for the probabilistic drought forecast over the climatological forecast. With a short lead time (left column), the probabilistic forecast dominantly beat the climatological forecast, with large
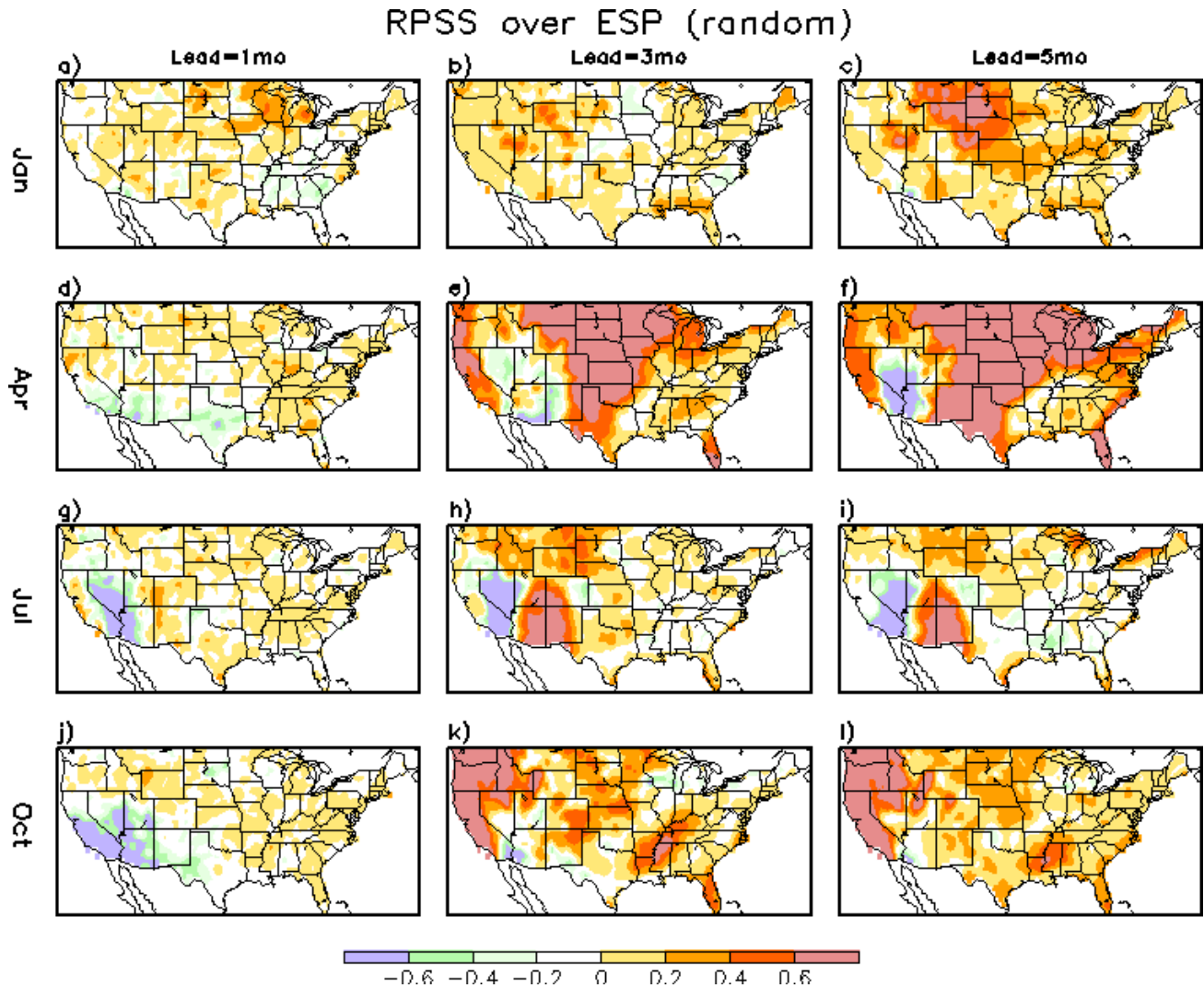
Fig. 6 The same as Fig. 3 but for the RPSS over the random (ESP) forecast.

positive RPSS score. Except limited region at AZ and NM at July and October initialized forecast, most area of USCONS indicated positive skills of probabilistic forecast. With increasing with lead time, the skills over climatological forecast are weakened as expected. However, at lead-5 month forecast, over the majority of USCONS, the skills are still positive. These positive skills indicate the forecasts are better than climatological forecast.

Similarly, Fig. 6 shows skill score RPSS for the probabilistic forecast over the "ESP" forecast, which combined the random retrieved precipitation time series with current drought condition. In the short leading, the probabilistic forecast show very weak skill over the random forecast. This implies the most forecast signal of probabilistic forecast come from the initial condition. With increasing the lead time, the probabilistic forecast show increasing skills over the random forecast, indicating the contribution of initial conditions are reducing and the contributions of forecast information are increasing. With the decreasing the impact of initial condition, the probabilistic forecast gradually display the value from the climate forecast

4. Conclusions

In this study, we evaluated the usefulness of probabilistic forecast for meteorological drought based on the precipitation forecast from Northern American Multi-model Ensemble (NMME). The total 29 years hindcasts, during 1982-2010, are evaluated against observed drought categories based on the CPC unified precipitation. The assessments show the meteorological drought forecasts based on the NMME display strong skills, both at

Grand Mean forecast and probabilistic forecast. The GM forecast show robust rank correlation at the different lead time over the most area of USCONS. The ratio with useful forecast signal (95% significant at student t testing) is more than the half area of USCONS, even at the lead four month forecast. The probabilistic forecast display strong skills over the climatological forecast at lead one to five months. This implies the objective forecast well beat the climatological drought forecast based on the historical occurrence.   The probabilistic forecasts also indicate very litter skills over the short leading random ESP forecast that initial information dominated. With increasing lead time, however, the values of climate forecast begin to override the impacts of initial condition.

References

Kirtman, B. P., and Coauthors, 2014: The North American Multimodel Ensemble Phase-1 seasonal-to-interannual prediction; Phase-2 toward developing intraseasonal prediction. *Bull. Amer. Meteor. Soc.*, **95**, 585-601.

Mo, K. C., 2008: Model-based drought indices over the United States. *J. Hydrometeor.*, **9**, 1212-1230.

Mo, K. C., and D. P. Lettenmaier, 2014: Objective drought classification using multiple land surface models. *J. Hydrometeor.,* **15**, 990-1010.

Xu, L., and K. C. Mo, 2018: Probabilistic drought forecasts based on the Northern American Multi-Model Ensemble (NMME). *NWS Sci. Technol. Infusion Clim. Bull., 42nd NOAA Annu. Clim. Diagn. Predict. Workshop*, Norman, OK, 23-26 October 2017, 144-147, doi:10.7289/V5/CDPW-NWS-42nd-2018.

Yoon, J.-H., K. Mo, and E. F. Wood, 2012: Dynamic-model-based seasonal prediction of meteorological drought over the Contiguous United States. *J. Hydrometeor.*, **13**, 463-482.

Evaluation of the National Water Model for Potential Application in the NLDAS Drought Monitor

Jesse Meng[1], Youlong Xia[1], and Kingtse Mo[2]

[1]*I. M. System Group at NOAA/NCEP/EMC, College Park, Maryland*
[2]*Climate Prediction Center, NOAA/NWS/NCEP*

1. Introduction

The NCEP North American Land Data Assimilation System (NLDAS, Ek *et al.*, 2011) Drought Monitor is a multi-model ensemble drought monitor and analysis system that provides land surface hydrological conditions across the contiguous United States (CONUS) domain in near real time. NLDAS runs four uncoupled land surface model simulations using a common meteorological forcing from the CPC North American Regional Reanalysis and the CPC daily global gauge precipitation analysis (Xie *et al.*, 2010). Daily, weekly, and monthly anomalies and percentiles of land surface water cycle variables including precipitation, soil moisture, snowpack, streamflow, and evapotranspiration, are calculated at 1/8th degree grids and provided to users including CPC and NIDIS (National Integrated Drought Information System, https://www.drought.gov/drought) for drought monitor and outlook. The NOAA National Water Model (NWM, Cosgrove, 2018) is a hydrologic model that simulates observed and forecast land surface water cycle over CONUS. NWM runs an hourly uncoupled analysis, and forecasts on short-range (18 hours), medium-range (10 days), and long-range (30 days) time scales on 1km and 250m grids. The simulations are forced with meteorological data from the NCEP forecast models (HRRR, RAP, GFS, and CFS) along with the MRMS radar and gauge-adjusted observed precipitation products. The Noah-MP land surface model is implemented in NWM to simulate land surface processes. The objective of this study is to make a comparison between the NLDAS and NWM products and to evaluate the potential application of NWM in monitoring and forecasting the drought conditions across the U.S., and to integrate NWM with NLDAS to support the CPC and NIDIS Drought Monitor and Outlook operations.

2. Results

Drought can be described conceptually as a deficiency in water supply over a temporal and spatial extent. Soil moisture content relative to climatology has been commonly used for drought assessment over regional to continental scales. The NLDAS and NWM monthly mean top 2-meter column volumetric soil moisture percentiles relative to their corresponding multi-decades retrospective simulations are analyzed and compared. Figure 1 presents a selected set of sample maps of monthly mean soil moisture percentiles of NLDAS and NWM, represented for August 2011 during the historical event of Texas drought. The official
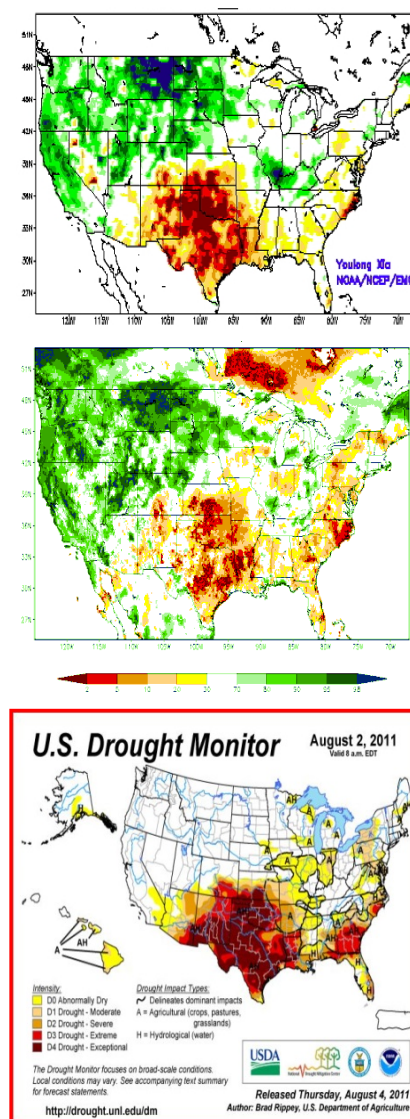
Fig. 1 Monthly 2-meter column soil moisture percentiles of August 2011 from NLDAS (top), NWM (middle), and US Drought Monitor guidance (bottom).

US Drought Monitor guidance upon the same time is included as a reference. Both NLDAS and NWM successfully depict the soil moisture deficit in the broad extent of Texas, Oklahoma, and Louisiana that is consistent with the US Drought Monitor.

3. Remarks

The NLDAS Drought Monitor uses a 31-year (1979-2009) retrospective simulation to generate the soil moisture climatology and percentiles. On the other hand, the NWM V1.2 retrospective runs for a 25-year (1993-2017) period that the climatology is generated from. The impact of such a mismatch on the drought condition assessment is under investigation.

References

Cosgrove, B., 2018: An update on the NOAA National Water Model and related activities, *AMS 32nd Conference on Hydrology*. Austin, Texas, 7-11 January, 2018.

Ek, M., and Coauthors, 2011: North American Land Data Assimilation System Phase 2 (NLDAS-2): Development and applications, *GEWEX News*, **21**, 6-7, https://www.gewex.org/gewex-content/files_mf/1432209506May2011.pdf

Xie, P., M. Chen, and W. Shi, 2010: CPC unified gauge-based analysis of global daily precipitation. *AMS 24th Conference on Hydrology*, Atlanta, Georgia, 18-21 January, 2010.

4. OBSERVATION, PREDICTION AND ATTRIBUTION OF RECENT HIGH IMPACT WEATHER AND CLIMATE EVENTS, AND IMPLICATION FOR EXTREME PRECIPITATION AND TEMPERATURES, HEAT/COLD WAVES, DROUGHTS AND WILDFIRES

43rd NOAA Annual Climate Diagnostics and Prediction Workshop

Santa Barbara, California

23-25 October 2018

Change in the Leading Mode of North America's Wintertime Stationary Eddies

Yu-Tang Chien[1] and S.-Y. Simon Wang[1, 2]

1Dept. Plants, Soils and Climate, Utah State University, Logan, UT
2Utah Climate Center, Utah State University, Logan, UT

1. Background

Extreme winter weather events in North America have become more frequent and increasingly destructive. According to the National Centers for Environmental Information report (NOAA 2019), during 1985-2005, Florida was the only state suffering billion-dollar losses related to freeze events in the eastern U.S. After 2006, the number of eastern states affected by these costly freeze-related disasters has doubled, along with a marked increase in the number of billion-dollar disasters caused by drought in western states. Past studies focusing on the 2013-2014 winter anomaly showed that the striking division of western U.S. drought and eastern U.S. cold-snaps have resulted from an atmospheric pattern referred to as the "North American Winter Temperature Dipole" (Singh *et. al.* 2016) or the "North American Winter Dipole" (Wang *et. al.* 2015), hereafter Dipole.

The polarity and location of this Dipole coincide with the wintertime stationary waves over North America, which feature a high-pressure ridge in the west and a low-pressure trough in the east. Oscillating in sync with the stationary waves, the positive-phase Dipole is associated with an anomalous ridge over the Gulf of Alaska and a deepened trough near the Great Lakes, thereby enhancing the east-west temperature contrast in North America (Voelker *et al.* 2019). While past studies suggested that the ridge in western U.S. (Swain *et al.* 2014) and the Dipole itself have amplified (Singh *et. al.* 2016), the trend suggests a one-sided response (*i.e.* only the positive phase inducive to drought in western U.S.) to internal and external variabilities, such as tropical Pacific heating (Hartmann 2015; Schulte and Lee 2017) and Arctic warming (Francis and Varus 2012; Overland *et al.* 2016). The intense Dipole reversal seen in 2016-17 winter suggests that the variation amplitude also increases leading to extreme conditions such as wet winters in California (Wang *et al.* 2017; Swain *et al.* 2018). These observations imply a change in the atmospheric circulation regime over North America, which is examined herein.

2. Analyses

Empirical orthogonal function (EOF) is the main analysis technique for this study. We subjected the monthly anomalies of geopotential height (Z) at 250 hPa from November through February, with the zonal mean removed to depict the stationary eddies (herein ΔZE250). For a running 30-year period, each EOF analysis contains 120 realizations (30 years x 4 months). The month-by-month arrangement of ΔZE250 reflects the strong sub-seasonal variability of winter climate over North America (Higgins *et al.* 2000). For the initial analysis of the atmospheric circulation, we use NCEP–NCAR reanalysis (Kalnay *et al.* 1996).

2.1 Change in leading patterns

The first mode of ΔZE250 during the earlier period of 1948-1979 is shown in Figure 1a. Explaining 18.6% of the variance, this leading EOF features a wave train emanating from the central Pacific to the U.S., coincident with the well-known Pacific North American (PNA) pattern. By superimposing the PNA contours, which was produced by correlating ΔZE250 with the PNA index from the NOAA Climate Prediction Center, the two patterns of EOF1 and PNA are in-phase. By comparison, the post-1980 EOF1 (Fig. 1b) shows a similar wave train but the wave centers are shifted from the PNA pattern by about a quarter phase. It appears that the post-1980 EOF1 becomes phase coincident with the Dipole centers (marked with X and + in North America). This result suggests that the leading mode of ΔZE250 variability has changed from a PNA-like pattern to one that resembles the Dipole. We should note that, by repeating the EOF analysis with seasonal mean instead of

_____

Correspondence to: S.-Y. Simon Wang, Dept. Plants, Soils and Climate, Utah State University, Logan, UT;
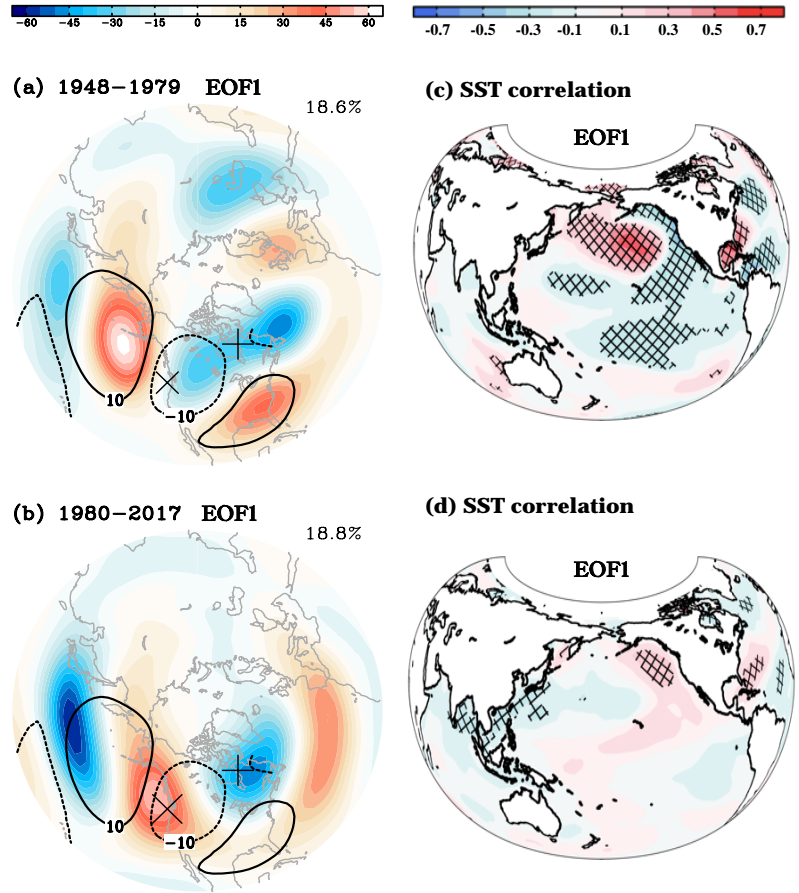E-mail: simon.wang@usu.edu

monthly interval, the leading pattern of the latter period would still be PNA, whereas the Dipole remains secondary (not shown).

By correlating the first principal component (PC1) time series with the monthly SST anomalies (Nov-Feb; using Extended Reconstructed SSTv4), the pre-1980 EOF1 corresponds to a La Niña-like pattern resembling the cold-phase Pacific Decadal Oscillation (PDO) (Fig. 1c), which supports the associated PNA atmospheric wave train (Fig. 1a). After 1980, the SST correlation map with respect to EOF1 changed dramatically and is absent of the PDO alongside most tropical signatures (Fig. 1d). This post-1980 SST pattern corresponding to EOF1 reveals the oceanic "Blob" along the West coast (Kintisch 2015), as well as robust negative anomalies in the Western North Pacific and the Bay of Bengal. This latter SST feature coincides with an ENSO precursor, called the Western North Pacific pattern (WNP), that saw amplification in recent decades (Wang *et al.* 2013). The marked difference between these SST patterns accompanying EOF1(ΔZE250) of two eras implicates two very different modes of sub-seasonal variability influencing North American winter.

Fig. 1 First EOF mode of monthly $\Delta Z_E 250$ during (a)1948-1979 and (b) 1980-2017 winters (EOF1 shading), superimposed with with the PNA pattern (contour) and the Dipole centers (marked with X and +) in North America. The correlation maps between monthly SST anomalies and the first principle component (PC1) are shown for the (c) 1948-1979 and (d) 1980-2017 periods. Hatched areas indicate significant values (p<0.01).

2.2 Evolution of the change

To examine the evolution in which the leading mode of ΔZE250 started to change, we adopted the running-EOF method, following Zhang *et al.* (2008). A series of EOF analysis was conducted in the 30-year window and repeated every five years. The leading EOFs are then subject to a spatial correlation analysis with the PNA pattern and the Dipole, forming a series of correlation coefficients with each 30-year period. This analysis was performed on newer reanalysis data: the ECMWF 20-Century Reanalysis (ERA20C) and the ERA-Interim. As shown in Fig. 2a, the running-EOF computed with all reanalysis data shows a decreasing trend in the correlations between EOF1 and PNA from 1970 to 2000. Meanwhile, the correlations increase between EOF1 and the Dipole, computed from the ΔZE250 of the 2013-2014 winter (Wang *et al.* 2014). Correspondingly, sliding correlations of the second running-EOF (EOF2) with the PNA show an opposite trend (Fig. 2b), suggesting that the Dipole used to be the second mode but has intensified, overtaking EOF1 during the 1990s.

The mechanism behind this decadal shift in the prevailing modes of variation is manifold. Previous studies proposed that the ENSO-forced PNA would move eastward in response to the spatial shift of the mean SST warming (Zhou *et al.* 2014). Interdecadal variability of the North Pacific sea level pressure can induce a shift in the PNA (Johnson and Feldstein 2010). Moreover, one could relate the Dipole to the maintenance of wintertime stationary waves (*e.g.*, Chang 2009). The western ridge of the North American stationary waves is primarily linked to the orographic forcing of the Tibetan Plateau, while the Rocky Mountains amplify the

eastern/downwind trough. Diabatic heating from the Western Pacific and North Pacific further enhances and shapes this ridge-trough pattern. Therefore, the observed Dipole amplification could be related to such forcings combined, *i.e.* jet stream-terrain interactions and diabatic heating.

2.3 Past and future of Dipole

The transition between the leading and secondary modes of atmospheric circulation suggests that the Dipole variance has increased (Singh *et. al,* 2016; Wang *et al.* 2015). To put the Dipole variances into historical and projected perspectives, we further examined the NOAA 20-Century Reanalysis data and the Community Earth System Model (CESM) Large-Ensemble Project with 40 members (Kay *et al.* 2015). By calculating the 30-year running variance of the Dipole index derived from Wang *et al.* (2014), we found that the Dipole variance has undergone a pronounced low-frequency fluctuation. As shown in Fig. 3, an inter-decadal variation on the order of 60 years is observed, evidenced in the longer-term reanalysis data. Both the NCEP-NCAR and ERA-Interim reanalyses indicate that the Dipole variance was largest in the early 21st century. Similar analysis of the CESM ensemble means reveal an increase in Dipole variance during the historical period (up to 2005 with increasing greenhouse gas) that is projected to continue under the high-emission (RCP 8.5) scenario. However, the projected ensemble-mean variance starts to decline after 2050, despite an increase in the ensemble spread; this suggests a rather uncertain future concerning the Dipole fluctuation. At this point, we can only attribute this late-21st century decline to natural variability as observed.
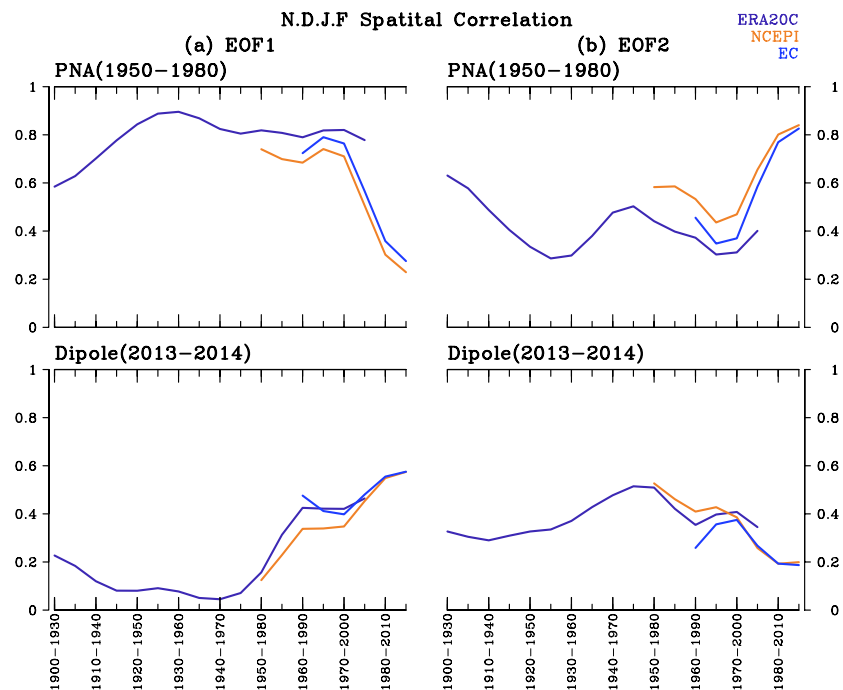
Fig. 2 Spatial correlation coefficients between the PNA/Dipole pattern and (a) EOF1 (b) EOF2 of $\Delta Z_E 250$ as in Fig. 1. This analysis is repeated throughout a 30-year Running-EOF window done every 5 years using three different reanalysis data sets as indicated on top of (b).
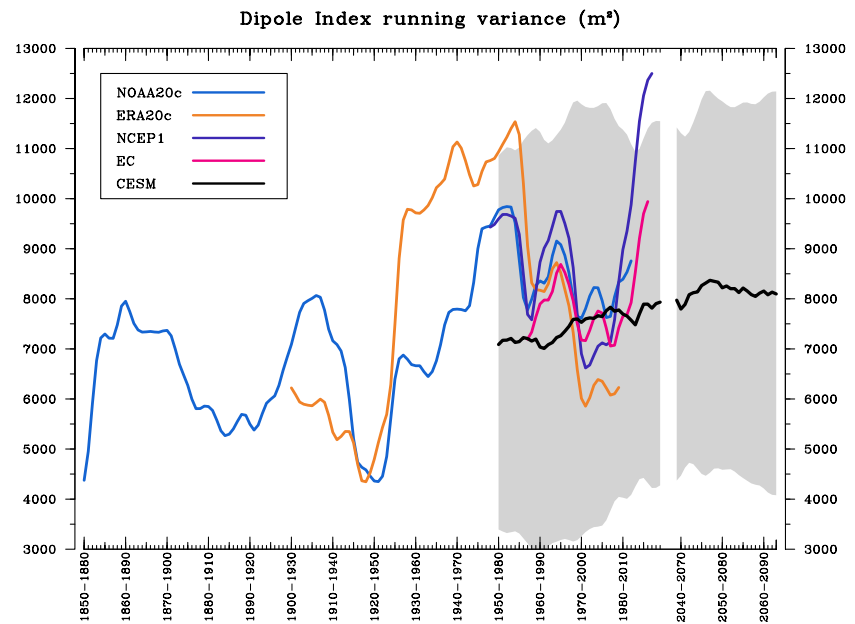
Fig. 3 The 30-years running variance of the Dipole index derived from Wang *et al.* (2014) using multiple reanalysis data sets as indicated at upper left. Gray shaded represents the spread of CESM 40-member ensemble calculated from two standard deviations above and below the ensemble mean.

3. Summary

The diagnostics undertaken here suggest that the leading mode of Northern Hemispheric atmospheric stationary waves underwent a notable change. Since the 1980s, the first mode of winter stationary eddies has changed from the PNA to the Dipole. Given that the EOF describes the variance of individual patterns, this finding also echoes the increased amplitude of the Dipole as observed. The CESM large-ensemble simulations forced with increasing greenhouse gas indicate that the Dipole variance will generally amplify alongside its low-frequency natural variability. This result implies that the variation of the atmospheric circulations over North America, especially in the subseasonal timescale, could continue to be dominated by the Dipole with the potential to sharpen the east-west temperature division across North America. Future examination of the dynamic processes leading to the Dipole amplification should consider jet-terrain interactions, tropical and extratropical diabatic heating, and the effect of Arctic amplification.

References

Chang, E. K. M., 2009: Diabatic and orographic forcing of northern winter stationary waves and storm tracks. *J Climate*, **22**, 670–688. doi:10.1175/2008JCLI2403.1

Francis, J. A., and S. J. Vavrus, 2012: Evidence linking Arctic amplification to extreme weather in mid-latitudes. *Geophys. Res. Lett.*, **39**, L068601, doi:10.1029/2012GL051000.

Hartmann, D. L., 2015: Pacific sea surface temperature and the winter of 2014. *Geophys. Res. Lett.*, **42**, 1894–1902, doi:10.1002/2015GL063083.

Higgins, R. W., J.-K. E. Schemm, W. Shi, and A. Leetmaa, 2000: Extreme precipitation events in the western United States related to tropical forcing. *J. Climate*, **13**, 793–820, doi: 10.1175/1520-0442(2000)013<0793:EPEITW>2.0.CO;2.

Johnson, N. C., and S. B. Feldstein, 2010: The continuum of North Pacific sea level pressure patterns: Intraseasonal, interannual, and interdecadal variability. *J. Climate*, **23**, 851–867. doi:10.1175/2009JCLI3099.1

Kalnay, E., and Coauthors, 1996: The NCEP/NCAR 40-year reanalysis project. *Bull. Amer. Meteor. Soc.*, **77**, 437–472, doi: 10.1175/1520-0477(1996)077<0437:TNYRP>2.0.CO;2.

Kay, J. E., and Coauthors, 2015: The Community Earth System Model (CESM) large ensemble project. *Bull. Am. Meteorol. Soc.*, **96**, 1333–1349, doi:10.1175/BAMS-D-13-00255.1.

NOAA National Centers for Environmental Information (NCEI), 2019: U.S. billion-dollar weather and climate disasters. https://www.ncdc.noaa.gov/billions/.

Overland, J. E., and Coauthors, 2016: Nonlinear response of mid-latitude weather to the changing Arctic. *Nature Climate Change*, **6**, 992–999, doi:10.1038/NCLIMATE3121.

Schulte, J. A., and S. Lee, 2017: Strengthening North Pacific influences on United States temperature variability. *Sci. Rep.*, **7**, 124, doi:10.1038/s41598-017-00175-y.

Singh, D., and Co-authors, 2016: Recent amplification of the North American winter temperature dipole. *J. Geophys. Res.: Atmos.*, **121**, 9911-9928, doi:10.1002/2016JD025116.

Swain, D. L., and Co-authors, 2014: The extraordinary California drought of 2013/2014: Character, context, and the role of climate change [in "Explaining Extremes of 2013 from a Climate Perspective"]. *Bull. Amer. Meteor. Soc.*, **95**, S3-S7.

—, B. Langenbrunner, J. D. Neelin, and A. Hall, 2018: Increasing precipitation volatility in twenty-first-century California. *Nature Climate Change*, **8**, 427.

Voelker, S. L., S.-Y. Wang, T. E. Dawson, J. S. Roden, C. J. Still, F. J. Longstaffe, and A. Ayalon, 2019: Tree-ring isotopes adjacent to Lake Superior reveal cold winter anomalies for the Great Lakes region of North America. *Scientific Reports*, **9**: 4412, doi:10.1038/s41598-019-40907-w.

Wang, S.-Y., L. Hipps, R. R. Gillies, and J.-H. Yoon, 2014: Probable causes of the abnormal ridge accompanying the 2013–2014 California drought: ENSO precursor and anthropogenic warming footprint. *Geophys. Res. Lett.*, **41**, 3220–3226. doi:10.1002/2014GL059748.

—, W.-R. Huang, and J.-H. Yoon, 2015: The North American winter 'dipole' and extremes activity: A CMIP5 assessment. *Atmos, Sci. Lett.*, **16**, 338-345.

—, J.-H. Yoon, E. Becker, and R. Gillies, 2017: California from drought to deluge. *Nat. Climate Change*, **7**, 465-468.

Zhang, X., A. Sorteberg, J. Zhang, R. Gerdes, and J. C. Comiso, 2008: Recent radical shifts of the atmospheric circulations and rapid changes in the Arctic climate system. *Geophys. Res. Lett.*, **35**, L22701, doi:10.1029/2008GL035607.

Zhou Z.-Q., S.-P. Xie, X.-T. Zheng, Q. Liu, and H. Wang, 2014: Global warming-induced changes in El Niño teleconnections over the North Pacific and North America. *J Climate*, **27**, 9050–9064, doi:10.1175/JCLI-D-14-00254.1.

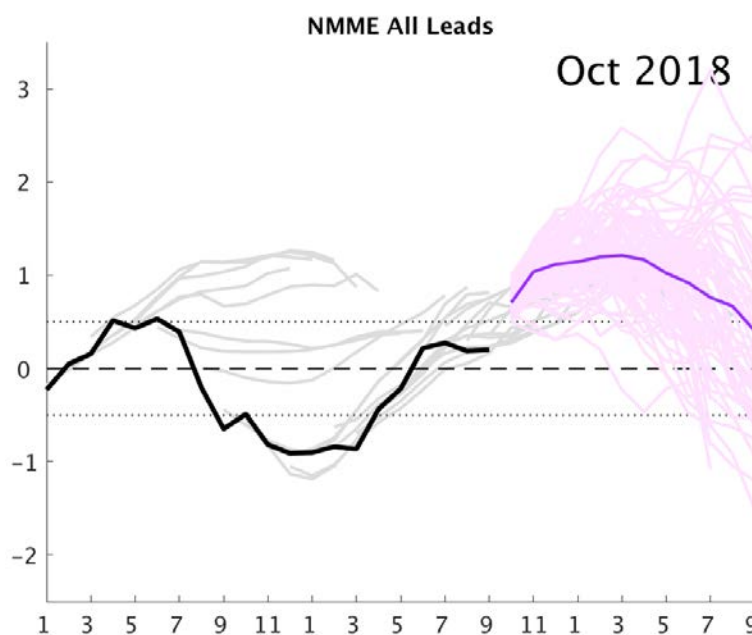# Overview of the 2017-18 La Niña and El Niño Watch in Mid-2018

Michelle L'Heureux

Climate Prediction Center, NOAA/NWS/NCEP

1. ENSO evolution and forecasts during 2017-18

A second-year, weak-to-moderate La Niña developed in the fall of 2017 and lasted through early spring of 2018. This La Niña followed a period of ENSO-neutral conditions during the first half of 2017. From January to May 2017, many model forecasts of the Niño-3.4 region of sea surface temperatures were predicting El Niño to occur during the latter part of 2017. While not alone in these predictions, the 100-member spread of the American Multi-Model Ensemble (NMME) lay outside of the observed evolution, in which instead of a developing El Niño, the tropical Pacific instead went into a La Niña in September-November of 2017 (as indicated by the Oceanic Niño Index value of -0.7°C). The ensemble mean predictions of the Niño-3.4 index from the NMME are indicated by the grey lines in Fig. 1. However, because these forecasts for El Niño during late 2017 were initialized early in the year and through the spring prediction barrier, a time of lower model skill, the CPC/IRI ENSO team never issued an El Niño Watch despite probabilities for El Niño that were elevated (well in excess of 50% chance in the models).

Because nearly all members from NMME were too warm for targets in mid-to-late 2017, verification using Ranked Probability Skill Scores (RPSS) were strongly negative for almost all forecast leads (orange lines in Fig. 2). The CPC official forecast assigned probabilities for El Nino that were greater than climatology, but they were much less bullish than the objective model guidance, so RPSS scores were not as negative as for NMME (green lines in Fig. 2).

Many dynamical and statistical models did not catch onto the possible La Niña of 2017-18 until the observed Niño-3.4 index values dropped to thresholds consistent with La Niña (-0.5°C in ERSSTv5 data (Huang *et al.* 2017) in September 2017). It wasn't until early September initializations of the NMME that the ensemble mean forecasted La Niña to occur and persist through the 2017-18 winter. At this point, both CPC official forecasts and model predictions consistently favored La Niña, and RPSS became positive for very short lead times

Fig. 1 Observed monthly Niño-3.4 index values (black line) from daily OISST (Reynolds *et al.* 2007) and once monthly forecasts of Niño-3.4 from the North American Multi-Model (NMME) from January 2017 through October 2018 (grey lines showing ensemble means). Departures are formed by removing monthly means during 1982-2010.

(Fig. 2, top row). A La Niña Watch was issued for the first time in early September 2017 and a La Niña Advisory was issued in early November 2017 as the onset of La Niña became apparent in both oceanic and atmospheric anomalies across the tropical Pacific Ocean.

Based on three-month, overlapping average values in the Niño-3.4 region, the La Niña was strongest during November 2017-January 2018 at -1.0°C relative to the 1986-2015 base period. By early May 2018, the La Niña Advisory was discontinued as the tropical Pacific Ocean returned to an ENSO-neutral state. Even while La Niña was ongoing in early 2018, many model predictions again predicted El Niño to develop during 2018. Because of the consistency of these model forecasts, even through the spring, the IRI/CPC eventually issued an El Niño Watch in early June 2018. The expectation was that El Niño would develop during the fall of 2018 and then persist into the winter 2018-19 (the NMME forecast initialized in early October 2018 is shown by

Fig. 2 The Ranked Probability Skill Score (RPSS) of the Niño-3.4 index for target seasons between November-January 2012 and July-September 2018 out to 7-months lead from the NMME (orange line) and CPC Official forecasts (green line).

the pink/purple lines in Fig. 1). However, prior to then, it was clear that the ensemble means from many dynamical models were over-predicting the level of warmth in the Niño-3.4 region for targets in the spring/summer of 2018. Instead Niño-3.4 index values were slightly positive, but shy of the +0.5°C threshold, even as the fall approached. The verification with RPSS reflects this over-prediction with a spike of negative skill in summer 2018 (Fig. 2).

2. Global temperature, precipitation, and circulation anomalies during DJF 2017-18 and their relation with ENSO

The second winter of consecutive La Niña events was accompanied by a more stereotypical La Niña pattern than the winter of 2016-17. In Fig. 4, the first La Niña is marked by the blue dot, while the second La Niña is noted with the red dot, so these two consecutive events can be directly compared. One prominent difference is that the 2017-18 winter La Niña was more strongly negative (based on Niño-3.4 index values) than the first winter, which may partially account for the more robust global footprint in the circulation and temperature (Figs. 3 and 4). In contrast to 2016-18, it is more common that the second year of La Niña is less intense than the first year, but some studies show that despite the weaker second year conditions, certain impacts can be greater (Okumura *et al.* 2017).

The left column of Fig. 3 shows observed climate anomalies during DJF 2017-18 and the right column shows the regression of these climate anomalies onto the Niño-3.4 index, which helps to diagnose the anomalies linearly associated with ENSO (note: there are also non-linear anomalies, but these are not presented herein). The regression presented in the right column are multiplied by a factor and multiplied by minus one, so that the La Niña anomalies can be seen more clearly and compared with the observations. In the top right corner of each row, the spatial correlation (with the spatial mean removed) between the observations and the ENSO
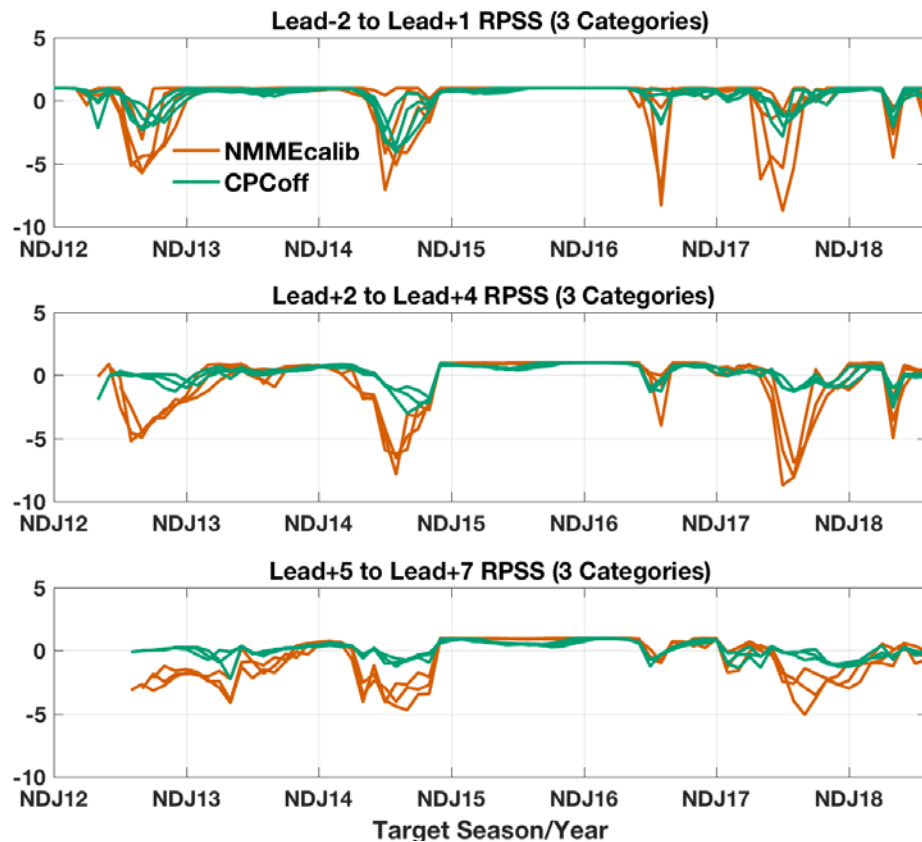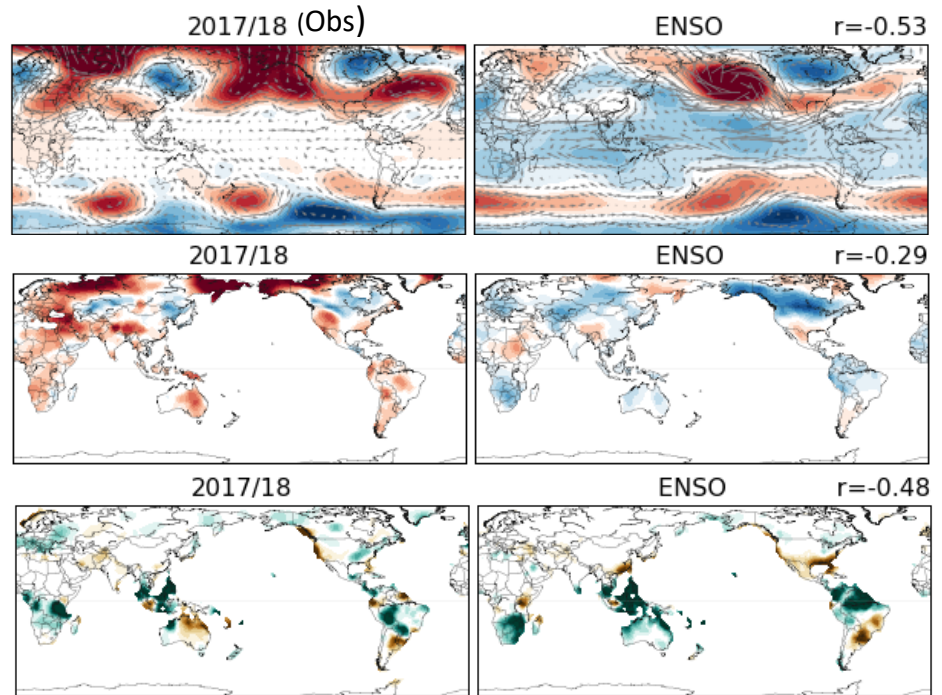
regression is displayed for 500-hPa geopotential height and winds (top row), surface temperature (middle row), and precipitation (bottom row).
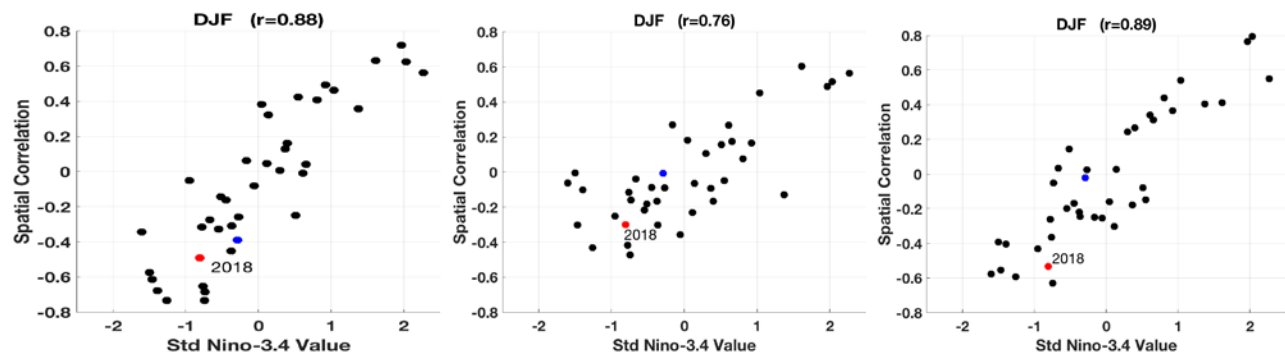
Both the circulation (top row) and precipitation (bottom) row patterns had large spatial correlations between the observations and expected linear ENSO patter (Fig. 3). The Southern Hemisphere extratropical circulation featured a positive Southern Annular Mode (or Antarctic Oscillation) pattern of above-average heights in the middle latitudes and below-average heights surrounding the South Pole. This is consistent with the expected linear relationship between ENSO and the SAM (L'Heureux and Thompson 2006). In the Northern Hemisphere, strong anomalous ridging was evident over the North Pacific Ocean, with an extension into the southern tier of the United States.

Fig. 3 December 2017-February 2018 (DJF) anomalies of 500-hPa geopotential height and winds (top row), surface temperature (middle row), and precipitation (bottom row). The left column shows the observational data, while the right column shows the reconstruction for 2017-18 (weighted regression map of the Niño-3.4 index). The reconstruction is multiplied by a factor of five to aid comparison. The r-values show the spatial correlation coefficient between the observational and the reconstructed anomalies (cosine weighted by latitude). Geopotential height and wind data is from the NCEP/NCAR Reanalysis, the temperature is from the gridded GHCN+CAMS dataset (Fan and van den Dool 2008), and precipitation data is from the gridded Precipitation Reconstruction Dataset (PREC) dataset (Chen *et al.* 2002). Departures are formed by removing monthly means during 1981-2010.

Completing the expected La Niña wave train, below-average heights were observed over Canada. Also mostly consistent with La Niña, DJF 2017-18 precipitation was enhanced over the Maritime Continent, northwestern Australia, parts of southeastern Africa (excluding the southern tip), Central America, and much of Peru/Bolivia. Reduced precipitation occurred over northern Argentina and parts of the southern tier of the United States. For temperature, the observed DJF 2017-18 anomalies were considerably warmer than the expected below-average temperatures over much of the globe (Fig. 3- middle row) and, as such, the spatial correlation was reduced relative to other climate anomalies.

Figure 4 shows scatterplots between the Niño-3.4 index values and the DJF 2017-18 spatial correlations (red dot) relative to other DJF seasons between 1982 and 2018 (black dots) for 500-hPa geopotential height (left panel), surface temperature (middle panel), and precipitation (right panel). At the top of each panel in Fig. 4, the temporal correlation is provided between the Niño-3.4 index value and the spatial correlations (between the observed maps and the ENSO regression). From this analysis, it is clear that precipitation and 500-hPa heights have the strongest linkage with Niño-3.4 (r is ~0.9), meaning that larger values of Niño-3.4 are generally associated with larger spatial correlations. Phrased another way, the similarity between the observed global anomalies and the "expected" ENSO pattern is higher with stronger ENSO events. Given that DJF 2017-18 was near minus one standard deviation in Niño-3.4 index, the spatial correlations were on the stronger side. Thus, the relatively stronger event appears to have accounted for the significant La Niña features across the globe, especially in the circulation fields and precipitation patterns. In contrast, the La Niña in 2016-17 (blue

Fig. 4 Scatterplots of the spatial correlation between the ENSO regression maps of 500mb geopoential height (left panel), temperature (middle panel) and precipitation (right panel) and the observed anomalies. The spatial correlation coefficient is on the y-axis and the seasonal average Nino-3.4 index value is on the x-axis. Each dot represents a single year between 1982 and 2018. The red dot indicates the 2017-18 La Niña (the spatial correlations are also presented in Figure 3) and the blue dot indicates the 2016-17 La Niña. At the top of each panel are the temporal correlations between the Niño-3.4 values (x-axis) and the spatial correlations (y-axis). The spatial mean is removed.

dot) was only marginally so by DJF and did not have notable spatial correlations. However, both events were within the historical spread of correlations shown in these scatter plots.

References

Huang, B., P. W. Thorne, V. F. Banzon, T. Boyer, G. Chepurin, J. H. Lawrimore, M. J. Menne, T. M. Smith, R. S. Vose, and H. Zhang, 2017: Extended Reconstructed Sea Surface Temperature, Version 5 (ERSSTv5): Upgrades, validations, and intercomparisons. *J. Climate,* **30**, 8179–8205.

Chen, M., P. Xie, J. E. Janowiak, and P. A. Arkin, 2002: Global land precipitation: A 50-yr monthly analysis based on gauge observations. *J. Hydrometeor.*, **3**, 249–266.

Fan, Y. and H. van den Dool, 2008: A global monthly land surface air temperature analysis for 1948-present. *J. Geophys. Res.-Atmos.*, **113**, D01103, doi:10.1029/2007JD008470.

L'Heureux, M. L. and D. W. Thompson, 2006: Observed relationships between the El Niño–Southern Oscillation and the extratropical zonal-mean circulation. *J. Climate,* **19**, 276–287.

Reynolds, R. W., T. M. Smith, C. Liu, D. B. Chelton, K. S. Casey, and M. G. Schlax, 2007: Daily high-resolution-blended analyses for sea surface temperature. *J. Climate*, **20**, 5473–5496.

Okumura, Y. M., P. DiNezio, and C. Deser, 2017: Evolving impacts of multiyear La Niña events on atmospheric circulation and U.S. drought. *Geophys. Res. Lett.*, **44**, 11,614-11,623, doi:10.1002/2017GL075034.

Operational Probabilistic Drought Prediction to Improve the Seasonal Drought Outlook

Kingtse C. Mo[1], Li Xu[1] and Dennis P. Lettenmaier[2]

[1]Innovim, LLC, and Climate Prediction Center, NOAA/NWS/NCEP
[2]Department of Geography, University of California, Los Angeles, California

1. Introduction

We provide a new frame work to forecast drought. At this moment, the CPC/NWS provides users the monthly and seasonal Drought Outlook. There is no estimate of forecast uncertainties. We will use the meteorological drought as an example. We plan to provide users the mean state of meteorological drought based on the Standardized Precipitation Index (SPI) and the probability for drought to occur in the Dx (x=1-4) categories. Users can assess the severity of drought and the likelihood for drought to occur in each category.

2. Data and procedures

The SPI measures the precipitation anomalies. We obtained Precipitation (P) forecasts from lead time one to six months from the North American Multi model ensemble (NMME) in real time. There are total 6 models: NCEP CFSv2, CMC1_CanCM3, CMC2_CanCM4, GFDL Flor , NASA GEOS 5 and NCAR CCSM4. Each model has 10 members so there are 60 members in total.

From P forecasts, we computed SPI6 and expressed SPI6 forecasts in percentiles. The grand mean is the mean of 60 members. We then mapped the mean to a uniform distribution function so forecasts will be between zero to one. The grand mean was verified against the SPI6 computed from the P analysis.

3. Real time probabilistic drought forecasts

The operational probabilistic forecasts have been in operation since June 2018 and continue until present. Figure 1 shows the grand mean and probability for drought to occur in D0 to D4 above categories for December 2018 based on forecasts initialized on 1 December 2018. Figure 1 indicates that drought remained in the Pacific Northwest and the severity was in D0-D1 category. The December 2018 was an El-Nino winter so it was expected to have dryness over the Pacific Northwest and wetness in the southern United States. Individual model also indicates dryness over the PNW and wetness over the Southeast.

We have provided forecasters and users probabilistic forecasts since March 2018 and have improved the operation based on comments from forecasters. These forecasts are posted at the CPC web site each month after the forecasts from the NMME are available.
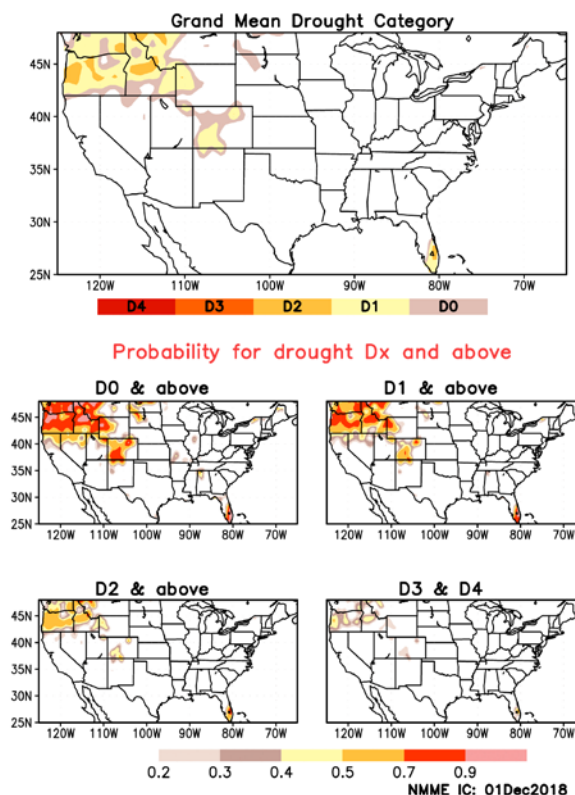
Fig. 1 (a) Probabilistic drought forecasts for lead 1 month for the initial conditions from December 2018. : Grand mean and probability for drought in Dx (x=1 to 4) above categories Contours are given by the color bar.

4. Evaluation of drought occurrence based on SPI6 hindcasts from the NMME

In this section, we used the January SPI6 hindcasts as an example. We obtained P hindcasts from the NMME archive for January from 1982-2010. We computed the SPI6 hindcasts the same way as the real time forecasts. There are total 60 members. The grand mean is the mean of 60 members and then is mapped onto a uniform distribution function. The grand mean was evaluated against the SPI6 computed from the P analysis based on the gridded P data. We used the Spearman's rank correlation for evaluation. The probability for drought occurrence was evaluated using the ranked probability skill score (RPSS) with climatology as the reference state.
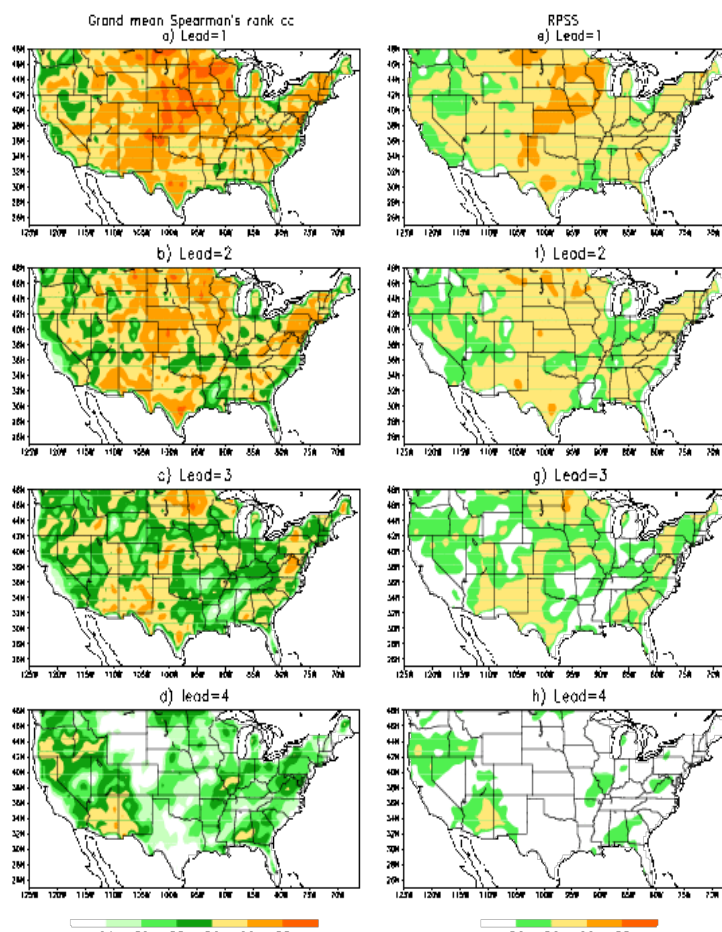
Figure 2 shows the Spearman's rank correlation coefficient for January initial conditions from lead one to 4 months. The skill is higher in the central United States for both grand mean and RPSS because winter is their dry season. The skill decreases as the lead time increases. For most places, the forecasts are skillful up to lead 3 months. The skill of the SPI forecasts comes from initial conditions because the P forecasts from the NMME are unskillful after one month. After 3 months, the impact of initial conditions diminishes and forecasts are no longer skillful. Because the CPC issues monthly and seasonal forecasts, the SPI6 forecasts can still provide useful guidance to forecasters.

The forecasts for July have similar level of skill except the Southwest. Because the NMME is not able to forecast the intensity and evolution of the North American Monsoon rainfall, the SPI6 forecast skill over the Southwest is overall low.

5. Future research plan

a) In order to provide forecasters the probabilistic drought forecast information quickly, we focused on the real time forecasts first. We will continue to provide forecasters probabilistic drought forecasts from lead one to 3 months and put forecasts on the web site.

Fig. 2 Spearman's rank correlation for January initial conditions from (a) lead one month, (b) lead two months, (c) lead 3 months and (d) lead 4 months. Shading values are given by the color bar. White areas indicate that the forecast is un-skillful with the correlation less than 0.37, (e)-(h) same as (a)-(d) but for RPSS.

b) We will continue to assess skill of SPI6 forecasts for other months. We will obtain the P hindcasts from the NMME archive from lead one to six months for forecasts initialized from all other months from 1982-2010. We will compute the grand mean and probabilistic drought categories and evaluate them against the SPI from the P analysis. We will evaluate hindcasts using the Spearmen's rank correlation and the RPSS.

c) Indication of forecast skill

We noticed that skillful set of forecasts has smaller spread among members. We will quantify the relationship between skill and spread. We will examine the relationship between spread and the reliability of forecasts.

Predictions and Predictability of the Northern Great Plains Record Low 2017 Summertime Precipitation

Andrew Hoell

NOAA/Earth System Research Laboratory Physical Sciences Division, Boulder, CO, USA

1. Introduction

Within a Northern Great Plains region, defined herein as South Dakota, North Dakota, and Montana east of 109˚W longitude (Figs. 1a, b), resides a complex reservoir system and agriculture industry upon which the local and national economies rely. The reservoir system captures water for consumption, generates hydroelectric power, sustains ecosystems, and supports navigation to promote commerce (Bureau of Reclamation 2011). Agriculture is prolific throughout the Northern Great Plains, as staple crops such as spring wheat, winter wheat, corn, and barley are grown in abundance (U.S. Department of Agriculture 2019). Droughts are not uncommon stressors of the region's agricultural productivity. Though being irregular, infrequent and of various severity and duration, droughts share the attribute of deficient precipitation.
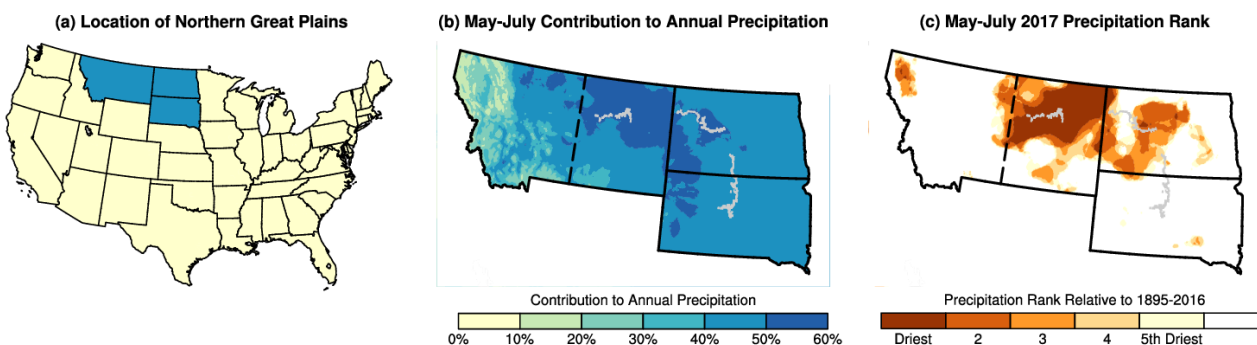
Fig. 1 (a) Location of the three states that constitute a Northern Great Plains region. (b) May-July contribution to the annual precipitation in percent. (c) May-July 2017 precipitation rank relative to 1895-2016. The 109˚W meridian is denoted by the dashed line in (b) and (c).

The 2017 spring and summer drought over Montana, North Dakota and South Dakota has been judged to be the most devastating in recent memory in this region (Fortin 2017). Economic losses resulting from the 2017 Northern Great Plains drought exceeded one billion dollars (NOAA/National Centers for Environmental Information 2018). The drought sparked wildfires and compromised water resources, which led to reduced agricultural production, the destruction of property, and livestock selloffs (U.S. Department of Agriculture 2017).

The 2017 drought arrived suddenly during the rainy season (Otkin *et al.* 2018, Hoell *et al.* 2019, Wang *et al.* 2019), which on average begins in spring, peaks during May-July (Figs. 2b), and ends during autumn. May-July precipitation ranked among the lowest on record over eastern Montana and portions of North Dakota and South Dakota dating back to at least 1895 (Fig. 2c).

Neither the drought's onset nor its severity was forecasted. Even as drought conditions emerged during mid-to-late May 2017 over Montana, North Dakota, and South Dakota (U.S. Drought Monitor 2017), further drought development was not anticipated within the following three months in NOAA's Seasonal Drought Outlook issued on May 18, 2017 (NOAA/Climate Prediction Center 2017a). Drought development was not anticipated because a failed rainy season was not expected. Instead, the NOAA forecast for May-July and June-

_____

August 2017 called for above-average precipitation over the Northern Great Plains (NOAA/Climate Prediction Center 2017b).

The lead times at which initialized prediction systems forecast the record low May-July precipitation that principally caused the 2017 Northern Great Plains drought are examined. The purposes of this examination are threefold: 1) to understand why drought was not forecast in advance of the season, 2) to identify at what lead times the cumulative precipitation deficits could be forecast with skill and 3) to provide insights into the prospects of early warning of future droughts.

2. Tools

a) Observed estimates

May-July 2017 precipitation ranks and the areally averaged May-July Northern Great Plains precipitation anomaly time series are based on the gridded National Centers for Environmental Information Precipitation Dataset version 1 (Vose *et al.* 2014). The Northern Great Plains is defined as Montana, North Dakota and South Dakota east of the 109˚W meridian. Anomalies are calculated relative to the 1982-2017 mean to align with the seasonal forecasts described in the following.

Eastern Montana precipitation is derived from the average of 16 stations (Table 1) drawn from the Global Historical Climatology Network (Menne *et al.* 2012). These 16 stations have reported almost continuously - at greater than 90% of days during each year since 1950 - and therefore provide a robust estimate of daily precipitation over the region. Anomalies for a given day are calculated relative to the 1950-2017 mean.

b) Seasonal forecasts

Table 1 GHCN stations that make up the observed eastern Montana precipitation time series.

Map Identifier	GHCN Station Identifier	Station Name	Latitude (°N)	Longitude (°W)
1	USC00241088	Bredette	48.15	105.30
2	USC00241231	Brusett 3N	47.46	107.31
3	USC00243013	Flatwillow 4 ENE	47.10	108.37
4	USC00243581	Glendive	47.10	104.72
5	USC00243727	Grass Range	47.02	108.80
6	USC00244358	Hysham	46.29	107.22
7	USC00245303	Mackenzie	46.14	104.72
8	USC00245596	Melstone	46.60	107.90
9	USC00245754	Mizpah 4 NNW	46.28	105.29
10	USC00246601	Plevna	46.42	104.52
11	USC00247214	Roundup	46.44	108.54
12	USC00247560	Sidney	47.72	104.13
13	USC00248165	Terry	46.79	105.30
14	USC00248957	Wilbaux 2E	46.99	104.16
15	USW00024037	Miles City	46.43	105.88
16	USW00094008	Glasgow Intl AP	48.21	106.62

Table 2 Models that make up the NMME ensemble.

Model	Ensemble Size	Reference
EMC: CFSv2	24	Saha *et al.* (2014)
CanCM4	10	Merryfield *et al.* (2013)
CanCM3	10	Merryfield *et al.* (2013)
GFDL: FLORa06	12	Vecchi *et al.* (2012)
GFDL: FLORb01	12	Vecchi *et al.* (2012)
GFDL: CM2.1	10	Zhang *et al.* (2007)
NASA: GEOS5	11	Vernieres *et al.* (2012)
RSMAS: CCSM4	10	Gent *et al.* (2011)

The ability of forecast models to predict areally averaged May-July Northern Great Plains precipitation in advance of the season is evaluated using April forecasts from the North American Multimodel Ensemble (NMME; Kirtman *et al.* 2014) and the European Centre for Medium-Range Weather Forecasts (ECMWF) SEAS5. In this analysis, NMME is a collection of 99 forecasts from eight different models listed in Table 2 that

span 1982-2017. ECMWF SEAS5 is a collection of 50 forecasts from a single model that span 1993-2017 (Stockdale 2018). Anomalies are calculated relative to the period mean of each model.

c) Sub-seasonal forecasts

The ability of forecast models to predict the temporal evolution of eastern Montana areally averaged precipitation anomalies is evaluated using forecasts from daily initializations of the Global Ensemble Forecast System (GEFS; Hamill *et al.* 2013), daily initializations of the Climate Forecast System Version 2 (CFSv2, Saha *et al.* 2013) and twice weekly initializations of the ECMWF model. Eastern Montana is defined as the area east of the 109°W meridian. Anomalies are calculated relative to the period of mean of each model.

3. Results

a) Seasonal forecasts

NMME and ECMWF forecast an increase in the likelihood of above average Northern Great Plains precipitation during May-July 2017, as evidenced by a slight shift in the distributions of forecast precipitation to anomalously wet conditions (Fig. 2). These predictions help to explain the lack of drought development forecast by NOAA's Seasonal Drought Outlook issued in May 2017 and the above-average May-July 2017 precipitation forecast also made by NOAA. While the prediction systems forecast an increased likelihood of above average precipitation, each system still forecast non-zero odds of dry conditions during May-July 2017, as the interquartile range of May-July forecast precipitation in both prediction systems was below average.

Given the poor precipitation forecast skill during 2017 over the Northern Great Plains, it is natural to probe the overall predictability in NMME and ECMWF during May-July over the region. This examination is performed by noting the magnitude of the shift in the distributions of forecast precipitation anomalies from zero relative to the magnitude of the spread of the forecast precipitation distributions. Larger shifts in the distribution of forecast precipitation anomalies from zero suggest greater levels of potential predictability.

The magnitude of the shifts in Northern Great Plains forecast precipitation anomaly distributions to wet or dry conditions are small relative to their spread (Fig. 2), suggesting low predictability of May-July precipitation in NMME and ECMWF. Note that the magnitude of ensemble mean anomalies are always smaller than observed anomalies for the more extreme summers. The spread, as estimated by the interquartile range, of the individual forecasts during a given year are consistently large and helps to explain why precipitation over the region is difficult to predict with skill. The mean forecast, as estimated by the median, hardly deviates from 0 in NMME and only begins to approach the magnitude of the spread in ECMWF during a handful of years since 1993. Slight differences between NMME and ECMWF forecasts, likely rooted in the way each ensemble is constructed, do not alter the interpretation of the results.
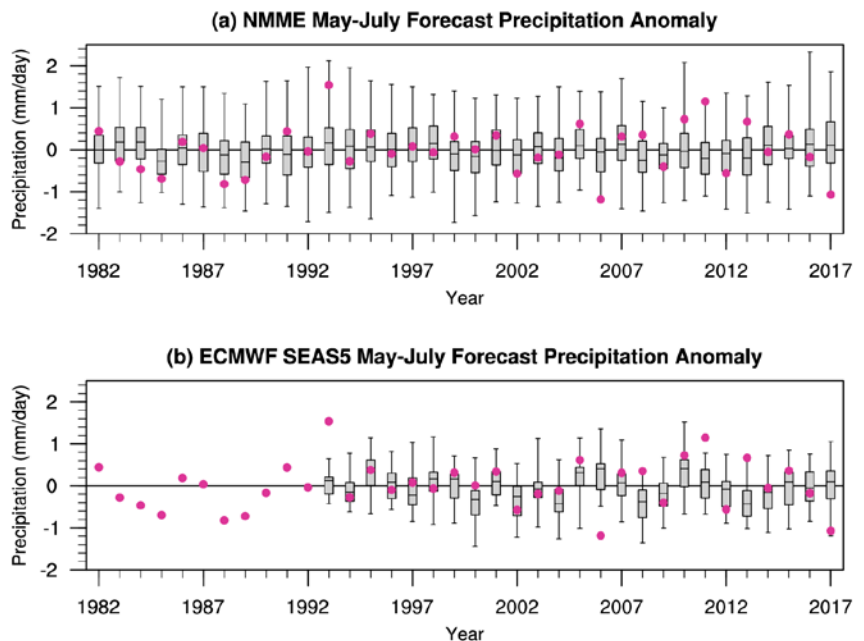
Fig. 2 For May-July averaged over the Northern Great Plains, precipitation anomaly (dot) and forecast precipitation anomaly in (a) NMME and (b) ECMWF made the preceding April (box and whisker). Boxes denote the interquartile range and whiskers the maximum and minimum.
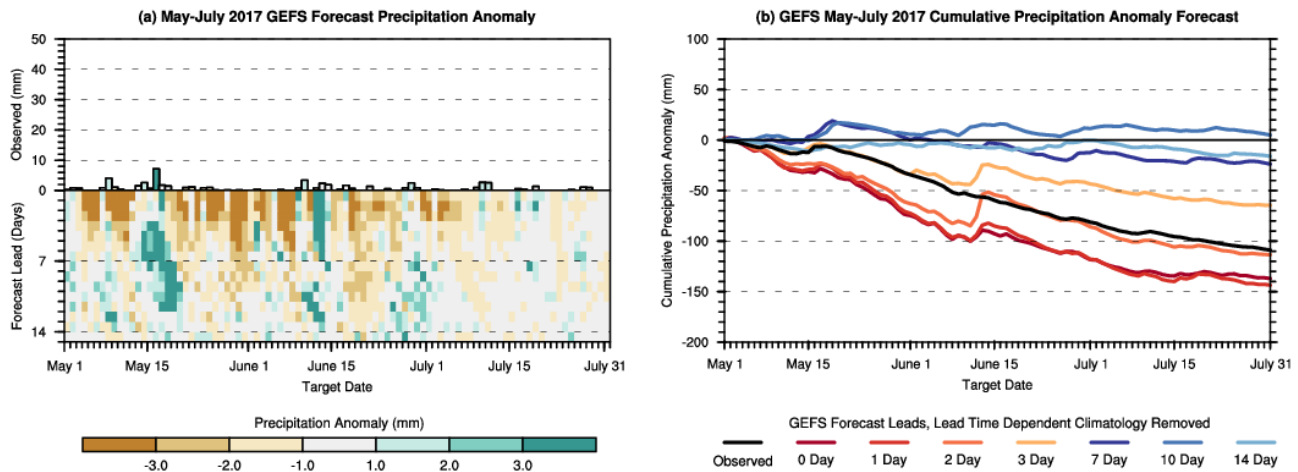
Fig. 3 (a) Observed daily precipitation (mm) and ensemble mean forecast daily precipitation anomaly (mm) as a function of lead time in GEFS averaged over eastern Montana. (b) Ensemble mean lead time dependent forecast of cumulative precipitation anomaly in GEFS averaged over eastern Montana.
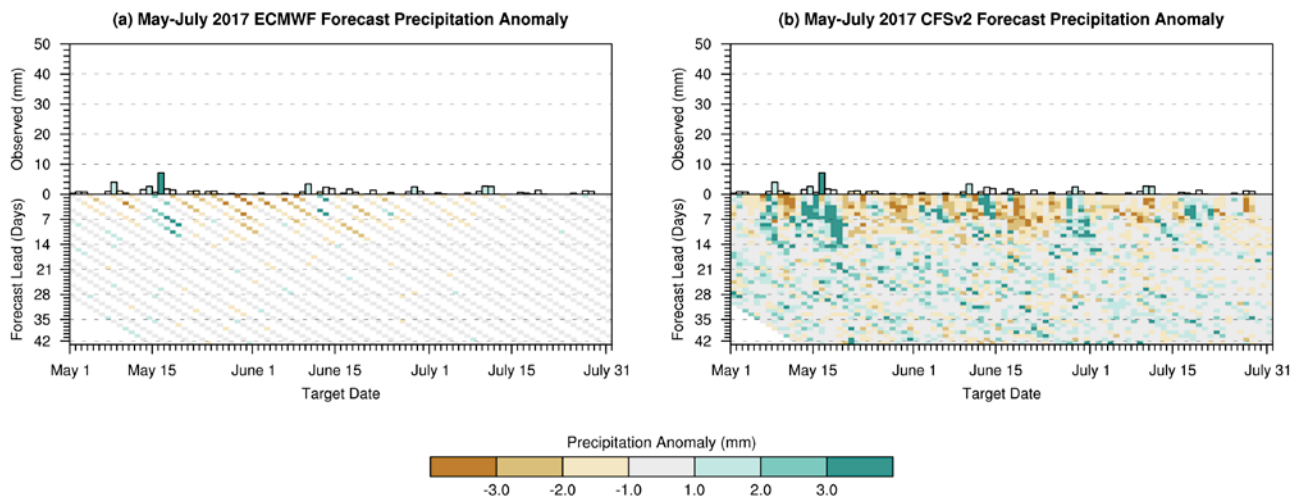
Fig. 4 Observed daily precipitation (mm) and ensemble mean forecast daily precipitation anomaly (mm) as a function of lead time in (a) ECMWF and (b) CFSv2 averaged over eastern Montana.

b) Sub-seasonal forecasts

Given that low May-July 2017 precipitation over the Northern Great Plains was not well forecast in advance of the season, the time scales at which precipitation deficits could be forecast over eastern Montana are probed. Eastern Montana is chosen because of record low May-July 2017 precipitation (Fig. 1a) and that its size is appropriate to analyze in the context of weather forecasts.

Anomalously wet and dry periods during May-July 2017 were foreseeable in GEFS approximately six to 12 days in advance of many events (Fig. 3a). Examples include the anomalously dry conditions during late May and early June and the anomalous wet conditions during mid-May. There was one notable period during which GEFS consistently called for above average precipitation up to two weeks in advance. This period, which occurred during the second week of June, did see precipitation over eastern Montana, but not the very heavy precipitation that was forecasted. The ECMWF and CFSv2 forecasts during May-July 2017 are similar to the GEFS forecasts (Fig. 4).

The GEFS prediction system captured the observed May-July 2017 cumulative precipitation deficits through sequences of up to three day forecasts (Fig. 3). By contrast, sequences of longer than five day GEFS

forecasts (7, 10, 14 days are highlighted in Fig. 3b) provided no indication that the seasonal evolution of precipitation would be different from average, despite the fact that some precipitation events were foreseeable at 6-12 days lead time. These analyses help to explain the lack of drought development being forecast by NOAA's Seasonal Drought Outlook in mid-May 2017. In so far as weather variability was fundamentally its cause, the indications for which could not be skillfully foreseen beyond a week in advance.

4. Summary

The predictability of the May-July 2017 drought over the Northern Great Plains was limited. The NMME and ECMWF prediction systems did not forecast below average May-July 2017 precipitation in advance of the season. Rather, both systems forecast an elevated probability of above average precipitation, which help to explain the lack of drought development forecast by NOAA in May 2017 during the three subsequent months. A sequence of shorter range weather forecasts from the GEFS indicate that cumulative precipitation deficits during May-July 2017 were only predictable through sequences of up to three day forecasts. Further, select anomalously wet and dry periods during May-July 2017 were foreseeable in GEFS, ECMWF and CFSv2 approximately six to 12 days in advance of the event.

References

Bureau of Reclamation, 2011: Great Plains region delivers benefits to nine states. Retrieved March 2019. [Available online at https://www.usbr.gov/gp/multimedia/publications/gp_benefits.pdf.]

Fortin, J., 2017: Wildfires choke Montana with ash and smoke as drought rages on. *New York Times, 9/7/2017*. [Available online at https://www.nytimes.com/2017/09/07/us/montana-wildfire-drought.html.]

Hamill, T. M., and Coauthors, 2013: NOAA's second-generation global medium-range ensemble reforecast dataset. *Bull. Amer. Meteor. Soc.*, **94**, 1553-1565.

Hoell, A., J. Perwitz, C. Dewes, K. Wolter, I. Rangwala, X.-W. Quan, and J. Eischeid, 2019: Anthropogenic contributions to the intensity of the 2017 United States northern Great Plains drought. *Bull. Amer. Meteor. Soc.,* **100**, S19-S24, doi:10.1175/BAMS-D-18-0127.1

Kirtman, B. P., and Coauthors, 2014: The North American Multimodel Ensemble: Phase-1 Seasonal-to-interannual prediction; Phase-2 toward developing intraseasonal prediction. *Bull. Amer. Meteor. Soc.*, **95**, 585-601.

Menne, M. J., I. Durre, R. S. Vose, B. E. Gleason, and T. G. Houston, 2012: An overview of the global historical climatology network-daily database. *J. Atmospheric Ocean. Technol.*, **29**, 897-910.

NOAA/Climate Prediction Center, 2017a: Seasonal drought outlook issued on May 18, 2017. [Available online at https://www.cpc.ncep.noaa.gov/products/archives/long_lead/PMD/2017/201705_PMD90D.]

NOAA/Climate Prediction Center, 2017b: Three month precipitation outlook issued in May 2018. [Available online at https://www.cpc.ncep.noaa.gov/products/archives/long_lead/gifs/2017/201705month.gif.]

NOAA/National Centers for Environmental Information, 2018: 2017 billion dollar disasters. [Available online at https://www.climate.gov/news-features/blogs/beyond-data/2017-us-billion-dollar-weather-and-climate-disasters-historic-year]

Otkin, J. A., M. Svoboda, E. D. Hunt, T. W. Ford, M. C. Anderson, C. Hain, and J. B. Basara, 2018: Flash droughts: A review and assessment of the challenges imposed by rapid-onset droughts in the United States. *Bull. Amer. Meteor. Soc.*, **99**, 911-919.

Saha, S., and Coauthors, 2013: The NCEP Climate Forecast System Version 2. *J. Climate*, **27**, 2185-2208.

Stockdale, T., S. Johnson, L. Ferranti, M. Balmaseda, and S. Briceag, 2018: ECMWF's new long-range forecasting system SEAS5. *ECMWF Newsletter*, **154**, 15-20, doi:10.21957/tsb6n1.

U.S. Department of Agriculture, 2017: A million acres scorched by Montana wildfires. [Available online at https://www.usda.gov/media/blog/2017/10/03/million-acres-scorched-montana-wildfires.]

U.S. Department of Agriculture, 2019: National Agricultural Statistics Service - Charts and Maps. Retrieved March 2019 [Available online at https://www.nass.usda.gov/Charts_and_Maps/Crops_County/index.php.]

U.S. Drought Monitor, May 18, 2017 [Available online at https://droughtmonitor.unl.edu/data/png/20170530/20170530_usdm.png]

Vose, Russell S., S. Applequist, M. Squires, I. Durre, M. J. Menne, C. N. Williams, Jr., C. Fenimore, K. Gleason, and D. Arndt, 2014: Gridded 5km GHCN-Daily Temperature and Precipitation Dataset (nCLIMGRID), Version 1. NOAA National Centers for Environmental Information. doi:10.7289/V5SX6B56 [November 2018].

Wang, H., S. D. Schubert, R. D. Koster, and Y. Chang, 2019: Attribution of the 2017 northern High Plains drought. *Bull. Amer. Meteor. Soc.*, **100**, S25-S29, doi:10.1175/BAMS-D-18-0115.1.

The Evolution and Status[1] of the 2017 Northern High Plains Drought and the Ongoing Southern Drought

Muthuvel Chelliah

Climate Prediction Center, NOAA/NWS/NCEP, College Park, MD

1. Introduction and background

Drought is a natural disaster occurring over land as a consequence of below normal rainfall over a period of time, affecting water supply, agriculture, livestock, and thus lives and economy. It may last from months to years. Last year, in 2017, over the United States, a drought emerged quickly in early May over the Northern Great Plains states of Montana, North and South Dakota. The losses are estimated to be in the few billion US dollars. This study is a follow up to the study/talk given at last year's Climate Diagnostics and Prediction Workshop meeting in Oklahoma entitled, "The sudden Onset of the current 2017 Northern High Plains Drought", plus now the added discussion on the status of, even a bigger, ongoing Drought in the Southern and Western United States.
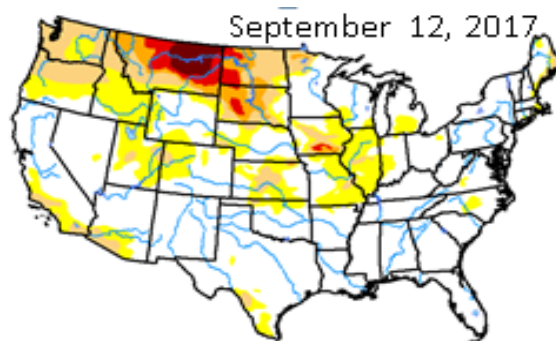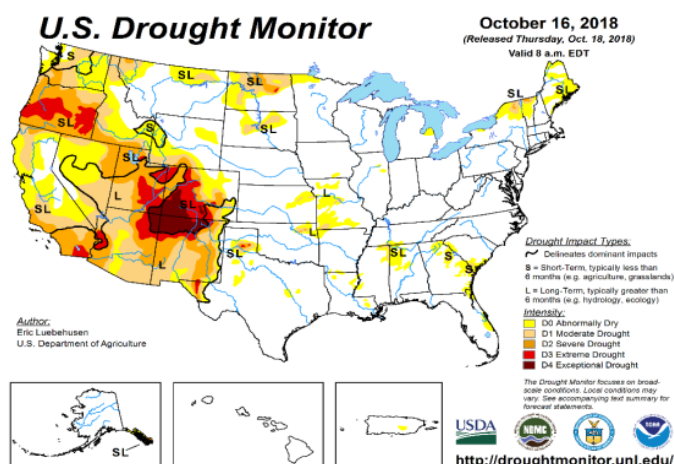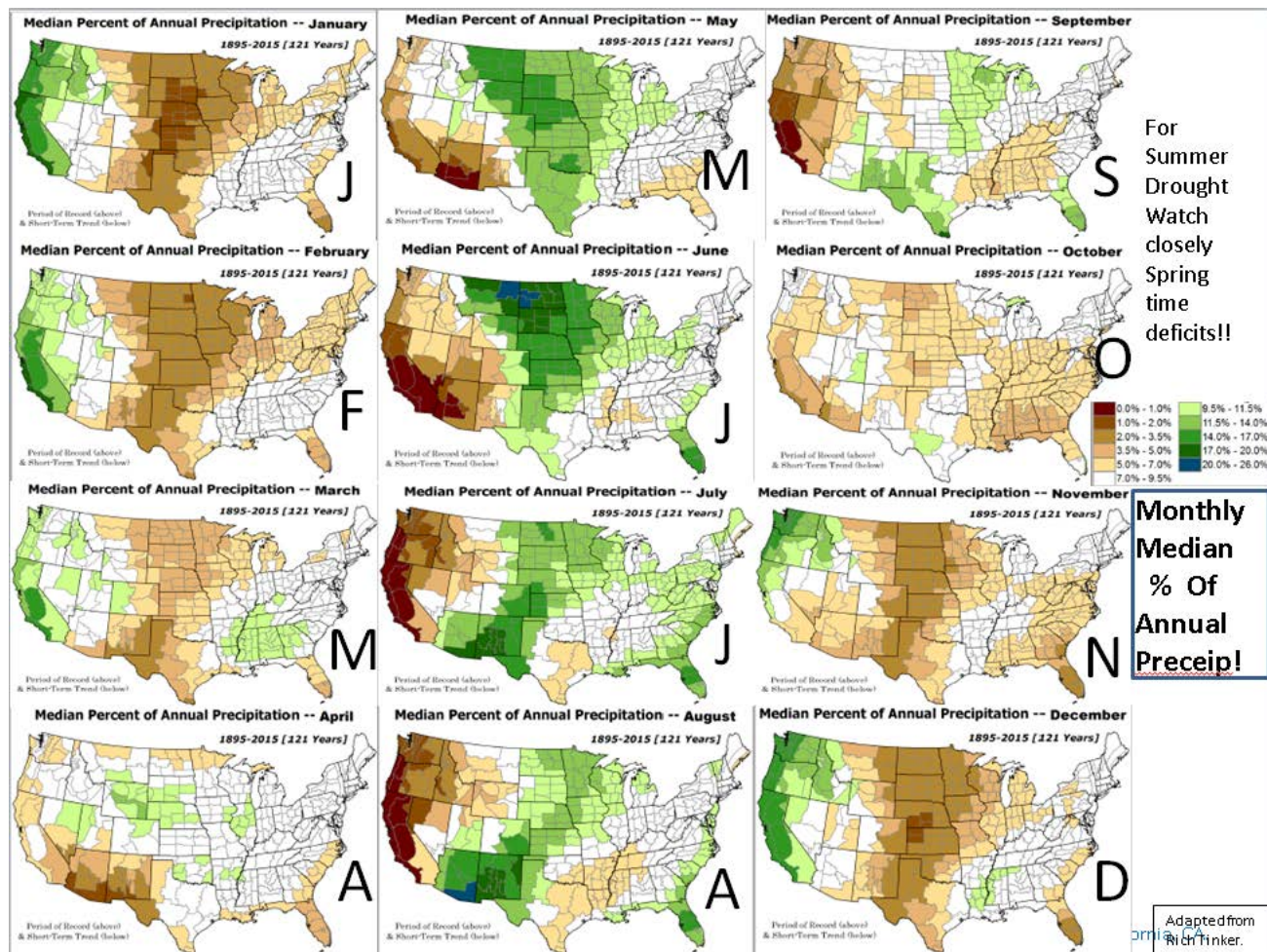

Fig. 1 The most recent DM at this time is on the left, and on the right is shown the DM when the Northern Plains Drought was near its maximum on 12th September 2017.

As regards to the 2017 Northern Plains Drought, on what happened and lessons learned, the following summary points from last year's study/talk were noted:

- Could the onset of the Drought have been addressed/caught by the Drought Monitor (DM) a bit early? - Yes!
- Was the accruing precipitation deficit in the Dakotas/Montana recognized a bit late? – Yes!
- Did we put too much trust on the model's/official rainfall forecast? – Yes!
- So, unlike flash floods, which can happen in a matte belowr of several hours or days, and can be forecast ahead of time to a certain extent, all droughts have to develop from week after week, month after month, precipitation deficit, accrued deficit of rainfall/ soil moisture conditions!
- That too depends on where? & when? Does the region have a limited-months-only rainfall season? Such as California/WA/OR/Northern Plains/Florida? Then the accrued rainfall deficit is critical, and must be watched carefully!

---

[1] as of this conference time, October 2018

Correspondence to: Muthuvel Chelliah, Climate Prediction Center, NOAA/NWS/NCEP, 5830 University Research Court, College Park, MD 20740; E-mail: Muthuvel.Chelliah@noaa.gov

Fig. 2 Annual March of the climatological monthly median % of Annual Precipitation over the United States.

So, until such time our (models'/official) rainfall forecasts improve to be more reliable and useful, existing/accrued P/SM deficits combined with realistic/cautious evaluation of whatever precipitation probability outlook, taking into account the rainfall seasonality in the region, may give us the best possible guidance of drought outlooks; will we have to develop/issue drought development probability based on existing dryness (drought monitor) and future precipitation forecast probability!! The three main take-away points in being able to assign/declare drought in a region and be able to forecast are:

- Keep watching regularly (every week!) the accrued/Accumulated Precipitation deficit in a given region over a continuous period ranging from weeks/month/seasons.
- Put this deficit in the context of what the climatological rainfall season is, for that region!! Is it a limited few months of the year, or is it more or less spread through out the year? When Is the rainfall deficit occurring?
- Future Rainfall/Temperature/Soil moisture forecast and its skill!

2. The rainfall conditions preceding and the current status of the two droughts

To better understand the evolution of the conditions preceding the above two droughts, let us first look at the climatological annual march of the precipitation over the United States, shown as the monthly median percent of annual precipitation in Fig. 2 below. It is clear that the MJJA is the main rainfall season over the Northern Plains states which experienced drought in 2017.

Early in 2017 (Jan/Feb, see above in Fig. 3), the focus was still on the major drought that was coming to an end in California, and on the drought in the southeast. Little attention was paid to the Northern Plains and
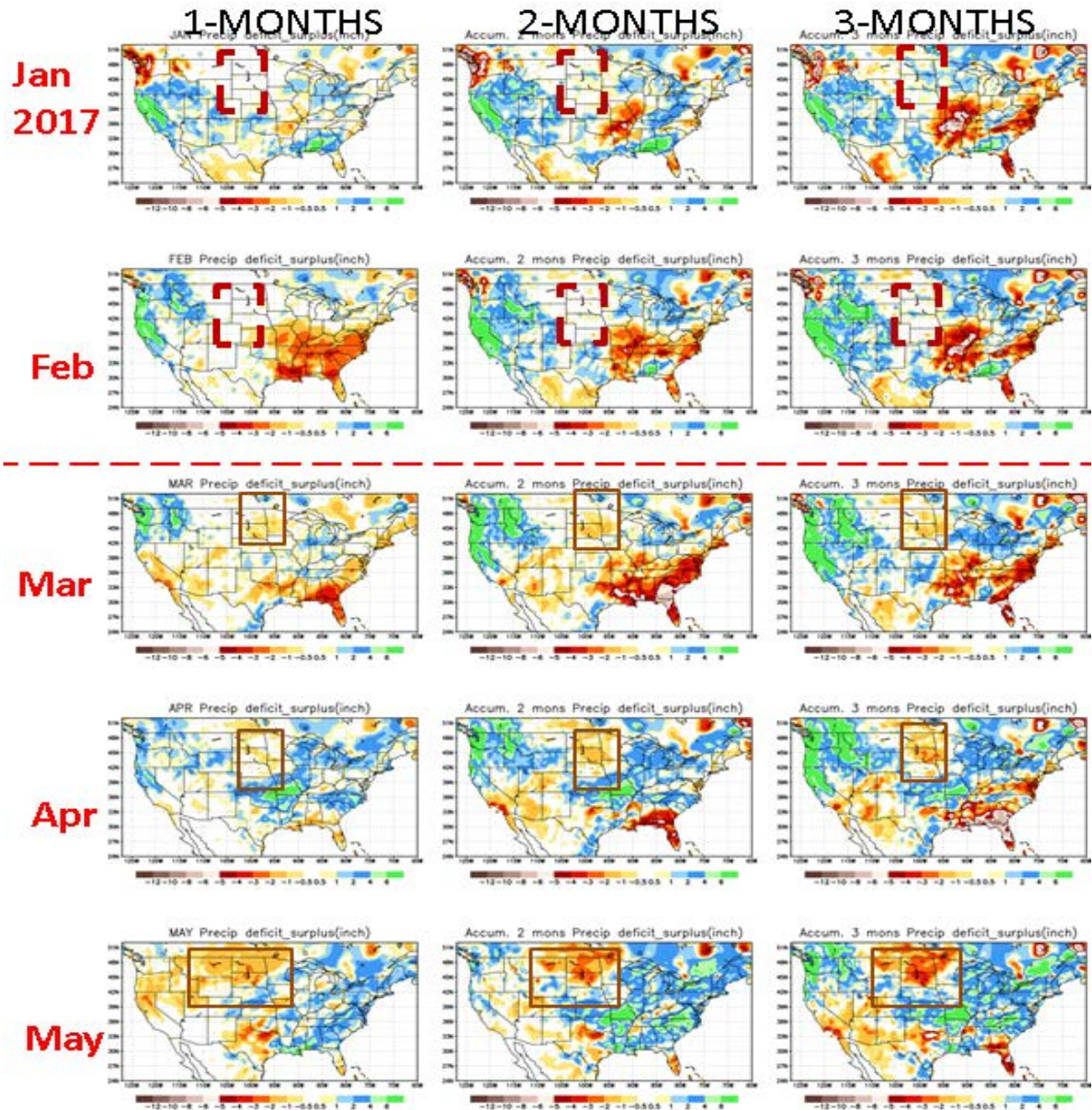
Fig. 3 Annual march of the previous 1-mon, 2-mon, 3- months actual accumulation of actual precipitation deficit/excess anomaly at month's end in January through May of 2017.

there were no signs of emerging drought there. Early signs of developing dryness/drought in the Northern Plains were beginning to emerge at the end of March (first in South Dakota), definitely in April, and firmly/fully established in May, after missing the expected rainfall in May, the first full month of the three month rainy season MJJ !

For regions with only a few months of main rainy season, say summer time in regions such as the Northern Plains, it is important to pay attention to the accruing rainfall deficits (from whatever little precipitation) in the months preceding the main rainy season. If rainfall deficits already exist in place in a region such as Montana/North and South Dakotas, leading up to the first month of the main rainy season, then to add to this

deficit, if the first month of the rainy season (say April/May) does not get the normal rainfall, then the drought is most likely to emerge there. That's exactly what happened in 2017 here in this region.

Figure 4 shows US drought monitor sampled every month from January 2017 through October 2018. The reason for the gradual increase in the drought area and intensity in the US south and west is the two back to back La Niñas (see Table 1) , which are generally associated with lack of precipitation and dryness in the South and Southwest (Fig. 5).
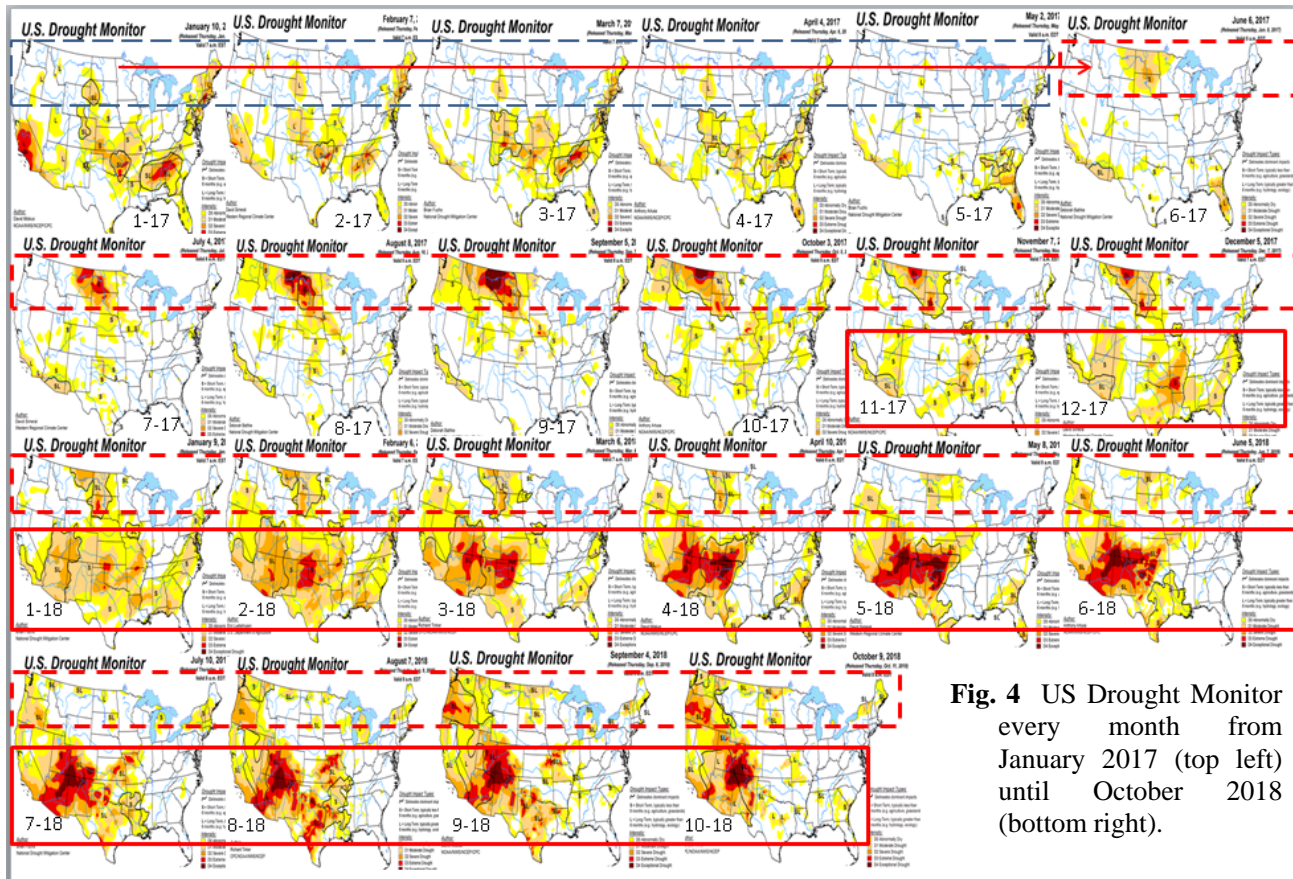
Fig. 4 US Drought Monitor every month from January 2017 (top left) until October 2018 (bottom right).

Table 1 2010-2018 cold and warm episodes by season.

Cold & Warm Episodes by Season

Year	DJF	JFM	FMA	MAM	AMJ	MJJ	JJA	JAS	ASO	SON	OND	NDJ
2010	1.5	1.3	0.9	0.4	-0.1	-0.6	-1.0	-1.4	-1.6	-1.7	-1.7	-1.6
2011	-1.4	-1.1	-0.8	-0.6	-0.5	-0.4	-0.5	-0.7	-0.9	-1.1	-1.1	-1.0
2012	-0.8	-0.6	-0.5	-0.4	-0.2	0.1	0.3	0.3	0.3	0.2	0.0	-0.2
2013	-0.4	-0.3	-0.2	-0.2	-0.3	-0.3	-0.4	-0.4	-0.3	-0.2	-0.2	-0.3
2014	-0.4	-0.4	-0.2	0.1	0.3	0.2	0.1	0.0	0.2	0.4	0.6	0.7
2015	0.6	0.6	0.6	0.8	1.0	1.2	1.5	1.8	2.1	2.4	2.5	2.6
2016	2.5	2.2	1.7	1.0	0.5	0.0	-0.3	-0.6	-0.7	-0.7	-0.7	-0.6
2017	-0.3	-0.1	0.1	0.3	0.4	0.4	0.2	-0.1	-0.4	-0.7	-0.9	-1.0
2018	-0.9	-0.8	-0.6	-0.4	-0.1	0.1	0.1	0.1				
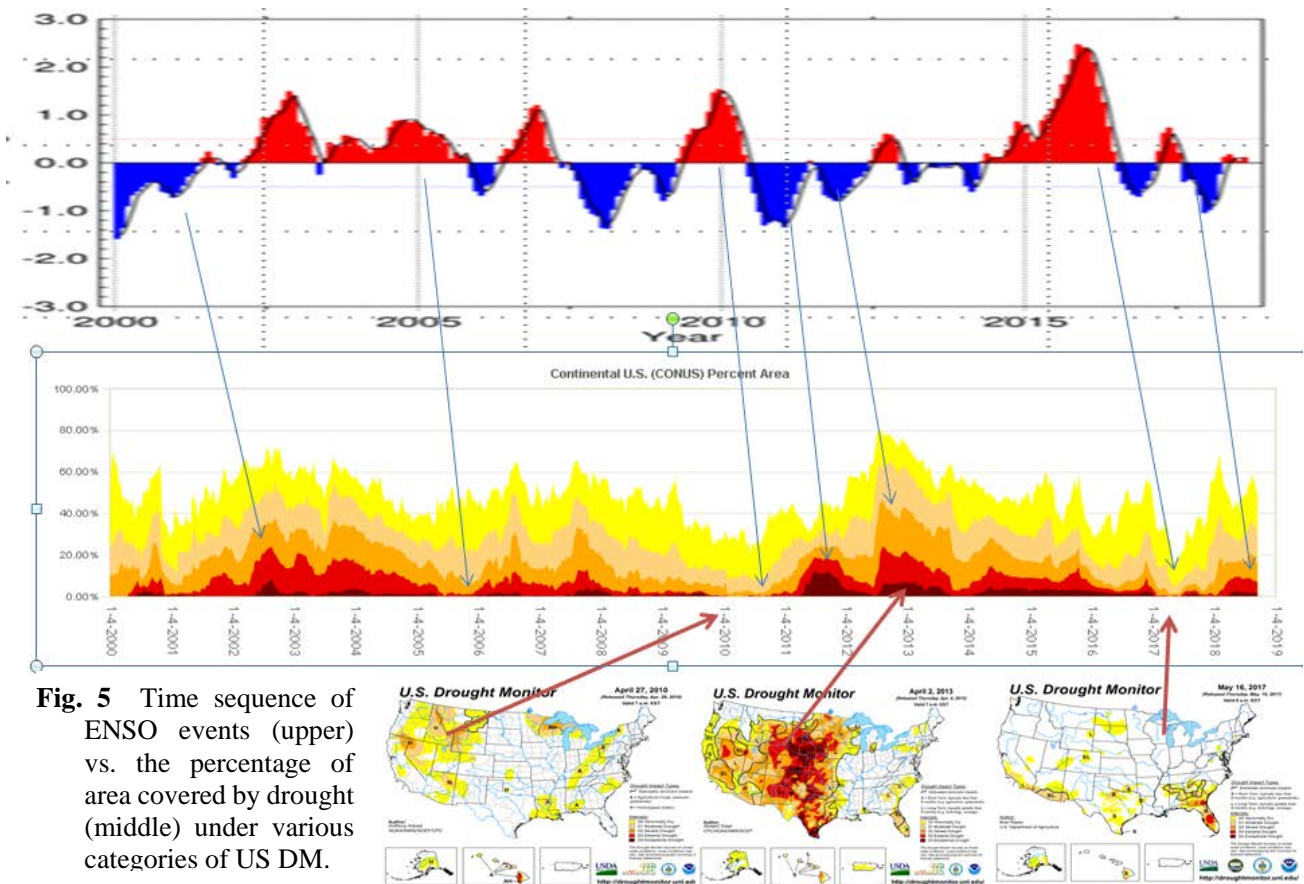
Fig. 5 Time sequence of ENSO events (upper) vs. the percentage of area covered by drought (middle) under various categories of US DM.

See also Fig. 5, which shows the time sequence of ENSO events vs. the percentage of area covered by drought under various categories (in the US Drought Monitor), following the various El Niño and La Niña events. The general El Niño/La Niña composites of US precipitation produced and shown in CPC web site (for example, not shown) also illustrates the general moistening (above normal precipitation) of US following an El Niño and the relative drying (below normal precipitation) of the country following a La Niña.

3. Summary

So, what is the status of the two droughts, the Northern High Plains Drought and the Southwest Drought? The 2017 Northern Plains Drought got a considerable reprieve from the 2018 rainfall season, is all but gone, and only very small parts of it still exist in a muted form in far northern North Dakota and vicinity. The drought in the southern or southwestern US, which also reflects the rainfall deficit from the two recent back to back La Niñas primarily in the four corners area states of AZ/NM/UT/CO, while it may likely improve with the upcoming El Nino rains, it is not clear if those rains will be sufficient to make up for these large earlier deficits.

It is very important to monitor the rainfall shortfalls on many time scales, ranging from weeks to at least a few years, and it is hard to represent these rainfall deficits at various time scales with just the S (short term) and L (long term) representation in the simple drought monitor, without precisely attributing what the S/L time scales correspond to.

Oceanic Water Cycle, Sea Surface Salinity, and the Implications for Extreme Precipitation in the US Midwest

Laifang Li[1], Raymond W. Schmitt[2], Caroline C. Ummenhofer[2], and Adwait Sahasrabhojanee[3]

[1]Earth and Ocean Science, Nicholas School of the Environment, Duke University, Durham, NC
[2]Department of Physical Oceanography, Woods Hole Oceanographic Institution, Woods Hole, MA
[3]Northeastern University, Boston, MA

1. Introduction

Moisture originating from the ocean surface is an ultimate source for precipitation on land. Over the global oceans, the largest moisture source regions are located over the subtropics where the excessive evaporation over precipitation has to be balanced by a net export of moisture (Schmitt 1995; Trenberth *et al.* 2011; Durack 2015). About a third of the subtropical moisture is transported and converged over the land area to sustain the terrestrial precipitation.

This ocean-to-land moisture transport leaves an imprint on sea surface salinity (SSS). Without an internal source of salt, surface freshwater flux associated with the oceanic water cycle is the only forcing mechanisms on SSS variation. Thus, the changes in SSS, interpreted as "Nature's rain gauge", reflect the variation of the oceanic water cycle (Curry *et al.* 2003; Durack and Wijffel 2010; Durack *et al.* 2012; Schmitt 2015).

The close relationship between the SSS and oceanic water cycle and the reliance of terrestrial precipitation on water input from the oceans indicate that SSS variation over moisture source regions can be potentially utilized as a predictor of precipitation on land. This study presents evidence that the springtime SSS over the subtropical North Atlantic can be indicative of summer precipitation over the US Midwest. We further show that the linkage between the preseason SSS and Midwest summer precipitation is through the memory of the soil moisture and a combination of thermodynamic and dynamic effects of soil moisture on the regional moisture balance.
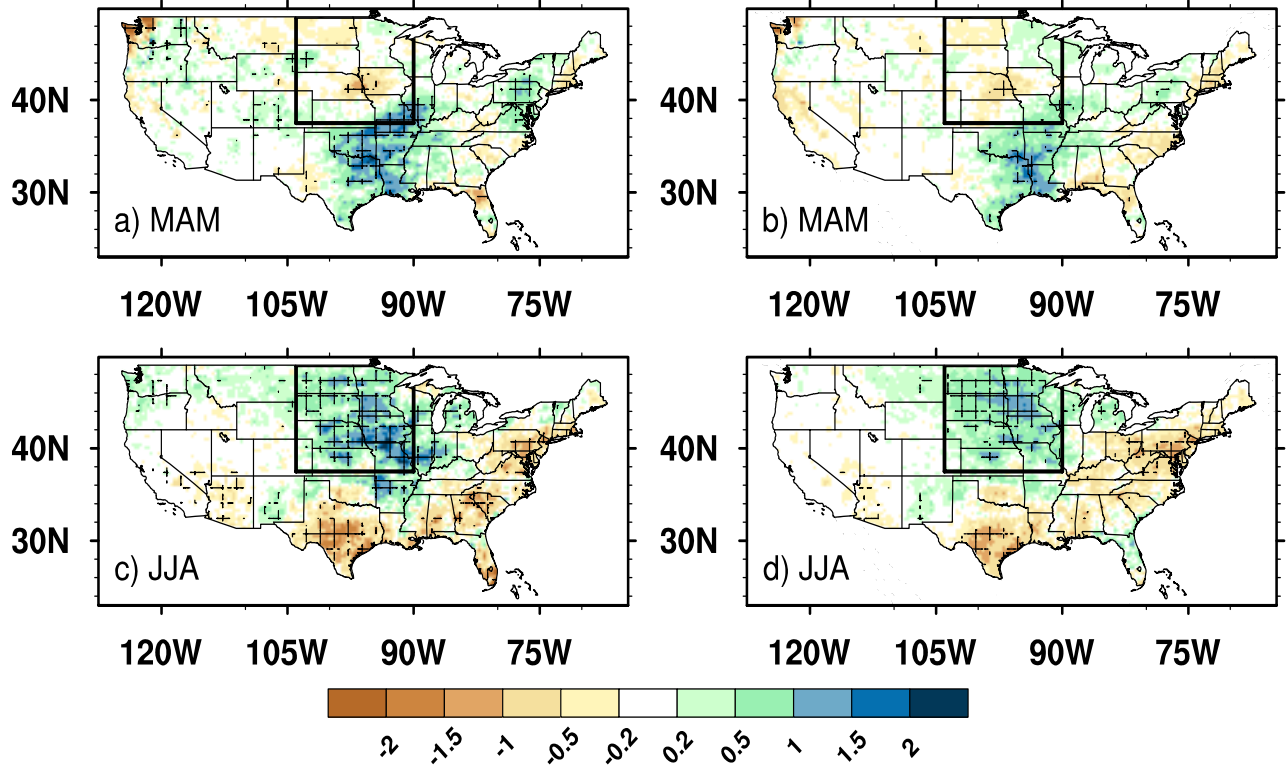
The prediction of US Midwest summer precipitation based on Random Forest algorithm suggests that preseason SSS outperforms SST-based predictors, in which a model incorporating SSS increases the explained variance by two folds. The SSS-based prediction is especially skillful in capturing the extremely wet summers in the US Midwest, such as the 1993 and 2008 cases. Thus, the newly identified salinity-based predictor can significantly improve the seasonal forecast of precipitation in the US Midwest, especially the extremes.

2. Data and methodology

The precipitation data are from the NOAA CPC US precipitation at 0.25° spatial resolution and daily temporal resolution (Higgins *et al.* 2000). Summer season is defined as the June-July-August (JJA).
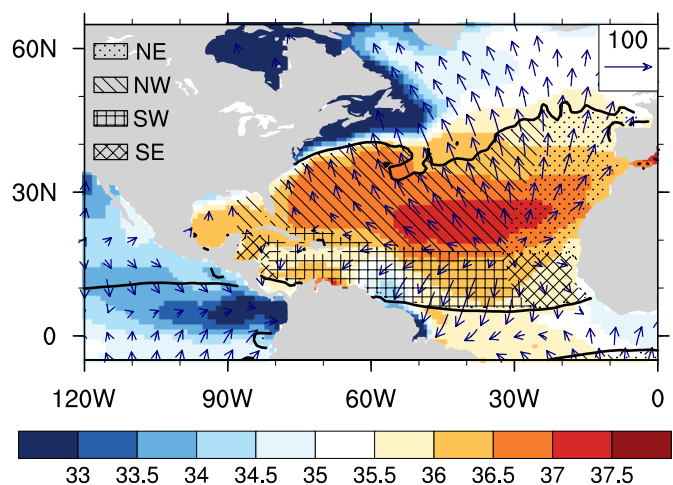
Fig. 1. MAM climatology (1950–2009) of SSS (shaded; PSU), moisture flux divergence (thick contours; mm day^{-1}) and the divergent component of moisture flux (vectors; kg m^{-1}s^{-1}) over the North Atlantic. The solid thick contour is the moisture flux divergence = 0 mm day^{-1} isoline, which defines the subtropical North Atlantic in this study. The domains used to calculate SSS indices in the four quadrants are stippled or hatched.

_____

Correspondence to: Laifang Li, Earth and Ocean Science, Nicholas School of the Environment, Duke University, Durham, NC; E-mail: laifang.li@duke.edu

Fig. 2 US precipitation anomalies (shaded; mm day⁻¹) as (a), (c) composite and (b), (d) regressed upon MAM NW
SSS index: (top) MAM and (bottom) JJA precipitation. The composite maps show precipitation difference
between the top and bottom 10% SSS cases. The regions with composite/regression precipitation anomalies
significant at the 0.05 level are hatched.

We construct a set of subtropical sea surface salinity (SSS) indices using the data archived by the EN4.2.1
(Good *et al.* 2013). We first define the subtropical ocean as an area of net divergence of atmospheric moisture
(Fig. 1). Next, the subtropical ocean is further divided into four areas according to the direction of the divergent
component of moisture flux. For example, the northwest (NW) is where the divergent component of moisture
flux is directed northwest toward the North America (Fig. 1). The SSS within the northwest subdomain is
averaged and the domain average defines the NW SSS index. The same definition applies to the NE, SW, and
SE SSS indices (Fig. 1, and Li *et al.* 2016).

We applied Random Forest (RF), a machine-learning algorithm (Breiman 2001), to predict precipitation on
land based on preseason salinity over the subtropical North Atlantic. In this study, we train the RF algorithm
with 11 predictors, including SSS, the persistence of regional precipitation, and nine climate indices
representing the oceanic and atmospheric modes of variability. All climate variables are averaged over MAM
to match the SSS predictor. The performance of the RF prediction is evaluated based on the coefficients of
determination: $R^2 = 1 - SS_{res}/SS_{tot}$ (*i.e.*, the portion of variance explained by the prediction model); $SS_{tot} =
\sum_{i=1}^{N}(Pr_i - \overline{Pr})^2$ is the total variance of observed precipitation; and $SS_{res} = \sum_{i=1}^{N}[f(X)_i - Pr_i]^2$ quantifies the
sum of precipitation variance unexplained by the RF prediction [$f(X)$].

3. Results

3.1 Relationships between pre-season salinity and US Midwest precipitation

Since the divergent component of moisture flux indicates where subtropical moisture will converge, the
above defined SSS indices reflect not only the changes in surface freshwater flux but also potential geographical
areas that will be influenced by the subtropical moisture flux. We focus on rainfall evolution over the US
following the springtime NW SSS in that the moisture flux from this portion of the subtropical oceans tends to
converge over the US (Fig. 1).

Both composite and linear regression analysis are applied to US precipitation. For the spring, the most significant precipitation anomalies associated with high NW SSS are located over the southern US (eastward of 100°W), where the positive precipitation anomalies exceed 1 mm day^{-1} (Fig. 2a-b). The positive precipitation anomalies appear to propagate northward to the Midwest in the summer (see mechanistic discussion below), leading to 1.5 – 2 mm day^{-1} above normal precipitation there (Fig. 2c-d). The composite and linear regression results are qualitatively similar, suggesting that the relationship between SSS and precipitation is generally linear and symmetric (Fig. 2)

Fig. 3 Schematic figure showing the way soil moisture bridges the 3-mon time lag between spring SSS and Midwest summer precipitation (see Li *et al.* 2018 for detail).

The processes linking the springtime SSS and precipitation in the southern United States and how they finally affect summer precipitation in the Midwest is evaluated and summarized in Fig. 3 (see details in Li *et al.* 2016, 2018). Initially, the increased moisture transport from ocean to land elevated soil moisture content in the Southern and Central US during the spring season. In the subsequent seasons, the high soil moisture content is preserved due to the 3-6-month land surface memory. The high soil moisture content serves as a moisture source to the local atmospheric column by increasing boundary layer humidity in the Southern and Central US. With the prevailing southerly wind in the summer, more moisture will be converged into the US Midwest, which is thermodynamically favorable for heavier precipitation (Meehl and Washington 1988; Delworth and Manabe 1989; Ek and Holtslag 2004). In addition, the spatial distribution of soil moisture influences precipitation through atmospheric dynamics, i.e. the intensity of the Great Plains Low-level jet (GPLLJ). Specifically, the increased soil moisture in the Central US enhances the west-to-east soil moisture gradient along the slope of the Rocky Mountains. The soil moisture content gradient increases the zonal pressure gradient and forces the GPLLJ to intensify to balance the enhanced pressure gradient (Fast and McCorcle 1990, 1991). The intensified GPLLJ brings more Gulf of Mexico moisture northward, favors moisture flux convergence in the Midwest, and thus contributes to high precipitation dynamically.

3.2 Improved rainfall prediction for the US Midwest

The physical linkage between springtime NW SSS and summer precipitation in the US Midwest suggests that pre-season SSS can be a physically meaningful predictor for Midwest precipitation (Fig. 3). We thus implemented the springtime NW SSS into the RF algorithm to predict summer precipitation over the US Midwest. According to the RF algorithm, the NW SSS is ranked as the most important rainfall predictor compared to the other 10 predictors: the importance factor of NW SSS is 0.98, but it drops to 0.53 for Niño 3.4, the second most important predictor (Fig. 4a). Using the top four predictors shown in Fig. 4a, we constructed an RF prediction model for Midwest summer precipitation. Fig. 4b shows that the four predictors together explain 41% of the observed precipitation variance, and the observed precipitation is within the 95% confidence interval (CI) of the predictions. The prediction without the NW SSS, however, largely underestimates the variability of Midwest precipitation, especially the extremely wet summer in 1993 and 2008 (Weaver et al. 2009). At the same time, the R^2 between the observation and prediction decreases to 0.16 (Fig. 4c).

3.3 Implications for extreme precipitation

The RF algorithm suggests that salty subtropical North Atlantic in the spring can be an indicator of extreme summer precipitation in the Midwest (Fig. 4). Assuming a linear relationship between SSS and precipitation, the positive SSS anomaly in 1993 will be followed by a 0.7 mm day^{-1} increase in Midwest summer precipitation, which alone explains 37% of the observed precipitation anomalies. In contrast, the previously identified ENSO predictor (Mei and Wang 2011) can only explain 8%, insufficient to account for the observed 1993 extreme
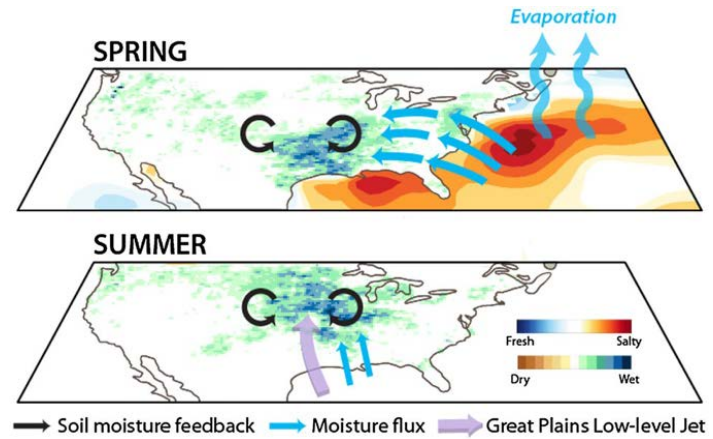
precipitation (Patricola *et al.* 2015). Further, the SSS-based prediction forecasts 0.47 mm day^{-1} precipitation anomalies in the summer of 2008. The predicted precipitation equates to 78% of the observed precipitation anomaly. Over the 1950-2015 period analyzed in this study, a higher-than-normal springtime subtropical North Atlantic SSS occurs in five out of six historical extreme precipitation events in the Midwest. Meanwhile, in all of the 6 years with the saltiest subtropical ocean, a wet summer ensued in the Midwest.

In conclusion, the results demonstrate improvements in predicting Midwest summer precipitation with the knowledge of springtime NW SSS, especially the extreme precipitation events. In addition to the previously identified ENSO link (Trenberth and Guillemot 1996; Barlow *et al.* 2001; Hoerling and Kumar 2003), incorporating preseason SSS into prediction models can thus benefit seasonal forecasting of Midwest summer precipitation.
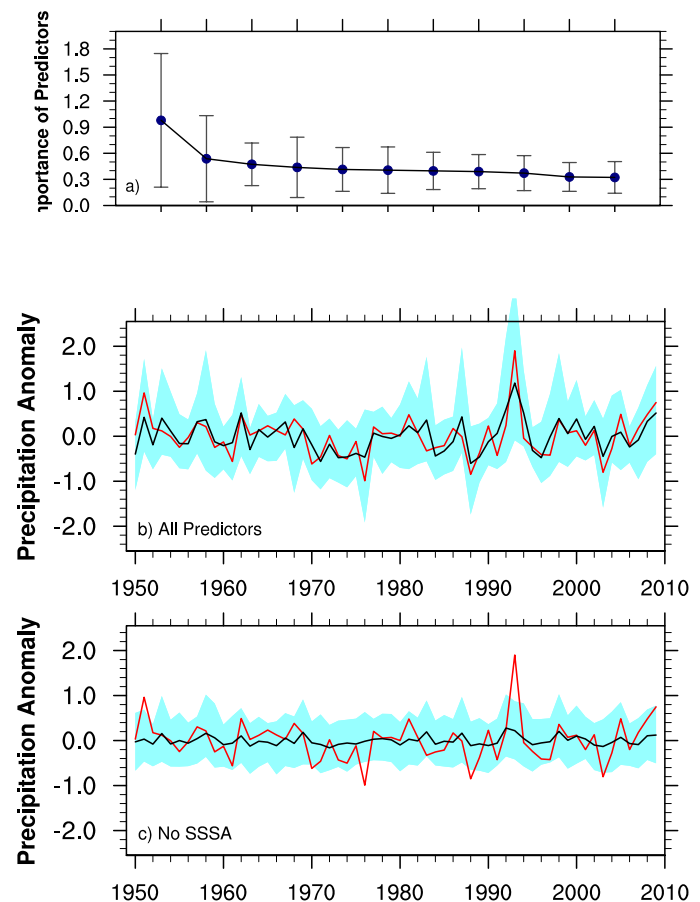
4. Conclusions

From the perspective of moisture exchange between ocean and land, this study explores the feasibility of terrestrial rainfall prediction using SSS over the subtropical North Atlantic. According to the direction of the divergent component of moisture flux, we defined a set of SSS indices (Fig. 1). We found that springtime SSS over the NW part of the subtropical North Atlantic is significantly correlated with summer precipitation over the US Midwest (Fig. 2). The

Fig. 4. (a) Importance of 11 predictors used in the RF model; (b) Prediction using top four predictors and (c) that without the NW SSS. In (b) and (c), the red (black) curves are the observations (predictions). The blue-shaded are the 95% CI of the predictions.

linkage between springtime SSS and Midwest summer precipitation is established through the ocean–land moisture transport, land surface–atmospheric coupling, and its impact on atmospheric dynamics and thermodynamics (Fig. 3).

The close relationship between springtime SSS and US Midwest summer precipitation indicates that salinity variations can provide predictive values for the US Midwest. By applying the RF algorithm to Midwest summer rainfall predictions, we show that NWSSS in the subtropical North Atlantic can generate higher prediction skill than previously identified for ENSO variability (Fig. 4). Thus, a knowledge of springtime SSS in the subtropical North Atlantic will be valuable for predicting summer precipitation over the US Midwest, an agricultural region vulnerable to floods and droughts.

References

Barlow, M., S. Nigam, and E. H. Berbery, 2001: ENSO, Pacific decadal variability, and U.S. summertime precipitation, drought, and stream flow. *J. Climate*, **14**, 2105-2128, doi:10.1175/1520-0442(2001)014<2105:EPDVAU>2.0.CO;2.

Breiman, L., 2001: Random forests. *Mach. Learn.*, **45**, 5–32.

Curry, R., B. Dickson, and I. Yashayaev, 2003: A change in the freshwater balance of the Atlantic Ocean over the past four decades. *Nature*, **426**, 826–829.

Delworth, T., and S. Manabe, 1989: The influence of soil wetness on near-surface atmospheric variability. *J. Climate*, **2**: 1447–1462.

Durack, P. J., 2015: Ocean salinity and the global water cycle. *Oceanography*, **28**, 20–31.

—, and S. E. Wijffels, 2010: Fifty-year trends in global ocean salinities and their relationship to broad-scale warming. *J. Climate*, **23**, 4342–4436.

—, and —, and R. J. Matear, 2012: Ocean salinities reveal strong global water cycle intensification during 1950 to 2000. *Science*, **336**: 455–458.

Ek, M. B., and A. A. M. Holtslag, 2004: Influence of soil moisture on boundary layer cloud development. *J. Hydrometeor.*, **5**, 86–99.

Fast, J. D., and M. D. McCorcle, 1990: A two-dimensional numerical sensitivity study of the Great Plains low-level jet. *Mon. Weather Rev.*, **118**, 151–164.

—, and —, 1991: The effect of heterogeneous soil moisture on a summer baroclinic circulation in the central United States. *Mon. Wea. Rev.*, **119**, 2140–2167.

Good, S. A., M. J. Martin, and N. A. Rayner, 2013: EN4: quality controlled ocean temperature and salinity profiles and monthly objective analyses with uncertainty estimates. *J. Geophys. Res. Oceans*, **118**, 6704–6716.

Higgins, R. W., W. Shi, E. Yarosh, and R. Joyce, 2000: Improved United States precipitation quality control system and analysis, ATLAS No. 7. NCEP/Climate Prediction Center, Camp Springs, p 40.

Hoerling, M., and A. Kumar, 2003: The perfect ocean for drought. *Science*, **299**, 691–694.

Li, L., R. W. Schmitt, and C. C. Ummenhofer, 2018: The role of the subtropical North Atlantic water cycle in recent US extreme precipitation events. *Clim. Dyn.*, **50**, 1291–1305.

—, —, —, and K. B. Karnauskas, 2016: Implications of North Atlantic sea surface salinity for summer precipitation over the US Midwest: mechanisms and predictive values. *J. Climate*, **29**, 3143–3159

Meehl, G. A., and W. M. Washington, 1988: A comparison of soil moisture sensitivity in two global climate models. *J. Atmos. Sci.*, **45**, 1476–1492.

Mei, R., and G. Wang, 2011: Impact of sea surface temperature and soil moisture on summer precipitation in the United States based on observational data. *J. Hydrometeor.*, **12**, 1086–1099.

Patricola, C. M., P. Chang, and R. Saravanan, 2015: Impact of Atlantic SST and high frequency atmospheric variability on the 1993 and 2008 Midwest floods: Regional climate model simulations of extreme climate events. *Clim. Change*, **129**, 397–411.

Schmitt, R. W., 1995: The ocean component of the global water cycle. *Rev. Geophys.*, **33** (Suppl.), 1395–1409.

—, 2015: Salinity and the global water cycle. *Oceanography*, **21**: 12–19.

Trenberth, K. E., and C. J. Guillemot, 1996: Physical processes involved in the 1988 drought and 1993 floods in North America. *J. Climate*, **32**, 1288-1298, doi:10.1175/1520-0442(1996)009<1288:PPIITD>2.0.CO;2

—, J. T. Fasullo, and J. Mackaro, 2011: Atmospheric moisture transports from ocean to land and global energy flows in reanalyses. *J. Climate*, **24**, 4907-4924.

Weaver, S. J., A. Ruiz-Barradas, and S. Nigam, 2009: Pentad evolution of the 1988 drought and 1993 flood over the Great Plains: An NARR perspective on the atmospheric and terrestrial water balance. *J. Climate*, **22**, 5366–5384.

# The Floods in Equatorial East Africa during MAM 2018 Rainfall Season

Wassila M. Thiaw, P. H. Kamsu-Tamo, and E. Bekele

Climate Prediction Center, NOAA/NWS/NCEP

ABSTRACT

The floods that occurred in equatorial East Africa (EEAF) during the spring of 2018 resulted in a major humanitarian crisis with an estimated 800,000 people affected, including injuries, disease outbreaks, and fatalities. The magnitude of the floods was only comparable to that of Oct – Dec 1997 and 1961. The heavy rains occurred in the background of a weak La Nina episode. EEAF is referred to as the region between 5°N and 5°S; 30°E – 40°E. The objective of this paper is to understand the mechanisms associated with these extremely heavy rainfall events.

The rainfall in MAM 2018 was marked with a strong intraseasonal variability surpassing the 90th climatological percentile over several days during the season. Prominent MJO events with varying magnitudes straddled the globe between December 2017 and June 2018. The MJO was significantly weak in March before regaining strength and eastward propagation in much of April. In early May, another moderate MJO event reemerged in Africa, and lasted through mid-June 2018. MJO modulates EEAF rainfall such that convection is enhanced (suppressed) during phases 2 and 3 (6 and 7) of the MJO activity. Analysis shows that rainfall upticks in MAM 2018 occurred during the phases 2 to 3 of the MJO. However, there are secondary peaks that occurred in periods when the MJO was inactive.
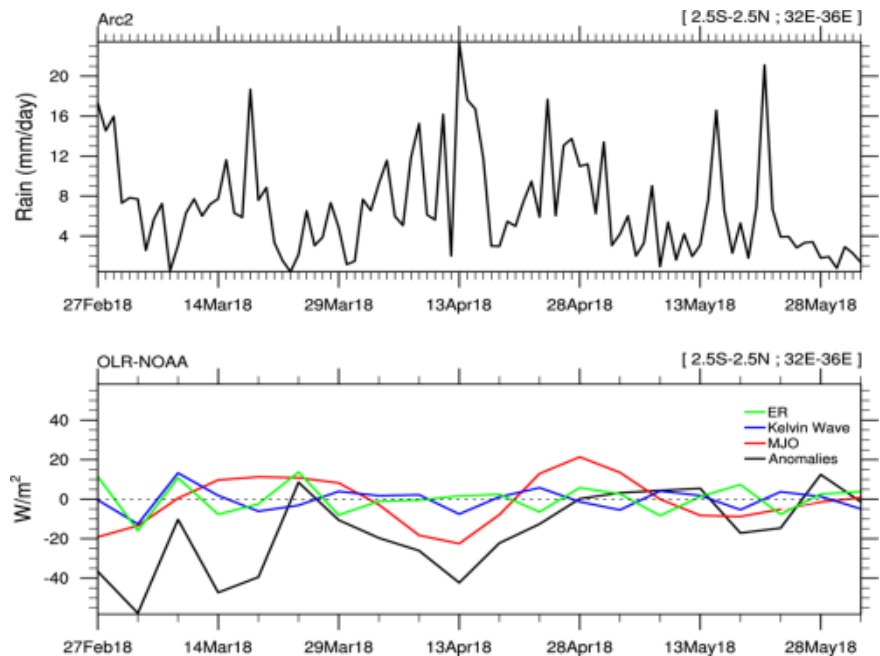
Fig. 1 (a) Evolution of daily rainfall in EEAF, and (b) OLR anomalies and contributions from CCEWs.

To determine the contributions of modes of variability on the intraseasonal timescale, we apply a space-time bandpass filter at each grid point in the OLR anomaly field to isolate propagating signals of Convectively Coupled Equatorial Waves (CCEWs). The heavy rains in Kenya in late March – early April were modulated by the MJO, with some evidence of Kelvin wave activity during this period (Fig. 1). However, during the first half of March, it seems the rains were mostly associated with propagation in the E. Rossby (ER) wave frequency, with some modulation from Kelvin waves and possibly other local factors as well. Tropical Cyclone Sagar played a significant role in the heavy rains in May 2018.

Santa Ana Events in California: Global Scale Teleconnections and Potential Subseasonal to Seasonal Predictability

Tom Murphree[1], Emily Szasz[1,2], and LT Kellen Jones, USN[1]

[1]Department of Meteorology, Naval Postgraduate School, Monterey, CA
[2]University of Southern California

1. Introduction

Wildfires in California have been especially destructive in recent years (*e.g.*, Keeley et al. 2009; Guzman-Morales et al. 2016; Mass and Owens 2019). Many of the most destructive fires have occurred in association with strong low-level, offshore, downslope synoptic wind events that occur during or soon after the end of the dry season (September-December). In southern California, especially coastal southern California, these offshore wind events are commonly referred to as Santa Ana events (*e.g.*, Raphael 2003; Rolinski *et al.* 2019). In other parts of California and western North America, dynamically similar offshore downslope wind events may be given different names (*e.g.*, Diablo winds in and near the San Francisco region; *cf.* Blier 1998). These wind events are forced by pressure gradient forces directed away from a low-level region of high pressure over or near the Great Basin and are most common in October-March (*e.g.*, Raphael 2003; Rolinski *et al.* 2019).

Santa Ana (SA) events typically last one to five days, but can last ten days or more (*e.g.*, Raphael 2003; Rolinski *et al.* 2019). SA winds increase the risk of serious wildfires, especially if they occur during or soon after the end of the summer dry season in the western US. The wildfires can, in turn lead to major societal disruptions (*e.g.*, loss or lives and property, evacuations, closings of schools and businesses, electric power outages; *e.g.*, Westerling *et al.* 2004; Keeley *et al.* 2009; Mass and Owens 2019).

We have conducted a preliminary investigation of how SA events are related to global scale, subseasonal to seasonal (S2S) processes. Our initial focus has been on characterizing and analyzing the global scale S2S anomalies associated with the development of SA events, as opposed to the synoptic to mesoscale focus of many prior studies of SA events (*e.g.*, Raphael 2003; Mass and Owens 2019). Our initial results indicate that: (a) global scale S2S processes are important in initiating SA events; and (b) variables associated with these processes may be useful predictors of SA favorable conditions at S2S lead times. The ability to skillfully predict these conditions could potentially improve the preparation for, and responses to, SA events. Jones *et al.* (2010) and Rolinski *et al.* (2019) discussed approaches to forecasting of SA events, but found low skill at S2S lead times (greater than about a week).

Our primary research questions were:

1. How are SA conditions over southern California (and dynamically related events over western North America) related to global scale climate variations?
2. What processes set up these conditions over southern California and western North America?
3. Can climate variation information be used to improve the understanding and prediction of these events?
4. What is the potential for skillful S2S prediction of these events?
5. What can we learn from these events about related S2S variations in western North America (*e.g.*, dynamically related temperature and precipitation anomalies in Alaska and the Great Plains)?

2. Data and methods

Our study region was global, especially the global tropics and extratropical northern hemisphere, but with a focus on western North America and especially southern California. Our study period was October-March 1974-2019, with a focus on November 1974-2018. We chose November as a focus month because: (a) November occurs after the dry season and, typically, before the start of substantial wet season precipitation in

_____

Correspondence to: Tom Murphree, Department of Meteorology, Naval Postgraduate School, Monterey, CA;
E-mail: murphree@nps.edu

the western US; and (b) a number of major wildfires associated with SA events have occurred in November (*e.g.*, the Camp Fire and Woolsey Fire in November 2018; *e.g.*, Cappucci 2018).

Our main variables and data sets were:

1. Daily and monthly mean atmospheric circulation variables and SST from the R1 and CFSR reanalysis data sets (Kalnay *et al.* 1996; Saha *et al.* 2010)
2. Bimonthly El Niño, La Nina, and neutral (non-El Niño and non-La Niña) information from the Multivariate El Niño Index (MEI) data set interpolated to monthly means (Wolter and Timlin 2011)
3. Daily mean Madden-Julian Oscillation (MJO) information obtained from the Bureau of Meteorology (Wheeler and Hendon 2004)

From the R1 and CFSR data, we created an index of SA events based on the area-averaged 850 hPa zonal wind (u850) over coastal southern California. This region extends from Santa Barbara to San Diego and includes both ocean and land. We used u850 for our SA index based on prior studies that indicate that the zonal wind is a good indicator of the occurrence of SA conditions (*e.g.*, Guzman-Morales 2016), and because the winds at 850 hPa facilitate the identification of periods of offshore flow in both low lying terrain (*e.g.*, over the ocean) and elevated terrain (*e.g.*, the coastal mountains of southern California). We identified SA events as periods in which the area-averaged, three-day running mean value of u850 in the southern California region was negative. The dates, numbers, and durations of the SA events that we identified using this method are very similar to those found in other studies using different methods for identifying SA events (*e.g.*, Raphael 2003; Jones *et al.* 2010; Guzman-Morales 2016).

We analyzed the anomalies for several variables for the SA dates that we identified, and 45 days before and after those dates. Our focus was on tropical and extratropical anomalous 850 and 200 hPa geopotential heights (ZA850 and ZA200) and tropical outgoing longwave radiation (OLRA). In particular, we analyzed the five-day mean anomalies for: (a) individual SA events in November 1974-2018; and (b) composites of multiple SA events in November 1974-2018. The composites represented different numbers of events, depending on the conditions we applied in the selection of the events. These conditions represented, for example the: (a) intensity and duration of the SA events; and (b) occurrence, phase, and intensity of climate variations (*e.g.*, El Niño-La Niña, MJO).

We used the resulting anomaly patterns to identify: (a) the temporal evolution of global scale anomalies associated with SA events; (b) teleconnections associated with SA events; and (c) precursors and potential predictors of SA events.

In this article, we focus on our results for SA events occurring in November. But these results are representative of our results for SA events in other months and for dynamically similar events in other parts of western North America.

3. Results

Figure 1 shows ZA850 for a major SA event in late October 2003 that contributed to several very destructive wildfires in southern California (*e.g.*, Westerling *et al.* 2004). The schematic black arrows in Figure 1 represent the corresponding wind anomalies. The positive ZA850 over western North America and offshore wind anomalies over southern California and much of the western US are typical of SA events, as are onshore wind anomalies over coastal British Columbia and southern Alaska.

Figure 2 shows ZA200 for the late October 2003 SA event, and for two other SA events in mid-November 2008 and early December 2017 that were also associated with major wildfires in southern California (*e.g.*, Keeley *et al.* 2009; Guzman-
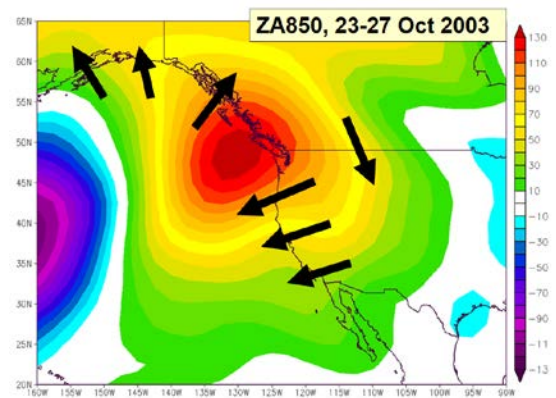
Fig. 1 Geopotential height anomalies at 850 hPa (ZA850) for 23-27 October 2003, a period in which during a major Santa Ana event and multiple wildfires occurred in southern California. The black arrows schematically indicate the associated wind anomalies at 850 hPa.
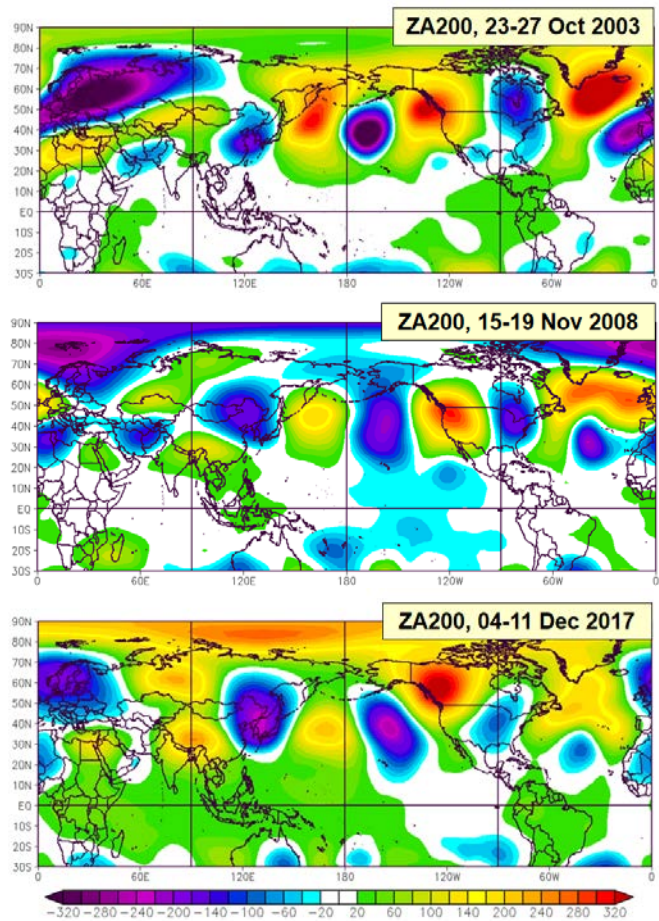
Morales 2016). Figure 3 shows ZA200 for a composite of the upper tercile of November SA events during the study period based on the magnitude of the u850 winds in coastal southern California (*i.e.*, the tercile with most offshore u850 winds). In all of the cases shown in Figures 2-3, there is: (a) a positive anomaly over western North America centered between 45-55 north latitude; and (b) an approximately zonal pattern of alternating positive and negative anomalies extending around the northern hemisphere extratropics (at about 20-70 north latitude). This zonal pattern of alternating positive and negative anomalies shown in Figures 2-3 indicates an anomalous planetary wave train with a zonal wave number 4-5 structure, with the strongest anomalies in the East Asia - North Pacific - North America region.

Figure 4 shows ZA200 for all days of the six Novembers with the greatest SA activity (the largest number of SA days), which were November 1976, 1980, 1989, 1992, and 2007. Note that the anomaly patterns are similar to those in Figures 2-3, although the anomalies are less pronounced over South Asia and there is more arcing in the wave train over the North Pacific and North America.

Animations of the ZA200 anomalies 45 days before and after individual and composite SA events in southern California (not shown) reveal that the anomalous wave trains shown in Figures 2-4 tend to: (a) develop as quasi-stationary wave trains that are first evident over South and East Asia two to four weeks prior to the SA events; and (b) then become more evident successively further to the east via eastward energy propagation into the North Pacific, North America, and North Atlantic.

These results indicate that SA events tend to be part of a global scale pattern of S2S anomalies that originates in the South Asia - East Asia sector several weeks prior to the SA events. These anomalies suggest that SA events are generated, at least in part, by anomalous wave train activity that teleconnects Asia to western North America. The MJO, and associated wave trains and teleconnections, have been identified as important factors in generating other types of anomalous conditions in western North America (*e.g.*,

Fig. 2 Geopotential height anomalies at 200 hPa (ZA200) for 23-27 October 2003, 15-19 November 2008, and 04-11 December 2017. In each period, a major Santa Ana event and multiple wildfires occurred in southern California.
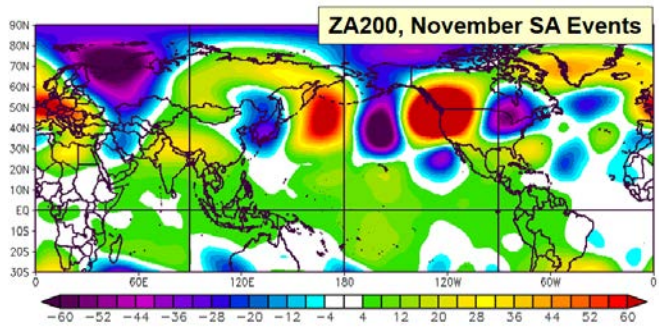
Fig. 3 Geopotential height anomalies at 200 hPa (ZA200) composited for the strongest Santa Ana events in southern California in November (the uppermost tercile of Santa Ana events).

temperature and precipitation anomalies), with the western North American anomalies lagging the initiating MJO conditions by two or more weeks (*e.g.*, Higgins et al. 2000; Mundhenk *et al.* 2018).

This led us to investigate the MJO activity occurring several weeks prior to SA events. Figure 5 shows the November composite ZA200 for 20 days after MJO phase 2. In this phase, the convective component of the

MJO occurs in the central tropical Indian Ocean and the convective component occurs in the tropical western Pacific (*e.g.*, Madden and Julian 1994). Note in Figure 5 the zonally oriented anomalous wave train with zonal wave number 4-5 structure in the northern midlatitudes, with a positive anomaly over western North America, similar to the composite ZA200 patterns based on SA events (see Figures 2-4 and the corresponding text).

Animations (not shown) of ZA200 based on phase 2 based composites (such as the composite in Figure 5) reveal an evolution of the extratropical anomalous wave train that is similar to that for the ZA200 composite based on SA events (such as that shown in Figure 3). These results indicate that MJO phase 2 may be an important factor in initiating SA events. Other results (not shown) indicate that phases 8, 1, and 3 (phases with anomalies that are similar to phase 2) may also contribute to the initiation of SA events.

Prior studies (*e.g.*, Raphael and Finley 2007; Guzman-Morales 2016; Rolinksi *et al.* 2019) have investigated the associations between El Niño, La Niña, and SA events. We found that El Niño and La Niña can alter the global scale anomaly patterns associated with SA events and with MJO phases 8-1-2-3. As an example, Figure 6a (6b) shows the November composite ZA200 for 20 days after MJO phase 2, similar to Figure 5, but with only neutral and El Niño (La Niña) days included in the composite. That is, La Niña (El Niño) days were excluded from the compositing for Figure 6a (6b). A comparison of Figures 5 and 6 indicates that El Niño and La Niña events can alter how MJO sets up SA conditions over western North America. In particular, these events can alter the overall extratropical anomalous wave train associated with MJO phase 2, including the location and orientation of the positive anomaly over western North America and, thereby alter the corresponding wind anomalies over southern California.

4. Conclusions

Our results indicate that SA favorable conditions in southern California (and related events elsewhere in the western US) are part of anomalous global S2S processes. The MJO, especially phase 1, 2, and 3, appears to be important in initiating these processes at lead times of several weeks. El Niño and La Niña may be important in modifying how MJO initiates SA favorable
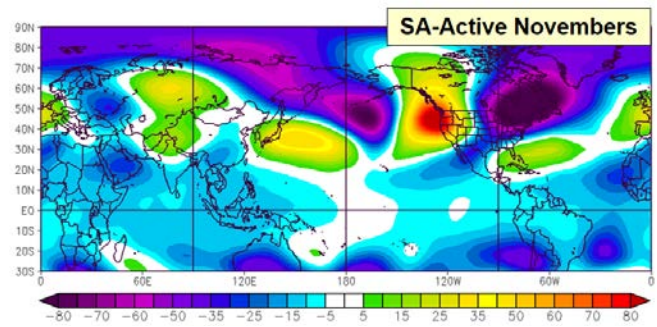
Fig. 4. Geopotential height anomalies at 200 hPa (ZA200) composited for the six Novembers with the most Santa Ana activity in southern California.
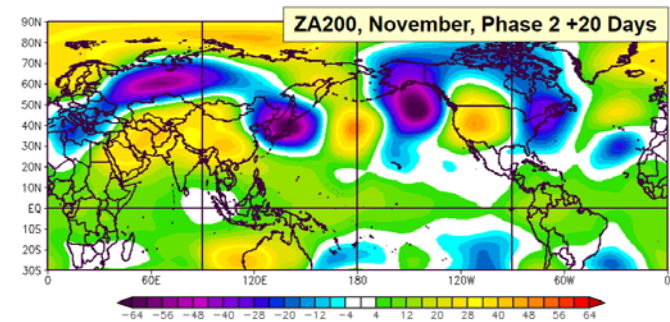
Fig. 5. Geopotential height anomalies at 200 hPa (ZA200) composited for all November days occurring 20 days after MJO phase 2.
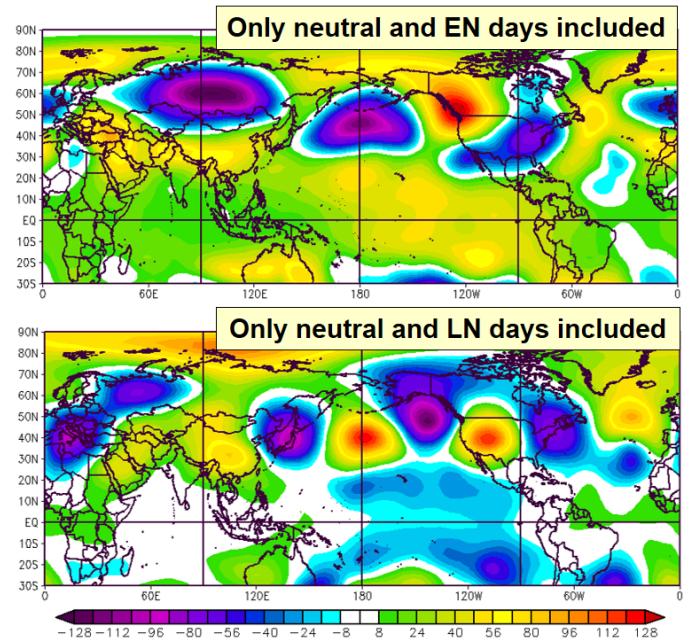
Fig. 6. Geopotential height anomalies at 200 hPa (ZA200) composited for November days occurring 20 days after MJO phase 2 but with: (a) only neutral and El Nino days included (upper panel); (b) only neutral and La Nina days included (lower panel).

conditions. The lead times associated with the process that create SA favorable conditions suggest that skillful S2S forecasting of these conditions may be possible. However, such forecasting would likely be complicated by the multiple processes that affect the setup of the extratropical anomalies associated with SA favorable conditions (*e.g.*, other climate variations, such as the Indian Ocean Dipole and the Arctic Oscillation; the extratropical background flow and other extratropical dynamic factors that help determine the wave train response to climate variations; *e.g.*, Sardeshmukh and Hoskins 1988).

The global scale pattern of anomalies that are favorable for SA conditions in southern California are also favorable for substantial anomalies in other variables and/or other locations. These include, for example, offshore wind anomalies over much of California and Oregon, and onshore wind anomalies and positive low-level temperature anomalies over southern Alaska. More generally, our initial results show that SA favorable anomalies tend to be part of a pattern of anomalous tropospheric ridging occurring over much of western North America. These larger scale anomalies support a wide range of anomalies that tend to extend from Alaska to northern Mexico and from the eastern North Pacific to central North America (*cf.* Swain *et al.* 2017). These preliminary findings suggest that improved understanding of the processes that generate anomalous ridging over western North America may contribute to a better understanding and prediction of SA events plus a wide range of related anomalies.

References

Blier, W., 1998: The Sundowner winds of Santa Barbara, California. *Wea. Forecasting*, **13**, 702–716, doi:10.1175/1520-0434(1998)013,0702:TSWOSB.2.0.CO;2.

Cappucci, M, 2018: After the fire disaster in Paradise, meteorologists mull how to improve warning system. *The Washington Post*, https://www.washingtonpost.com/weather/2018/11/28/after-fire-disaster-paradise-meteorologists-mull-how-improve-warning-system/?utm_term=.7b0f2c813

Guzman-Morales, J., A. Gershunov, J. Theiss, H. Li, and D. Cayan, 2016: Santa Ana winds of Southern California: Their climatology, extremes, and behavior spanning six and a half decades, *Geophys. Res. Lett.*, **43**, doi:10.1002/2016GL067887.

Higgins, R. W., J.-K. E. Schemm, W. Shi, and A. Leetmaa, 2000: Extreme precipitation events in the western United States related to tropical forcing. *J. Clim*ate, **13**, 793-820.

Jones, C., F. Fujioka, and L. M. V. Carvalho, 2010: Forecast skill of synoptic conditions associated with Santa Ana winds in Southern California. *Mon. Wea. Rev.*, **138**, 4528–4541, doi: 10.1175/2010MWR3406.1.

Kalnay, E., M. Kanamitsu, R. Kistler, W. Collins, D. Deaven, L. Gandin, M. Iredell, S. Saha, G. White, J. Woollen, Y. Zhu, A. Leetmaa, R. Reynolds, M. Chelliah, W. Ebisuzaki, W. Higgins, J. Janowiak, K. Mo, C. Ropelewski, J. Wang, R. Jenne, and D. Joseph, 1996: The NCEP/NCAR 40-year reanalysis project. *Bull. Amer. Meteor. Soc.,* **77**, 437–471.

Keeley, J. E., C. J. Fotheringham, and M. A. Moritz, 2004: Lessons from the 2003 wildfires in southern California. *J. Forecast.*, **102**, 26–31.

Keeley, J. E., H. Safford, C. J. Fotheringham, J. Franklin, and M. Moritz, 2009: The 2007 Southern California wildfires: Lessons in complexity. *J. Forecast.*, **107**, 287–296.

Madden, R., and P. Julian, 1994: Observations of the 40–50 day tropical oscillation – a review. *Mon Wea. Rev.*, **122**, 814–837.

Mass, C, and D. Owens, 2019: The northern California wildfires of 8-9 October 2017. *Bull. Amer. Meteor. Soc.*, 23-5-256, doi:10.1175/BAMS-D-18-0037.1.

Mundhenk, B., E. Barnes, E. Maloney, and C. Baggett, 2018. Skillful empirical subseasonal prediction of landfalling atmospheric river activity using the Madden–Julian oscillation and quasi-biennial oscillation. *npj Clim. Atmos. Sci.*, 1:20177, doi:10.1038/s41612-017-0008-2.

Raphael, M. N., 2003: The Santa Ana winds of California. *Earth Interact.*, **7**, 1–13, doi:10.1175/1087-3562(2003)007,0001:TSAWOC.2.0.CO;2.

Raphael, M., and J. Finley, 2007: The relationship between El Niño and the duration and frequency of the Santa Ana Winds of southern California. *The Professional Geographer*, **59**, 184-192, doi: 10.1111/j.1467-9272.2007.00606.x.

Rolinski, T., S. Capps, and W. Zhuang, 2019: Santa Ana winds: A descriptive climatology. *Wea. Forecasting*, **34**, 257-275, doi: 10.1175/WAF-D-18-0160.1.

Saha, S., and Coauthors, 2010: The NCEP climate forecast system reanalysis. . *Bull. Amer. Meteor. Soc.*, **91**: 1015–1057.

Sardeshmukh, P. D. and Hoskins, B. J., 1988: The generation of global rotational flow by steady idealized tropical divergence. *J. Atmos. Sci.*, **45**, 1228–1251.

Swain, D., D. Singh, D. Horton, J. Mankin, T. Ballard, and N. Diffenbaugh, 2017: Remote linkages to anomalous winter atmospheric ridging over the northeastern Pacific. *J. Geophys. Res.*, **12**, 194-209, doi: doi:10.1002/2017JD026575.

Westerling, A., D. R. Cayan, T. J. Brown, B. L. Hall, and L. G. Riddle, 2004: Climate, Santa Ana winds and autumn wildfires in southern California. *Eos, Trans. Amer. Geophys. Union*, **85**, 289–296, doi:10.1029/2004EO310001.

Wheeler, M. C., and H. H. Hendon, 2004: An all season realtime multivariate MJO index: Development of an index for monitoring and prediction. *Mon. Wea. Rev.*, **132**, 1917–1932.

Wolter, K., and M. S. Timlin, 2011: El Niño/Southern Oscillation behaviour since 1871 as diagnosed in an extended multivariate ENSO index (MEI.ext). *Intl. J. Climatology*, **31**, 1074-1087.

Flash Drought Characteristics and Prediction

L. Gwen Chen[1,2], Jon Gottschalck[2], Rich Tinker[2], Adam Hartman[2,3],
David Miskus[2], and Anthony Artusa[2]

[1]*Earth System Science Interdisciplinary Center/Cooperative Institute for Climate and Satellites,
University of Maryland, College Park, MD*
[2]*Climate Prediction Center, NCEP/NWS/NOAA, College Park, MD*
[3]*Innovim, LLC., Greenbelt, MD*

1. Introduction

Drought can develop and intensify in a short amount of time and result in major agricultural losses if they are not predicted and detected in a timely manner. Understanding the characteristics of flash drought events, when and where these events occur, their causes, and the prediction of the onset of such events on subseasonal timescales is of critical importance for impact assessment, disaster mitigation, and loss prevention. In this study, we define a flash drought event as a drought event with greater than or equal to two categories degradation in a 4-week period based on the U.S. Drought Monitor (USDM; Svoboda *et al.* 2002). We examine the characteristics of flash drought events, their temporal and spatial distributions, and distinctions from conventional, slowly-evolving drought based on rasterized USDM data from 2000 to 2017. We also identify a list of major flash drought events and investigate the causes leading to the rapid development using concurrent Phase 2 of the North American Land Data Assimilation System (NLDAS-2) data (Xia *et al.* 2012a and b). Unlike conventional drought, which is mainly driven by precipitation deficits, anomalously high evapotranspiration (ET) rates, caused by anomalously high temperatures (e.g., during heatwaves) and/or anomalously high incoming radiation, are usually present before the onset of flash drought. As a result, monitoring rapid changes in ET, along with precipitation (P) and soil moisture (SM), can provide early warnings of flash drought development. An experimental tool was created at NOAA's Climate Prediction Center (CPC) to predict the areas vulnerable for flash drought development using near real-time NLDAS-2 monitoring data, and has been used to support the operational production of CPC's Monthly Drought Outlook (MDO) since April 2018. We briefly introduce the tool in this paper and evaluate its performance during the 2018 warm season.

2. Flash drought characteristics

To analyze flash drought characteristics, we utilize historical USDM maps from 2000 to 2017. USDM maps are produced weekly in ArcGIS shapefile format through expert synthesis of various data sources, including precipitation, soil moisture, streamflow, snow water equivalent and snowpack, crop and vegetation conditions, and reservoir and groundwater levels (Svoboda *et al.* 2002). These data sources are coupled with inputs from local, state, regional, and federal levels (*e.g.*, local impact reports) to depict short- and long-term drought conditions. USDM maps contain valuable information of drought occurrence and severity, and are used by U.S. government agencies for official drought declarations. In order to use USDM as a data source for numerical analysis, we rasterized USDM maps into gridded outputs with 1/8 degree resolution covering the contiguous United States (CONUS).

Figure 1 shows the maps of drought occurrence percentage based on the rasterized 2000-2017 USDM data (the sample size is 939) for all 12 months. Drought can occur year-round and everywhere in the United States. However, some regions, such as Nevada, Arizona, and southern California, are more prone to drought than others, and drought occurrence is largely dependent on geographical location. In the maps, an east-west contrast is observed for all months, indicating that the western United States are more vulnerable to drought. Due to the slowly-evolving nature of drought, there are small variations among seasons. Yet, a slight increase in drought
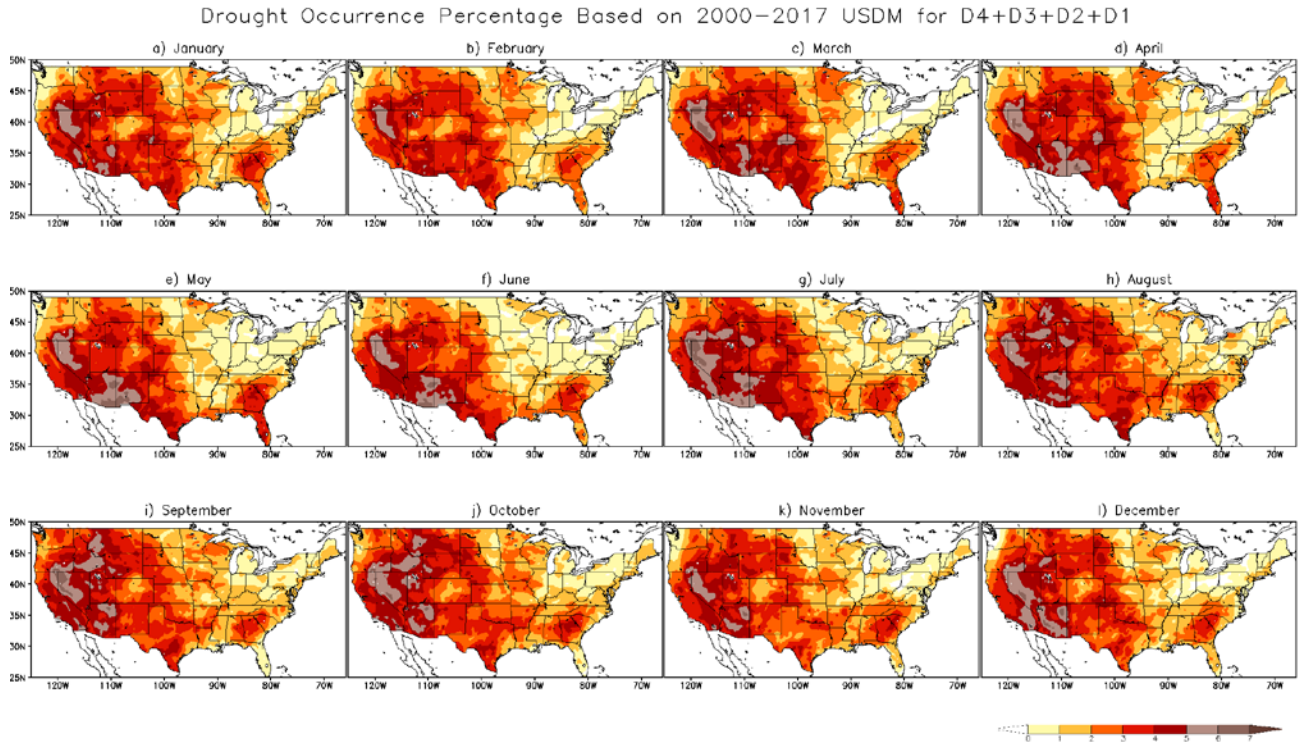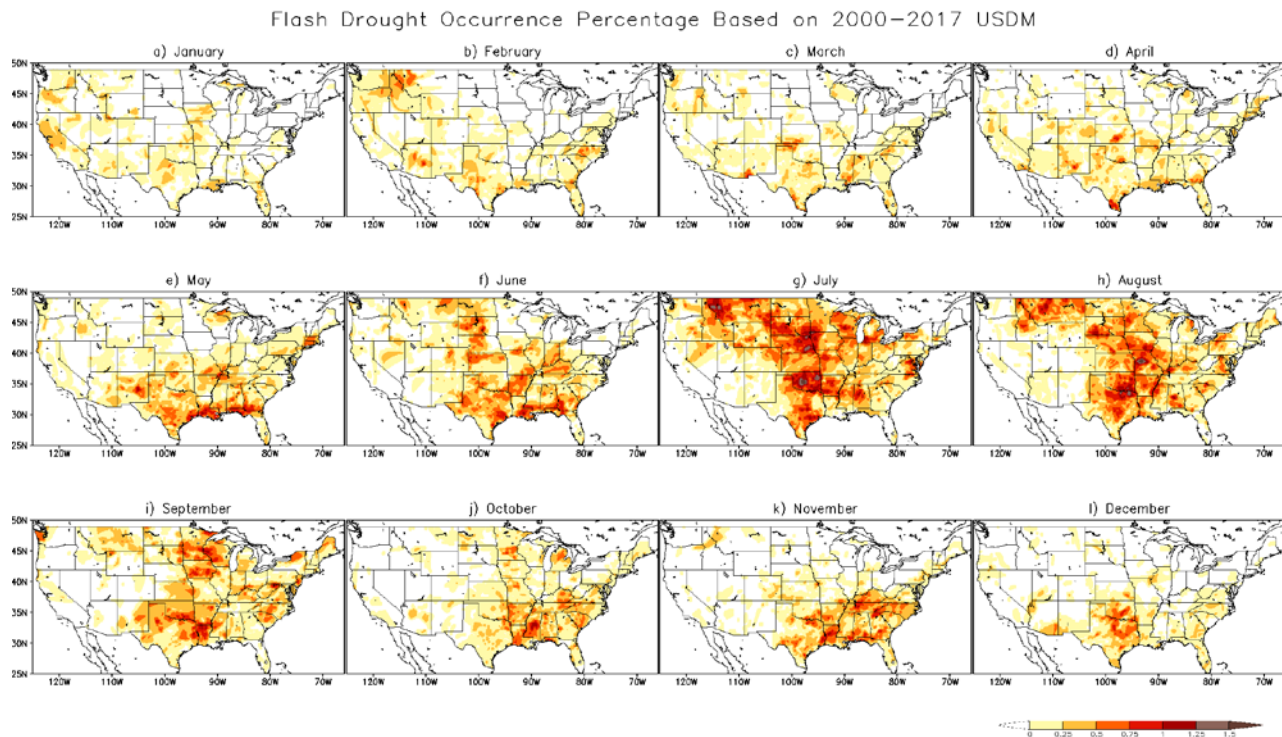

Fig. 1 Maps of drought occurrence percentage based on rasterized 2000-2017 USDM data for (a) January, (b) February, (c) March, (d) April, (e) May, (f) June, (g) July, (h) August, (i) September, (j) October, (k) November, and (l) December.

occurrence appears over the central and southern United States during the warm season, implying that temperature (T) or its related quantities (e.g., ET) may play a role in drought manifestation in summertime.

Figure 2 presents the maps of flash drought occurrence percentage (the sample size is 935) for all 12 months. In this analysis, a flash drought event is defined as a drought event with greater than or equal to two categories degradation in a 4-week period based on USDM, and this figure shows when and where these events occurred. Clearly, flash drought has preferred seasons and regions to occur. Unlike conventional, slowly-evolving drought that can occur year-round, most events occurred in the warm season and over the central United States. This characteristic is very different from conventional drought driven mainly by precipitation deficits, suggesting that different approaches may be needed to predict flash drought. By cross-examining the spatial and temporal patterns of flash drought occurrence with T and ET climatological maps derived from 1981-2010 NLDAS-2 data (figures not shown), there is strong coherence between the flash drought occurrence maps and ET climatological maps. This result further suggests that flash drought development is more related to ET processes than T effects.

To illustrate how flash drought occurred over time, Figure 3 shows the time series of the fraction of area within the CONUS that experienced flash drought development from 2000 to 2017. It is seen that flash drought occurred frequently throughout the 18 years, although some years only have a small fraction of the CONUS experiencing flash drought development. During these 18 years, five years (*i.e.*, 2000, 2003, 2006, 2007, and 2012) had widespread fast development of drought, and four out of the five years (except 2003) occurred after or during an La Nina episode, indicating that the Southern Oscillation plays an important role in widespread flash drought development over the United States. The 2012 flash drought over the central Great Plains (Hoerling *et al.* 2014) is historic, with about 18% of the CONUS experiencing sudden deterioration of conditions at the peak of drought development. The significance of this drought (and the damages it caused) has led to the awareness of flash drought and motivated the inauguration of the MDO at CPC in 2013.

In order to investigate the antecedent conditions prior to the rapid development of drought, NLDAS-2 data of the five years with widespread flash drought development were gathered and analyzed. We looked at the

Fig. 2 Maps of flash drought occurrence percentage based on rasterized 2000-2017 USDM data for (a) January, (b) February, (c) March, (d) April, (e) May, (f) June, (g) July, (h) August, (i) September, (j) October, (k) November, and (l) December.

time series of P, T, SM, ET, and runoff, their anomalies and standardized drought indices, as well as the evolution of these five droughts. The goal is to look for common features during the drought development phase. We found that all five droughts had sudden decreases in ET anomaly over the drought regions before onset. We also noticed sharp declines in SM anomaly associated with the sudden decreases in ET anomaly. Temperatures during the development periods were warmer than normal, due to heatwaves in the regions, and the 3-month standardized precipitation indexes were negative for all five droughts. These results, consistent with the findings by others (*e.g.*, Otkin *et al.* 2015 and Otkin *et al.* 2018), suggest that closely monitoring rapid changes in ET (a responding variable to T), along with P and SM conditions, can provide early warnings of flash drought development.

3. Flash drought prediction

Based on the findings above, we developed an experimental tool to predict areas vulnerable for flash drought development using near real-time NLDAS-2 monitoring data. The tool calculates the Rapid Change Index (RCI) proposed by Otkin *et al.* (2015) using 7-day mean ET anomalies. RCI is the accumulated magnitude of moisture stress changes (standardized differences) occurring over multiple weeks. Drought is likely to develop when RCI is negative. Because RCI changes with time, like all drought variables, it is difficult to capture drought developing signals by monitoring RCI maps. In order to create an intuitive drought prediction map that directly depicts drought tendency as the MDO, we count the number of occurrences that RCI is less than -0.5 over the last 30 days and plot the count maps with selected thresholds specifying P and SM conditions. The new tool started running on April 1, 2018 and has been providing real-time predictions (updated daily) to support MDO's production since then.

The top row of Figure 4 displays the new tool's predictions from April to September 2018. In these maps, yellow-to-red colors indicate areas with potential drought development or intensification. The higher the count, the more likely for drought to develop. In the end of April 2018, the new tool indicated that areas over eastern ND, northwestern MN, southern IA, and northern MO were vulnerable to flash drought development and verified well with USDM issued on 29 May 2018 (bottom row). The tool also suggested that drought may
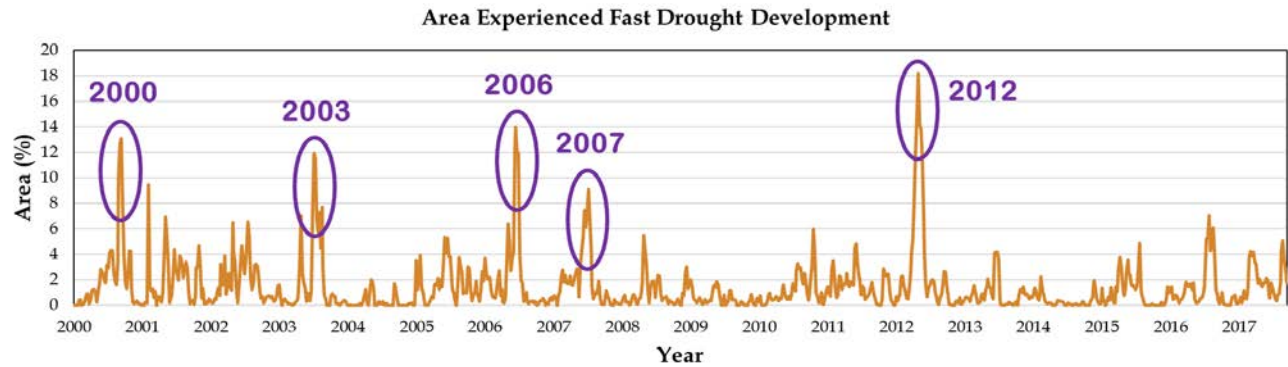
Fig. 3 Time series of the fraction of area within the contiguous United States experiencing flash drought development from 2000 to 2017.

intensify over KS, parts of OK, and northern TX; however, rainfall in May over this region (as forecasted) brought relief and improved drought conditions. Drought was not developed until June and July when heatwaves moved into the region. At the end of May 2018, the new tool indicated that flash drought may develop over western TX and LA, consistent with the MDO (third row). This prediction was verified by USDM on 26 June 2018 (bottom row). The new tool did not capture the drought development in New England and Pacific Northwest, as these two regions are not prone to flash drought. At the end of June 2018, the new tool again suggested widespread drought development over MO, AR, and eastern KS, as well as CO and UT. Aided by the heatwaves in this region, this prediction was successfully verified by USDM on 31 July 2018 (bottom row). However, the area over northeastern SD, in opposition to the development, was improved by rainfall that occurred in July. In August and September, wet conditions emerged over the MO/KS region and a series of rainstorms gradually erased the summer flash drought.

The interplay between precipitation and high temperature appears to be a challenge for flash drought prediction. The first stage of the tool is solely based on NLDAS-2 monitoring data and does not take into account forecast information. Therefore, it highlights areas with potential flash drought development if the current conditions persist into the next month. Predictions that meet this requirement (*e.g.*, areas over CO and UT for July prediction) are usually verified well. In the next stage, we will add CFSv2 forecast information into the tool to help restrain the development areas and provide potential drought improvement information.

4. Summary and Conclusions

We have examined flash drought characteristics using historical USDM and NLDAS-2 data. Unlike conventional drought that can occur year-round and everywhere in the United States, flash drought occurs mostly in the warm season and central United States. Instead of being driven by precipitation deficits, flash drought development is mainly driven by ET processes. By closely monitoring rapid changes in ET, along with P and SM conditions, we are able to predict areas vulnerable for flash drought development. An experimental flash drought prediction tool was created using the Rapid Change Index (Otkin *et al.* 2015) calculated from weekly changes of 7-day mean ET anomaly. The new tool started running on April 1, 2018 and has been used to support the operational production of CPC's Monthly Drought Outlook. Preliminary assessment of the tool shows promising results in predicting flash drought development, and the interplay between precipitation and high temperature appears to be a challenge for flash drought prediction. To improve the performance of the tool, we will add CFSv2 forecast information to help restrain the development areas and provide potential drought improvement information. A full-length technical paper (Chen *et al.* 2019) is in preparation to document details of the study of flash drought characteristics. Another paper will be written to document the methodology and assessment of the flash drought prediction tool once it is finalized.

References

Chen, L. G., J. Gottschalck, R. Tinker, A. Hartman, D. Miskus, and A. Artusa, 2019: Flash drought characteristics based on U.S. Drought Monitor, in preparation.
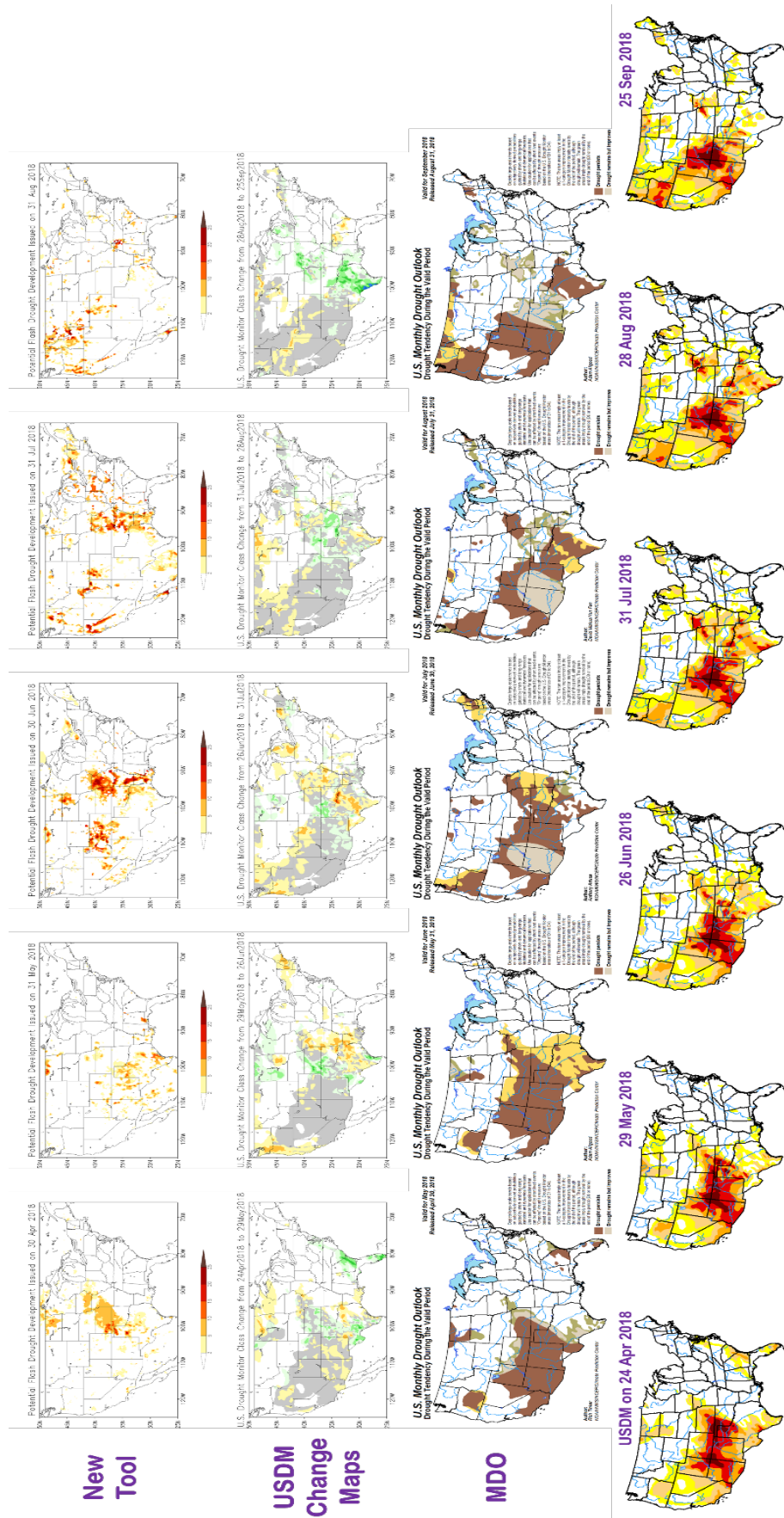
Fig. 4 Flash drought predictions during April-September 2018 and their verifications. Top row shows the predictions from the new tool, second row shows the USDM change maps, third row shows the predictions from the Monthly Drought Outlook, and fourth row shows the USDM maps at the end of each month.

Hoerling, M., J. Eischeid, A. Kumar, R. Leung, A. Mariotti, K. Mo, S. Schubert, and R. Seager, 2014: Causes and predictability of the 2012 Great Plains drought. *Bull. Amer. Meteor. Soc.*, **95**, 269–282.

Otkin, J. A., M. C. Anderson, C. Hain, and M. Svoboda, 2015: Using temporal changes in drought indices to generate probabilistic drought intensification forecasts. *J. Hydrometeor.*, **16**, 88–105.

Otkin, J. A., M. Svoboda, E. D. Hunt, T. W. Ford, M. C. Anderson, C. Hain, and J. B. Basara, 2018: Flash droughts: A review and assessment of the challenges imposed by rapid-onset droughts in the United States. *Bull. Amer. Meteor. Soc.*, **99**, 911–919.

Svoboda, M., and Coauthors, 2002: The drought monitor. *Bull. Amer. Meteor. Soc.*, **83**, 1181–1190.

Xia, Y., and Coauthors, 2012a: Continental-scale water and energy flux analysis and validation for the North American Land Data Assimilation System project phase 2 (NLDAS-2): 1. Intercomparison and application of model products. *J. Geophys. Res.*, **117**, D03109.

Xia, Y., and Coauthors, 2012b: Continental-scale water and energy flux analysis and validation for the North American Land Data Assimilation System project phase 2 (NLDAS-2): 2. Validation of model-simulated streamflow. *J. Geophys. Res.*, **117**, D03110.

Quantifying the Agreement Between Observed and Simulated Extratropical Modes of Interannual Variability

Jiwoo Lee, Kenneth R. Sperber, Peter J. Gleckler, Céline J. W. Bonfils, and Karl E. Taylor

Program for Climate Model Diagnosis and Intercomparison (PCMDI),
Lawrence Livermore National Laboratory (LLNL), Livermore, California

ABSTRACT

Using Historical simulations of the Coupled Model Intercomparison Project-5 (CMIP5) models and multiple observationally-based datasets, we employ skill metrics to analyze the fidelity of the simulated Northern Annular Mode (NAM), the North Atlantic Oscillation (NAO), the Pacific North America pattern (PNA), the Southern Annular Mode (SAM), the Pacific Decadal Oscillation (PDO), the North Pacific Oscillation (NPO), and the North Pacific Gyre Oscillation (NPGO). We assess the benefits of a unified approach to evaluate these modes of variability, which we call the common basis function (CBF) approach, based on projecting model anomalies onto the observed empirical orthogonal function (EOF). The CBF approach circumvents issues with conventional EOF analysis, including the need to correct for arbitrary signs of EOF's, and the need to test if higher-order model modes better compare with the observed modes. Compared to conventional EOF analysis of models, the CBF approach indicates that models compare significantly better with observations in terms of pattern correlation and root-mean-squared-error (RMSE) than heretofore suggested. In many cases, models are doing a credible job at capturing the observationally-based estimates of patterns; however, errors in simulated amplitudes can be large and more egregious than pattern errors.
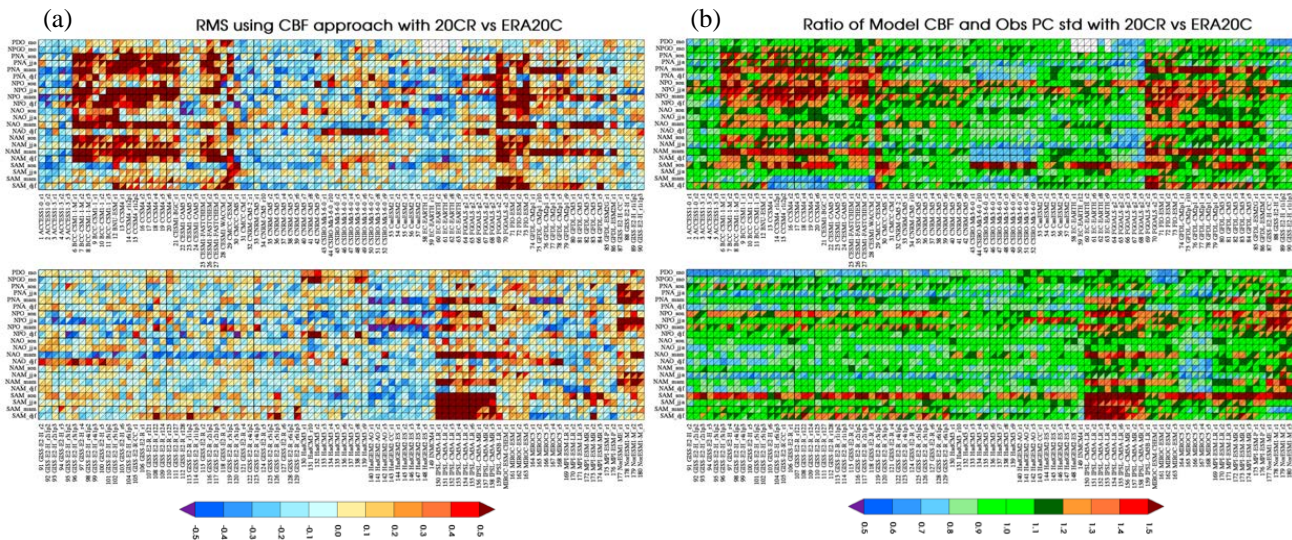
Fig. 1 Portrait plot of (a) the relative RMSE with respect to the median RMSE in each row. For sea-level pressure based modes (PNA, NPO, NAO, NAM, and SAM) in the upper-left hand triangle the model results are shown relative to 20CR whereas in the lower-right triangle the model results are shown relative to the ERA-20C. For SST based modes (PDO and NPGO), results are shown relative to HadISSTv1.1 (upper-left triangle) and HadISSTv2.1 (lower-right triangle). (b) The ratio of simulated to observed temporal variability as estimated by the standard deviations of the PC time series. Missing data is shown in white. The ratios are unitless. (From Lee *et al.* 2018)

_____

Correspondence to: Jiwoo Lee, Program for Climate Model Diagnosis and Intercomparison (PCMDI), Lawrence Livermore National Laboratory (LLNL), Livermore, California; E-mail: lee1043@llnl.gov

Sensitivity tests demonstrate that the results from our objective tests are relatively insensitive to methodological considerations (CBF vs. conventional approach), observational uncertainties in pattern (as determined by using multiple datasets), and internal variability (when multiple realizations from the same model are compared). The skill metrics proposed in this study can provide a useful summary of the ability of models to reproduce the observed EOF patterns and amplitudes (Fig. 1). Additionally, the skill metrics can be used as a tool to objectively highlight where potential model improvements might be made. We advocate more systematic and objective testing of simulated extratropical variability, especially during the non-dominant seasons of each mode, when many models are performing relatively poorly.

This work has been published in the *Climate Dynamics* in July 2018.

Reference

Lee, J., K. R. Sperber, P. J. Gleckler, C. J. W. Bonfils, and K. E. Taylor, 2018: Quantifying the agreement between observed and simulated extratropical modes of interannual variability. *Clim. Dyn.*, doi:10.1007/s00382-018-4355-4.

Influence of Positive IOD Events on the Northeastward Extension of the Tibetan High in Boreal Summer to Early Autumn

Kazuto Takemura and Akihiko Shimpo

Climate Prediction Division, Japan Meteorological Agency

1. Introduction

The Indian Ocean Dipole (IOD) is one of the main patterns of the sea surface temperature (SST) anomaly over the Indian Ocean among those patterns whose zonal contrast is in the equatorial region (*e.g.*, Saji *et al.* 1999; Saji and Yamagata 2003). IOD events generally begin in late spring, peak in autumn, and end in winter, and they exert a large influence on the climate not only in the countries around the Indian Ocean but also globally (Guan and Yamagata 2003; Saji and Yamagata 2003). Previous studies indicated the statistical relationship between positive IOD (P-IOD) events and equivalent barotropic positive height anomalies in the Northern Hemisphere mid-latitudes associated partly with an enhancement of the Tibetan High. However, the related mechanism for the equivalent barotropic height anomaly remains unclear. The results of the aforementioned studies motivate us to focus on P-IOD events preferentially given their stronger influence on the East Asian climate.

In the present study, we examine (i) the statistical characteristics of past P-IOD events since 1958 and (ii) how P-IOD events affect the enhancement of the Tibetan High. This line of attack is important for improving our knowledge about the IOD influence on the Japanese climate and how to monitor and predict that influence.

2. Data and methodology

We used three-month means from July to September (JAS) of JRA-55 (Kobayashi *et al.* 2015) and COBE-SST (Ishii *et al.* 2005) to diagnose the atmosphere circulation and the oceanographic conditions. Those three months correspond to the period from boreal summer to early autumn in the Northern Hemisphere. Normal circulation is defined as the 55-year average from 1958 to 2012 and anomaly is defined as any deviation from that.

We conducted a composite analysis to determine the statistical characteristics of the pure P-IOD events that occurred in eight of the years between 1958 and 2012, namely 1961, 1967, 1994, 2006, 2007, 2008, 2011,
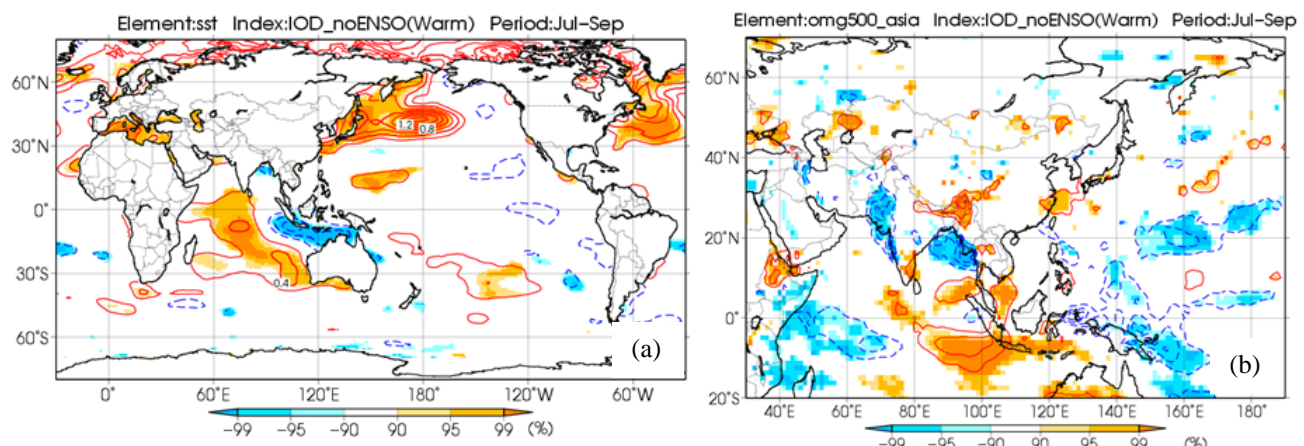

Fig. 1 Composite anomaly maps of JAS mean of (a) sea surface temperature (SST) and (b) 500-hPa vertical p-velocity in pure positive Indian Ocean Dipole (P-IOD) events from July to September. The contour lines denote the composite anomalies at intervals of (a) 0.2°C and (b) 1×10^{-2} Pa/s. The shading indicates the statistical confidence levels.

Correspondence to: Kazuto Takemura, Climate Prediction Division, Japan Meteorological Agency;
E-mail: k-takemura@met.kishou.go.jp

and 2012. To extract those IOD events, we define the dipole mode index (DMI) after *Saji et al.* (1999) as the difference between the SST deviation averaged over the western part (10°S–10°N, 50–70°E) of the equatorial Indian Ocean and that averaged over the eastern part (10°S–Eq., 90–110°E). The SST deviation is defined as the deviation from the latest sliding 30-year mean. A P-IOD event is recognized if the three-month running mean DMI exceeds +0.4°C for at least three consecutive months. To assess the impacts of IOD events alone, we extracted the pure P-IOD events from the P-IOD+ENSO events by removing those years in which ENSO events occurred simultaneously.

To examine the atmospheric responses to the diabatic heating anomalies associated with enhanced convective activities, we used a linear baroclinic model (LBM; Watanabe and Kimoto 2000, 2001) comprising primitive equations linearized exactly about a basic state defined as the 30-year average from 1981 to 2010. The model was expanded horizontally by spherical harmonics having an equation with the resolution of T42 and discretized vertically by a finite difference to 40-sigma levels.

3. Results

Figure 1 shows the composite SST and 500-hPa vertical p-velocity anomaly during the pure P-IOD events. The SST anomaly over the Indian Ocean is positive over the western to central parts and negative over the eastern part (Fig. 1a), exhibiting the typical P-IOD pattern. Corresponding to the SST anomaly over the Indian Ocean, the 500-hPa vertical velocity anomalies indicate that convective activity is enhanced over the western part of the ocean and suppressed over the eastern part (Fig. 1b). The 850-hPa streamfunction anomaly shown in Fig. 2a exhibits a clear anticyclonic circulation anomaly over the area from the seas south of India to the Maritime Continent, implying that the Rossby-wave response to the suppressed convective activity is seen (Fig. 1b). The anticyclonic circulation anomaly brings a stronger-than-normal lower-tropospheric westerly wind over the area from the Arabian Sea to the seas east of the Philippines (Fig. 2b), corresponding to an enhanced Asian
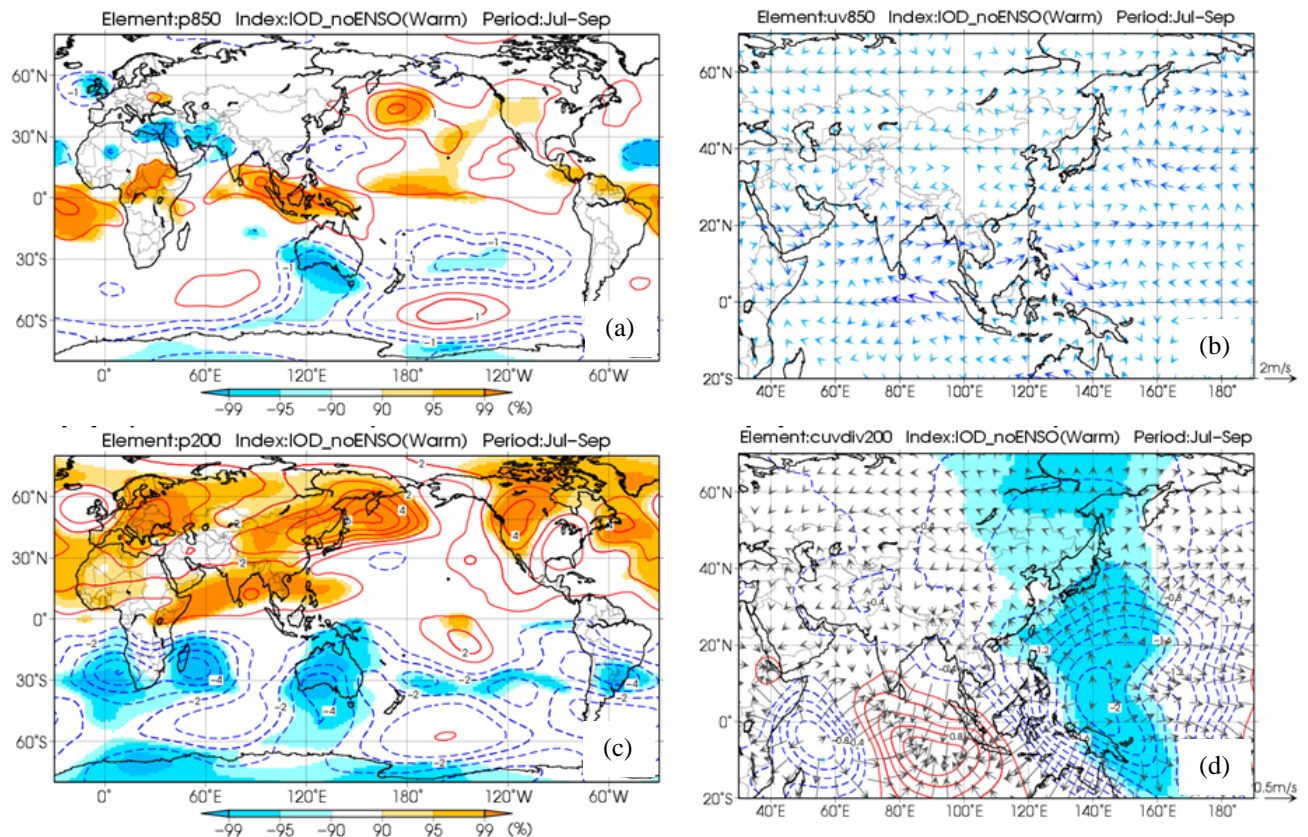
Fig. 2 As Fig. 1 but for composite anomaly maps of (a) 850-hPa streamfunction, (b) 850-hPa horizontal wind (vectors), (c) 200-hPa streamfunction, and (d) 200-hPa velocity potential and divergent wind (vectors). The contour intervals are (a) 0.5×10^6 m^2/s, (c) 1×10^6 m^2/s, and (d) 0.2×10^6 m^2/s.

summer-monsoon circulation. The westerly-wind anomaly arrives at the seas east of the Philippines and exhibits stronger-than-normal convergence with the trade winds (Fig. 2b), contributing to the enhanced monsoon trough over the area. These stronger-than-normal monsoon circulation and monsoon trough are associated with enhanced convective activities in the latitudinal band from 10°N to 20°N such as western India, the Bay of Bengal, and the wind area of the western North Pacific (Fig. 1b). The relationship between the P-IOD events and the stronger-than-normal Asian summer-monsoon circulation is also suggested by some previous studies such as Ashok *et al.* (2004) and Yang *et al.* (2010), and the enhanced convective activity over the western North Pacific can be explained by the stronger-than-normal monsoon circulation and corresponds partly to the positive SST anomaly to the east of the Philippines (Fig. 1a).

In the upper troposphere, a significant divergence anomaly is seen over a wide area of the western North Pacific (Fig. 2d) associated with the enhanced convective activity over and around the area (Fig. 1b). This causes northward divergent wind anomalies over the area from the seas east of the Philippines to East Asia across the strong meridional gradient of potential vorticity associated with the Asian jet stream. Over East Asia, the Asian jet stream shifts northward from its normal position (Fig. 3a) and the 200-hPa height shows a zonally elongated positive anomaly over the latitudinal band of 40°N (Fig. 3b), indicating a northeastward extension of the Tibetan High. To identify the origin of the height anomaly, the composite absolute-vorticity advection term in the Rossby-wave source is calculated with reference to Sardeshmukh and Hoskins (1988). The advection term shown in Fig. 3c indicates negative-vorticity forcing over the northern part of East Asia, contributing to the northward shift of the Asian jet stream (Fig. 3a) and the northeastward extension of the Tibetan High (Fig.
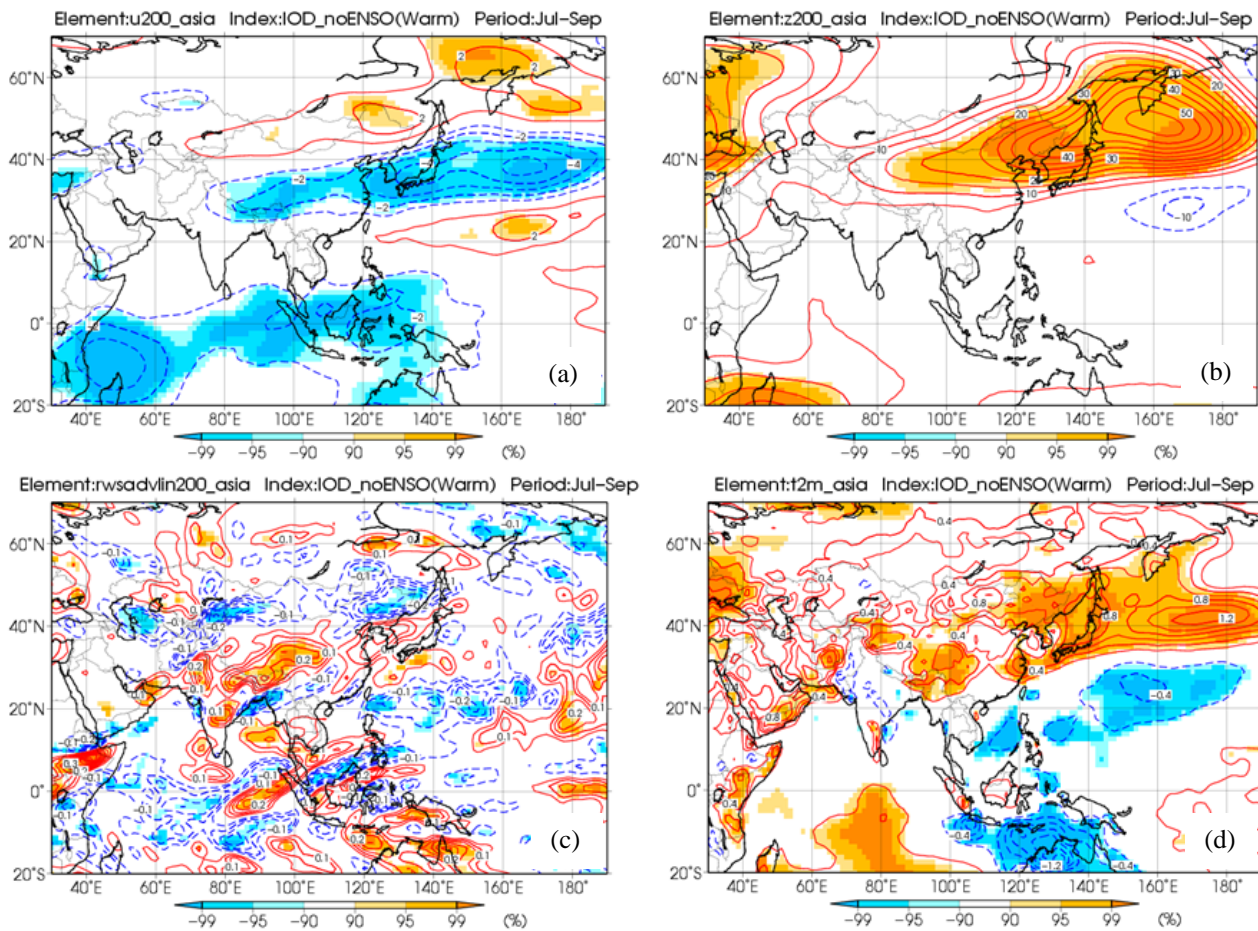

Fig. 3 As Fig. 1 but for composite anomaly maps of (a) 200-hPa zonal wind, (b) 200-hPa geopotential height, (c) 200-hPa absolute-vorticity advection by divergent wind, and (d) 2-m temperature. The contour intervals are (a) 1 m/s, (b) 5 m, (c) 0.05×10^{-5} $s^{-1}d^{-1}$, and (d) 0.2°C.

3b). The 2-m temperature shown in Fig. 3d exhibits significant positive anomalies over a wide area of East Asia, contributing to the significantly hot conditions in boreal summer and the late-summer heat over the area.

Deterministic numerical experiments are performed using the LBM. The LBM is solved with two types of hypothetical elliptical heat source centered at the points 5°S, 100°E (Experiment 1, Fig. 4a) and 5°N, 150°E (Experiment 2, Fig. 4c) with reference to the composite 500-hPa vertical p-velocity (Fig. 1b) and 200-hPa velocity potential (Fig. 2d). These two experiments are implemented to assess the impact of suppressed convective activity over the eastern equatorial Indian Ocean associated with the P-IOD events for Experiment 1 and the stronger-than-normal lower (resp. upper) tropospheric convergence (resp. divergence) over the western North Pacific for Experiment 2. The vertical integrated heating anomaly shown as the colored shading in Figs. 4a and 4b indicates cool and warm sources over the eastern Indian Ocean and the western North Pacific, respectively. The LBM responses of the 850-hPa streamfunction and horizontal wind (Fig. 4b) to the P-IOD-associated cool source (Fig. 4a) show anticyclonic circulation anomalies over the North Indian Ocean and the associated lower-tropospheric westerly-wind anomalies over the area from the Arabian Sea to the seas east of the Philippines, corresponding to the composite lower-tropospheric circulation anomaly shown in Figs. 2a and 2b. These responses indicate that the P-IOD-associated suppressed convective activity over the eastern equatorial Indian Ocean helps to enhance the Asian summer-monsoon westerly wind. Furthermore, the LBM responses of the 200-hPa velocity potential and divergent wind (Fig. 4d) to the warm source to the east of the Philippines (Fig. 4c) show a divergence anomaly and the associated northwestward divergent flow toward the northeastern part of East Asia (Fig. 4b), also corresponding well to the composite anomaly characteristics (Fig. 2d). These two LBM experiments suggest that the P-IOD events have an indirect impact on the northeastward extension of the Tibetan High through the enhanced Asian summer-monsoon circulation.
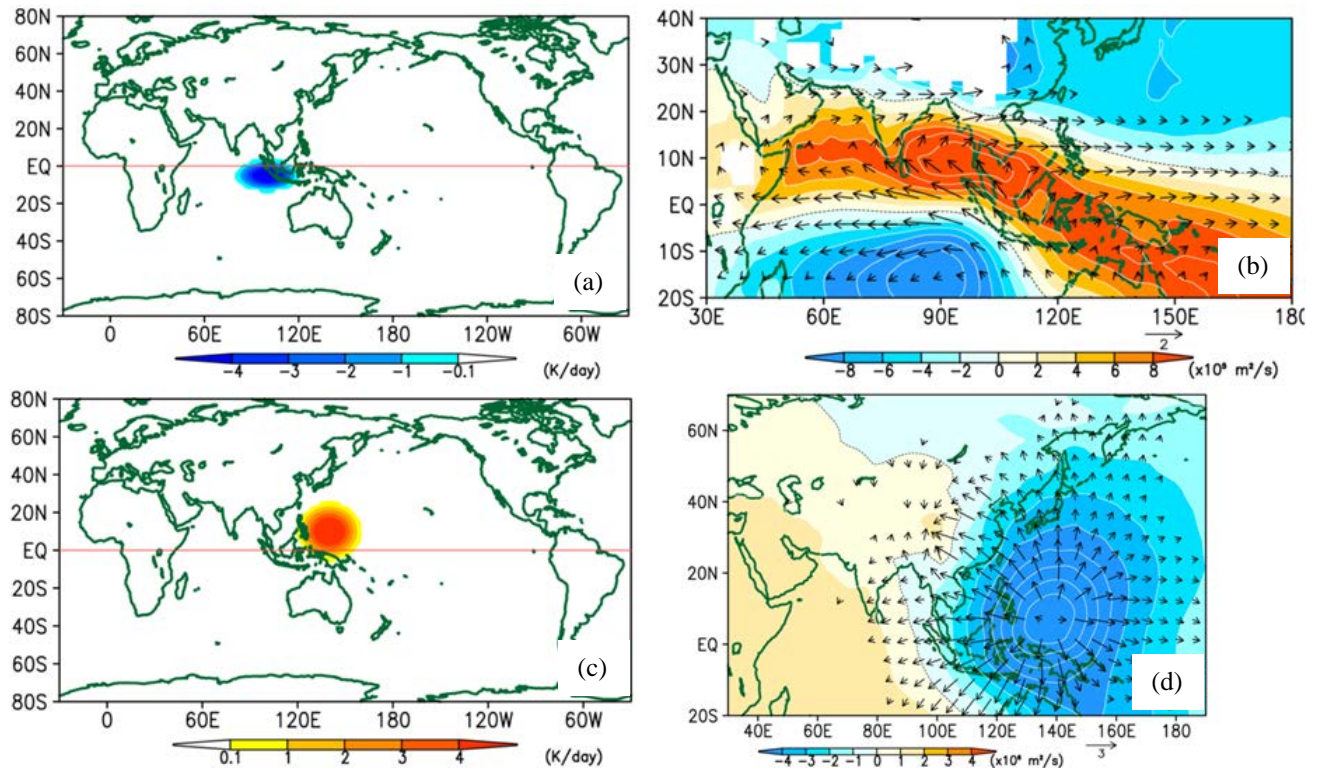
Fig. 4 Steady linear responses of (b) 850-hPa streamfunction anomaly (contours and shading) and horizontal wind anomaly (vectors) to (a) a cool source at 5°S, 100°E, and (d) 200-hPa velocity potential anomaly (contours and shading) and divergent wind anomaly (vectors) to (c) a warm source at 10°N, 140°E in the linear baroclinic model (LBM). The anomalies represent deviation from the basic states defined as normal during the period from July to September. (a) and (c) show vertically integrated heat forcing with a maximum amplitude of 8 K/d, a longitudinal width of 20°, a latitudinal width of (a) 8° and (c) 15°, and a gamma vertical distribution around the 400-hPa level. The contour intervals are (b) 2×10^5 m^2/s and (d) 1×10^6 m^2/s.

4. Conclusions

This study investigated the dynamic relationship and processes between P-IOD events and the northeastward extension of the Tibetan High, and its impact on the East Asian climate from boreal summer to early autumn based on a statistical analysis and LBM experiments. The composite analysis of P-IOD events with ENSO events removed shows a zonal contrast of the anomalous convective activities in the equatorial Indian Ocean associated with the P-IOD-related SST anomaly. The lower-tropospheric anticyclonic circulation anomaly in response to the suppressed convective activity over the eastern Indian Ocean contributes to enhance (i) the lower-tropospheric westerly wind of the Asian summer-monsoon circulation and the associated monsoon trough and (ii) the convective activity over the western North Pacific. The positive SST anomalies to the east of the Philippines may also contribute partly to the enhanced convective activity over that region. The resultant significant divergent wind over the western North Pacific in the upper troposphere crosses the Asian jet stream and provides strong negative-vorticity forcing over the northern part of East Asia, contributing to the northeastward extension of the Tibetan High. This circulation anomaly is presumed to contribute to the significantly hot conditions in boreal summer and the late-summer heat over East Asia. The responses of (i) the anticyclonic circulation anomaly over the North Indian Ocean and the Asian summer-monsoon westerly in the lower troposphere to the P-IOD-associated suppressed convective activity and (ii) the upper-tropospheric divergence to the enhanced convective activity over the western North Pacific are expressed well by the LBM numerical experiments. These impacts on the East Asian summer climate can be understood as remote and indirect influences of pure P-IOD events via the enhanced Asian summer-monsoon circulation.

Clarification of the relationship between IOD events and the East Asian summer climate is also important for assessing the predictability and progress of operational seasonal forecasting. For future perspectives on operational seasonal forecasting, using the predicted indices representing the IOD condition gives us a potential way to predict the climate from late summer to autumn in and around East Asia as suggested in previous studies.

References

Ashok, K., Z. Guan, and T. Yamagata, 2004: Individual and combined influences of ENSO and the Indian Ocean Dipole on the Indian summer monsoon, *J. Climate*, **17**, 3141–3155.

Guan, Z., and T. Yamagata, 2003: The unusual summer of 1994 in East Asia: IOD teleconnections. *Geophys. Res. Lett.*, **30**, 1544, doi:10.1029/2002GL016831.

Ishii, M., A. Shouji, S. Sugimoto, and T. Matsumoto, 2005: Objective Analyses of Sea-Surface Temperature and Marine Meteorological Variables for the 20th Century using ICOADS and the Kobe Collection. *Int. J. Climatol.*, **25**, 865-879.

Kobayashi, S., Y. Ota, Y. Harada, A. Ebita, M. Moriya, H. Onoda, K. Onogi, H. Kamahori, C. Kobayashi, H. Endo, K. Miyaoka, and K. Takahashi, 2015: The JRA-55 reanalysis: general specifications and basic characteristics. *J. Meteorol. Soc. Japan*, **93**, 5–48.

Saji, N. H., B. N. Goswami, P. N. Vinayachandran, and T. Yamagawa, 1999: A dipole mode in the tropical Indian Ocean. *Nature*, **401**, 360–363.

Saji, N. H., and T. Yamagata, 2003: Possible impacts of Indian Ocean Dipole events on global climate. *Clim. Res.*, 25, 151–169.

Sardeshmukh, P. D., and B. J. Hoskins, 1998: The generation of global rotational flow by steady idealized tropical divergence. *J. Atmos. Sci.*, 45, 1228–1251.

Watanabe, M., and M. Kimoto, 2000: Atmospheric-Ocean thermal coupling in the Northern Atlantic: A positive feedback. *Quart. J. Roy. Meteor. Soc.*, 126, 3343–3369.

Watanabe, M., and M. Kimoto, 2001: Corrigendum. *Quart. J. Roy. Meteor. Soc.*, 127, 733–734.

Yang, J. L., Q. Liu, and Z. Liu, 2010: Linking observations of the Asian Monsoon to the Indian Ocean SST: Possible roles of Indian Ocean Basin mode and Dipole mode. *J. Climate*, **23**, 5889–5902.

The 2018 US Heat Season and the Performance of the SEHOS Forecasting Tool at the CPC

Evan M. Oswald

Climate Prediction Center, NOAA/NWS/NCEP, and Innovim, LLC

1. Tools at the CPC

What is called the "Subseasonal Excessive Heat Outlook System", or SEHOS, was constructed in 2016 at the Climate Prediction Center (CPC) in conjunction with University of Maryland Cooperative Institute for Research in Environmental Sciences (UM CIRES). It provides a real-time probabilistic forecast of the occurrence of heat waves (or "excessive heat events") with lead times of 8 to 14 days. It is a direct and simple interpretation of any given forecast models' output in terms of the chances of a heat wave. A heat wave here consists of consecutive dates over either the 90th or 95th historical percentile values for the time of year and at this location. In addition to producing the probability of a heat wave occurring, also estimated are the heat wave start date and duration length, the forecast period's single-day and/or running average (2 or 3 days) maximum temperature and standardized anomalies, the historical 90th and 95th percentile values for the period, and the probabilities of exceedance of three absolute thresholds. All products come in both heat index and dry air temperature varieties, but they also come in a "hybrid" variety. These hybrid probabilities are the maximum probability/value between the heat index and temperature at any given location or in any of the various daily products.

The SEHOS uses forecasts of daily maximum temperature and heat index from two operational ensemble forecast systems/models: the ECMWF Ensemble Prediction System (ECENS) and the Global Ensemble Forecast System (GEFS). In addition, a third model-output is also utilized: an equal weighted blend of the two sets of SEHOS outputs (denoted "ECENS-GEFS"). The historical reforecasts of these models during the summertime from 1996-2014 are used, in conjunction with the NCEP R1 reanalysis, to calibrate the raw probabilistic forecasts. This is done using reliability mapping with the locally (both spatially and calendar-wise) sampled paired reforecasts and observations.

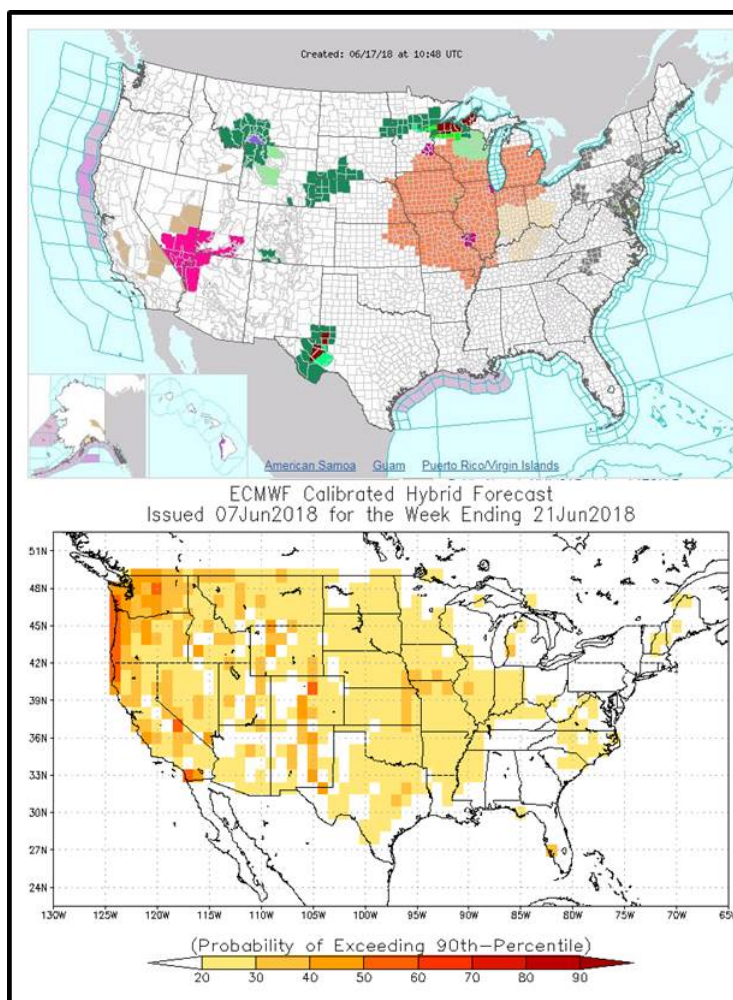**Table 1** The forecasts' skill historically, and during summer 2018.

WK 2[a]	*National AUC-ROC*	*National SEDI*
GEFS	0.61, 0.64	0.24, 0.30
ECENS	0.63, 0.67	0.28, 0.34
BLEND	0.63, 0.68	0.28, 0.36
WK 34[b]		
CFS	0.58	0.21
ECMWF	0.59	0.23

a For WK2, the first value corresponds to skill forecasting the 2018 heat season events, and the second value to historical period (~1999-2014). Both values correspond to the 90th percentile based events.

b For WK34, all values correspond to probabilities of 3-dates (not 6).

All three models are calibrated separately. Skill score metrics used to quantify the accuracy of the models include the area under the receiving operating curve (AUC-ROC) and the maximum symmetric external dependence index value (maximum over the range of thresholds by which one can diagnose "heat wave" or "no heat wave", but herein denoted as the "Max. SEDI"; Ferro and Stephenson, 2011). Generally speaking the models have accuracy/skill about a third of the way from "random guess" to "perfect predictor". The ECENS-

_____

GEFS model performs the best and the ECENS model the second best. Interestingly, the heat waves based on heat index-based heat waves saw more accuracy (on average, 28% vs. 34%) than the dry air heat waves did. Spatially, the models have the greatest skill in the Southern Plains.

An important tool called the "Probabilistic Extremes Tool" has been used by CPC forecasters since 2014. This tool produces daily maximum and minimum temperature forecasts during the week 2 period (days 8-14). These forecasts are formatted as the probability of exceeding a range of absolute (*e.g.* over 100F) and relative thresholds (*e.g.* below the 5th percentile, over the 90th percentile). Daily resolution probabilistic forecasts are helpful to CPC forecasters when they need support forecasting start and stop dates of heat waves, albeit potentially at the expense of skill (*i.e.* temporal averages are easier to forecast beyond week 1). This tool also provides the climatological values and percentiles associated with the various thresholds, at the forecasted time of year. With respect to air temperatures, while daily maximums and minimums are both considered, heat index is not forecasted within this tool. A limited form of this tool is also available to the public via the CPC webpage. In addition to air temperatures, this tool is also available for precipitation and 10m wind speed. The only dynamical model that currently drives the temperature forecasts from this tool is the GEFS, but forecasts from the ECENS and Canadian Ensemble Forecasts (CAN) are

Fig. 1 (Top) National Weather Service Watches, Warnings and Advisories map the morning of June 17, 2018. Orange represents heat advisories for the afternoon, and the embedded magenta colors are excessive heat warnings. (Bottom) Probabilistic forecasts of a heat wave during the week ending on June 21st, as issued on June 7th by the ECENS powered version of the week 2 tool.

said to be forthcoming. Calibration of the probabilistic forecasts was accomplished via ensemble regression (Unger *et al.* 2009) and an in-house observational 2-meter above ground level (AGL) temperature dataset over the 1986-2010 period. Skill scores of the real-time forecasts were calculated using the ranked probability skill metric from 2014-2017. Skill scores vary depending on the lead time and percentile values, but generally range from about 4-16% of the way to "perfect" from "random guess".

Forecasting at for the week 3-4 timescale, while still currently experimental in nature at the CPC, is currently supported by a different suite of dynamical based tools. It doesn't have a snazzy name – perhaps indicative that it is still very new (developed in 2018). This tool leverages the ECENS (Mondays and Thursdays) and the CFS model (daily) model forecast outputs in order to forecast the presence of multiple extremely high daily mean temperatures in week 3-4. Forecast guidance for this tool is less weather-based than the two previously mentioned tools: focusing on daily mean temperatures rather than daily maximum, and only requiring a number of (3 or 6) hot (over the 92.5th percentile) dates and thus dropping the *consecutiveness* aspect of the requirement. There is also provided (uncalibrated) guidance for the timing within the period for the dominant signal (*i.e.* spatial location). The CFS model is taken as a 3-day super-ensemble consisting of a meager

12 ensemble members, while the ECENS is not a super-ensemble but has over 4x (51) the number of ensemble members. Probability is taken as the percent of the ensemble members that have or exceed the number of required hot dates during the 2-week forecast period. The raw probability is then calibrated using the historical relationship (*i.e.* reliability mapping) between forecast probabilities and observed frequency over all locations and dates (*i.e.* its' not dynamic in space and calendar date).

The week 3-4 tool suite skill was measured using the AUC-ROC and SEDI metrics. Nationally, the ECENS had a 0.59 AUC-ROC and the CFS had a 0.58 when forecasting 3-or-more hot dates during the 2-week period; so about 16-17% of the way to "perfect" from "random guess". The same metric, but for 6-or-more days, was either the same or a very similar value. In regards to the nation-wide SEDI metric the ECMWF had a 0.23 and the CFS had a 0.21 when forecasting 3 or more hot dates. Therefore, the skill of this tool is roughly 22% of the way to "perfect" from "random guess".
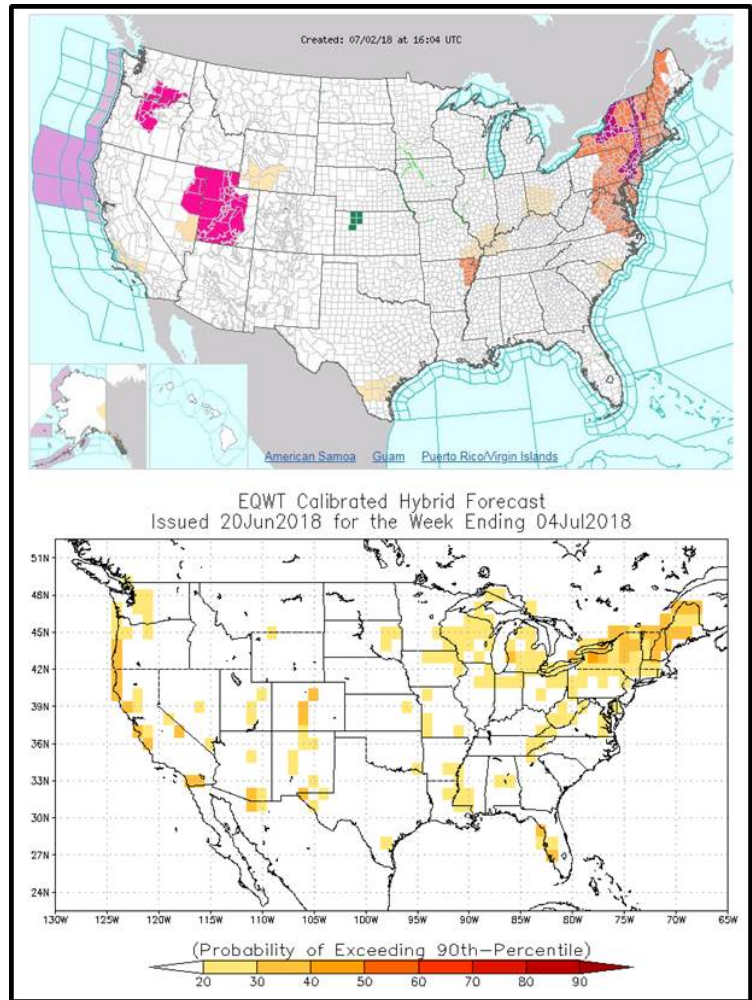
2. Overview of the 2018 season

The summer of 2018 was very hot compared to historical norms, especially in the Southwestern, Southern Plains and Northeastern regions. Nationally, it compared well with other recent warm summers such as 2011, 2012, and 2016. Examination of nation-wide "google search

Fig. 2 (Top) Same as Figure 1 but for the morning of July 2nd, 2018. (Bottom) Probabilistic forecasts of a heat wave during the week ending on July 4th, as issued on June 20th by the GEFS-ECENS equal-weighted blend forecast powered version of the week 2 tool.

frequency" for terms such as "heat wave" and "hot weather" illustrated 5-6 prominent spikes throughout the summer with one such extremely large episode in early July. While it is subjective, our analysis delineated about 15 warm-season heat waves in the US in 2018. At the end of this article we will discuss in detail a handful of the more prominent episodes.

The skill of the forecasts in the 2018 heat season was comparable to forecasts from the model over the recent historical period. Skill metrics (Table 1) were calculated for all the models against historical observations (NCEP/NCAR R1 dataset) over the 1999-2014 period, at a minimum, and with sample sizes ranging from 400-4,400. The week 2 models (GEFS, ECENS, GEFS-ECENS) demonstrate more skill than the Week 34 models (CFS, ECENS). The former are just under a third of the way towards "perfect predictor" from "random guess", while the latter are just under a fifth of the way towards "perfect predictor". However, for the 2018 period, we saw a modest decrease in that skill (in regards to week 2 forecasting) to just over a quarter of the way towards perfect prediction.

3. **Case studies of 2018**

An extremely hot period in the central of the US on Father's day marked the first extensive event of the heat season, which (depending on location) spanned June 14/16-18/20. It covered several states (*e.g.* from the
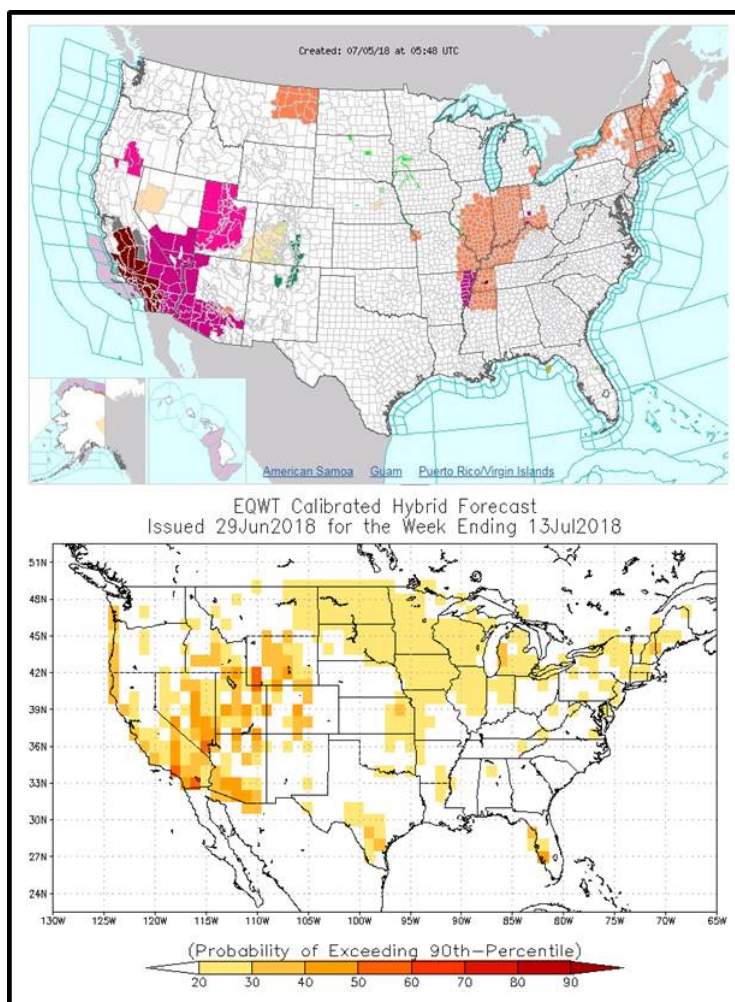
Central Plains through to the Great Lakes; Fig. 1, top) and several population centers, lasted 4-5 dates, and bore extremely hot temperatures in both daytime and nighttime temperatures. For instance, in Lincoln, Nebraska, there were 5 consecutive dates breaking the daily record. Additionally, high dewpoint temperatures drove the heat index values into the low 100's. For this event, drought was not present in the region. Air quality ranged from good to unsafe-for-sensitive-groups, with worse air quality in the eastern part of the region.

Analysis of the news headlines throughout the summer suggested the social disruption of this event was moderate compared to the other events in 2018. Since many schools were just wrapping up the school year, school closings comprised the bulk of the headlines. This region has a large number of residents and therefore any heat wave can make headlines, somewhat heedlessly. However relatively speaking, this region in mid-to-late June is not especially vulnerable to episodes of mid-90s temperature and high (upper 60s) humidity (modest hospital admission increases, no infrastructure damage, etc.).

For consistency from event-to-event and across models, all forecasts are evaluated from the perspective of a 9-day lead to the beginning of the event. Additionally, we will focus on the Week 2 tools (SEHOS). Overall the forecast accuracy was mediocre when the 16th was 9 days the lead of the forecasts, and

Fig. 3 (Top) Same as Fig. 1 but for the morning of July 5th, 2018. (Bottom) Probabilistic forecasts of a heat wave during the week ending on July 13th, as issued on June 29th by the GEFS-ECENS equal-weighted blend forecast powered version of the week 2 tool.

the skill varied with model. On one hand the GEFS-based forecasts completely failed to indicate a threat in the region with probabilities almost all sub-20%. The spatial pattern suggested an event in the Southern Plains. Conversely the ECMWF had probabilities of mostly 20-30% (30-40% maximum) and a spatial pattern with some resemblance of the observed event (Fig. 1, bottom). The resulting blended forecast had an even-handed mix of both sub-20% and 20-30% probabilities in the impacted region, but the spatial pattern still suggested a greater chance of a heat wave in the Southern Plains rather than the impacted region.

Some heat waves have a migratory nature to them, traveling slowly from one part of the country to another. The subject of the second case study was one of these, and it was actually broken into 4 "chapters" in our internal analysis: June 22-25 in the Texas-Southern Plains, June 24/26-June 27/July 2 in the Deep South, June 27-June 30/July 1 in the Middle Mississippi-Great Lakes, and finally June 29-July 5 in the Northeast-Mid-Atlantic. The beginning of the event brought 100°F degree weather to parts of Texas for the first time in the summer. Air quality was not an issue, and the duration was not overly long. However, the temperatures were very high and the region was predominantly in moderate drought. After Texas, the event baked the Lower Mississippi Valley in the Deep South for 3.5-7.5 dates – depending on location. High dewpoints contributed to heat index values over 105°F. Air quality was not an issue during this part of the event. Then this large, migrating heat wave moved into the center of the US for a few days. Dewpoints were high (low 70s) and
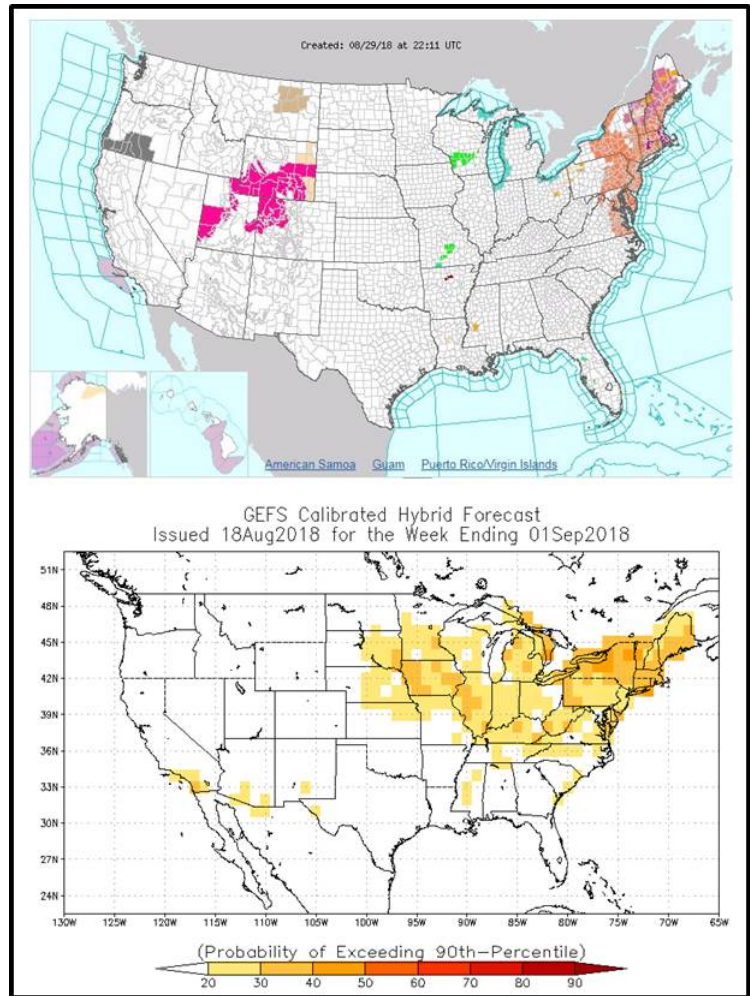
pushed heat index values over 105°F in many locations. Overnight lows were high-to-extreme, depending on location, including into the low 80's on some evenings in some locations (*e.g.* Kansas City). Strong small-scale variability in the strength of the anomalies seemed to reflect the soil moisture patterns; this region ranged from extreme drought to normal soil moisture. After baking the central US, the heat wave settled into the Great Lakes region and then the densely-populated Northeastern US (Fig. 2, top). The degree of temperature extremes (e.g. anomalies) in the Northeastern US were the greatest this migrating heat wave recorded. The Great Lakes region had typical soil moisture content, but much of the Northeast was dry or in (low-level) drought. Mild air quality issues accompanied the event, except for dramatic air pollution in the NYC-Philly-NJ area for a single afternoon.

Albeit with its fair share of stories regarding children being trapped in hot cars, heat exhaustion of athletes, stressed agriculture, opening of cooling centers; the level of societal impacts during the first half of the episode was fairly typical for mid-summer heat waves. However the latter half had notably large societal impacts, the most conspicuous being 70-plus deaths in Quebec as well as in the Great Lakes an alarming number (over 12) of road (highway) closures due to cement buckling. Mild air quality issues accompanied the event, except for

Fig. 4 (Top) Same as Figure 1 but for the morning of August 29th, 2018. (Bottom) Probabilistic forecasts of a heat wave during the week ending on September 1st, as issued on August 18th by the GEFS forecast powered version of the week 2 tool.

dramatic air pollution in the NYC-Philly-NJ area on one afternoon. A rash of daily historical records were also broken during the last leg of the heat wave from Vermont to New York City.

The beginning of the episode, in Texas-Southern Plains, was not well forecasted by either dynamical model. Albeit the quality of the forecasts improved as the episode progressed and therefore the forecasts were generally OK for the Middle Mississippi-Great Lakes of the US. For example, the blended forecast has 20-30% coverage in most of the impact region, with some 30-40% and some sub 20%. By the end of the event, when the heat was in the Northeast, forecasts from the ECMWF for most of the impacted region showed 20-30% probabilities and the spatial pattern resembles the observed region impacted (Fig. 2, bottom).

A four-day episode of record breaking heat hit Southern California and parts of the Desert Southwest the weekend following the 4th of July (July 5-8; Fig. 3, top). For example, San Diego and Las Angeles both saw multiple/consecutive single-day records fall. Several single-day records fell in the desert, too. At the desert southwest locations absolute thresholds of 110-115 were met, in lieu of relative thresholds. Air quality was an issue, usually only moderately but very elevated risk existed in the Los Angeles area. Drought was an issue, ranging from moderate (Southern California (SoCal)) to extreme (Desert Southwest). Societal impacts were modestly larger than usual and included a postal worker dying in their mail-truck, and over 20,000 customers going without power.

The forecasts were relatively good for this event. The GEFS- and ECMWF-based forecasts predominantly had probabilities of 20-30% of a heat event in SoCal, and chances of 110°F exceedance over 50% in the desert southwest locations. The blended forecast (Fig. 3, bottom) was slightly superior to either individual model-based forecast, and for both SoCal locations (relative thresholds) and the Desert Southwest locations (absolute thresholds).

The weekend before Labor Day displayed a substantial 3.5-day heat wave that impacted an estimated 68 million Americans from Chicago to New York City. The western portion of the episode hit the Midwest and Great Lakes for 4 dates (August 25-28). It was accompanied by very high dewpoints (>=74°F average in Indianapolis) that drove extremely high nighttime temperatures and heat index values. Daily high heat index values ran in the upper 90's to mid-100's, which is very hot for this time of year and part of the country. It had moderate air quality levels, any issues due exclusively to PM2.5. The only drought in the region impacted a substantial portion of Michigan, with moderate-to-severe drought. The eastern portion of the heat wave hit New England and the Mid-Atlantic states for a couple dates (August 27/28-29/30; Fig. 4, top). Again very high dewpoints across the region drove heat index values over 100-105°F and several single-day-record nightly low temperatures to be broken. The eastern chapter of this event also saw locations (VT, PA, RI, NY) with extreme daily high air temperatures. Drought did impact some of the northern areas (upstate NY, VT, NH, ME).

While certainly some daily records that fell, the numbers of societal impacts were minimal. Perhaps many residents still had the knowledge and resources to beat the heat. Some headlines included school closings and the US Open needing to be shut down for a day.

The western portion of the episode was not as well forecasted as the eastern portion, as this was primarily due to the ECENS's ability to forecast the episode. The GEFS had good skill with the western portion of the impacted region showing half 20-30% and half 30-40%, and in the eastern portion they were predominantly 30-40% (Fig. 4, bottom). The ECMWF did much better for the eastern portion of the event.

References

Ferro, C. A. T., and D. B. Stephenson, 2011: External dependence indices: improved verification measures for deterministic forecasts of rare binary events. *Wea. Forecasting*, **26,** 699-713. doi: 10.1175/WAF-D-10-05030.1.

Unger, D. A., H. van den Dool, E. O'Lenic, and D. Collins, 2009: Ensemble regression. *Mon. Wea. Rev..* **137**, 2365-2379. doi: 10.1175/2008MWR2605.1.

Characterizing Concurrent Hot and Dry Spell Events
Across Crucial Breadbasket Regions

Ariel Avgi[1], Ehsan Najafi[1,2], and Indrani Pal[1]

[1]*NOAA Center for Earth System Sciences and Remote Sensing Technologies (NOAA-CREST),
CUNY CREST Institute, New York*

[2]*Department of Civil Engineering, City University of New York (City College), New York*

1. Introduction

In regions across the world, from the Americas to Australia, there is evidence of an increasing number of compound climate extremes (Gallant and Karoly 2010; Mazdiyasni and AghaKouchak 2015; Armal *et al.* 2016; Armal *et al.* 2018a; Armal *et al.* 2018b; Najafi and Khanbilvardi 2018a; Najafi *et al.* 2018b; Lima *et al.* 2018; Armal and Al-Suhili 2019). Co-occurring conditions such as high temperatures and dry spells or high temperatures and excess precipitation are considerably more intense and destructive than any one condition individually (Zscheischler *et al.* 2017). In food growing regions, these co-occurring extremes can have negative impacts such as declined yield—a risky consequence in a global society that is fast approaching a population of eight billion people to feed (Najafi *et al.* 2016; Najafi *et al.* 2017; Matiu *et al.* 2017; Zampieri *et al.* 2017; Najafi *et al.* 2018c).

Studies focusing on co-occurring climate extremes in food growing regions have indicated that hot and dry extremes leave more negative impacts than other co-occurring extremes (Troy *et al.* 2015; Lesk *et al.* 2016). Focusing on wheat, the threshold at which wheat begins to be negatively affected by temperature is 30 degrees Celsius (Zampieri *et al.* 2017). With the combination of extreme heat indicated by the number of days that exceed this threshold during the growing season and dry conditions based on the minimum monthly value of the Standardized Precipitation Evapotranspiration Index (SPEI) during the growing season, we characterize the variability and trends of concurrent hot and dry extreme events in every growing region of both spring and winter wheat. By uniquely focusing on global wheat croplands and the risk of these concurrent climate extremes, we draw conclusions about how climate is changing with respect to this crucial crop.

2. Data and methodology

Global wheat croplands were defined based on NASA's MIRCA2000 dataset (https://webmap.ornl.gov/wcsdown/dataset.jsp?ds_id=10015) that displays the locations of irrigated and rainfed wheat lands as well as the number of hectares being grown at each location. This dataset has been widely used in the literature on crop modeling and climate science (Deryng *et al.* 2014; Zampieri *et al.* 2017; Heino *et al.* 2018; Najafi *et al.* 2018c, Najafi *et al.* 2018d, Najafi *et al.* 2019a, Najafi *et al.* 2019b). Only locations that used at least 1% of the land within a grid cell, or at least 67 acres, for crop growth were considered. The irrigated and rainfed lands were combined for analysis in this study; regard for management measures in place such as irrigation were not crucial given our interest in exploring concurrent hot and dry extremes in all significant wheat growing regions.

To make the distinction between spring and winter varieties of wheat, we first used the extrapolated SAGE Crop Calendar Dataset to define the growing season for winter and spring wheat yielding locations (https://nelson.wisc.edu/sage/data-and-models/crop-calendar-dataset/netCDF0-5degree.php) and then narrowed and restricted the areas in consideration by applying Iizumi's Global sowing and harvesting windows of major crops dataset for winter and spring wheat varieties (http://search.diasjp.net/en/dataset/global_crop_calendar_2000). We overlaid the map of global wheat croplands based on the MIRCA2000 dataset onto the medium season, rainfed spring and winter maps based on Iizumi's data set. Cropping all areas that were not common between the data sets, we produced three mappings:

_____

(1) Locations where only spring wheat is grown, (2) Locations where only winter wheat is grown, and (3) Locations where both spring and winter wheat are suitable for growing.

We defined extreme hot events by the total number of days during a growing season that exceeded 30-degrees Celsius and extreme dry spell events by the minimum monthly SPEI magnitudes during the same growing season (Wang *et al.* 2018). To understand extreme hot and dry events relative to location, we considered the 75th percentile thresholds for each location. We described each location that exceeded the 75th percentile threshold for both temperature (T30) and minimum SPEI during a growing season as having experienced a concurrent extreme event (CEE). The following analyses are focused on the top ten wheat producing countries based on Food and Agriculture Organization of the United Nations (FAO) average production from 2001-2013: China, India, USA, Russia, France, Canada, Germany, Pakistan, Australia, and Turkey.

3. Results

To understand how CEEs have changed over time, we sought to look broadly at the differences in impacts experienced between the IPCC's baseline period from 1961-1990 and the most current decades since 1990 (1991-2013) for spring and winter varieties of wheat. Despite the shorter period after 1990 (only 23 years as opposed to 29), we still observe a surge of concurrent extreme events across the growing areas. We have separated the spring (winter) wheat growing locations into locations that grow only the spring (winter) variety and locations that are suitable for growing both varieties. The respective growing seasons were used for the locations that are suitable for growing both varieties. Thus, "spring (only)" and "winter (only)" will refer to locations that do not include the areas suitable for both varieties and "spring (total)" and "winter (total)" will refer to locations that include the areas suitable for both varieties.

Beginning with the spring wheat variety, a significant difference in the means was found in the frequency of CEEs for spring (only) growing areas. However, more "extreme" CEEs, based on the number of days exceeding 30 degrees Celsius in dry growing areas, were found in the baseline period. Looking at the major producing regions of wheat globally, India experienced more events along its western coast line and less events in the eastern region of the country in the period after 1990. Furthermore, Australia experienced more CEEs in the eastern part of the country in the period after 1990. Transitioning to the spring (total) growing areas, we found the difference in the frequency of CEEs was insignificant. However, the additional affected major producers were China and the United States. After 1990, China observed an increase in the number of seasons impacted by CEEs, most notably post-2000. In the United States we observed a spatial shift in the concentration of impacted locations before and after 1990. During the baseline period, the events are generally concentrated in the north, and in the period after 1990, there is a greater number of CEEs in the southern United States.

In general, the winter wheat growing season was found to experience less hot and dry extreme conditions as compared to the spring wheat growing season. Overall, though, we found a significant increase in the frequency of CEEs across winter (total) growing areas in the period after 1990 compared to the baseline period. Focusing on the major wheat producing countries, we observed a spatial shift in the United States with the dispersion of extreme events after 1990. We also observed a spatial decrease in the number of impacts in southern Australia after 1990. Finally, the location of impacts in Turkey remained essentially the same in the decades before and after 1990. It is important to note that these observations were made for locations considered suitable for both spring and winter wheat, and not croplands exclusive to winter wheat. The winter (only) growing areas also experienced a significant increase in the frequency of CEEs in the period after 1990 compared to the baseline period and the observations made are the same as those for the winter (total) growing areas but on a smaller scale. In particular, the expansion of CEEs to the northwest region of the United States and southern Canada in the last decade is a common feature of both growing area maps.

Looking into the individual extremes over the entire time period considered, 1961-2013, we note that there is lack of significant trends in T30 or SPEI, leading us to conclude that these extremes are not necessarily driven more by temperature or dryness in any one area but are unique events.

CEEs are unique occurrences that affect spring and winter wheat croplands in different places at different times. With a focus on the major producers of wheat worldwide, Asian countries (China, India, and Pakistan)

experienced CEEs only during the spring growing season while the United States and Australia experienced CEEs in both the spring and winter growing seasons. This study confirms that as climate changes, the co-occurrence of hot and dry extreme events will increase. Furthermore as observed, they will increase in croplands that grow essential grains for food security. The croplands affected by these CEEs are different for spring and winter varieties of wheat, and from these results, agricultural scientists in industry can recommend improvements for management practices based on expected conditions. Our focus on the major producers of wheat can be studied further by analyzing the potential economic effects these climate extremes have had on global grain prices. Alternatively, similar work can be done focusing on food-insecure nations and the spatio-temporal effects of CEEs there. Considering CEEs during different stages of crop growth rather than just the full growing season is another way the data can be transformed to tell another story about how compound hot and dry extremes are affecting croplands and global food security.

References

Armal, S., N. Devineni, and R. Khanbilvardi, 2016: A multilevel Poisson regression model to detect trends in frequency of extreme rainfall events. *American Geophysical Union Fall Meeting 2016*, San Francisco, CA, USA, 12–16 December 2016, AGU, Abstract #NH51B-1957.

—, —, and —, 2018a: Trends in extreme rainfall frequency in the contiguous United States: Attribution to climate change and climate variability modes. *J. Climate*, **31**, 369-385, doi:10.1175/JCLI-D-17-0106.1

—, —, and —, 2018b: New York City's water system performance analysis based on current and projected demands. *American Geophysical Union Fall Meeting 2018*, Washington, DC, USA, 10–14 December 2018, AGU, Abstract #H41I-2167.

—, and R. Al-Suhili, 2019: An urban flood inundation model based on cellular automata. *Int. J. Water*, in press.

Deryng, D., D. Conway, N. Ramankutty, J. Price, and R. Warren, 2014: Global crop yield response to extreme heat stress under multiple climate change futures. *Environ. Res. Lett.*, **9**, 34011.

Gallant, A. J. E., and D. J. Karoly, 2010: A combined climate extremes index for the Australian region. *J. Climate*, **23**, 6153 - 6165.

Heino, M., M. J. Puma, P. J. Ward, D. Gerten, V. Heck, S. Siebert, and M. Kummu, 2018: Two-thirds of global cropland area impacted by climate oscillations. *Nat. Commun.*, **9**, 1257.

Lesk, C., P. Rowhani, and N. Ramankutty, 2016: Influence of extreme weather disasters on global crop production. *Nature*, **529**, 84.

Lima, C. H. R., A. AghaKouchak, and J. T. Randerson, 2018: Unraveling the role of temperature and rainfall on active fires in the Brazilian Amazon using a nonlinear Poisson model. *J. Geophys. Res.: Biogeosciences*, **123**, 117–128.

Matiu, M., D. P. Ankerst, and A. Menzel, 2017: Interactions between temperature and drought in global and regional crop yield variability during 1961-2014. *PLoS ONE*, **12**, doi:10.1371/journal.pone.0178339.

Mazdiyasni, O., and A. AghaKouchak, 2015: Substantial increase in concurrent droughts and heatwaves in the United States. *PNAS*, **112**, 11484–11489.

Najafi, E., N. Devineni, R. Khanabilvardi, and F. Kogan, 2016: Global crop yields, climatic trends and technology enhancement. *American Geophysical Union Fall Meeting 2016*, San Francisco, CA, USA, 12–16 December 2016, AGU, Abstract #H32C-07.

—, —, I. Pal, and R. Khanbilvardi, 2017: The space-time variation of global crop yields, detecting simultaneous outliers and identifying the teleconnections with climatic patterns. *American*

Geophysical Union Fall Meeting 2017, New Orleans, LA, 11–15 December 2017, AGU, Abstract #GC31D-1035

—, and R. Khanbilvardi, 2018a: Clustering and trend analysis of global extreme droughts from 1900 to 2014. https://arxiv.org/pdf/1901.00052v2

—, I. Pal, and R. Khanbilvardi, 2018b: Diagnosing extreme drought characteristics across the globe. *NWS Sci. Technol. Infusion Clim. Bull., 42nd NOAA Annu. Clim. Diagn. Predict. Workshop*, 121-125, doi:10.7289/V5/CDPW-NWS-42nd-2018.

—, N. Devineni, R. M. Khanbilvardi, and F. Kogan, 2018c: Understanding the changes in global crop yields through changes in climate and technology. *Earth's Future*, **6**, 410-427, doi: 10.1002/2017EF000690

—, —, I. Pal, and R. Khanbilvardi, 2018d: Evaluating the sustainable pathways to maximize staple crops production. *American Geophysical Union Fall Meeting 2018*, Washington, DC, 10 -14 December 2018, AGU, Abstract #GC51I-0899

—, I. Pal, and R. Khanbilvardi, 2019a: Climate drives variability and joint variability of global crop yields. *Sci. Total Environ.*, **662**, 361–372.

—, —, and —, 2019b: Data of variability and joint variability of global crop yields and their association with climate. *Data in Brief*, **23**, 103,745, doi:10.1016/j.dib.2019.103745.

Troy, T. J., C. Kipgen, and I. Pal, 2015: The impact of climate extremes and irrigation on US crop yields. *Environ. Res. Lett.*, **10**, 054013.

Wang, L., S. Liao, S. Huang, B. Ming, Q. Meng, and P. Wang, 2018: Increasing concurrent drought and heat during the summer maize season in Huang-Huai-Hai Plain, China. *Int. J. Climatol.*, **38**, 3177–3190.

Zampieri, M., A. Ceglar, F. Dentener, and A. Toreti, 2017: Wheat yield loss attributable to heat waves, drought and water excess at the global, national and subnational scales. *Environ. Res. Lett.*, **12**, 064008.

Zscheischler, J., and S. I. Seneviratne, 2017: Dependence of drivers affects risks associated with compound events. *Science Advances*, **3**, e1700263, doi:10.1126/sciadv.1700263.

5. IMPROVING MODELS, FORECASTS AND OBSERVATIONAL DATA SETS

43rd NOAA Annual Climate Diagnostics
and Prediction Workshop

Santa Barbara, California

23-25 October 2018

Joined CanSIPS-CFSv2 Seasonal Forecast

Marko Markovic[1], Zeng-Zhen Hu[2], Bertrand Denis[1], Arun Kumar[2], and Dave DeWitt[2]

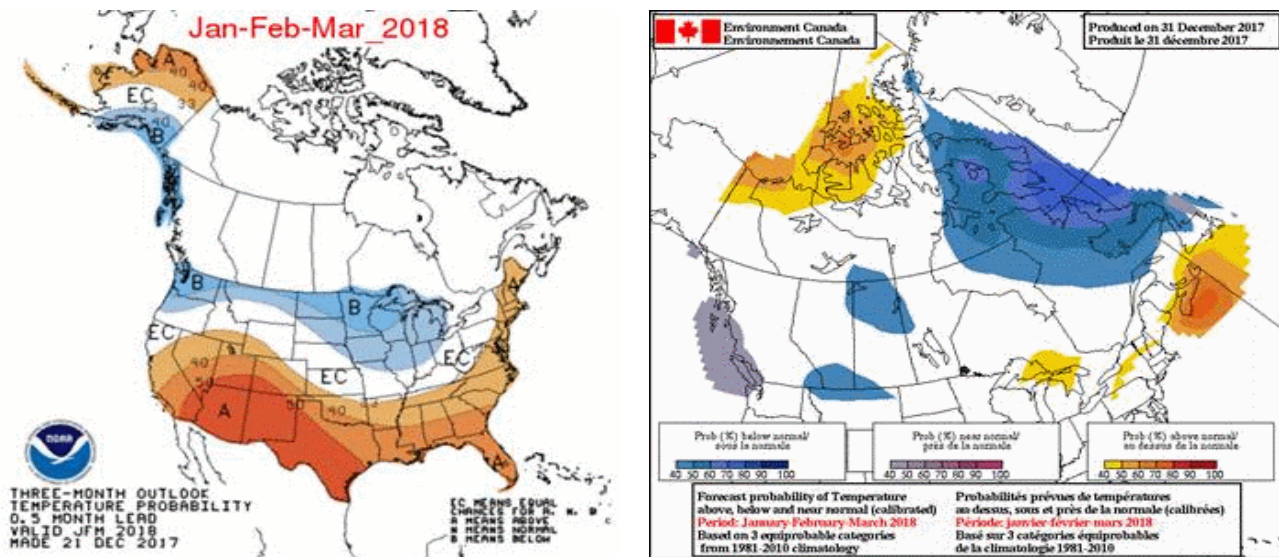[1]*Environment and Climate Change Canada, Meteorological Service of Canada*
[2]*Climate Prediction Center, NOAA/NWS/NCEP*

1. Introduction

The CanSIPS-CFSv2 seasonal forecast, or "The White Space Project," is a joint effort by Environment and Climate Change Canada (ECCC) and National Oceanic and Atmospheric Administration (NOAA) to deliver a geographically contineous seasonal forecast over the North American continent. At present, both ECCC and the Climate Prediction Center (CPC) of NOAA, perform their respective seasonal forecasts independently on a monthly basis. By doing this, each country applies a geographical mask over their counterpart leaving a "white space" to dominate for the seasonal forecast map of North America (see Fig. 1).

The principal goal of this project is to use the combined CanSIPS (Merryfield *et al.* 2013) and CFSv2 (Saha *et al.*, 2014) forecasts for the benefit of having a continuous forecast across the United States and Canada borders. One example of such a project is hydrological monitoring over the Great Lakes managed by the International Joint Commission, where the two countries have an agreement on the water quality (https://www.ijc.org/en/watersheds/great-lakes, accessed 27/12/2018).

Another significant goal of this project is an overall improvement of the seasonal forecasts stemming from the multi-model approach. Both countries will benefit from this approach with more skillful seasonal forecasts over the North American continent. Multi-model seasonal forecasting has been recognized to have better results than the single-model forecasting technique.


Fig. 1 On the left: Seasonal January-February-March 2018 lead 0 seasonal forecast, issued by the Climate Prediction Center. On the right: as on the left, but issued by Environment and Climate Change Canada.

2. Motivation for the zero-lead forecast

Motivation for this project comes from the fact that both ECCC and the CPC are the operational forecasting centres with an operational production cycle for dynamical seasonal forecasts on a particular day of the month.

_____

This is very important for the production of the "zero-lead month" (*i.e.* difference between the forecast target season and the forecast release is zero) seasonal forecasts, which are known to have better skill scores compared to the forecasts with longer leads (Wang *et al.*, 2010).

The North American Multi-Model Ensemble (NMME) is an example of a project that combines seasonal forecasts stemming from several North American climate models (Kirtman *et al.* 2014). Once per month, the NMME issues seasonal forecasts for North America targeting seasons having lead times of one to five months. The fact that the combined NMME forecast encompasses real-time seasonal forecasts from a number of production centres makes it very challenging to provide the zero-lead seasonal forecast. Therefore, the combined CanSIPS-CFSv2 real-time seasonal forecasts can be a complementary product to the North American Ensemble, filling the zero-lead gap. Figure 2 shows a comparison between the March-April-May (MAM) historical (1982-2010) percent correct skill scores of zero-lead and one-month lead time seasonal forecasts for near-surface temperature over Canada. Zero-lead forecast skill, calculated for only one model (*i.e.* CFSv2, Fig. 2a), is substantially higher than one-month lead time forecast skill from the Multi-Model Ensemble mean (Fig. 2b, six models in total), highlighting the importance of the shorter lead time forecasts over the longer lead multi-model ensemble forecasting approach. Globally performed analysis (not shown) of the percent correct score confirms the results over Canada in MAM and all other seasons.
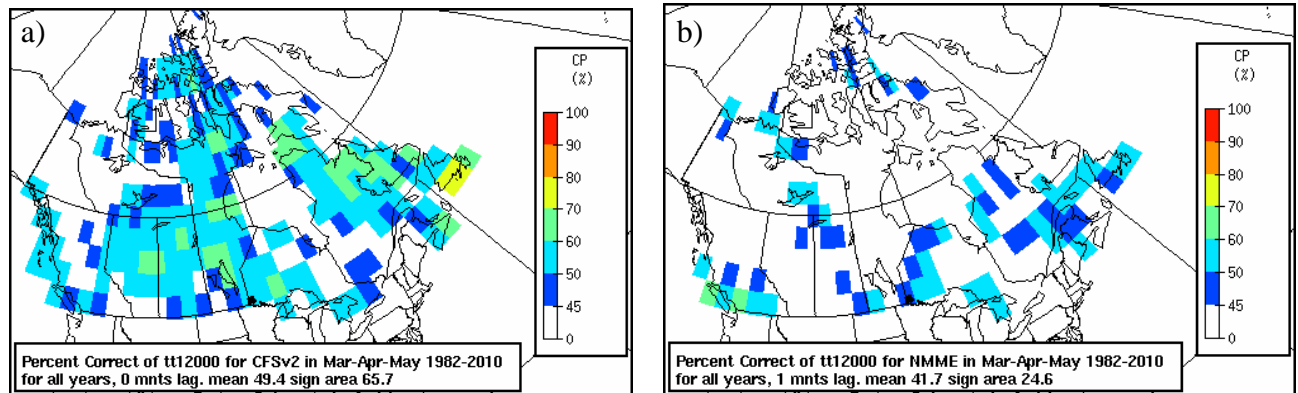
Fig. 2 Historical (1982-2010) percent correct score for MAM season for a) CFSv2 ensemble mean lead 0, and b) North American Multi-Model Ensemble mean, lead 1.

3. Experimental setup of the joined CanSIPS-CFSv2 real-time forecasts

Since the CanSIPS and CFSv2 models use different methods to initialize their respective real-time seasonal forecasts, we used the following configuration, which has been found to be the most suitable for this type of product. To construct the combined seasonal forecast, we have used 20 ensemble members of the CanSIPS system having the "burst initialization" (*i.e.* all ensemble members are launched at the same time) executed on the last day of each calendar month and the 20 ensemble members of the CFSv2 model that have lagged initial conditions. As the combined CanSIPS-CFSv2 real-time forecast is constructed on the first day of each calendar month, we have used the 20 CFSv2 ensemble members executed with lags closest to the end of the month. This configuration enables the combined system to be as close as possible to zero-lag. The combined forecast is an ensemble prediction using 40 ensemble members that are given equal weight. The ensemble members for the historical CanSIPS and CFSv2 ensembles, needed for the estimation of the system's climatology and historical forecast skill, are selected using a similar approach as for the real-time forecast ensembles.

Once operational then at the end of each calendar month, we will be issuing a joined CanSIPS-CFSv2 ensemble seasonal forecast for zero and one-month lead times.

4. Products of the joined system

The CanSIPS and CFSv2 models are combined to form a multi-model ensemble mean where each ensemble member is equally weighted. The flagship product of the joined CanSIPS-CFSv2 forecasting system is the probabilistic forecast for near-surface temperature (Fig.3 on the top left), precipitation and sea-surface

temperature. In addition to the probabilistic forecast, we also provide an anomaly forecast (Fig. 3 in the top right for temperature) and a deterministic seasonal forecast (Fig. 3 on the bottom left for temperature). The anomaly forecast is an important complement to the probabilistic seasonal forecasting approach, which makes it possible to associate the probability value with the magnitude of an anomaly. The deterministic approach is useful for seasonal forecast evaluation using simple and understandable skill score measures, such as the correlation coefficient or the percent correct skill score. The joined system seasonal forecasts may be accessed at the following web page:

http://collaboration.cmc.ec.gc.ca/cmc/saison/Joined_CanSIPS_CFSv2/site_web/#t/11/2018/m123/on
(username and password available upon request to marko.markovic@canada.ca).
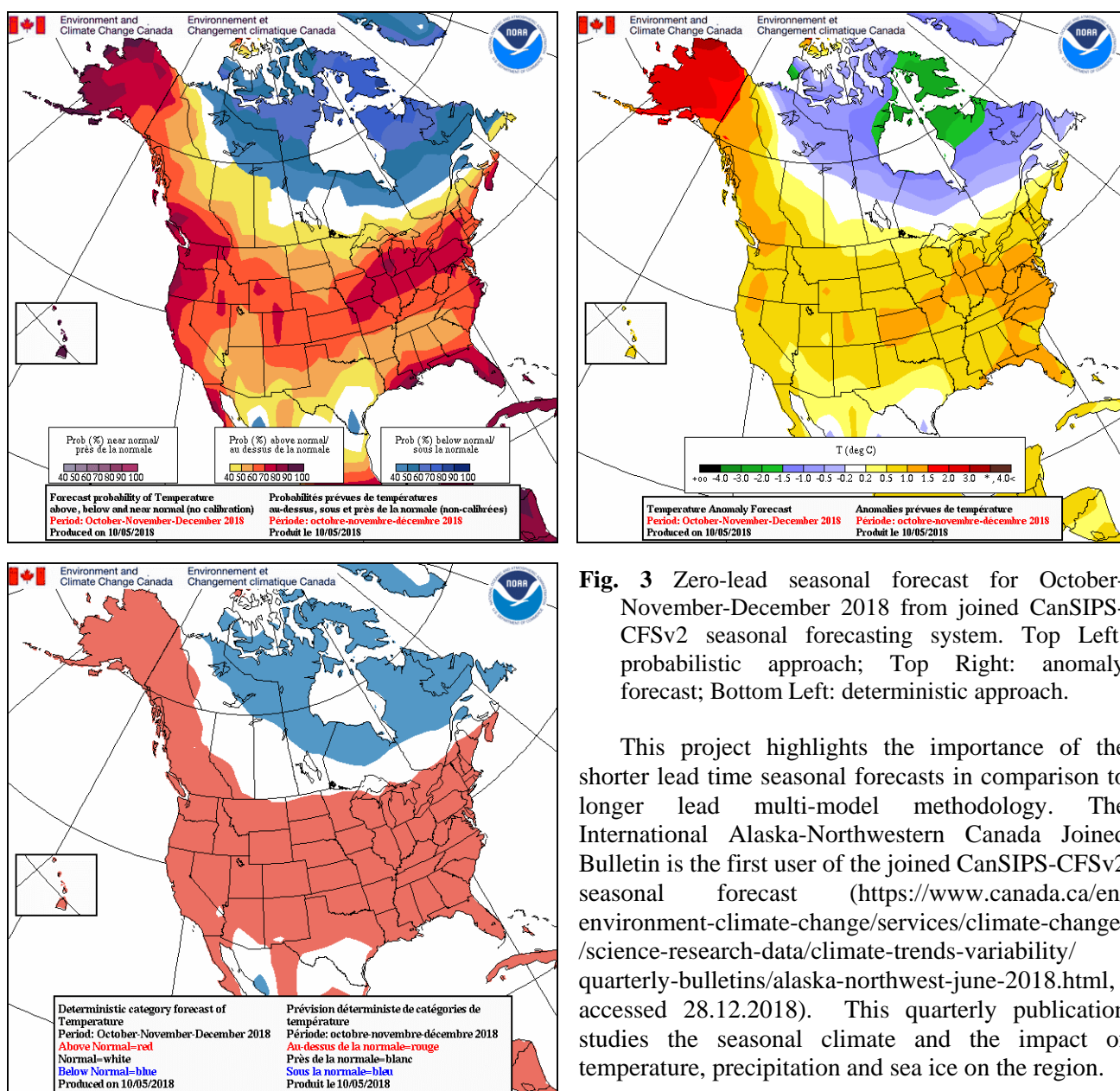
Fig. 3 Zero-lead seasonal forecast for October-November-December 2018 from joined CanSIPS-CFSv2 seasonal forecasting system. Top Left: probabilistic approach; Top Right: anomaly forecast; Bottom Left: deterministic approach.

This project highlights the importance of the shorter lead time seasonal forecasts in comparison to longer lead multi-model methodology. The International Alaska-Northwestern Canada Joined Bulletin is the first user of the joined CanSIPS-CFSv2 seasonal forecast (https://www.canada.ca/en/ environment-climate-change/services/climate-change /science-research-data/climate-trends-variability/ quarterly-bulletins/alaska-northwest-june-2018.html, accessed 28.12.2018). This quarterly publication studies the seasonal climate and the impact of temperature, precipitation and sea ice on the region.

In order to finalize the joined CanSIPS-CFSv2 seasonal forecast project, we need to perform the forecast calibration. This technique is known to improve seasonal forecasts by mitigating forecast biases, such as overall overconfidence, that most of the forecasting systems possess, especially for the higher observational frequencies (Kharin and Zwiers, 2003). Seasonal climate assessments in the northern regions of North America (*e.g.* Alaska, Yukon) would greatly benefit from

seasonal forecasts of sea ice. Therefore, our next step will be the inclusion of the real-time sea-ice forecasts in our forecasting system. Verification of the previous CanSIPS-CFSv2 seasonal forecast should also be included as an important component of the forecasting system. This step would shed light on the system's overall performance and would also build the "forecasting confidence" of the new forecasting system.

References

Merryfield, W. J., and Coauthors, 2013: The Canadian seasonal to interannual prediction system. Part I: models and initialization. *Mon. Wea. Rev.*, **141**, 2910–2945.

Saha, S., and Coauthors, 2014: The NCEP Climate Forecast System Version 2. *J. Climate*, **27**, 2185–2208. doi: http://dx.doi.org/10.1175/JCLI-D-12-00823.1

Wang, W., M. Chen, and A. Kumar, 2010: An assessment of the CFS real-time seasonal forecasts. *Wea. Forecasting*, **25**, 950–969, https://doi.org/10.1175/2010WAF2222345.1

Kirtman, B. P., and Coauthors, 2014: The North American multimodel ensemble: Phase-1 seasonal-to-interannual prediction; Phase-2 toward developing intraseasonal prediction. *Bull. Amer. Meteor. Soc.*, **95**, 585–601.

Kharin, V. V. and F.W. Zwiers, 2003: Improved seasonal probability forecast. *J. Climate*, **16**, 1684–1701.

An Investigation of Prediction and Predictability of NCEP Global Ensemble Forecast System (GEFS)

Yuejian Zhu[1], Wei Li[2], Eric Sinsky[2], Hong Guan[3], Xiaqiong Zhou[2], and Bing Fu[2]

[1]Environmental Modeling Center, NOAA/NWS/NCEP
[2]IMSG at Environmental Modeling Center, NOAA/NWS/NCEP
[3]SRG at Environmental Modeling Center, NOAA/NWS/NCEP
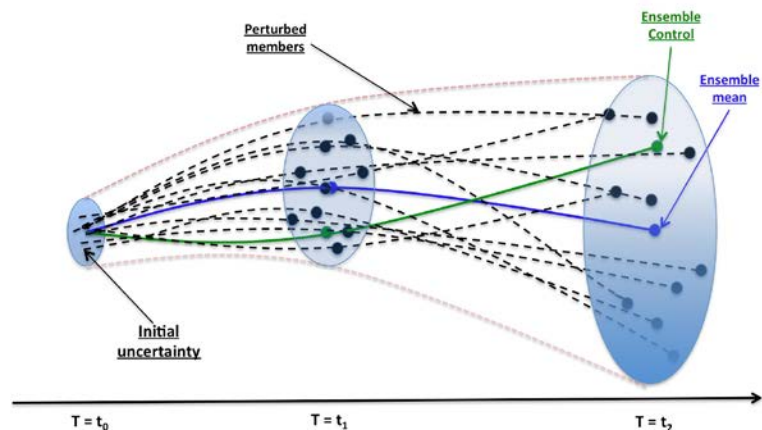
1. Introduction

In recent years, the requirements for seamless forecast information have increased significantly for users that provide valuable guidance for public safety, quality of life, and business decisions that drive economic growth. A better understanding of predictability and numerical model prediction skills are greatly enhancing our capabilities for prediction and guidance for time scales ranging from weather, week-2, subseasonal to seasonal.

The predictability was originally introduced theoretically as a scientific question (Lorenz 1969); then it was investigated numerically and empirically based on the hypotheses (Lorenz 1982; 1996) for weather forecast. Following up the pioneer works, Shukla (1998) and many others also revealed predictability for seasonal and/or climate prediction. Until most recently, study of intrinsic predictability of state-of-art numerical modeling system has been used to further investigate potential predictability (Ying and Zhang 2017).

Considering both initial and model uncertainties, a state-of-art ensemble forecast system could be an optimum numerical system to quantitatively present the predictability across timescales which include weather and beyond. When assuming a perfect dynamical and physical model and a perfect ensemble system, forecast accuracy of each perturbed (and unperturbed or control) member should be "bias free", and have equal forecast skill statistically. Any individual forecast could be a "proxy truth" as well. Meanwhile, ensemble mean from this optimum system should present best prediction statistically, in the results, the average skill of ensemble mean forecast against individual perturbed (and control) forecast should represent potential forecast skill (or predictability).

Fig. 1 Schematic diagram of an ensemble forecast starting from initial analysis/perturbations at t=0, growing with time evolution. Solid green is for unperturbed (ensemble control) forecast; solid blue represents ensemble mean; and dash blacks are perturbed ensemble forecasts. The shaded areas represent uncertainties of initial and forecasts.

2. Ensemble system

The NCEP Global Ensemble Forecast System (GEFS), by using a set of initial perturbations generated from EnKF analysis (Fig. 1; Zhou *et al.* 2016; Zhou *et al.* 2017), has been in daily operation since 1992. It has been providing reliable weather and week-2 probabilistic forecast guidance that has translated into valuable information for the general public. With many science enhancements in past years, current GEFS, especially SubX version, has reached super performance across the scales from weather to subseason (Zhu *et al.* 2017;

_____

Correspondence to: Yuejian Zhu, Environmental Modeling Center, NOAA/NWS/NCEP, 5830 University Research Court, College Park, MD 20740; E-mail: yuejian.zhu@noaa.gov

2018). The two latest versions of NCEP GEFS have been used in this study, one of them is GEFS SubX version (Zhu *et al.* 2018; Li *et al.* 2019; Zhu *et al.* 2019; Guan *et al.* 2019) and another one is FV3-GEFS version (Zhou et al. 2019), that used Finite Volume dynamical core, higher (and uniform) resolution and GFDL Micro Physics (replace Zhao-Carr Micro Physics). The FV3-GEFS version has higher and uniform horizontal resolution (about 25 km) when compares to GEFS SubX version (33 km for 0-8 days; 55 km for 8-35 days). All ensembles are running 20 perturbed forecasts and one control forecast.

3. Evaluation methodology

The GEFS model performance has been presented in many studies (Zhou *et al.* 2017; Zhu *et al.* 2018), but the GEFS extended forecast to cover subseasonal timescales has only recently been evaluated (Zhu *et al.* 2018; Li *et al.* 2019; Guan *et al.* 2019) as part of the NOAA SubX (Subseasonal multi-model Experiments) project through an 18-year reforecast. The study proposed here involves a comparison of GEFS SubX results with those from the newly developed FV3-based GEFS, which includes a different dynamical core, horizontal resolution, microphysics, *etc.*

Various metrics could be used to assess the prediction skill and predictability of the forecast system, with dependencies on forecast elements, different spatial/temporal scales, and different forecast regions. In this investigation, anomaly correlation (AC) has been used to assess forecast skill and potential skill for weather. Meanwhile, the bivariate anomaly correlation (RMM1 and RMM2), a traditional real-time multivariate (RMM) MJO index (WH index; Wheeler and Hendon 2004; Lin *et al.* 2008; Gottschalack *et al.* 2010), has been used to evaluate tropical forecast skill and potential forecast skill.

In order to present an upper limit of prediction skill, the following principal assumptions (hypotheses) are applied to this evaluation: 1) Initial perturbations represent true observed uncertainty; 2) Numerical model is perfect and "bias-free"; 3) Ensemble system is perfect; 4) Ensemble forecast spread really represents true forecast uncertainty; 5) All individual perturbed forecasts could be proxy truth (and equal); 6) Ensemble mean will be best forecast solution for large scale forecast. Figure 2 demonstrates the root mean square (RMS) error of the ensemble mean and ensemble spread for Northern Hemisphere 500 hPa height of one-year statistics. The FV3-GEFS has less RMS error and a better ratio of RMS error and spread than GEFS SubX forecast. The RMS errors of both experiments have cross over climatological error around day 17, which means day-to-day forecast has lost skill beyond day 17. Meanwhile, ensemble spread has reached saturation level

Fig. 2 Northern Hemisphere (NH) 500 hPa geopotential height RMS error (solid) and ensemble spread (dash) of 35 days forecasts from one year experiments based on two ensemble systems (SubX version - black and FV3 version - red). The RMS difference between analysis and climatological mean shows in green dash line (90 meters). The climatological variance around mean has been drawn on the right.

approximately at a similar range as the RMS difference between analysis and climatology (heavy dash green line), which indicates a good ensemble system has been used.

4. Results

One year experiments (April 2017 - April 2018) have been carried out for weather forecast and MJO evaluation. The NCEP Global Data Assimilation System (GDAS) analyses and NCEP/NCAR 40 years reanalysis climatology have been used to calculate forecast skills.

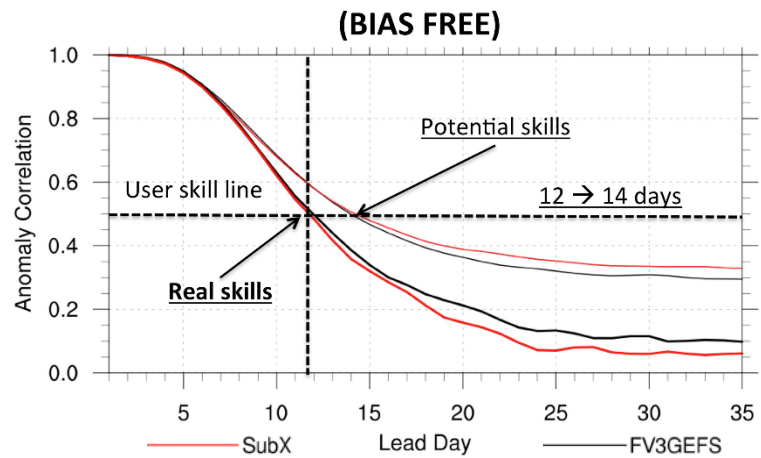### 4.1 Overall NH extratropical weather forecast

Anomaly correlation is used to measure the real forecast skill and potential forecast skill (or predictability) of the 500 hPa geopotential height (Fig. 3). Apparently, FV3 GEFS (heavy-black) has slightly better skill than SubX GEFS (heavy-red) for all lead times (Fig. 3). Both of FV3 GEFS and SubX GEFS show similar potential forecast skills (thin lines) which indicate that a current forecast skill could be extended for an additional two days (from 12 days to 14 days) by using 50% AC as a skillful forecast. A potential forecast of SubX GEFS is also slightly better than FV3 GEFS for longer lead-time, which may be due to 1). SubX GEFS has less spread than FV3 GEFS for longer lead-time (see Fig. 2 dash lines); 2). Current FV3 GEFS has a disadvantage for longer range forecast; further improvement may be required.

4.2 NH extratropical weather forecast of different spatial/temporal scales

The 500 hPa geopotential height has been decomposed to planetary scale (zonal wave 1-3); long wave (zonal wave 4-9); and synoptic weather pattern (zonal wave 10-20). The AC scores of these three groups have been presented in Fig. 4. Since the performance of FV3 GEFS is similar to SubX GEFS forecast for weather (Fig. 3), Fig. 4 only presents the AC scores for SubX GEFS version only in order to express three group scores clearly. The results demonstrate 1). The skills are different between these groups; 2). The planetary wave has more skill (12.5 days) than long wave (10.5 days) and synoptic weather forecast (7 days); 3). All three scale groups have potential forecast skills than current forecast skills about 1-2.5

Fig. 3 Northern Hemisphere (NH) 500 hPa geopotential heights Pattern Anomaly Correlation (PAC) of the ensemble mean for 35 days forecast from one year experiments (April 2017 - April 2018). There are two experiments which are SubX version (red) and FV3 version (black). The real forecast skills (thick) and potential prediction skills (thin) are presented, and marked as 12 days (real) and 14 days (potential).
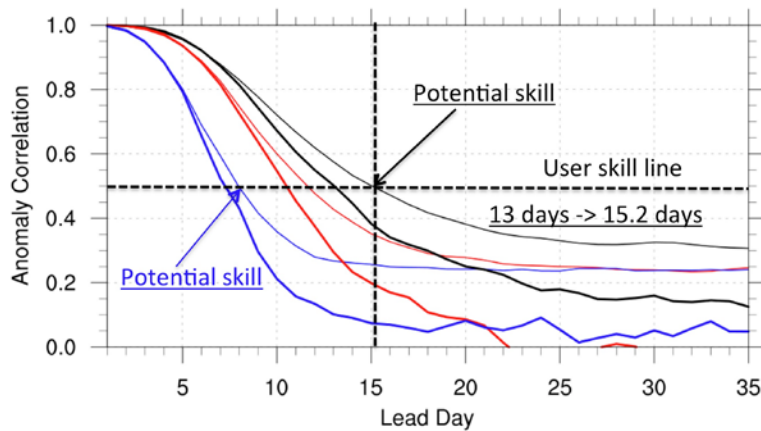
Fig. 4 Northern Hemisphere (NH) 500 hPa geopotential height Pattern Anomaly Correlation (PAC) of regrouped ensemble mean (zonal wave 1-3 (Length scale > 10000 km); 4-9 (10000 km < length scale > 3000 km); and 10-20 (3000 km > length scale > 1500 km) for SubX GEFS 35 days forecast from one year experiments (April 2017 - April 2018). The real forecast skills (thick) and potential prediction skills (thin) are presented for each group (zonal wave 1-3s are black; 4-9s are red; and 10-20s are blue).

days, planetary wave could have 15 days (> 2 weeks) potential forecast skill. Therefore, the forecast skill highly depends on a system or forecast task.

4.3 MJO evaluations

The evaluation of the bivariate anomaly correlation of RMMs has focused on the period of one year (May 1st, 2017 - April 6, 2018) for FV3 GEFS only. Figure 5 has demonstrated the current forecast skill (20 days - 50% of AC) and potential prediction skill (32 days - 50% of AC). The result may indicate that 1) There is a

good predictability of MJO event; 2) There is a large room to improve our model system includes dynamical, physical schemes, ensemble perturbations and many others (such as coupling atmosphere-ocean).

5. Summary

This is preliminary practice by using NCEP GEFS to assess potential forecast skills or predictability for NH mid-latitude weather forecast and tropical prediction. The AC scores of NH 500 hPa geopotential height indicate both of FV3 GEFS and SubX GEFS have similar real forecast skills with slightly advantage from FV3 GEFS. In contrast to real forecast skill, a potential forecast skill or predictability shows a similar conclusion for short lead-time forecast, but SubX GEFS has more

Fig. 5 The same 1-year experiment as figure 2-4, but for FV3 GEFS version only. A real MJO skill (black, *i.e.* analysis as reference) and potential MJO skill (red, *i.e.* control member as reference) of ensemble mean are presented.

potential forecast skills (or higher predictability) for longer lead-time (Fig. 3), which could indicate that either SubX GEFS may be a little under dispersive (spread is less than error; imperfect system) or FV3 GEFS may need more improvement to enhance its predictability.

For tropical prediction of FV3 GEFS, a difference of real forecast skill and potential forecast skill (or predictability) of MJO demonstrates a large potential capability (from 20 days to 32 days) of our system. A potential improvement could come from good forecast uncertainty representation; atmospheric circulation anomaly; enhanced MJO related tropical convection; interaction with ocean (coupling) and others.

References

Gottschalck, J., and Coauthors, 2010: A framework for assessing operational Madden-Julian oscillation forecasts: A CLIVAR MJO working group project. *Bull. Amer. Meteor. Soc.,* **91,** 1247-1258, doi:10.1175/2010BAMS2816.1.

Guan, H., Y. Zhu, E. Sinsky, W. Li, X. Zhou, D. Hou, C. Melhauser, R. Wobus, 2019: Systematic error analysis and calibration of 2-m temperature for the NCEP GEFS Reforecast of SubX Project. *Wea. Forecasting,* doi:10.1175/WAF-D-18-0100.1.

Li, W., Y. Zhu, X. Zhou, D. Hou, E. Sinsky, C. Melhauser, M. Pena, H. Guan and R. Wobus, 2019: Evaluating the MJO forecast skill from different configurations of NCEP GEFS extended forecast. *Clim. Dyn.,* **52**, 4923-4936, doi:10.1007/s00382-018-4423-9.

Lin, H., G. Brunet and J. Derome, 2008: Forecast skill of the Madden-Julian oscillation in two Canadian atmospheric models, *Mon. Wea. Rev.*, **136**, 4130-4149.

Lorenz, E. N., 1969: Atmospheric predictability as revealed by naturally occurring analogues. *J. Atmos. Sci.,* **26**, 636–646, doi:10.1175/ 1520-0469(1969)26,636:APARBN.2.0.CO;2.

——, 1982: Atmospheric predictability experiments with a large numerical model. *Tellus,* **34**, 505–513, doi: 10.3402/tellusa.v34i6.10836.

——, 1996: Predictability — A problem partly solved. *Proc. Seminar on Predictability*, Reading, United Kingdom, ECMWF, 1–18.
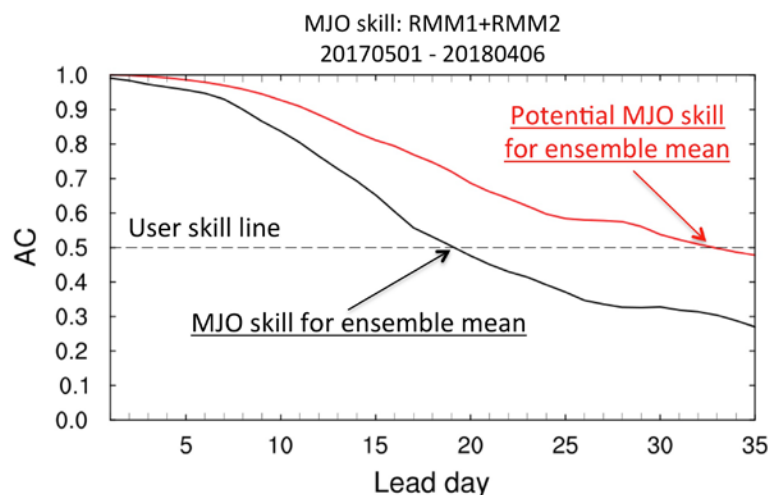
Shukla, J., 1998: Predictability in the midst of chaos: A scientific basis for climate forecasting, *Science,* **282**, Issue 5389, 728-73, doi:10.1126/science.282.5389.728.

Wheeler, M. C. and H. H. Hendon, 2004: An all-season real-time multivariate MJO index: Development of an index for monitoring and prediction. *Mon. Wea. Rev.*, **132,** 1917–1932, doi:10.1175/1520-0493(2004)132<1917:AARMMI>2.0.CO;2.

Ying, Y., and F. Zhang, 2017: Practical and intrinsic predictability of multiscale weather and convectively coupled equatorial waves during the active phase of an MJO. *J. Atmos. Sci.,* **74**, 3771-3785.

Zhou, X., Y. Zhu, D. Hou, and D. Kleist 2016: Comparison of the ensemble transform and the Ensemble Kalman Filter in the NCEP Global Ensemble Forecast System. *Wea. Forecasting,* **31**, 2058-2074.

——, ——, ——, Y. Luo, J. Peng and D. Wobus, 2017: The NCEP Global Ensemble Forecast System with the EnKF initialization. *Wea. Forecasting,* **32**, 1989-2004.

——,——, B. Fu, D. Hou, J. Peng, Y. Luo and W. Li, 2019: The development of next NCEP Global Ensemble Forecast System. *NWS STI Clim. Bull., 43rd NOAA Annu. Clim. Diagn. Predict. Workshop,* Santa Barbara, CA, 23-25 October 2018.

Zhu, Y., X. Zhou, M. Pena, W. Lei, C. Melhauser, and D. Hou, 2017: Impact of sea surface temperature forcing on weeks 3 and 4 forecast skill in the NCEP Global Ensemble Forecasting System. *Wea. Forecasting*, **32,** 2159-2174, doi: 10.1175/WAF-D-17-0093.1.

——, ——, W. Li, D. Hou, C. Melhauser, E. Sinsky, M. Pena, B. Fu, H. Guan, W. Kolczynski, R. Wobus, and V. Tallapragada, 2018: Toward the improvement of subseasonal prediction in the National Centers for Environmental Prediction Global Ensemble Forecast System, *J. Geophys. Res.: Atmos.,* **123**, 6732-6745, doi: 10.1029/2018JD028506.

——, W. Li, X. Zhou, and D. Hou, 2019: Stochastic representation of NCEP GEFS to improve subseasonal forecast. In the book of *Current trends in the Representation of Physical Processes in Weather and Climate Models*, Editors: Dr. Randells *et al*., Springer Atmospheric Science, 317-328.

The Development of Next NCEP Global Ensemble Forecast System

Xiaqiong Zhou[1], Yuejian Zhu[2], Bing Fu[1], Dingchen Hou[2], Jiayi Peng[1], Yan Luo[1], and Wei Li[1]

[1]IMSG at Environmental Modeling Center, NOAA/NWS/NCEP
[2]Environmental Modeling Center, NOAA/NWS/NCEP

1. Introduction

The current operational Global Ensemble Forecast System (GEFS v11) was implemented at Dec. 2015 (Zhou *et al.*, 2017). It uses a semi-Lagrangian global spectrum model (NCEP GFS/GSM version 12.0.0) with the horizontal resolutions T_L574 (34 km) for the first 8 days and T_L384 (52 km) for the second 8 days. There are 64 vertical levels on sigma pressure hybrid layers. The initial conditions for 20 ensemble members are generated from GSI/EnKF hybrid analysis by adding the 6-h EnKF forecast ensemble perturbations (Zhou *et al.*, 2016). The stochastic total tendency perturbation (STTP) scheme is used to represent model uncertainties by perturbing the total tendency of the model prognostic variables (surface pressure, temperature, wind, and humidity) with an empirical formula (Hou *et al.* 2006, 2008).

GEFS version 12 (FV3-GEFS) is still under development and will be implemented at Q3FY2020. FV3-GEFS uses the NOAA new generation global forecast model with the GFDL Finite-Volume Cubed-Sphere (FV3) dynamical core (Lin and Rood, 1997; Lin 2004). The physics package remains similar with the one used in the current operational GFS except some updates. In this new system, the GFS convection scheme is updated with a scale-aware parameterization (Han *et al.* 2017). The convection scheme is also modified to reduce excessive cloud top cooling for the model stabilization. The GFDL cloud microphysics scheme with five predicted cloud species (cloud water, cloud ice, rain, snow and graupel) will replace the Zhao-Carr microphysics scheme with only total cloud water. Other updates also include a revised bare-soil evaporation to reduce dry and warm bias, an updated parameterization of ozone photochemistry with additional
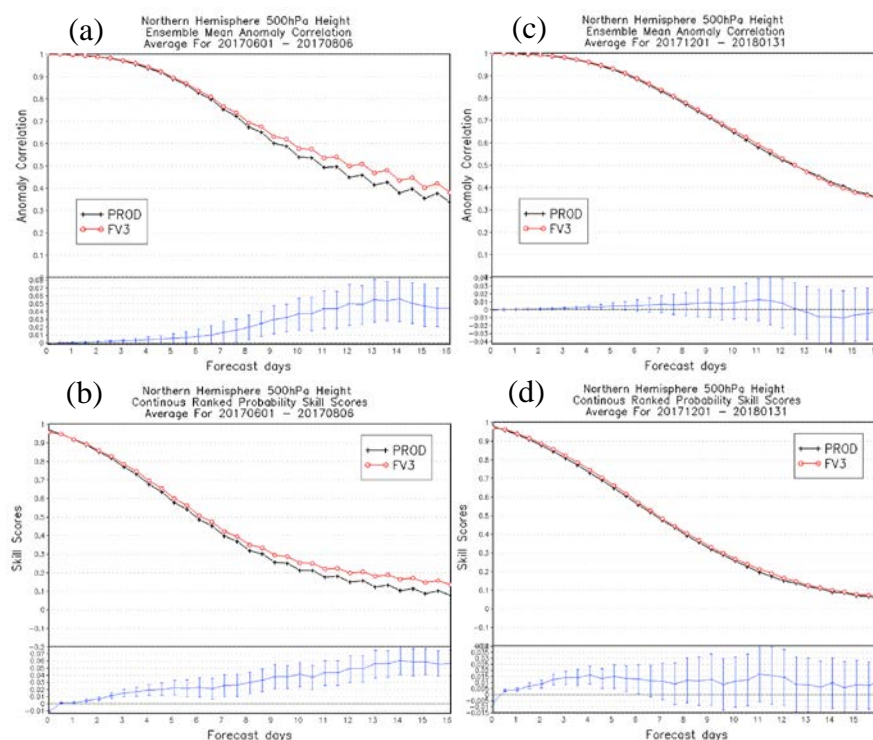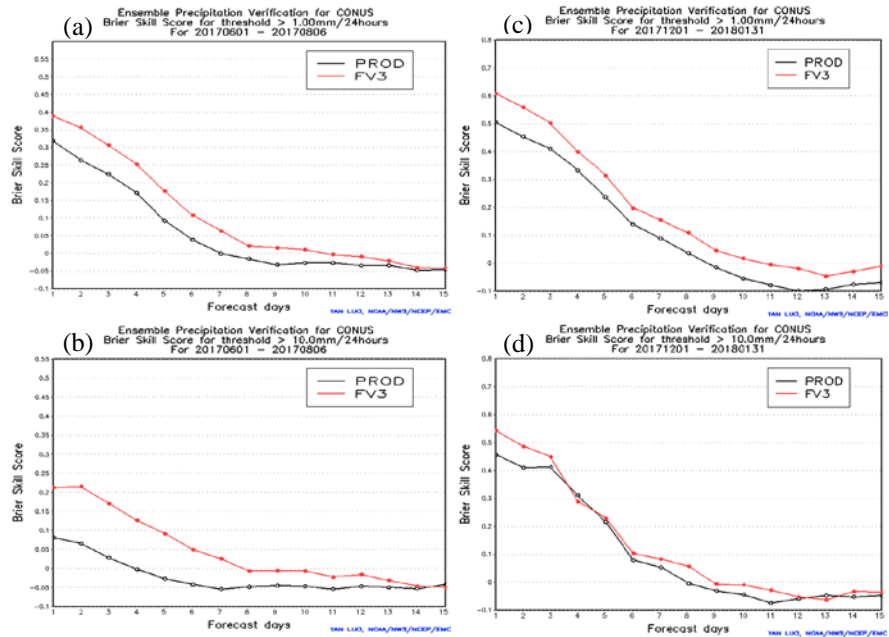

Fig. 1 (a) PAC and (b) CRPSS for the 500-hPa geopotential height over the NH for the warm season (2017060100-2017080600). (c) and (d) are as same as (a) and (b) except for the cold season (2017120100-20170130). The black curves represent the operational GEFS and the red ones represent the FV3GEFS. The lower graphs show the difference and bootstrap significance test (blue bars). The difference is significant at the 95% confidence level when the value is outside the bars.

_____

Correspondence to: Xiaqiong Zhou, IMSG at Environmental Modeling Center, NOAA/NWS/NCEP;
E-mail: xiaqiong.zhou@noaa.gov

production and loss terms (McCormack *et al.* 2006) and a new parameterization of middle atmospheric water vapor photochemistry (McCormack *et al.* 2008).

In contrast to the current operational GEFS v11, FV3-GEFS will extend the forecast from 16 to 35 days with increased and uniform horizontal resolution through model integration (about 25 km). A Near-Surface Sea Temperature (NSST) model is used to predict the vertical profile of sea temperature between the surface and a reference level (about 5m) by only considering two physical process: diurnal thermocline layer warming and thermal skin layer (also known as sub-layer) cooling (Li 2015). This scheme could resolve SST diurnal variabilities and provide a more realistic thermal boundary condition for the atmosphere. A 2-tiered representation of the foundation temperature (sea temperature at the NSST reference level) is used to better represent the variation of ocean temperature forcing with the forecast time (Zhu *et al.* 2018; Wei *et al.* 2018). The STTP scheme used in the operational GEFS is replaced by a stochastic physics suite. It has three components, including 1)

Fig. 2 BSS for the ensemble mean precipitation greater than (a) 1mm (24 h)$^{-1}$ and (b) 10 mm (24h)$^{-1}$ averaged over the warm season. (c) and (d) are as same as (a) and (b) except for the cold season.
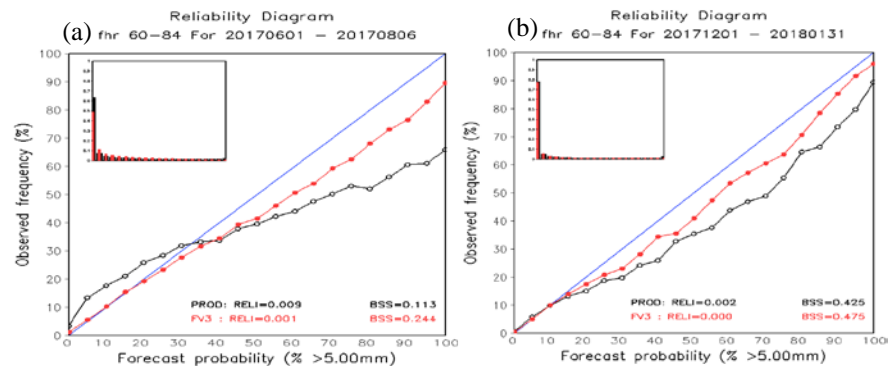
Fig. 3 Reliability of precipitation > 5mm/day calculated with the 21 probability categories from a 21-member ensemble for the (a) warm season and (b) cold season. The top-left inset in each plot shows the proportion of cases in each probability category.

stochastically perturbed physics tendencies (SPPTs; Buizza *et al.* 1999; Palmer 1997, 2001), 2) stochastically perturbed planetary boundary layer humidity (SHUM), and 3) stochastic kinetic energy backscatter (SKEB; Berner *et al.* 2009; Shutts 2005) to represent model uncertainty. All these three schemes use a random pattern generator and AR(1) process to produce spatially and temporally correlated perturbations with horizontal length/time scales up to five different categories: 500 km/6 hours, 1000 km/3 days, 2000 km/30 days, 2000 km/90 days and 2000 km/1 year.

2. Experiment and verification

Experiments with the FV3-GEFS configuration as discussed in the previous section were performed for one warm season (from Jun. 1 to Aug. 8, 2017) and one cold season (from Dec. 1 2017 to Jan. 30 2018). The initial conditions for the control run and ensemble members are generated by using hybrid analysis and EnKF 6-hour forecasts from FV3GFS parallel runs. The FV3-GEFS performance is verified against the hybrid analysis of FV3GFS parallel runs and compared with the operational GEFS against its own analysis.
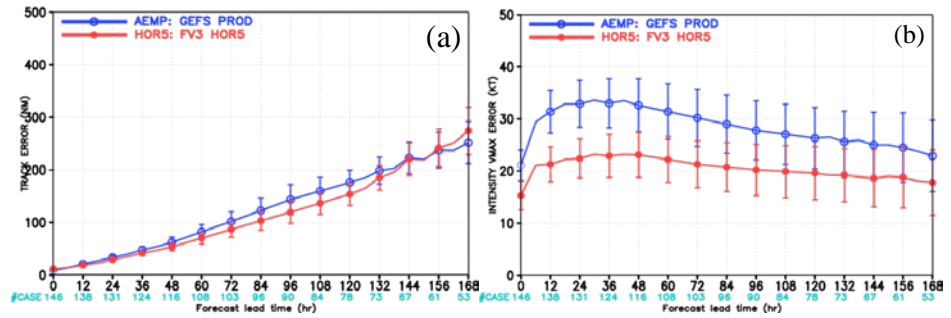
The comparison shows that FV3-GEFS improves the ensemble-mean forecasts of 500 hPa geo-potential height with higher pattern anomaly correlation (PAC) and continuous rank probability skill scores (CRPSSs) in the Northern Hemisphere (NH) than that in the operational GEFS (Fig. 1). The improvement is generally statistically significant at 95% confidence level and the skillful forecast (PAC> 0.6)

Fig. 4 Tropical cyclone forecast (a) track and (b) intensity errors over Atlantic basin for 2017 hurricane season. The blue curves represent the operational GEFS ensemble mean, while the red curves represent the FV3GEFS. The number of TC cases verified for the forecast lead time from 0 - 168 hr listed below the X axis.

extends 12 hrs in the warm season (Fig 1a). Similar improvement can be seen in the cold season but the difference between FV3-GEFS and the operational GEFS in the cold season is not statistically significant (Fig 1c and Fig.1d).

Quantitative precipitation forecasts (QPFs) and probabilistic QPFs are verified against the climatology-calibrated precipitation analysis (CCPA) over the contiguous United States (CONUS). In the categorical verification methods, precipitation is categorized by the 24-h accumulated precipitation with threshold amounts greater than 1, 5, 10, and 20 mm. Brier skill score (BSS) uses the 10-yr mean of CCPA as the climatology to calibrate the Brier score in order to avoid the dependence on the event frequency. FV3-GEFS generally outperform the operational GEFS in terms of precipitation BSSs in each category over CONUS. The BSSs for the precipitation categorized with the threshold amounts greater than 1mm and 10 mm in both warm and cold seasons are shown in Fig. 2. Reliability diagrams display the observed probabilities conditioned with the forecast probabilities of all forecast samples. They provide information about probability forecast bias. If the forecasts have perfect reliability (no bias), the reliability curve would lie along the diagonal line. The comparison shows that FV3-GEFS reliability curves are generally closer to the diagonal line than those from the operational GEFS. The probabilities for higher probability categories are overestimated as the reliability curve is located at the right side of the diagonal line. Apparently, the issue of overestimated probability in FV3-GEFS is significantly improved compared with the operational GEFS (Fig. 3). For the low probability categories, FV3-GEFS presents close perfect reliability.

The 2017 hurricane season over Atlantic was a catastrophic season. There are 17 named storms of which 10 became hurricanes including six major hurricanes (Category 3, 4 or 5) – two category-4 hurricanes (Hurricane Harvey and Jones) and two category-5 hurricanes (Hurricane Irma and Maria). The forecasted tropical cyclone tracks are promising with slightly smaller errors in FV3-GEFS in the first 5-6 days but with larger errors in longer lead times (Fig. 4a). The intensity forecasts are significantly improved (Fig. 4b) as the tropical storms are more intense in the new system than in the operational GEFS.

The MJO prediction skill using Wheeler-Hendon MJO indices (Wheeler and Hendon 2004) in FV3-GEFS is compared with the experimental GEFS extended forecast system which was developed to support the Subseasonal Experiment (SubX) project (Fig. 5). The comparison shows that the skillful MJO prediction with AC > 0.5 extends from 20 days in Subx GEFS to 22 days in FV3-GEFS.
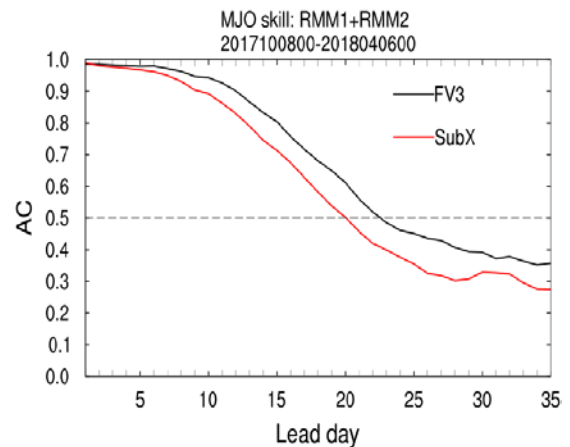
Fig. 5 MJO prediction anomaly correlation skills of using Wheeler–Hendon indices for FV3GEFS (black curve) and SubX (red curve).

3. Summary and discussion

NCEP FV3-based GEFS is scheduled for implementation at Q3FY2020a system. The integration of this new system with all pre-processes and post processes is almost completed and the configuration of FV3-GEFS (GEFS v12) is close to be frozen. The preliminary results from the experiments based on FV3-GEFS was studied. The performance of FV3-GEFS is promising based on the comparison with the operational GEFS for one warm season (from Jun. 1 to Aug. 8, 2017) and one cold season (from Dec. 1 2017 to Jan. 30 2018). FV3-GEFS is generally more skillful than the operational system over extratropical regions with respect to the ensemble mean and probability forecasts of large-scale patterns. The improvement of precipitation forecast over CONUS are very encouraging. FV3-GEFS outperforms the operational GEFS in terms of the reliability and BSSs of precipitation forecasts. In addition, the performances of FV3-GEFS in tropical cyclone track and intensity forecast and MJO skill forecasts are generally positive. Note that this is a preliminary study with very limited sample size. Comprehensive verification will be performed after 2.5-year parallel testing with FV3-GEFS is finished in the near future.

References

Berner, J., G. J. Shutts, M. Leutbecher, and T. N. Palmer, 2009: A spectral stochastic kinetic energy backscatter scheme and its impact on flow-dependent predictability in the ECMWF Ensemble Prediction System. *J. Atmos. Sci.*, **66**, 603–626, doi:10.1175/2008JAS2677.1.

Buizza, R., M. Miller, and T. N. Palmer, 1999: Stochastic representation of model uncertainties in the ECMWF Ensemble Prediction System. *Q. J. Royal Meteorol. Soc.*, **125**, 2887–2908, doi:10.1002/qj.49712556006.

Han, J, W. Wang, Y. C. Kwon, S.-Y. Hong, V. Tallapragada, and F. Yang, 2017: Updates in the NCEP GFS cumulus convection schemes with scale and aerosol awareness. *Wea. Forecasting*, **32**, 2005-2017.

Hou, D., Z. Toth, and Y. Zhu, 2006: A stochastic parameterization scheme within NCEP global ensemble forecast system. *18th Conf. on Probability and Statistics in the Atmospheric Sciences*, Atlanta, GA, Amer. Meteor. Soc., 4.5, https://ams.confex.com/ams/Annual2006/techprogram/paper_101401.htm.

——, ——, ——, and W. Yang, 2008: Impact of a stochastic perturbation scheme on NCEP Global ensemble Forecast System. *19th Conf. on Probability and Statistics in the Atmospheric Sciences*, New Orleans, LA, Amer. Meteor. Soc., 1.1, https://ams.confex.com/ams/88Annual/techprogram/paper_134165.htm.

Li, X., J. Derber and M. Shrinivas, 2015: An atmosphere-ocean partially coupled data assimilation and prediction system developed within the NCEP GFS/CFS. *European Geosciences Union General Assembly 2015*, Vienna, Austria.

Lin, S.-J., 2004: A "vertically Lagrangian" finite-volume dynamical core for global models. *Mon. Wea. Rev.*, **132**, 2293-2302.

——, and R. B. Rood, 1997: An explicit flux-form semi-Langrangian shallow-water model on the sphere, *Q. J. Royal Meteorol. Soc.,* **123**，2477-2498.

McCormack, J. P., S. D. Eckermann, D. E. Siskind , and T. J. McGee, 2006: CHEM2D-OPP: A new linearized gas-phase ozone photochemistry parameterization for high-altitude NWP and climate models, *Atmos. Chem. Phys.*, **6**, 4943–4972.

——, K. W. Hoppel, and D. E. Siskind, 2008: Parameterization of middle atmospheric water vapor photochemistry for high-altitude NWP and data assimilation. *Atmos. Chem. Phys.*, **8**, 7519-7532.

Palmer, T. N., 1997: On parametrizing scales that are only somewhat smaller than the smallest resolved scales, with application to convection and orography. *Workshop on New Insights and Approaches to Convective Parametrization*, Reading, United Kingdom, ECMWF, 328–337.

——, 2001: A nonlinear dynamical perspective on model error: A proposal for non-local stochastic-dynamic parametrization in weather and climate prediction models. *Q. J. Royal Meteorol. Soc.*, **127**, 279–304, doi:10.1002/qj.49712757202.

Shutts, G., 2005: A kinetic energy backscatter algorithm for use in ensemble prediction systems. *Q. J. Royal Meteorol. Soc.*, **131**, 3079–3102, doi:10.1256/qj.04.106.

Wheeler, M. C, H. H. Hendon, 2004: An all-season real-time multivariate MJO index: development of an index for monitoring and prediction. *Mon. Wea. Rev.*, **132**, 1917–1932.

Wei, L., Y. Zhu, X. Zhou, D. Hou, E. Sinsky, C. Melhauser, M. Peña, H. Guan and R. Wobus. 2018: Evaluating the MJO prediction skill from different configuration of NCEP GEFS extended forecast. *Clim. Dyn.,* **31**, 1-14.

Zhou, X., Y. Zhu, D. Hou, and D. Kleist. 2016. Comparison of the ensemble transform and the ensemble Kalman filter in the NCEP global ensemble forecast system. *Wea. Forecasting,* **31**, 2058–2074.

——, ——, ——, Y. Luo, J. Peng, and D. Wobus. 2017. The NCEP global ensemble forecast system with the EnKF initialization. *Wea. Forecasting,* **32**, 1989–2004.

Zhu, Y., X. Zhou, W. Li, D. Hou, C. Melhauser, E. Sinsky, M. Peña, B. Fu, H. Guan, W. Kolczynski, V. Tallapragada, 2018: Toward the improvement of subseasonal prediction in the National Centers for environmental prediction global ensemble forecast system. *J. Geophys. Res.: Atmos,* **123**, 6732–6745.

Toward Improving Short-Lead Monthly Forecast

Peitao Peng, Mike Halpert, Stephen Baxter and Mike Charles

Climate Prediction Center, NOAA/NWS/NCEP

1. Introduction

It is well known that weather forecast skill decays fast with lead time, meanwhile, big anomalies of variables occurred in early period of a month could have big impact to their monthly mean values, thus for a short-lead monthly forecast, its skill could be improved by appropriately leveraging the decay in skill.

In this study, this idea was tested by weighting CFS forecasts of four sub-monthly periods (*i.e.*, days 1-3, days 4-7, days 8-14, and days 15-30) with their historical skill. It is found that such aggregated 30-day forecasts do have higher skill than the simple mean of the 30-day forecast.

2. Data

Model data used in this study are CFSv2 45-day hindcast for the period of 1999-2010 and forecast for the period of 2011-2017. Variables to be verified are surface air temperature (SAT) and precipitation (Prec). The verification data, both SAT and Prec are from Climate Prediction Center (CPC) analyses.

3. Procedures

We first calculated the skill of the CFS hindcast for the four sub-monthly periods, that is, days 1-3, days 4-7, days 8-14 and days 15-30, then construct 30-day mean forecast by aggregating forecast values from each of the sub-monthly periods. This was done by weighting the sub-monthly forecasts with their corresponding hindcast skill:

$$f_w = \frac{1}{30} \sum_{n=1}^{4} d_n f_n AC_n$$

where, n is the sub-period index, d the number of days in sub-period, f the forecast, and AC the temporal anomaly correlation skill in hindcast. The earlier sub-monthly periods thus have heavier weights in the weighted forecast.

3. Results

Figure 1 shows the hindcast AC skill of SAT and Prec for the four sub-monthly periods. It is obvious that the skill decays fast with lead time, and the days 15-30 almost has no skill.

Figure 2 presents the skill of the weighted and un-weighted 30-day forecast. The improvement of the weighted forecast looks tiny for SAT, but quite obvious for Prec.
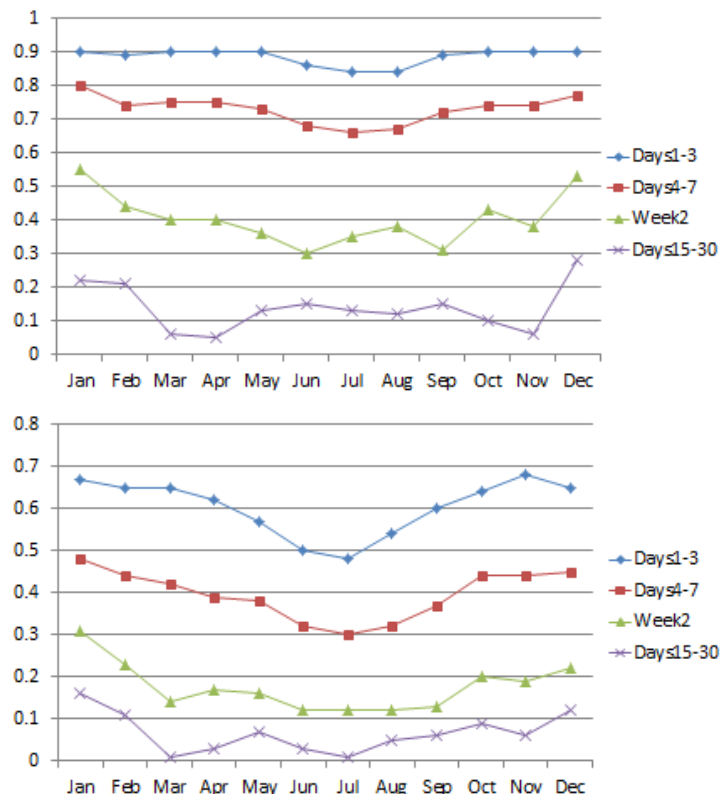
Fig. 1 Hindcast AC skill averaged over CONUS for the 4 sub-monthly periods. The upper panel is for SAT and lower panel for Prec.
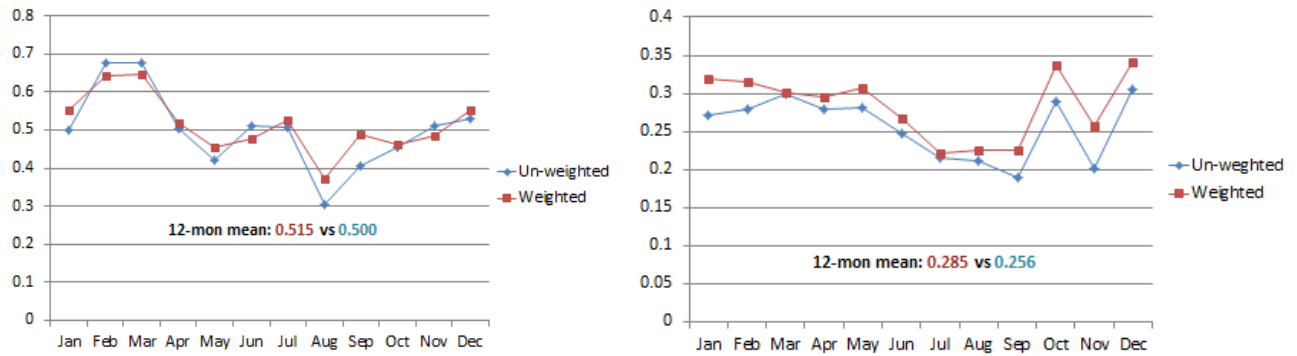
Fig. 2 Skill (AC) comparison between the weighted and un-weighted short-lead 30-day SAT (left) and Prec (right) forecast. The skill is averaged over CONUS.

4. Summary

   i. Forecast skill decays fast from early to late sub-monthly periods;

  ii. Skill weighted short-lead 30-day forecast has marginal but consistent improvement in skill for Prec, but not obvious for SAT;

 iii. As expected, big Prec anomalies in early periods are more likely to dominate monthly mean anomalies than SAT;

 iv. Possible reasons for the improvement to be limited are considered as follows.

     a) Big anomalies don't always occur in early periods;

     b) Skill-dependent weighting makes the forecast skewed to higher frequency, and thus could downplay lower frequency variability, such as aliased from seasonal and inter-annual variability.

The Aleutian Low – Beaufort Sea Anticyclone: A New Climate Index for Seasonal Melt of the Pacific Arctic Cryosphere

Christopher J. Cox[1,2,3], Robert S. Stone[4], David C. Douglas[5],
Diane Stanitski[6], and Michael R. Gallagher[1,2,32]

[1]*Cooperative Institute for Research in Environmental Sciences (CIRES), Boulder, CO*
[2]*NOAA Physical Sciences Division (PSD), Boulder, CO*
[3]*University of Colorado, Boulder, CO*
[4]*Science and Technology Corporation (STC), Boulder, CO*
[5]*United States Geological Survey (USGS) Alaska Science Center, Juneau, AK*
[6]*NOAA Global Monitoring Division (GMD), Boulder, CO*

ABSTRACT

Recent springtime climate extremes have been observed along the northern coast of Alaska. The dates when snow melted at Utqiaġvik (formerly Barrow) in 2015 and 2016 were the 4th and 1st earliest recorded, respectively, since 1902. These early years were followed by the latest date of snowmelt since 1988 in 2017 and the latest date since 1947 in 2018. The range of these melt dates spans 41 days across the months of May and June, expressing large interannual variability in the arrival of spring in northern Alaska during recent years. Previous work implicates northward advection of warm air circulating around the Aleutian Low during years of early melt and blocking by the Beaufort High during years of later melt, and it is the juxtaposition of the two pressure centers that is influential for northern Alaska. However, the spatial and temporal variability of the melt timing is also sensitive to subtle variations in the way air circulates around these dominant pressure centers. For example, while the Beaufort High helped preserve snowpack at Utqiaġvik in 2017, circulation patterns also favored the transport of warmer air to points along the northern coast east of Utqiaġvik, which contributed to an earlier melt there. This suggests that the position of a high-pressure ridge to the east of the Aleutian Low is also important in modulating the timing of snowmelt regionally. We investigate these relationships using reanalysis, satellite retrievals, and surface-based data sets. We expand the analysis spatially beyond terrestrial snow cover to also analyze the spatial patterns in the timing of the onset of melt over sea ice in the Chukchi and Beaufort seas. We introduce a new 4-point climate index based on regional 850 hPa GPH called the Aleutian Low – Beaufort Sea Anticyclone (ALBSA). ALBSA tracks the synergy of the Aleutian Low and Beaufort High and is shown to explain some of the variance in the melt metrics over both the terrestrial and marine
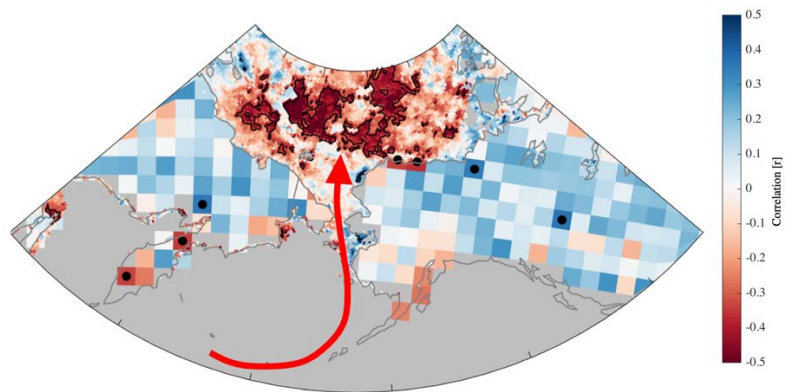
Fig. 1 Correlation (r) between ALBSA in May 1979-2017 and a combination of satellite observations; the date of snow melt derived from the Northern Hemisphere Snow Cover Extent (NH-SCE) (terrestrial regions) (Estilo *et al.* 2015) and the date of melt onset over sea ice derived from SSM/I passive microwave data (sea ice regions) (Markus *et al.* 2009). Dots (land) and solid contour (ocean) denote areas of statistically significant correlation (p < 0.05).

_____

Correspondence to: Christopher J. Cox, CIRES, University of Colorado, and NOAA Physical Sciences Division, Earth System Research Laboratory, Boulder, Colorado; E-mail: christopher.j.cox@noaa.gov

regions. The index is therefore suitable for monitoring changes in regional circulation and may be useful for developing seasonal-scale predictive tools.

Reference

Estilow, T. W., A. H. Young, and D. A. Robinson, 2015: A long-term Northern Hemisphere snow cover extent data record for climate studies and monitoring. *Earth System Science Data*, **7**, 137-142. doi:10.5194/essd-7-137-2015.

Markus, T., J. C. Stroeve, and J. Miller, 2009: Recent changes in Arctic sea ice melt onset, freezeup, and melt season length. *J. Geophys. Res. - Oceans*, **114**, C12024, doi:10.1029/2009JC005436.

Water in the Arabian Peninsula

Muge Komurcu[1], Adam Schlosser[1],
Ibtihal Alshehri[2], Tariq Alshahrani[2], Waleed Alhayaza[2], Adnan AlSaati[2,3]

[1]*Massachusetts Institute of Technology, Joint Program on the Science and Policy of Global Change,
Center for Global Change Science, Cambridge, MA*
[2]*King Abdulaziz City for Science and Technology, Riyadh, Saudi Arabia*
[3]*Massachusetts Institute of Technology, Center of Complex Engineering Systems, Cambridge, MA*

ABSTRACT

Increasing temperatures, changes in damaging extreme events, rising costs of energy, heightened environmental consciousness, degraded land productivity, and overburdened water resources are among a variety of stressors that can stem from regional changes in the natural, managed, and built environments. Over the Arabian Peninsula, water can play a multi-faceted role to not only the sustainability but also the vulnerability of prosperity and continued growth across its populated areas. Therefore, simulating future changes in the regional climate – with particular attention to the changing characteristics of precipitation – is key to those adjustments. However, global model projections are too coarse to represent the unique surface and atmospheric features of the region. To help assess changes in regional climate and support regional sustainability efforts, we perform convection permitting regional climate modeling simulations and dynamically downscale Community Earth System Model (CESM) projections under a high-impact emission scenario using the Weather Research and Forecasting (WRF) model to 4 km horizontal resolution. Preliminary results focusing on historical and future changes in the mean and extremes of climate variables are presented here.
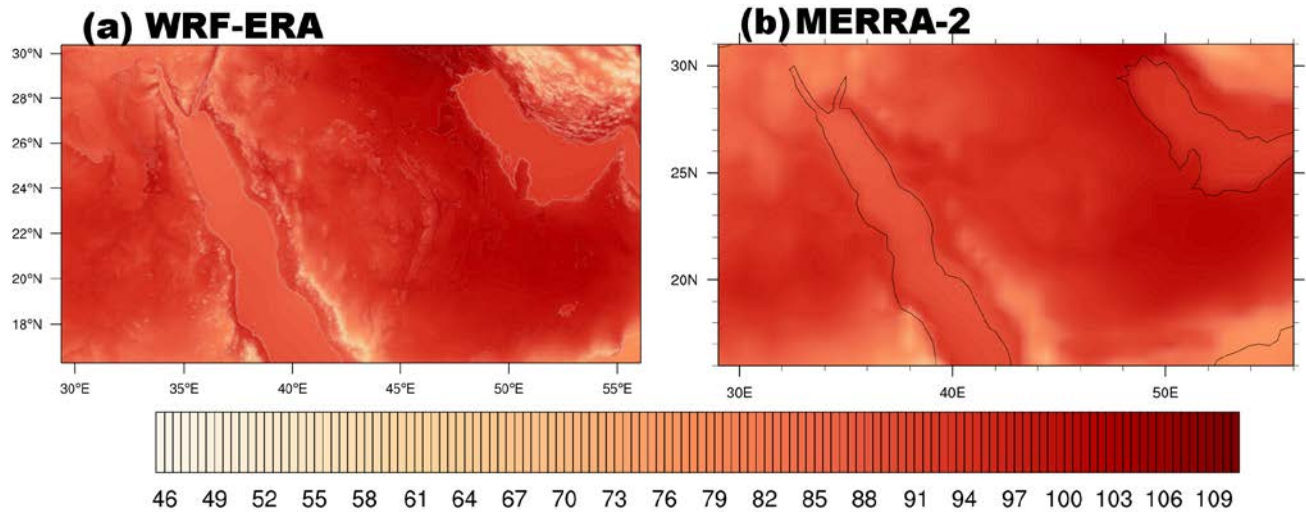
1. Introduction

Water consumption in the **Kingdom of Saudi Arabia (KSA)** has been increasing. As part of Vision 2030 investment activities (https://vision2030.gov.sa/en), several investments have been made and are planned in the region in the near future such as new solar power operated desalinization plants, sustainable infrastructure and touristic areas to attract global attention. Furthermore, recently KSA has been experiencing intense extreme precipitation events: For example, Jeddah floods of 2009, 70 mm of rain was recorded at Jeddah meteorological station. The event led to flooding that cost lives of 122 people while 350 were missing. Damaged businesses created a huge cost ($270 million) to the economy. Hence, structure and infrastructure failure due to intense precipitation events (Ameur, 2016) and the financial and cost

Fig. 1 WRF model domain used in this study.

associated with recovery have become a main concern for the Kingdom. Particularly of interest is estimating the changes in the intensity and frequency of extreme events (precipitation, heat waves, and dust storms) affecting the region under climate change. For planning new touristic areas, engineering heat withstanding infrastructure, and choosing locations of new infrastructure that will serve the cities, future climate information is needed in local scales. In this study, we are using global model projections to drive a regional climate model

_____

Correspondence to: Muge Komurcu, Massachusetts Institute of Technology, Joint Program on the Science and Policy of Global Change, Center for Global Change Science, Cambridge, MA; E-mail: muge@mit.edu

Fig. 2 August mean temperatures at 2 meters [K] from (a) WRF-ERA (b) MERRA-2 averaged over 2008-2017.

to produce high-resolution climate variables under a high impact emissions scenario. We will use these high-resolution projections 1) to study changes in regional climate and climate extremes and 2) as input for hydrological and flood models to assess future changes in water resources, guide sustainable infrastructure design under climate change and help future urban city planning and expansion efforts in the Kingdom of Saudi Arabia.

2. Methods

To obtain high resolution climate projections, we dynamically downscaled the bias corrected CESM projections under Representative Concentration Pathway (RCP) 8.5 (Bruyère *et. al.*, 2014) using the WRF Model v3.6.1. Our methodology and model setup are similar to Komurcu *et al.* (2018). In WRF, we use three nested domains of 36, 12 and 4 km horizontal resolution. Model domain, nesting and parameterization setup were established after a series of sensitivity runs on MIT's Svante High Performance Computing System. The model domain used in this study is shown in Fig. 1. To assess future changes in climate, we perform dynamical downscaling of CESM projections for two time periods representative of present day (2008-2017) and mid-century (2041-2050).

3. Results

Results presented in this paper are preliminary. Figure 2 shows August mean temperatures from WRF-ERA (WRF driven by ERA-Interim data) and MERRA-2 (Modern-Era Retrospective Analysis for Research and Applications version 2) averaged over 2008 to 2017. WRF-ERA is able to simulate similar temperatures
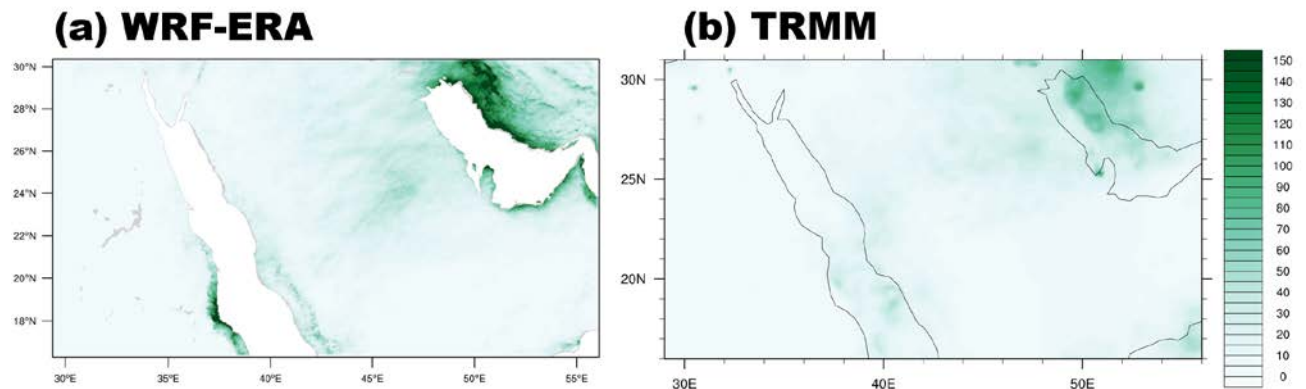
Fig. 3 November precipitation rates [mm/month] averaged over 2008-2017 as simulated from (a) WRF-ERA and observed/retrieved from (b) TRMM.
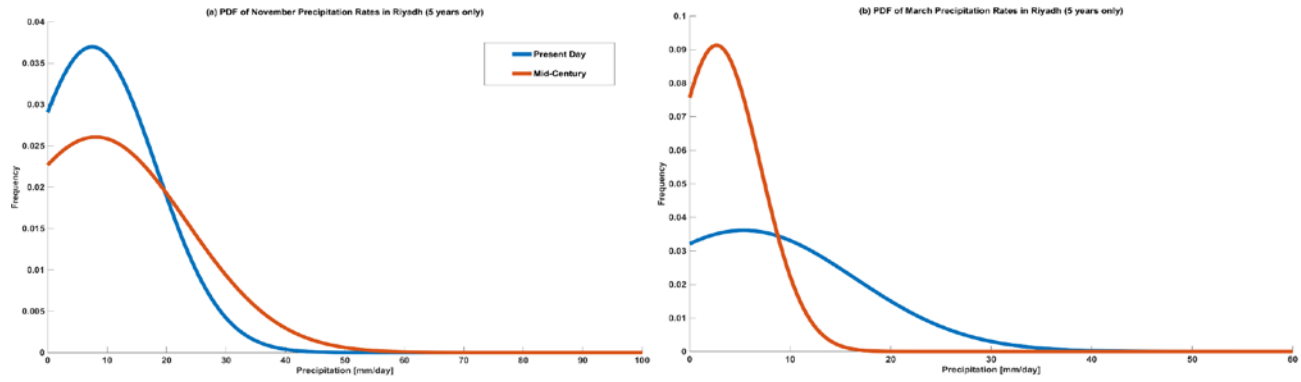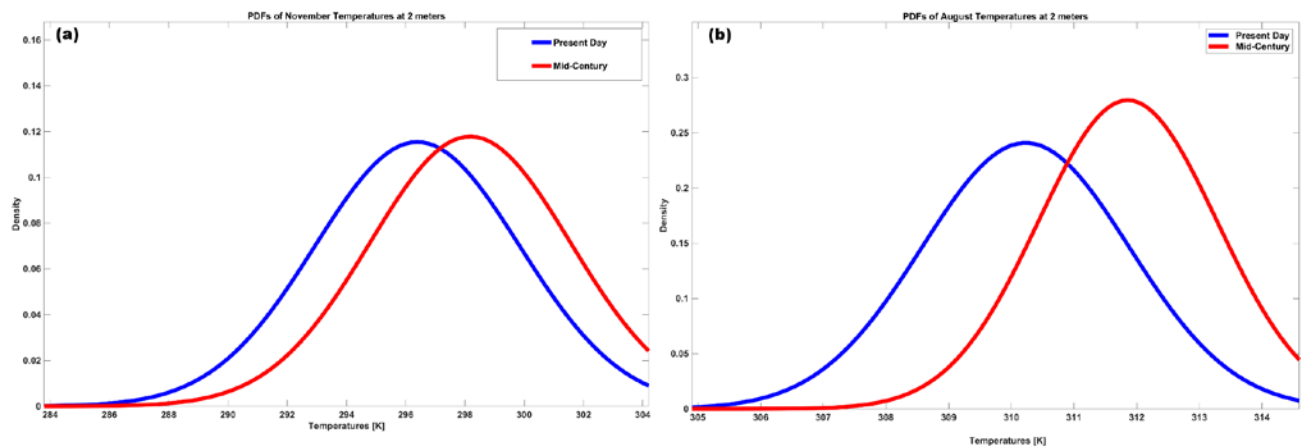
Fig. 4 PDFs of present day (blue) and mid-century (red) precipitation rates (mm/day) in Riyadh for (a) November and (b) March.

to those from (MERRA-2) and provides the detailed, high-resolution temperature data needed for local climate change assessments and sustainability studies.

November precipitation rates from (a) WRF-ERA and (b) TRMM (Tropical Rainfall Measuring Mission) are presented in Fig. 3. WRF-ERA is generally able to capture the observed precipitation structure and locations of increase in precipitation rates. There is a slight positive bias along certain coast lines and in the center of the Kingdom in WRF-ERA compared to TRMM, which may be associated with the higher resolution (hence more detailed representation of the topographical features) in our WRF simulations compared to TRMM. Due to a lack of a dense, homogeneous network of historical observations of precipitation rates, it is difficult to establish the biases beyond a comparison with TRMM. Nevertheless, these biases need to be taken into account while interpreting future projections of precipitation rates.

Figure 4 a and b show the probability density functions (PDFs) of present day and mid-century precipitation rates (mm/day) in Riyadh for November and March respectively for 5 years. We find that while mid-century mean precipitation rates reduce in November compared to present day climate, extreme precipitation events become more intense and frequent. In March, more precipitation events occur mid-century while extreme events become rare compared to present day climate.

In Fig. 5, we present the PDFs of temperatures for November and August for five years of the simulated time period. We find that while temperatures increase for both November and August by mid-century, this rate of increase is more pronounced in August.

Fig. 5 PDFs of daily temperatures at 2 meters for present day (blue) and mid-century (red) climate for (a) November and (b) August.

4. Conclusions and future work

Our preliminary analysis shows that there are significant differences between mid-century and present-day mean and extreme climate in the Kingdom's capital Riyadh. Work is currently underway to 1) expand the projections to span 20 years in each time period, 2) extend the regions studied 3) use high resolution projections generated in further analysis related to the sustainability of the region.

References

Ameur F., 2016: Floods in Jeddah, Saudi Arabia: Unusual phenomenon and huge losses. What prognoses. FLOODrisk 2016 - 3rd European Conference on Flood Risk Management, *E3S Web Conf.*, **7**, doi:10.1051/e3sconf/20160704019.

Bruyère, C. L., J. M. Done, G. J. Holland, and S. Fredrick, 2014: Bias corrections of global models for regional climate simulations of high-impact weather. *Clim. Dyn.*, **43**, 1847-1856, doi:10.1007/s00382-013-2011-6.

Komurcu, M., K. A. Emanuel, M. Huber, and R. P. Acosta, 2018: High-resolution climate projections for the northeastern United States using dynamical downscaling at convection-permitting scales. *Earth and Space Science*, **5**, 801–826, doi:10.1029/2018EA000426.

CWB CFS 1-Tier Hindcast Analysis and Forecast Verification

Tzu-Yu Wu[1, 4], Hann-Ming Henry Juang[2, 4], Yun-Lan Chen[1], Pang-Yen Liu[1], Shin-I Lin,
Jen-Her Chen[3], and Mong-Ming Lu[5]

[1]*Meteorology Research and Development Center, Central Weather Bureau, Taiwan*
[2]*Environmental Modeling Center, NCEP, NWS, NOAA, USA*
[3]*Meteorological Information Center, Central Weather Bureau, Taiwan*
[4]*Department of Atmospheric Sciences, National Central University, Taiwan*
[5]*Department of Atmospheric Sciences, National Taiwan University, Taiwan*

1. Introduction

One-tier global atmospheric and oceanic seasonal and climate modeling is a trend for both research and operational centers. NCEP developed dynamical seasonal forecast system before 2000 (Kanamitsu *et al.* 2002) and moved to one-tier model CFS v1.0 (NCEP GFS coupled with GFDL MOM3) in 2004 (Saha *et al.* 2006). ECMWF started improving system 1 (Stockdale *et al.* 1998) since 1996, and moved to one-tier with system 2 (T95L40) in 2003 (Anderson et al. 2003), and recently with higher resolutions.

In 2010, Central Weather Bureau (CWB) in Taiwan began to develop its own global atmosphere-ocean coupling model. Based on NCEP CFS package, NCEP global atmospheric model was replaced by CWB's own global atmospheric model (CWB GFS in resolution of T119L40, Paek *et al.* 2015) and coupled with the GFDL MOM3 (TCWB1T). It takes six years to build the couple model to be routinely operation, including workflow construction, model tuning with adjusting cloud physics *etc.*, 20 more years hindcast, and ensemble member bias correction etc. It is used to provide seasonal forecast and ENSO forecast up to 9 months. It started operating routinely in 2017 at Taiwan CWB.

Fig 1 Niño 3.4 regional SST anomaly forecast for DJF by TCWB1T was close to the OISST trend at the initial time from June to November.

Fig 2 Fraction of variance explained by EOF modes 1 through 5 for SST anomaly. purple line is TCWB1T, black line is ERSST.
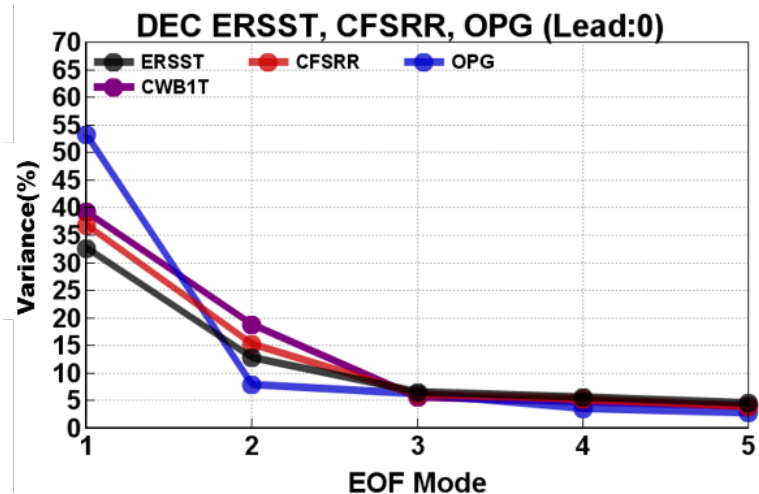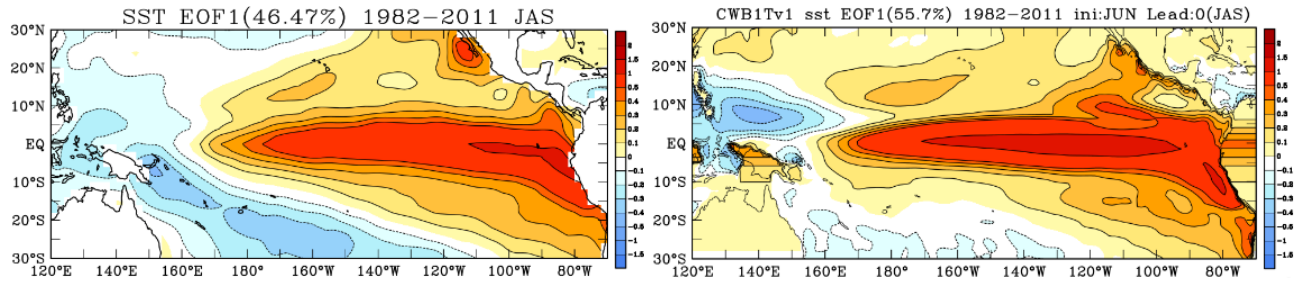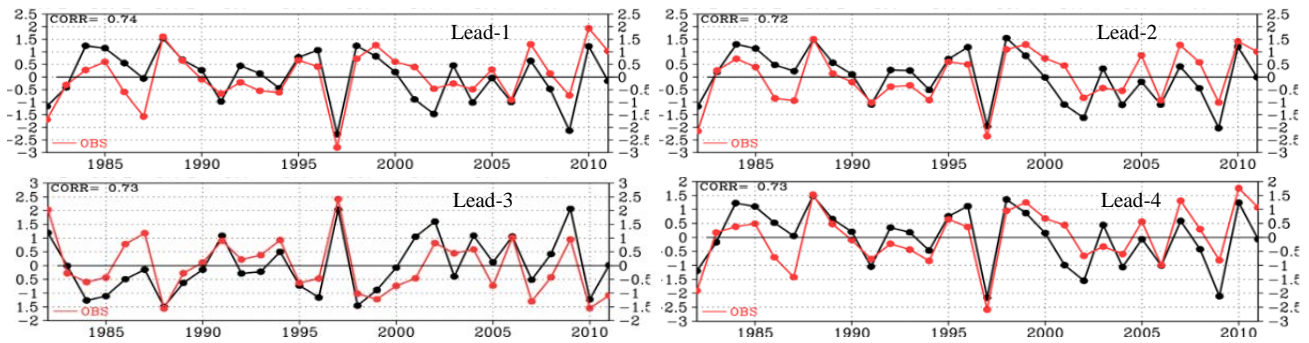
2. Data and experimental design

Based on NCEP CFS v2 reforecast (hindcast) data set, we follow the method of their hindcast member selection for our hindcast design. The NCEP CFS v2 hindcast was running 4 cycles for selected 6 dates for any

Fig. 3-1 The EOF1 of ERSST (left) and TCWB1T (right) lead 0 month SST forecast.

**Fig. 3-2** The leading (from lead 0 to lead 4) anomaly correlations of PCA are above 0.72.

given month. The dates are 1, 6, 11, 16, 21, and 26 of any given month. Due to our resource problems, we did two experiments. The first set, we have accomplished two cycles, 00z and 12z with dates of 1, 6, 11, 16, 21, and 26, and the second, we have only accomplished one cycles 00z with dates of 1, 3, 6, 8, 11, 13, 16, 18, 21, 23, 26, 28 of any given month. The results shows that more dates are more important than more cycles, so we choose one cycle 00z, the second set, to do reforecast from 1982 to 2011.

3. Results

3.1 Hindcast analysis (1982-2011)

By analyzing SST of hindcast data from 1982 to 2011, we found that NINO3.4 regional SST anomaly forecast for DJF was close to the OISST trend at the initial time from June to November (Fig. 1). Figure 2 show the fraction of variance explained by EOF modes 1 through 5 for SST anomaly. TCWB1T (purple line) is close to ERSST (black line). The result of EOF1 analysis shows that El Niño pattern of TCWB1T similar to ERSST (Fig. 3-1), the anomaly correlation between TCWB1T and ERSST is more than 0.72 from lead-012 (JAS) to lead-456 (NDJ) (Fig. 3-2).

The SST forecasting ability is better than T2M and precipitation, only captured over tropical sea. The forecasting ability of TCWB1T shows that winter is better than summer (Fig. 4).
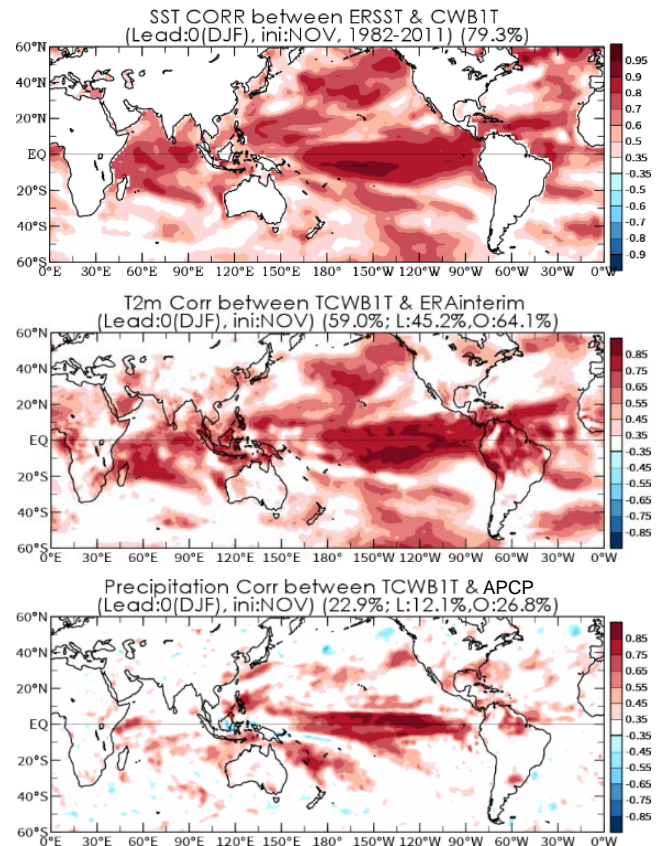
Fig. 4 The DJF forecast anomaly correlations of SST, T2M, precipitation between TCWB1T and observation/reanalysis in November. Only correlations significant at 0.05 are presented.

3.2 Forecast verification

We are starting MJO analysis on the operational forecast results of TCWB1T this year. During the season of DJFM from 2012 to 2018, 22 days of correlation coefficient between the observation and the forecast of RRM1 and RRM2 index from the model of TCWB1T are higher than 0.5 (Fig. 5). It indicates that CWB CFS1Tier can be used for ENSO as well as MJO forecasts.

4. Future work

We will have a newly updated TCWB1T this year 2019. It will have improved dynamic, corrected low boundary conditions, adjusted microphysics, better initial condition and climatology fields. And we will finish everyday hindcast run from 1999 to present in August. In the future, we will increase model resolution of atmosphere and ocean model. For example, CWB GFS T239L60 couple with GFDL MOM3 or MOM5. CWB 1-Tier is a seasonal forecast model that will be used for operational S2S in the near future (ex. MJO and BSISO (Boreal Summer Intraseasonal Oscillation) forecasts).
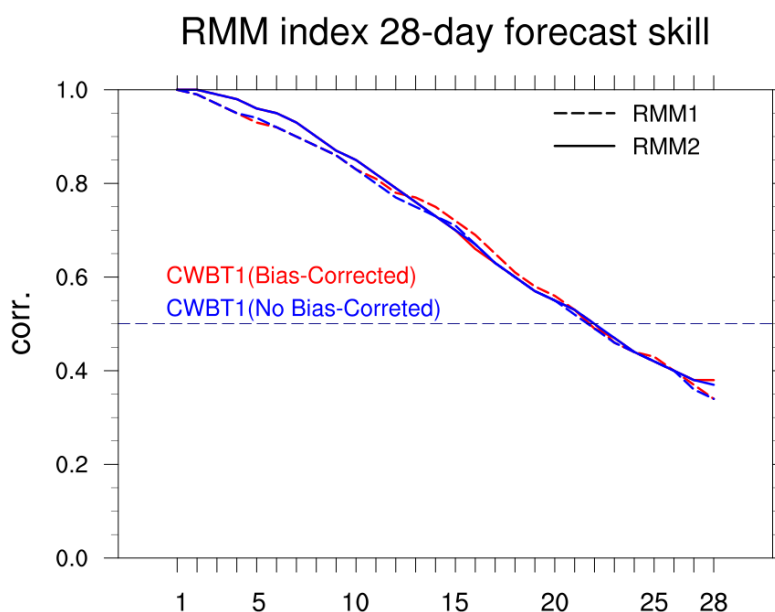
Fig. 5 From 2012 to 2018, the 28-day forecast anomaly correlations of DJFM RMM1 and RMM2 index.

References

Anderson, D. L. T., T. Stockdale, M. A. Balmaseda, L. Ferranti, F. Vitart, P. Doblas-Reyas, R. Hagedorn, T. Jung, A. Vidard, A. Troccoli, and T. Palmer, 2003: Comparison of the ECMWF seasonal forecast systems1 and 2, including the relative performance for the 1997/8 El Niño. ECMWF Technical Memorandum 404, 93pp. https://www.ecmwf.int/sites/default/files/elibrary/2003/7728-comparison-ecmwf-seasonal-forecast-systems-1-and-2-including-relative-performance-19978-el.pdf

Kanamitsu, M., and Coauthors, 2002: NCEP dynamical seasonal forecast system 2000. *Bulletin Amer. Meteor. Soc.*, **83**, 1019-1037, doi:10.1175/1520-0477(2002)083<1019:NDSFS>2.3.CO;2

Paek, H., J.-Y. Yu, J.-W. Hwu, M.-M. Lu, T. Gao, 2015: A source of AGCM Bias in simulating the western pacific subtropical high: different sensitivities to the two types of ENSO. *Mon. Wea. Rev.*, **143**, 2348-2362.

Saha, S., and Coauthors, 2006: The NCEP Climate Forecast System. *J. Climate*, **19**, 3483–3517.

Stockdale, T. N., D. L. T. Anderson, J. O. S. Alves, and M. A. Balmaseda, 1998: Global seasonal rainfall forecasts using a coupled ocean–atmosphere model. *Nature*, **392**, 370–373.

CPC's New Consolidated Hybrid Statistical/Dynamical Model for Seasonal Prediction of Temperature and Precipitation

Daniel Barandiaran

Climate Prediction Center, NOAA/NWS/NCEP, College Park, MD
*and*
Innovim, LLC, Greenbelt, MD

1. Introduction

It has been known for some time that CPC could benefit from a new seasonal forecast consolidation that will serve as a 'first guess' for the forecaster, with the aim of improving forecast reliability and month-to-month consistency across forecast and forecasters. The prior consolidation, implemented in 2006, had the positive benefit of leading to increased forecast coverage and improved 'all forecasts' skill scores (Baxter 2016). There are, however, some limitations of this consolidation that reduce its usefulness to CPC forecasters. First, the consolidation uses climate division data (CD-102) with coverage of the continental United States only. Second, the consolidation makes use of decades-old statistical tools and only one dynamical model input, namely the Climate Forecast System (CFS). Finally, the consolidation process itself is something of a black box, for instance giving little information to the forecaster regarding the contribution of various components of the consolidation to overall forecast skill.

Since the implantation of the operational consolidation in 2006, there have been advances in model post-processing and calibration (*e.g.*, Unger *et al.* 2009; Ou *et al.* 2016; van den Dool *et al.* 2017) that have been implemented across many of CPC's operational forecast products and tools. An effort was therefore initiated to take advantage of such methodologies as well as to make use of newer statistical tools and a larger pool of dynamical models, therefore creating a robust forecast tool that can more easily be utilized by the forecaster.
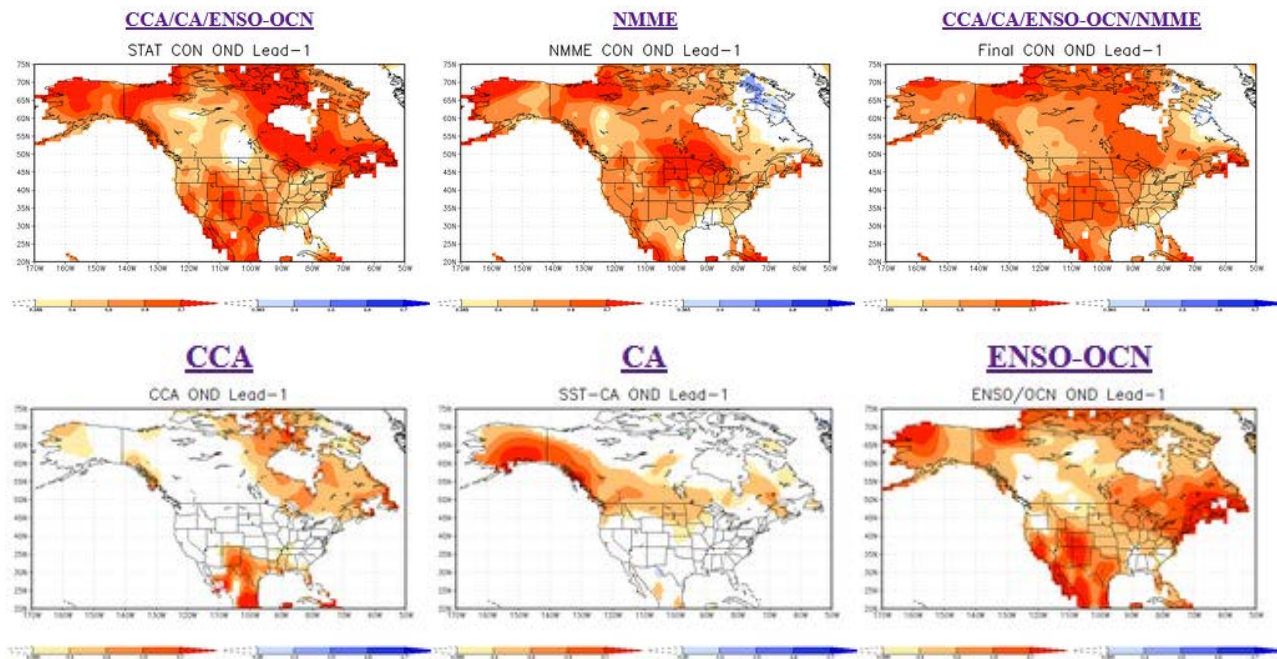
2. Methods and data

The primary goal of this project was to apply a probability anomaly correlation (PAC) calibration to a new suite of empirical forecast tools, and consolidate those tools with the constituent models of the National Multi-model Ensemble (NMME) system, which have been PAC-calibrated in real-time since 2016. The PAC
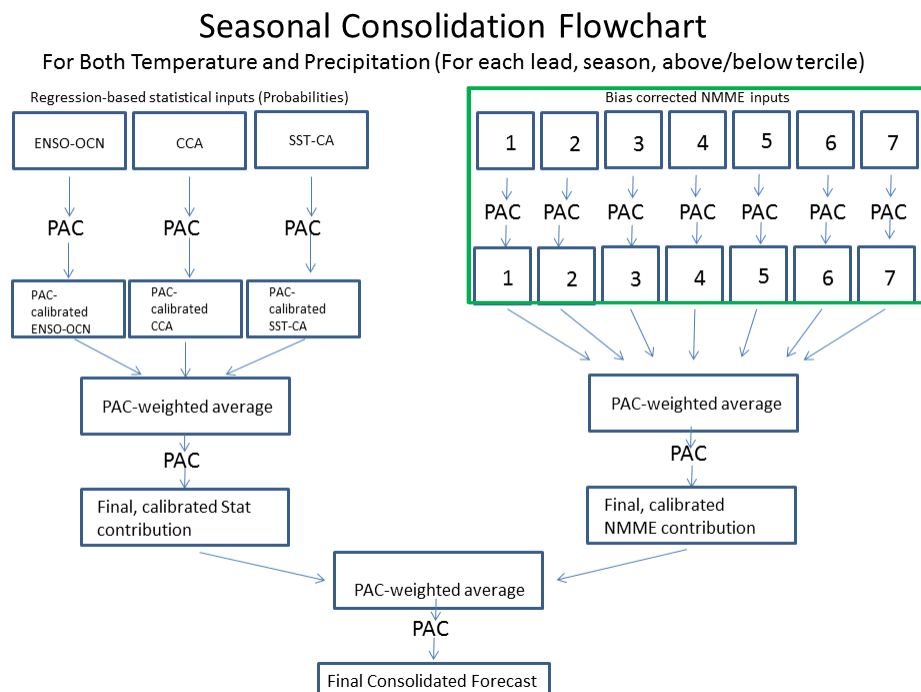

Fig. 1 Seasonal consolidation flowchart. The green box indicates process that currently executes operationally upstream of the consolidation. All other processes are included as part of this experimental consolidation process.

Correspondence to: Daniel Barandiaran, Climate Prediction Center, NOAA/NWS/NCEP, 5830 University Research Court, College Park, MD 20740, and Innovim, LLC, Greenbelt, MD; E-mail: daniel.barandiaran@noaa.gov

Season 1 T2m forecast

Fig. 2 Sample output graphics available to forecasters for the Lead-1 temperature forecast.

Skill for Season 1 T2m
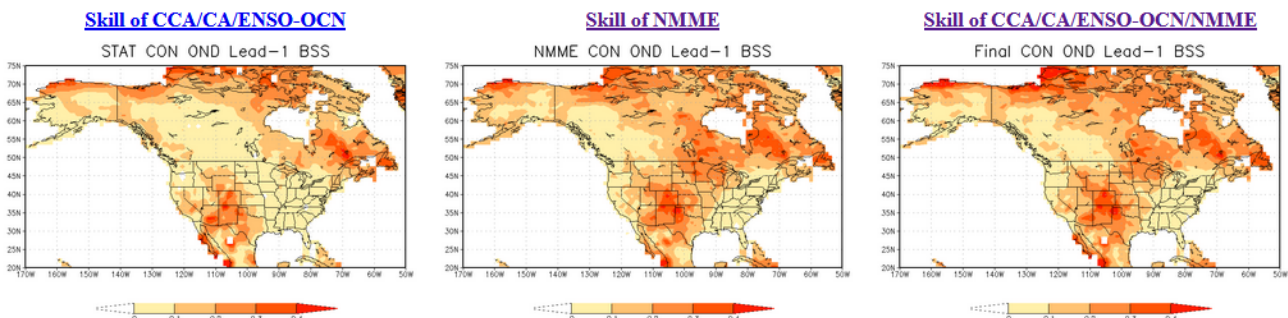
Fig. 3 Sample historical Brier skill score (BSS) graphics output alongside the forecast graphics.

methodology, acting on probability anomalies, is analogous to traditional linear regression acting on temperature and precipitation anomalies themselves; the former minimizes the Brier score, while the latter minimizes the mean squared error (van den Dool *et al*. 2017).

The suite of empirical forecast tools being used in the consolidation include a canonical correlation analysis-based model (CCA, Barnston and He 1996), constructed analog based on sea surface temperatures (SST-CA, van den Dool *et al.* 2003), and a hybrid El Niño-Southern Oscillation/long term trends forecast tool (ENSO-OCN, Barandiaran and Baxter 2017). These statistical models are all calibrated using GHCN (Global Historical Climatology Network)+CAMS (Climate Anomaly Monitoring System) for temperature (Fan and van den Dool 2008) and CPC's gridded precipitation reconstruction (Chen *et al.* 2002).

The new consolidation flow chart is shown in Fig. 1. The premise is to apply PAC calibration to each of the constituent models for both the statistical and dynamical model inputs, and then each stream, statistical (left) and dynamical (right), is combined by weighting based on the PAC coefficient (ranging from 0 to 1, with negative values set to 0). Because the combination of models is often more skillful than each model separately, the results at this point are expected to be underconfident. Therefore, a second pass PAC calibration will

minimize the Brier score of the *combination* of forecast tools. This process is repeated to consolidate the statistical and dynamical forecast streams.

3. Results

Forecast probabilities and skill metrics are output and archived in real-time in both NetCDF and binary data formats, and forecast graphics are output and archived. A web interface was created where the forecaster can access the consolidation forecasts from both the NMME and statistical tools, and their final consolidation. An example of the graphics forecasters had access to for the September seasonal forecast cycle is shown in Fig. 2. Importantly, forecasters can see whether contributions to the forecast are coming from statistical models or the NMME. The statistical model stream is further broken down into its three constituent models. Associated skill maps are displayed as well, where the average of the hindcast Brier skill score for above- and below-normal temperature probabilities is plotted for that lead and target season (Fig. 3).

Evaluation of the consolidation was conducted by calculating the BSS for each lead and season as well as associated reliability statistics. The statistical and dynamical model components are compared to understand where the statistical guidance adds value to the
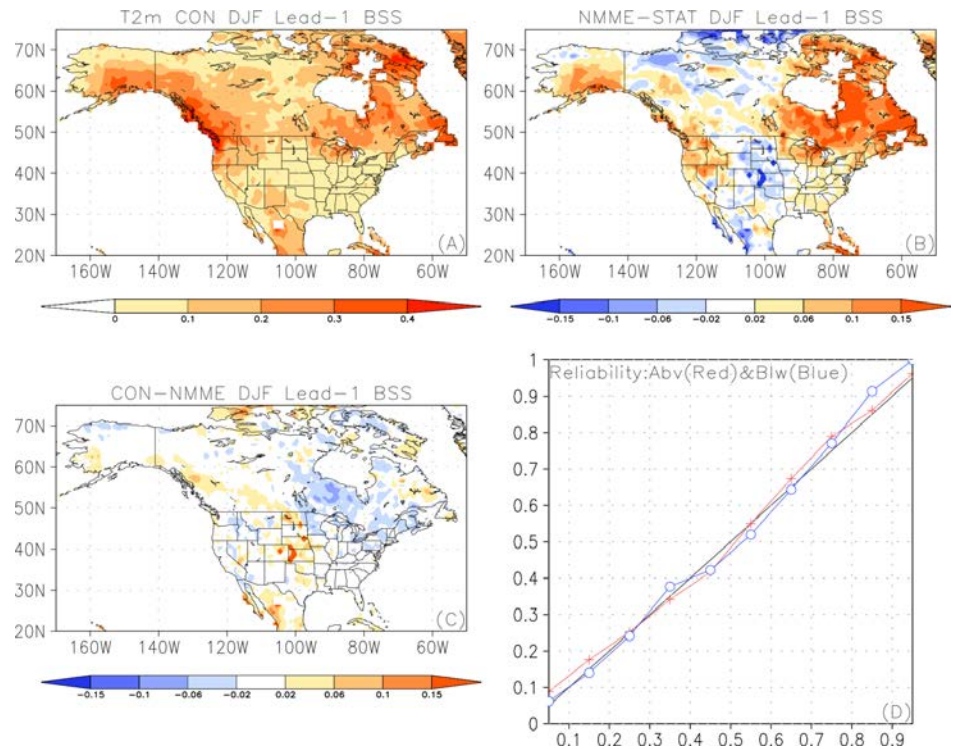
Fig. 4 Panel (a) shows the average Brier skill score (BSS) for Lead-1 above- and below-normal temperature forecasts for December-February (DJF). Panel (b) shows the BSS difference between the NMME stream and the statistical stream. Panel (c) shows the BSS difference.
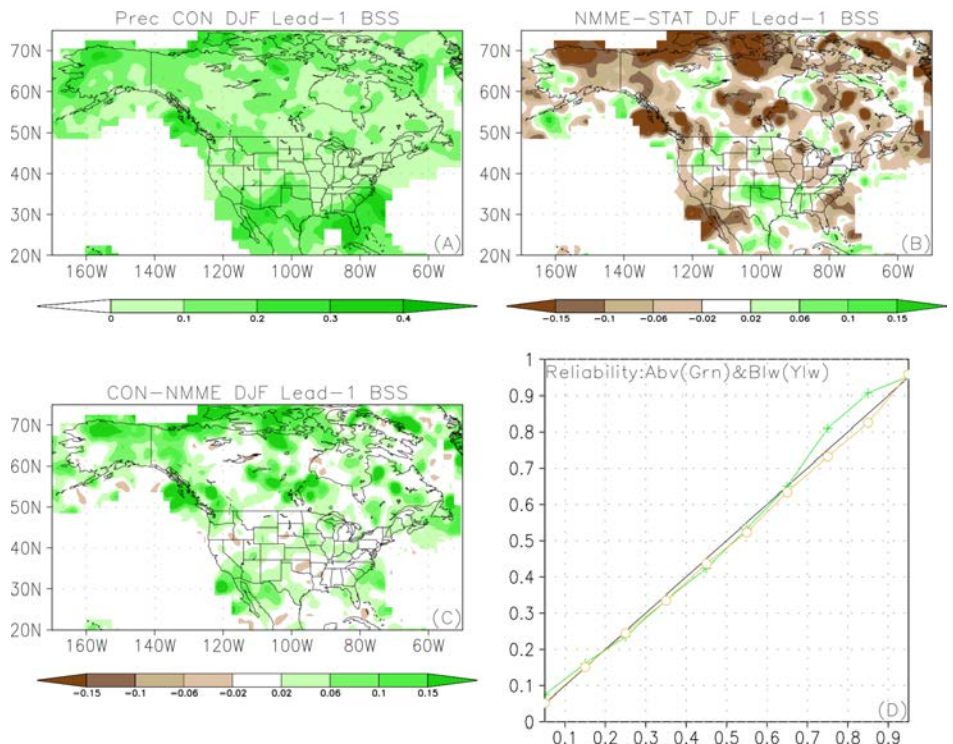
Fig. 5 Same as Fig. 4 except for Lead-1 DJF precipitation forecasts. In this case, the statistical forecast tools generally enhance the skill of the forecast (Panel C).
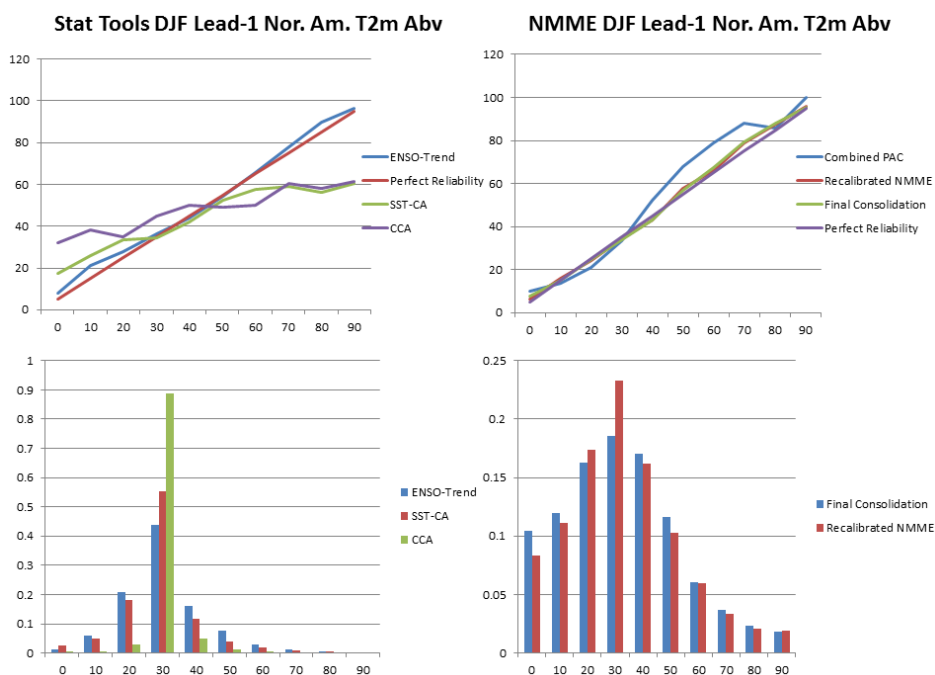
state-of-the-art dynamical model guidance. Finally, some comparison is made to the current NMME guidance utilized by forecasters.

The average BSS for Lead-1 temperature forecasts of December-February (DJF) is shown in Fig. 4a. As expected, skill is modest across much of the CONUS, except where ENSO and long-term trends are most important. The difference between the average BSS of NMME model consolidation and the statistical model consolidation is shown in Fig. 4b; the statistical models outperform the NMME only in low-skill areas over the central CONUS. Figure 4c shows the difference in BSS between the final

Fig. 6 This figure highlights the reliability and frequency of Lead-1 forecasts of above-normal temperatures for December-February from the statistical models (left) and the NMME and final consolidation (right). Importantly, the NMME as used by seasonal forecasters (blue line, upper right) is notably underconfident.

consolidation and the NMME constituent; this can be thought of as the value added by the inclusion of the statistical guidance. There are areas where the statistical guidance clearly adds value, but it is mostly mixed. Figure 4d shows the reliability of above- and below-normal temperature forecasts from the final consolidation, respectively. As expected given this established methodology, the final consolidation is reliable across forecast probabilities. Figure 5 shows the same except for DJF Lead-1 precipitation forecasts. In this case, an obvious ENSO skill signature is seen, with the highest forecast skill over regions where seasonal precipitation is known to be more correlated to ENSO.

Finally, Fig. 6 shows a more in-depth breakdown of tools for the Lead-1 DJF temperature forecast. This reveals that the addition of the statistical models maintains reliability while adding resolution (increasing the frequency with which larger probabilities are forecast). Additionally, it shows that the NMME as currently used by CPC forecasters is quite under confident. The second pass PAC calibration in this case increases the probabilities to match forecast skill.

4. Summary

- The latest seasonal forecast tools, including constituent models from the NMME and newly derived empirical models, are consolidated and recalibrated using the probability anomaly correlation (PAC) methodology.
- The forecast consolidation occurs in two phases: the first in which statistical and dynamical tools are consolidated separately, and the second in which these two streams are consolidated (Fig. 1).
- Real-time forecast graphics are available to forecasters, along with associated skill metrics (Figs. 2 and 3).
- The inclusion of statistical tools improves the forecast skill for precipitation in all seasons. For temperature the impact is less notable, though there is some evidence that forecast resolution improves (Figs. 4, 5, and 6).

References

Barandiaran, D., and S. Baxter, 2017: Benchmark statistical model for seasonal prediction of temperature and precipitation. *42nd NOAA Annu. Clim. Diagn. Predict. Workshop*, Norman, OK, 23-26 October 2017, https://www.nws.noaa.gov/ost/climate/STIP/42CDPW/posters/IMG_4825.JPG.

Barnston, A. G., and Y. He, 1996: Skill of canonical correlation analysis forecasts of 3-month mean surface climate in Hawaii and Alaska. *J. Climate*, **9**, 2579-2605, doi:10.1175/1520-0442(1996)009<2579:SOCCAF>2.0.CO;2

Baxter, S., 2016: Evaluating CPC's operational seasonal temperature forecasts: Why aren't we beating a categorically warm forecast? *NWS Sci. Technol. Infusion Clim. Bull., 41st Annu. Clim. Diagn. Predict. Workshop*, Orono, ME, October 3-6 2016, 61-63, doi:10.7289/V5JS9NH0.

Chen, M., P. Xie, J. E. Janowia, and P. A. Arkin, 2002: Global land precipitation: A 50-yr monthly analysis based on gauge observations. *J. Hydrometeor.*, **3**, 249-266, doi:10.1175/1525-7541(2002)003<0249:GLPAYM>2.0.CO;2

Fan, Y., and H. van den Dool, 2008: A global monthly land surface air temperature analysis for 1948-present. *J. Geophys. Res.*, **133**, D01103, doi:10.1029/2007JD008470.

Ou, M. H., M. Charles, and D.C. Collins, 2016: Sensitivity of calibrated week-2 probabilistic forecast skill to reforecast sampling of the NCEP Global Ensemble Forecast system. *Wea. Forecasting*, **31**, 1093-1107, doi:10.1175/WAF-D-15-0166.1.

Unger, D. A., H. van den Dool, E. O'Lenic and D. Collins, 2009: Ensemble regression. *Mon. Weather Rev.*, **137**, 2365-2379, doi:10.1175/2008MWR2605.1.

van den Dool, H., E. Becker, L. Chen, and Q. Zhang, 2017: The probability anomaly correlation and calibration of probabilistic forecasts. *Wea. Forecasting*, **32**, 199-206, doi:10.1175/WAF-D-16-0115.1.

—, J. Huang, and Y. Fan, 2003: Performance and analysis of the constructed analogue method applied to U.S. soil moisture over 1981–2001. *J. Geophys. Res.*, **108**(D16), 8617, doi:10.1029/2002JD003114.

NOAA's MAPP-CTB Projects Update: Community R2O Contributions to the Improvement of Operational S2S Climate Prediction

Jiayu Zhou[1] and David DeWitt[2]

[1]Climate Mission, Office of Science and Technology Integration, NOAA/NWS Headquarters
*[2]Climate Prediction Center, NOAA/NWS/NCEP*

1. Introduction

NOAA's Modeling, Analysis, Predictions and Projections - Climate Test Bed (MAPP-CTB) projects support research to significantly increase the accuracy, reliability, and scope of NWS Climate Prediction Center operational seasonal-to-subseasonal (S2S) climate probabilistic forecast products. Out of twenty-six funded projects, twelve are on track to be completed by the end of fiscal year 2018, seven are in progress with an adjusted deliverable schedule, and seven are new development projects. This extended summary provides stakeholders an update on 1) completed projects leading to an improved operational prediction capability, 2) prominent progress of ongoing projects, and 3) challenging new developments supported by leveraging the research community. The CTB management solicits feedback on optimal project performance to accelerate the transition from research to operations for service improvement toward the NWS strategic goal of a "Weather-Ready-Nation".

2. Completed projects leading to an improved operational prediction capability

2.1 System implementations:

i) NCEP GEFS for monthly forecast (PI: Y. Zhu, EMC, NOAA/NWS/NCEP)

A real-time monthly GEFS version with the identical configuration as reforecast but larger ensemble size (21 members) is being conducted every Wednesday since July 2017. Finished a 17-yr reforecast with a high-resolution (34 km for 0-8 days and 52km for 8-35 day) model and 11 member ensemble. Eleven real-time priority variables are delivered to CPC. Other priority 2 and 3 variables are delivered to IRI. The weeks 3&4 forecast has been assessed. MJO forecast skill (from 12.5 days to 22 days) and NH 500hPa height ensemble mean AC scores (from 0.35 to 0.404) are improved after applying the new stochastic physics perturbation (SPs), updated SST (CFSBC) and new convective schemes (CNV). (Fig.1).
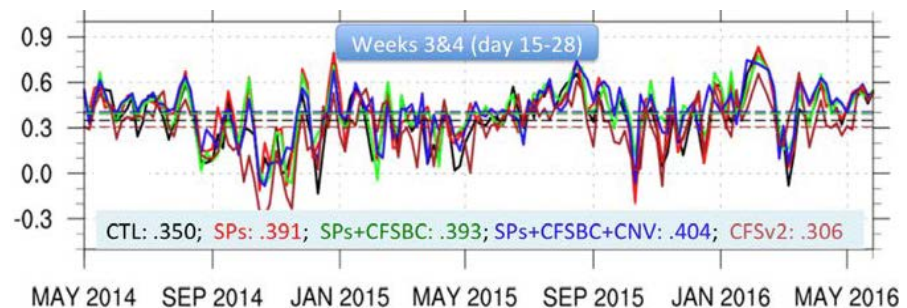
Fig. 1 Pattern Anomaly Correlation (PAC) for Northern Hemisphere 500 hPa geopotential height for lead weeks 3&4 during the period from May 2014 to May 2016. Control (CTL) is in black, SPs in red, SPs+CFSBC in green, SPs+CFSBC+CNV in blue and CFSv2 in brown with period average PAC scores for each configuration (numbers in the bottom of plot with corresponding color). (Courtesy of Y. Zhu)

ii) Improved turbulence and cloud processes (PI: S. K. Krueger, University of Utah)

The Simplified Higher-Order Closure (SHOC) and Chikira-Sugiyama-Arakawa-Wu (CSAW) unified cumulus parameterization have been implemented and tested in NEMS/GSM and GFS with FV3 dynamical core (FV3gfs). SHOC, CSAW along with Morrison-Gettelman double moment microphysics have been implemented in the Interoperable Physics Driver 4 of the NEMS/FV3 model.

_____

Correspondence to: Jiayu Zhou, Climate Mission, Office of Science and Technology Integration, NOAA/NWS Headquarters, 1325 East West Highway, SSMC2, Silver Spring, MD 20910; E-mail: jiayu.zhou@noaa.gov

iii) NMME Phase 2 (PI: RSMAS, B. Kirtman, University of Miami)

NMME Partner Agreement was signed by all parties and the Community Earth System Model (CESM), and the retrospective forecast completed. NMME operational forecasts continue to be delivered on time. A new procedure for estimating forecast spread is developed.

iv) Real-time multi-model sub-seasonal predictive capability (SubX) (PI: B. Kirtman, RSMAS, University of Miami)

The SubX began making real-time predictions in July 2017. The data are provided to CPC as guidance to their week 3-4 forecast products and also to IRI for posting on the IRI Data Library. Completed re-forecast database. Comprehensive skill evaluation showed the benefit of the MME over any individual model.

v) U.S. monitoring and prediction system for flash droughts (PI: D. P. Lettenmaier, University of California)

An experimental real time flash drought monitor is on the CPC website. Experimental real time flash drought forecast in three categories based on the CFSv2 seasonal forecasts has been implemented.

vi) Ensemble-based sea ice analysis and forecasting (PI: J. Carton, University of Maryland)

Sea ice modeling and data assimilation (EnKF) capability has been implemented in CFS, and a full year sea ice analysis using the new ensemble-based system completed.

2.2 System new components

i) Lake-effect process (PI: J. Jin, Utah State University)

The 16-year retrospective forecasts with nine leads were performed with CFS and CFS-Flake. These forecasts for the Great Lakes region were quantitatively analyzed with different metrics, showing the predicted surface skin temperature, precipitation, and lake ice spatial distribution with the coupled CFS-Flake were significantly improved

ii) CCSM4 (SubX) (PI: B. Kirtman, RSMAS, University of Miami)

Real-time Community Climate System Model 4.0 (CCSM4) subseasonal forecasts began in July 2017. All priority 1 variables from all the hindcasts have been provided to IRI.

iii) Navy Earth System Model (NESM) (PI: N. Barton, Naval Research Laboratory)

Demonstrated that NESM forecasts can be supplied to NOAA in a timely manner for S2S operational products. Completed the re-forecasting effort from 1999 to start of the real-time experiment, and supplied these outputs to NOAA and IRI.

2.3 System analysis and optimization

i) Estimation of NASA GEOS-5 MJO forecast skill and land surface feedback (PI: D, Achuthavarier, Universities Space Research Association)
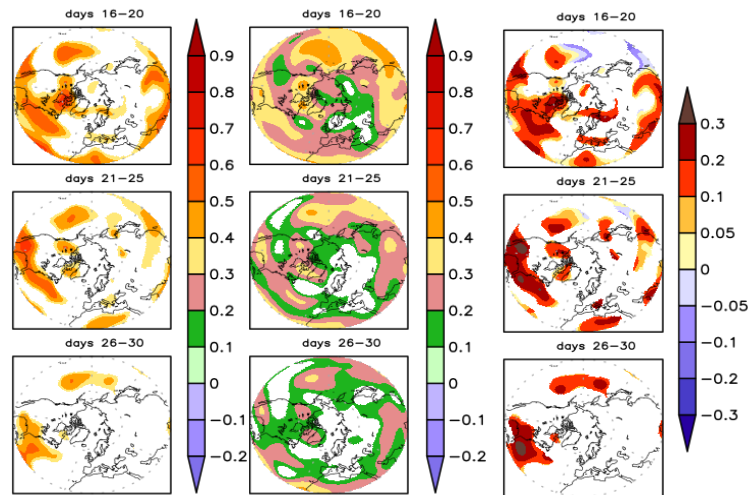
Fig. 2 Anomaly correlation coefficient for 5-day averaged H500 anomalies from GEOS-S2S hindcasts when (left column) forecast initialization contains MJO in phases 3 or 7, (middle column) for all forecasts irrespective of MJO signal in initial conditions, and (right column) difference between the two. The rows represent 5-day averaged fields as the forecast progresses from day-16 to day-30. Verification is performed against MERRA-2 data, and forecasts cover the period 1999-2015. All forecasts are initialized over an extended winter period (November through March). The results are promising in that increased skill (the red shading in the right column) is observed up to days 26-30, especially over the eastern US, suggesting a typical MJO-NAO teleconnection pattern. It indicates higher skill of H500 anomalies prediction when an MJO in phases 3 or 7 is present in the initial conditions. (Courtesy of D, Achuthavarier)

The near real-time production of sub-seasonal forecasts commenced at GMAO, NASA/GSFC on July 25, 2017, and since then, the forecasts (consisting of 10 Priority-1 variables) have been submitted to CPC every Wednesday. In addition, 39 output fields from the forecasts are being submitted to the IRI's SubX data repository. Figure 2 shows a promising result.

ii) NMME skill, predictability and optimum combination (PI: T. Delsole, George Mason University)

Developed a new method for determining the ensemble size and initialization frequency of the lagged ensemble that minimized the MSE. Identified the optimal lagged ensemble for monthly, subseasonal and seasonal forecasts in CFSv2. Developed new, rigorous methods (code available online) for comparing forecast skill.

iii) Assessment of CFS severe weather predictions (PI: M. Tippett, Columbia University)

The automated 00 UTC CFS ensemble mean severe weather guidance dashboard has been transitioned to application (www.spc.noaa.gov/exper/CFS_Dashboard/).

3   Progress from projects on finalization

One-year no-cost extensions are granted to seven projects in final stage for completion. Here are some prominent achievements shown in project reports.

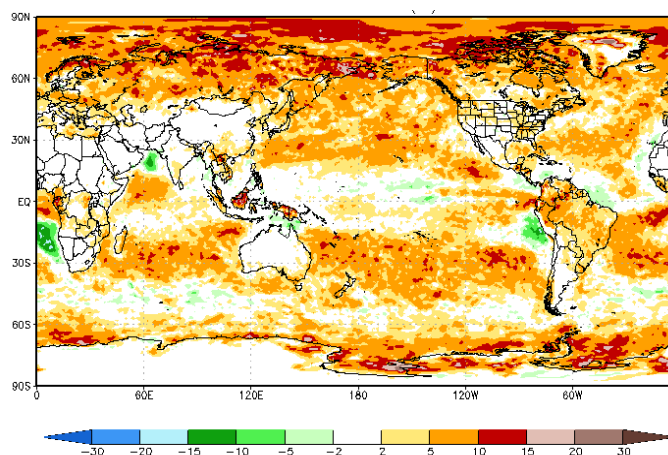i) Improved cloud and boundary layer processes (PI: C. S. Bretherton, University of Washington)

The new scheme has neutral results in the short and medium range forecast skill metrics used by NCEP, but has the benefit of increasing

Fig. 3 Mean difference of low (<680 hPa) cloud fraction (%) for the forecasts with the new scheme (EDMF-TKE) with respect to the control forecasts (EDMF-CTL). The forecast period for the mean difference calculation is from 1 Dec 2016 to 6 Dec 2017, and the low cloud fraction is the average of 102, 108, 114, and 120 forecast hours. (Courtesy of C. S. Bretherton)
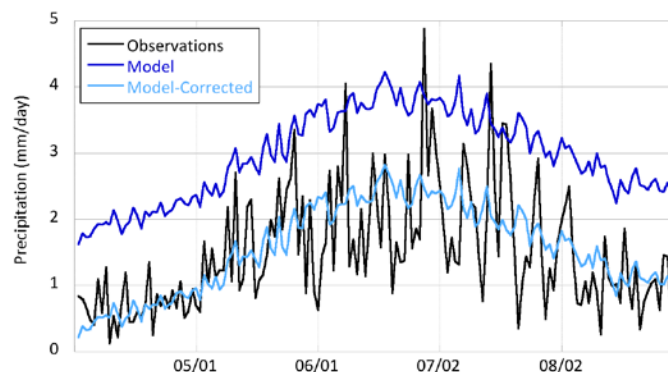
Fig. 4 Tanana Valley-West climatological seasonal cycle of daily precipitation from observations (black), raw model forecast (dark blue) and corrected model forecast using quantile mapping (light blue). The plot shows a seasonal cycle averaged over 1994-2010. (Courtesy of U. Bhatt)

forecast global low cloud cover by 5%, in better agreement with satellite observations as shown in Fig. 3.

ii) Seasonal forecast application for AK wildland fire management (PI: U. Bhatt, University of Alaska)

The key index, Buildup Index (BUI), from the Canadian Forest Fire Weather Index System (CFFWIS) represents potential fuel availability and flammability. It is based on cumulative scoring of daily temperature, relative humidity, and precipitation. The biases in temperature and precipitation result in systematic biases in BUI for Interior Alaska. The quantile mapping method is used, which shifts the cumulative distribution of the model forecast to match the observed distribution to reduce biases as seen in Fig. 4.

iii) Subseasonal excessive heat outlook system (PI: A. Vintzileos, ESSIC, University of Maryland)

The global heat-impact oriented subseasonal excessive heat system runs experimentally on real time at the University of Maryland since May 2018 and provides probabilistic forecasts of the wet and dry Excess Heat Factor (EHF). Preliminary results are presented in Fig. 5. Further exploring the margins provided by acclimatization and the geographical modulation of the danger level is going to proceed.

iv) Eddy-permitting hybrid global ocean data assimilation system (PI: S. G. Penny, University of Maryland)

The bulk of the software engineering for Hybrid-GODAS has been recently completed, allowing for initial performance tests on the whole system to begin on the Gaea supercomputer. The code has been made publically available online while development and tuning continues. Figure 6 shows the Hybrid-DA improvement, especially in the tropical Atlantic, a region that the existing GODAS often has trouble with. (https://github.com/UMD-AOSC/hybrid-godas).
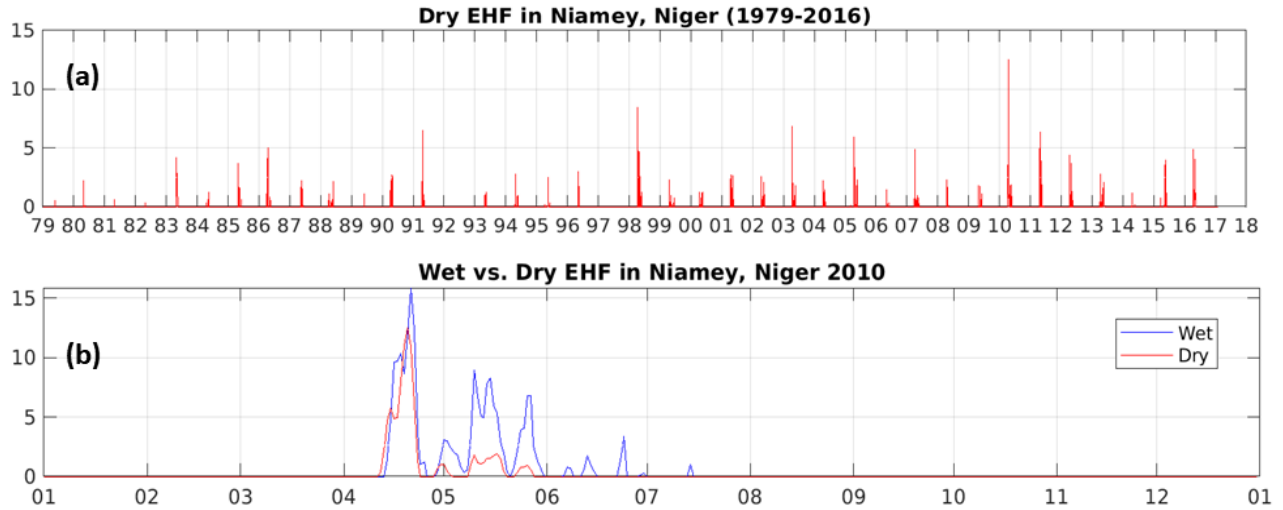
Fig. 5 (a) The dry EHF as calculated using ERA-Interim data from 1979-2016 at the closest grid point to Niamey airport, Niger. The reported excessive heat wave, which occurred in April 2010 is well captured. (b) Both dry and wet EHF are successful in capturing the April 2010 event, however, during May as the monsoon season approaches the wet EHF shows higher sensitivity. The wind induced skin evaporation and lower solar incoming radiation provide relief from excessive heat. (Courtesy of A. Vintzileos)
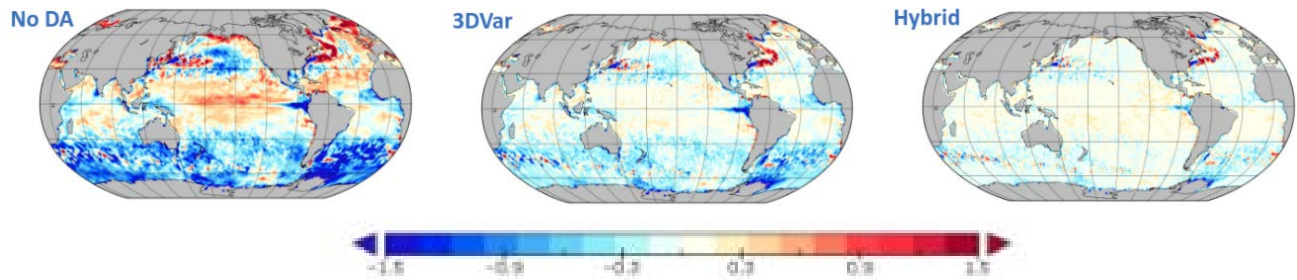

Fig. 6 Comparison of SST bias over a three month test period using no data assimilation (left), 3DVar only (middle) and hybrid LETKF/3DVar (right). (Courtesy of S. G. Penny)

Also projects at the final stage are 1) modeling and data infrastructure (PI: C. Deluca, CIRES, University of Colorado), 2) S2S climate products for hydrology and water management (PI: A. Wood, NCAR), and 3) operational transition of soil moisture and snow data assimilation in NLDAS (PI: Christa Peters-Lidard, NASA/GSFC).

4   Challenging new developments supported by leveraging the research community

In FY 2018, seven projects are newly supported, focusing on testing and demonstrating experimental prediction methodologies or systems developed in the broader community for operational purposes, and improving multi-model ensemble prediction systems by utilizing new or higher-resolution models, improved forecast initialization practices, and upgrades to other aspects of the system.
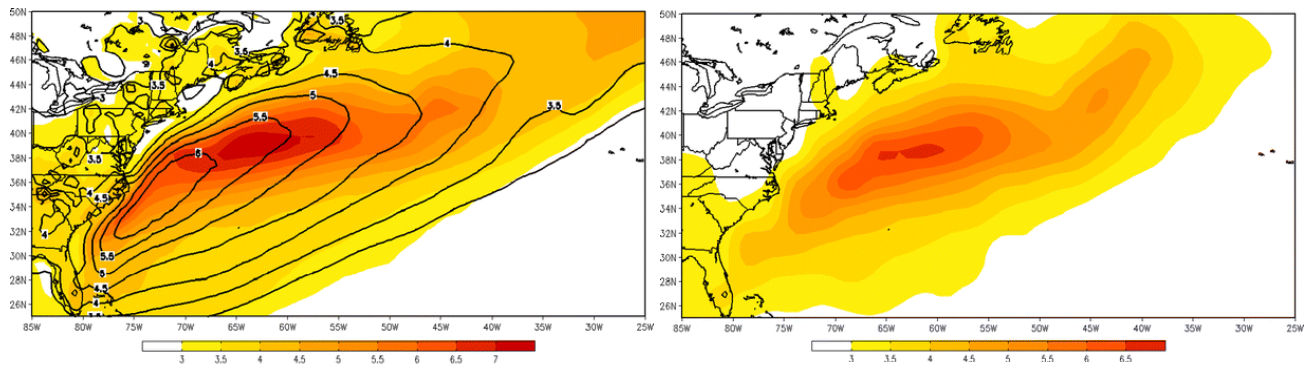
Fig. 7 Time mean precipitation simulations in mm day-1 with low (contours) and high (shaded) model resolutions (left panel), and the climatological precipitation of CPC Merged Analysis of Precipitation (right panel). It demonstrates the presence of resolved ocean eddies modified the mean climate. (Courtesy of B. Kirtman)
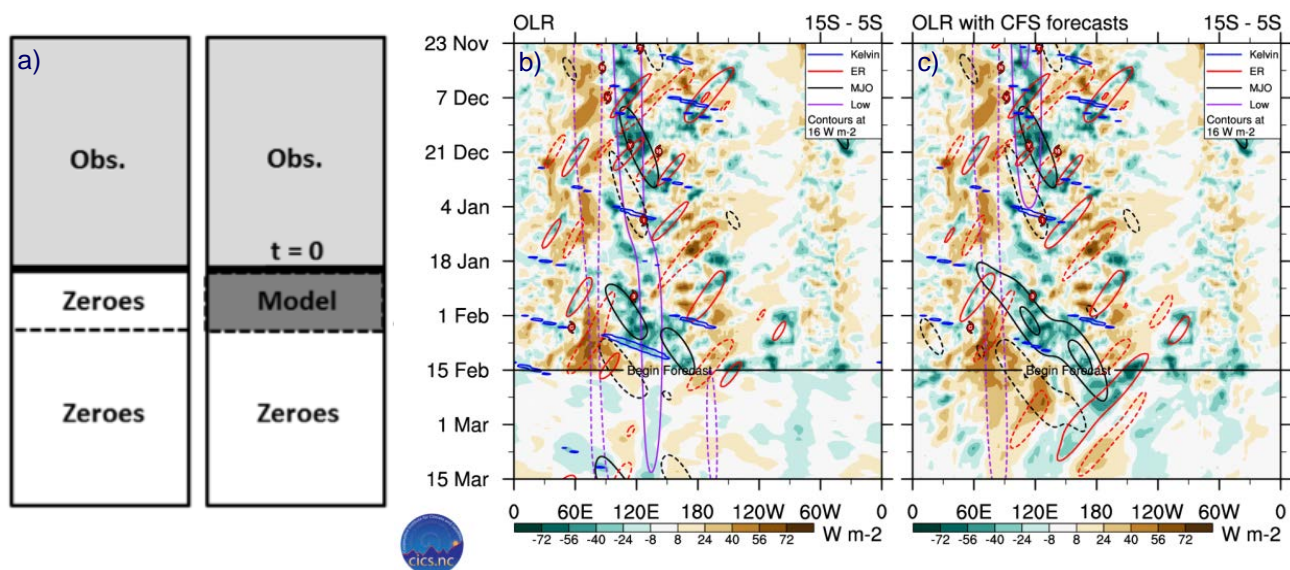
Fig. 8 (a) Schematic comparison between original Wheeler–Weickmann method (left) and the new methodology (right). Latter pads additionally with 45-day CFSv2 forecasts, which are more accurate than the zeros used in former. The new methodology combines recent observations with CFSv2 forecasts for Fourier filtering of the MJO, the low-frequency interannual variability, and convectively coupled equatorial waves, honing the most predictable aspects of the tropical S2S variability while removing less predictable small-scale noise. (b) and (c) compare the two methods using examples from 16 February 2017. The filtered OLR anomalies (contours) are broadly similar in the past, diagnostic data. However, the CFSv2-padded anomalies (see in panel c) maintain higher amplitudes since the CFSv2 is able to simulate these modes to a degree. (Courtesy of C. J. Schreck III)

i) Sensitivity analysis of NMME seasonal predictions to ocean eddy resolving coupled models (PI: B. Kirtman, RSMAS, University of Miami)

Develop ocean eddy resolving global coupled prediction system to test the hypothesis of that the presence of oceanic mesoscale features, i.e. fronts and eddies, significantly modifies local air-sea coupling, which in turn affects the local representation of the predictable large scale climatic features (Fig. 7). Predictions will be made remotely but data given to CPC.

ii) Novel statistical-dynamical forecasts for tropical S2S drivers (PI: C. J. Schreck III, NCICS, North Carolina State University)

Transition tropical S2S diagnostics from the demonstration platform at NCICS.org/mjo (Fig. 8) into the operational environment at CPC.

iii) Predicting atmospheric rivers (AR) and their impacts in weeks 2-5 based on the state of the MJO and QBO (PI: E. A. Barnes, Colorado State University)

Transition to operations the anomalous atmospheric river (AR) frequency forecast tool based on the observed state of the Madden-Julian Oscillation (MJO) and Quasi Biennial Oscillation (QBO). It is demonstrated that robust AR frequency anomalies can be seen more than 4 weeks ahead due to the propagation of the MJO, and the sign of the anomalous frequencies are a strong function of QBO phase as shown in Fig. 9.
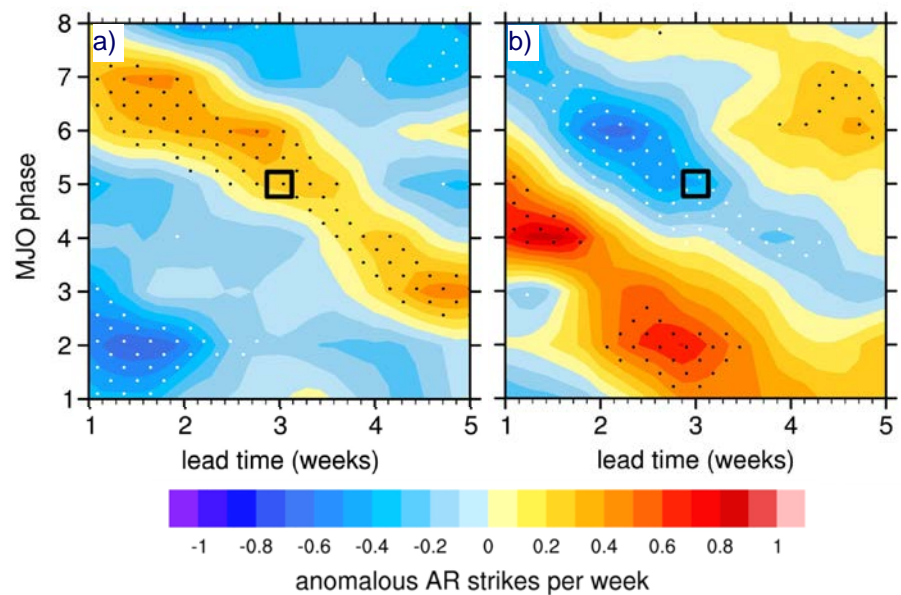
Fig. 9 ERA-Interim composites of anomalous AR strikes-per-week for the Pacific Northwest following days when the MJO was in a particular phase during (a) easterly and (b) westerly QBO periods. (Courtesy of E. A. Barnes)

FY18 new projects will also make following contributions: 1) a new technique for improved MJO prediction (PI: C. Zhang, PMEL, NOAA), 2) probabilistic multimodel, calibrated subseasonal global forecast products (P.I: A. W. Robertson, IRI, Columbia University), 3) S2S prediction improvement with NCAR's CESM2-WACCM (PI: J. H. Richter, NCAR - CGD), and 4) a hybrid statistical-dynamical system for the seamless prediction of daily extremes and S2S climate variability (PI: D. Collins, CPC, NOAA/NWS/NCEP).

5. Remarks

Recent comprehensive skill metric based on all CPC extended to long range outlooks revealed continuous improvement of CPC products, which was inseparable with progresses of ongoing R2O activities. The improvements were reflected in newly implemented systems, tools and products. In view of future challenges, on which researches present to raise prediction skill and hence boost credibility of seasonal-to-subseasonal climate service, we placed hopes on our research partners and people in field with considerable effort, and sufficient and sustained investment to work together on trying to make a break through.

Project new publications

Bell, R. J., and B. P. Kirtman, 2018: Seasonal forecasting of winds, waves and currents in the North Pacific. *J. Operational Ocean*, doi:10.1080/1755876X.2018.1438342.

DelSole, T., L. Trenary, and M. K. Tippett, 2018: The weighted-average lagged ensemble. *J. Adv. Model. Earth Syst*, **9**, 2739-2752, doi:10.1002/2017MS001128.

Lima, L.N., L.P. Pezzi, S.G. Penny, and C. A. S. Tanajura, 2019: An investigation of ocean model uncertainties through ensemble forecast experiments in the Southwest Atlantic Ocean. Journal of Geophysical Research: Oceans, 124, 432-452, https://doi.org/10.1029/2018JC013919

Skubel, R. A., B. P. Kirtman, C. Fallows, and N. Hammerschlag, 2018: Patterns of long-term climate variability and predation rates by a marine apex predator, the white shark Carcharodon carcharias. *Mar. Ecol. Prog. Ser.*, **587**, 129-139, doi:10.3354/meps12424.

Tippett, M. K., L. Trenary, T. DelSole, K. Pegion, and M. L'Heureux, 2018: Sources of bias in the monthly CFSv2 forecast climatology. *J. Appl. Meteor. Climatol.*, **57**, 1111-1121, doi:10.1175/JAMC-D-17-0299.1.

Trenary, L., T. DelSole, M. K. Tippett, and K. Pegion, 2018: Monthly ENSO forecast skill and lagged ensemble size. *J. Adv. Model. Earth Syst*, **10**, 1074-1086, doi:10.1002/2017MS001204.

York, A., U Bhatt, R Thoman, and R. Ziel, 2018: Wildland fire in boreal and Arctic North America, [in "State of the Climate in 2017"], *Bull. Amer. Meteor. Soc.*, **99**, S167-S169, doi:10.1175/2018BAMSStateoftheClimate.1.

Zhang, Q., J. Jin, and L. Zhu, 2018: Modelling of water surface temperature of three lakes on the Tibetan Plateau using a physically based lake model. *Atmosphere-Ocean*, doi:10.1080/07055900.2018.1474085.

Zhu, Y., X. Zhou, W. Li, D. Hou, C. Melhauser, E. Sinsky, M. Pena, B. Fu, H. Guan, W. Kolczynski, R. Wobus, and V. Tallapragada, 2018: Towards the improvement of sub-seasonal prediction in the NCEP Global Ensemble Forecast System (GEFS), *Journal of Geophysical Research*, 6732-6745, doi:10.1029/2018JD028506

Zhu, Y., W. Li, E. Sinsky, H. Guan, X. Zhou, and D. Hou, 2018: An Assessment of subseasonal forecast using extended Global Ensemble Forecast System (GEFS), [in 42nd NOAA Climate Diagnostics and Prediction Workshop Special Issue, Climate Prediction S&T Digest], NWS Science & Technology Infusion Climate Bulletin Supplement, 150-153, https://doi.org/10.7289/V5/CDPW-NWS-42nd-2018.

Understanding the Space-Varying Trends in Global Extreme Precipitation

Saman Armal and Reza Khanbilvardi

Department of Civil Engineering,
NOAA-Cooperative Center for Earth System Sciences and Remote Sensing Technologies,
Center for Water Resources and Environmental Research,
City University of New York (City College), New York, NY

1. Introduction

During the recent years, efforts have been made to investigate the time-varying trends in extreme events as one of the relevant aspects of climate change across different scales (Asadieh and Krakauer 2015; Armal *et al.* 2016; Armal *et al.* 2018a; Najafi *et al.* 2019a; Armal and Al-Suhili, 2019). Yet, there is a little understanding on space-varying trend of extreme rainfall events. For understanding the impact of anthropogenic forcing on occurrence of extremes, researchers (Sillmann *et al.* 2017; Vautard *et al.* 2016; Yiou *et al.* 2017) often separate the indirect effect on changing circulation pattern (also called dynamical process) from thermo-dynamic pathway. The dynamic process is more specific to local scale (Pfahl *et al.* 2017) and is frequently associated with regional anomalous weather pattern. However, it is fairly small compared with the uncertainty that introduced by internal climate variability (Deser *et al.* 2014). Therefore, it is more fruitful to investigate the modes of internal variability, peculiarly characterized by anomalous sea surface temperature and barometric pressure pattern especially quasi-periodically oscillations indices *e.g.* El Niño/Southern Oscillation (ENSO), the Pacific Decadal Oscillation (PDO), the North Atlantic Oscillation (NAO) and other so-called modes of variability (Hartmann *et al.* 2013; Trenberth *et al.* 2015; Najafi *et al.* 2018a; Najafi *et al.* 2018b; Najafi *et al.* 2018c; Armal *et al.* 2018b; Najafi *et al.* 2019b). This study extracts and validates an index to study the space-varying trends in simultaneous extreme precipitation events. It correlates the frequency of simultaneous extremes with Global Surface Anomaly Temperature (GST) as a proxy of thermodynamic pathway, and a number of climate variability modes (ENSO, NAO, PDO and AMO), as a proxy of internal climate variability.
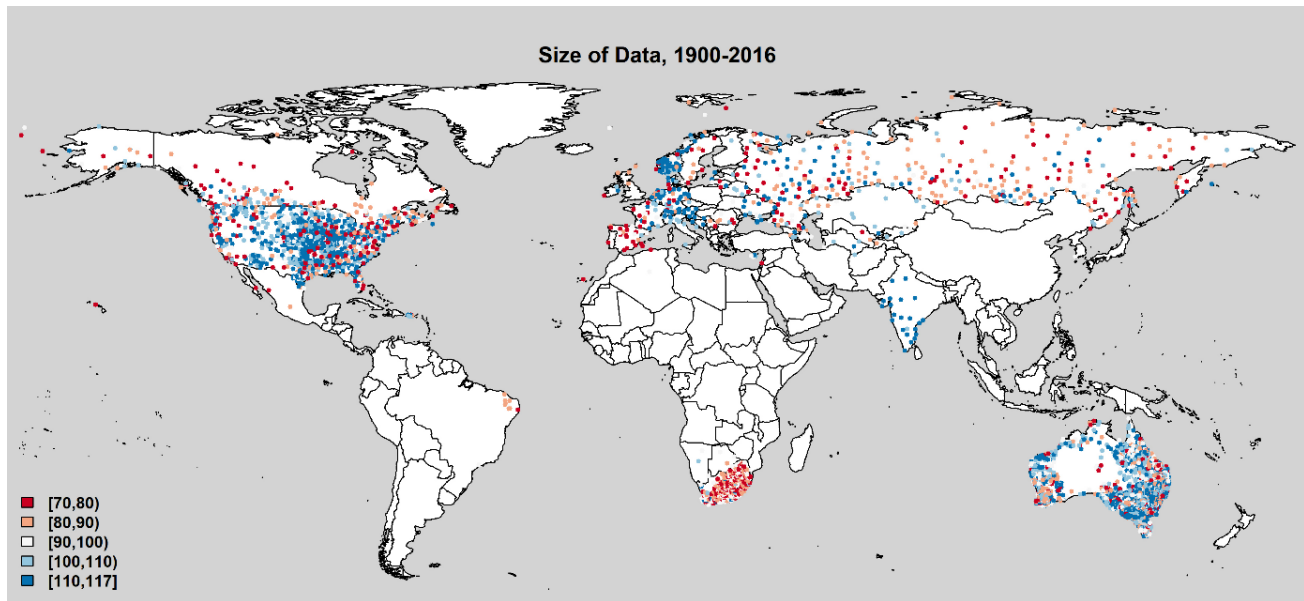
2. Methodology

In a few examples of applying spatial indices, researchers either look at the grids with highest and lowest 30% of the values, associated with the number of wet and dry grids, in each year of global data (Donat *et al.* 2016) or rely on the high percentile index of daily data over limited spatial extent (Fischer and Knutti 2015). The global ratio of daily extremes (GRDE) is designed to aggregate in-situ extremes over space. For each day of data, we consider the total number of stations with rainfall events exceeding a threshold of 99% of the full period. The product data is a time-series of daily total number of stations which are showing a value above 99% threshold. To minimize the effect of data scarcity in our analysis, the number of stations with extreme events is divided by the number of stations with available data:

$$GRDE_d = \frac{\sum_{i=1}^{NS} \delta_{id}}{NS} \quad , \quad \delta_{id}^j = \begin{cases} 1 & if \quad P_{id}^j \geq P_i^* \\ 0 & if \quad P_{id}^j < P_i^* \end{cases}$$

where d is the day index, i is the numerator index for stations with available data, P_{id}^j is the jth daily rainfall of station i in a year, and P_i^* is the rainfall exceeding threshold for that station. NS is the total number of stations with available data in the day d. δ is the binary indicator function.

At first, we implement GRDE aggregation over different continents to extract the top 20 days with higher values. These dates are applied to daily composites of perceptible water content (PWC) anomalies (mean - total

_____

Correspondence to: Saman Armal, Department of Civil Engineering, NOAA-Cooperative Center for Earth System Sciences and Remote Sensing Technologies, Center for Water Resources and Environmental Research, City University of New York (City College), New York, NY 10031; E-mail: sarmal000@citymail.cuny.edu

Fig. 1 We looked at more than 100,000 GHCN (Global Historical Climatology Network - daily database https://www.ncdc.noaa.gov/oa/climate/ghcn-daily/) stations across the globe and extracted the total daily precipitation from those that have data from 1900 - 2016 (117 years). From this data, we selected high-quality stations using the following procedure. First, for each year, if more than 40% of days is missing data, we flag this as a missing year. Next, only stations that have at least 70 years of complete data are selected. This process yielded 6185 stations across the globe.

mean) to perceive whether there is any distinctive circulation pattern over the region (note that the historical climate data starts from 1948, hence the selected dates for composite maps are limited to this period). Moreover, these patterns are compared to the global spatial distribution of stations that experience at least one extreme in the top 20 dates. The extent of anomalous PWC yields information about the occurrence of extremes in rest of the world.

Also, we apply Generalized Extreme Value (GEV) fit distribution on yearly maximum GRDE and inform the location parameters with GST as an indicator for thermodynamic pathway and ENSO, NAO, PDO and AMO as an indicator for dynamical process.

$$GRDE_{y,max} \sim GEV\big(\mu_y \mid GST + ENSO + NAO + PDO + AMO, \sigma, \varepsilon\big)$$

Here μ_y is the location parameter, σ is the scale parameter and ε is the shape parameter. For every continent as well as Northern/Southern hemisphere, we randomly chose 100 blocks with 60-yr size of data, and performed the GEV fit distribution. Furthermore, we exclude the all the estimations which are outside the 95 confidence interval.

3. Results

We present the results of our analysis for three continents: North America, Europe and Australia. Figure 2 indicates the location of global stations that shows at least one day of extreme precipitation in the top 20 GRDE. Fig. 2-a is based on the top 20 days with highest percentage of simultaneous extreme events in North America, Fig. 2-b is based on Europe and Fig. 3-c is based on Australia.

The PWC composite maps identify the anomaly of total water content in the selected days. Unlike Europe, both North America and Australia confirm the occurrence of wide spread extreme rainfall with positive anomaly values of PWC. Notably, in the top 20 GRDE of North America many stations flags with extreme rainfall in Australia. Reciprocally, the same feature is observed in North-west America, in the top 20 GRDE days of Australia. Another possible linkage is evident in the top 20 GRDE of Europe, when many stations in North America are identified with an extreme rainfall. The PWC maps suggest spread of spatial anomalous field across
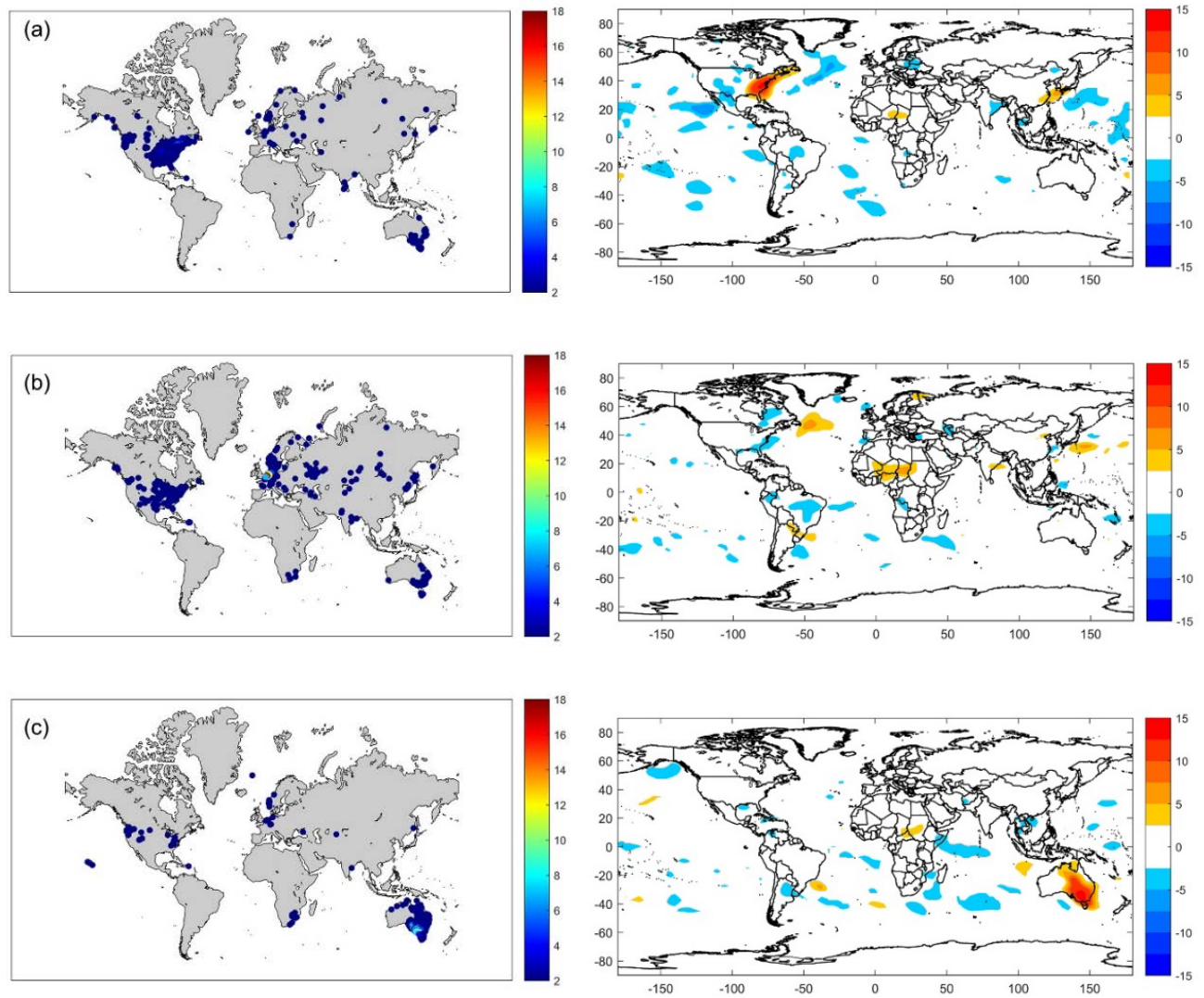
Fig. 2 Continent-based maps of stations with at least one event in the first 20 days of with highest GRDE for (a) North America, (b) Europe and (c) Australia. The corresponding anomaly maps on the right indicate the anomaly of perceptible water content (kg/m^2) in the respective days.

the globe, with no significant impact over Europe. The number of extremes is concentrated over relatively small area and induced by few number of stations.

Figure 3 shows the values obtained for location parameters for different continents. This values are obtained from 100 bootstrapping block over GEV analysis. None of the results suggest the impact of high to medium frequency modes of climate variability on the occurrence of simultaneous extreme rainfall. In Europe/Australia, there is a strong positive/negative correlation between trend in GRDE and global surface temperature anomaly. The response of North America to GST highly varies but the median is close to zero. Moreover, in North America/Australia, positive/negative AMO links to frequency of the simultaneous extreme events. The linkage of AMO variation with strength of Thermohaline Circulation (THM) (García‑García and Ummenhofer 2015) can regulate the climate across the globe and impact the occurrence of global extremes.

References

Armal, S., N. Devineni, and R. Khanbilvardi, 2016: multilevel Poisson regression model to detect trends in frequency of extreme rainfall events. *American Geophysical Union Fall Meeting 2016*, San Francisco, CA, USA, 12–16 December 2016, AGU, Abstract #NH51B-1957.

—, —, and —, 2018a: Trends in extreme rainfall frequency in the contiguous United States: Attribution to climate change and climate variability modes. *J. Climate*, **31**, 369–385, doi:10.1175/JCLI-D-17-0106.1.

—, —, and —, 2018b: New York city's water system performance analysis based on current and projected demands. *American Geophysical Union Fall Meeting 2018*, Washington, DC, USA, 10–14 December 2018, AGU, Abstract #H41I-2167.

— and R. Al-Suhili, 2019: An urban flood inundation model based on cellular automata. *International Journal of Water*, *in press*.

Asadieh, B., and N. Y. Krakauer, 2015: Global trends in extreme precipitation: Climate models versus observations, *Hydrol. Earth Syst. Sci.*, **19**, 877–891, doi:10.5194/hess-19-877-2015.

Deser, C., and Coauthors, 2014: Projecting North American climate over the next 50 years: Uncertainty due to internal variability, *J. Climate*, **27**, 2271–2296, doi:10.1175/JCLI-D-13-00451.1.

Fig. 3 The values of GEV location parameters for North America (top), Europe (middle), and Australia (bottom).

Donat, M. G., and Coauthors, 2016: More extreme precipitation in the world's dry and wet regions, *Nature Climate Change*, **6**, 508–513, doi:10.1038/nclimate2941.

Fischer, E. M., and R. Knutti, 2015: Anthropogenic contribution to global occurrence of heavy-precipitation and high-temperature extremes, *Nature Climate Change*, **5**, 560–564, doi:10.1038/nclimate2617.

García-García, D. and C. C. Ummenhofer, 2015: Multidecadal variability of the continental precipitation annual amplitude driven by AMO and ENSO, *Geophys. Res. Lett.*, **42**, 526–535, doi:10.1002/2014GL062451
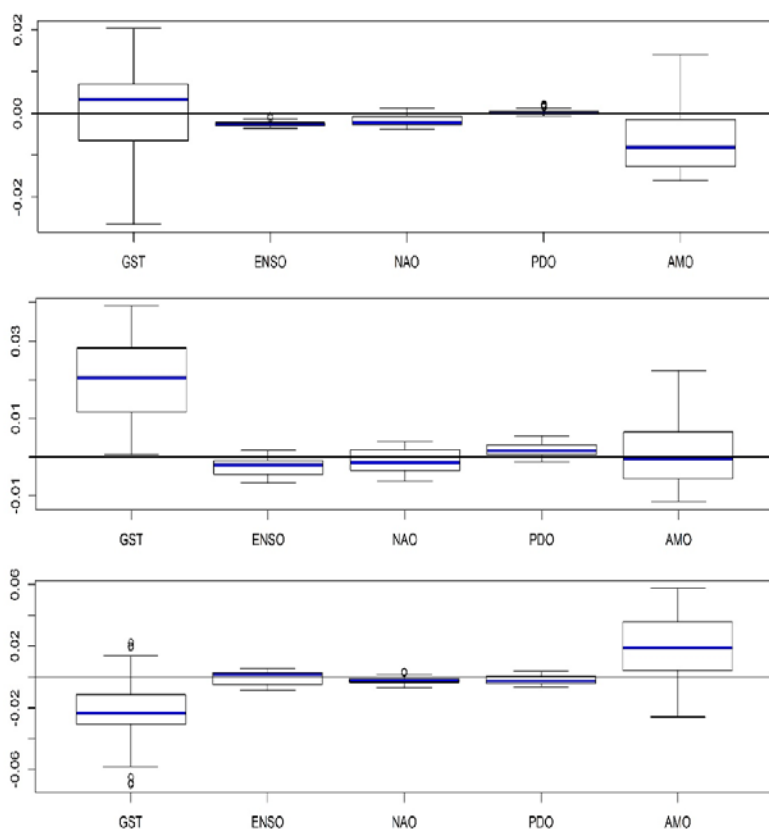
Hartmann, D. L., and Coauthors, 2013: Observations: Atmosphere and surface. *Climate Change 2013: The Physical Science Basis. Contribution of Working Group I to the Fifth Assessment Report of the Intergovernmental Panel on Climate Change*, T. F. Stocker, D. Qin, G.-K. Plattner, M. Tignor, S. K. Allen, J. Boschung, A. Nauels, Y. Xia, V. Bex and P. M. Midgley, Eds., Cambridge University Press, 159–254, doi:10.1017/CBO9781107415324.008.

Najafi, E and R. Khanbilvardi, 2018a: Clustering and trend analysis of global extreme droughts from 1900 to 2014, https://arxiv.org/pdf/1901.00052v2

—, I. Pal, and R. Khanbilvardi, 2018b: Diagnosing extreme drought characteristics across the globe. *NWS Sci. Technol. Infusion Clim. Bull., 42nd NOAA Annu. Clim. Diagn. Predict. Workshop*, 121-125, doi:10.7289/V5/CDPW-NWS-42nd-2018.

—, N. Devineni, R. M. Khanbilvardi, and F. Kogan, 2018c: Understanding the changes in global crop yields through changes in climate and technology. *Earth's Future*, **6**, 410-427, doi:10.1002/2017EF000690

—, I. Pal, and R. Khanbilvardi, 2019a: Climate drives variability and joint variability of global crop yields. *Sci. Total Environ*, **662**, 361–372.

—, —, and —, 2019b: Data of variability and joint variability of global crop yields and their association with climate. *Data in Brief*, **23**, 103,745, doi: https://doi.org/10.1016/j.dib.2019.103745.

Pfahl, S., P. A. O'Gorman, and E. M. Fischer, 2017: Understanding the regional pattern of projected future changes in extreme precipitation, *Nature Climate Change*, **7**, 423–427, doi:10.1038/nclimate3287.

Sillmann, J., and Coauthors, 2017: Understanding, modeling and predicting weather and climate extremes: Challenges and opportunities, *Weather and Climate Extremes*. 18, 65-74, doi:10.1016/j.wace.2017.10.003.

Trenberth, K. E., J. T. Fasullo, and T. G. Shepherd, 2015: Attribution of climate extreme events, *Nature Climate Change*, **5**, 725–730, doi: 10.1038/nclimate2657.

Vautard, R., and Coauthors, 2016: Attribution of human-induced dynamical and thermodynamical contributions in extreme weather events, *Environ. Res. Lett.*, **11**. 1-9, doi:10.1088/1748-9326/11/11/114009.

Yiou, P., and Coauthors, 2017: A statistical framework for conditional extreme event attribution, *Adv. Stat. Clim., Meteorol. Oceanogr.*, **3**, 17–31. doi:10.5194/ascmo-3-17-2017.

APPENDIX

PHOTO GALLERY

43rd NOAA Annual Climate Diagnostics and Prediction Workshop

Santa Barbara, California

23-25 October 2018

Corwin Pavilion

University of California, Santa Barbara
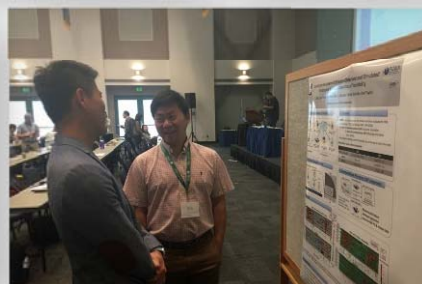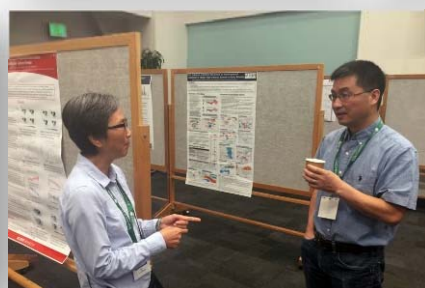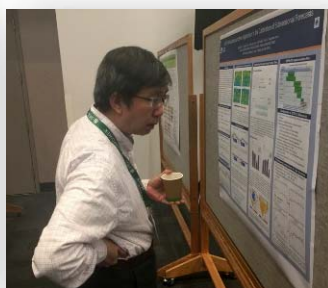
October 23-25, 2018

For complete album

https://www.nws.noaa.gov/ost/climate/STIP/43CDPW/photos.htm

In Session

Invited Talk

Q & A

Poster

Tony Barnston Tribute

Session Break

NWS Science and Technology Infusion Climate Bulletin

Featured Special Collections

(https://www.nws.noaa.gov/ost/STIClimateBulletin/Collections.htm)

Climate Prediction Science and Technology Digest
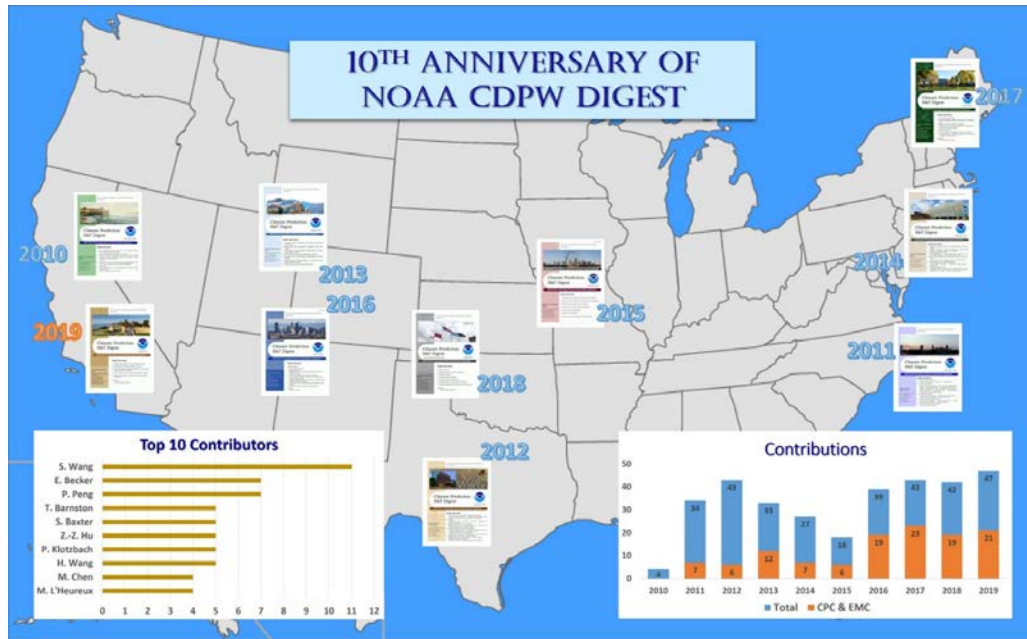
NOAA Climate Test Bed Joint Seminar Series
Extended Summaries Collection Volume
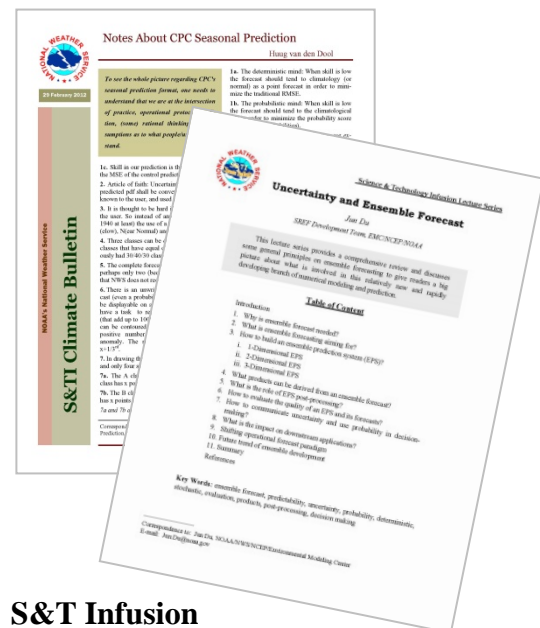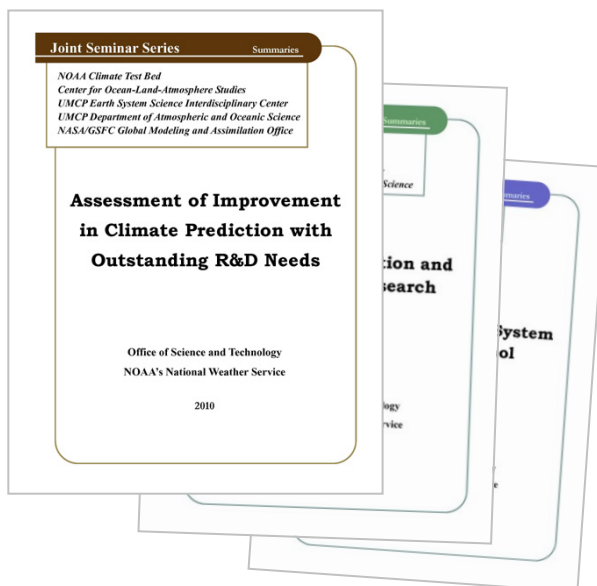
S&T Infusion
Lecture Series & Notes